# Transport in biological systems. Monolithic method for fluid-structure interaction

Chen-Yu Chiang

## To cite this version:

Chen-Yu Chiang. Transport in biological systems. Monolithic method for fluid-structure interaction. Numerical Analysis [math.NA]. Sorbonne Université; National Taiwan University (Taipei), 2019. English. NNT : 2019SORUS477 . tel-02931834

HAL Id: tel-02931834
https://theses.hal.science/tel-02931834v1

Submitted on 7 Sep 2020

ÉCOLE DOCTORALE SCIENCES MATHÉMATIQUES DE PARIS CENTRE
SORBONNE UNIVERSITÉ

DEPARTMENT OF ENGINEERING SCIENCE AND OCEAN ENGINEERING
COLLEGE OF ENGINEERING
NATIONAL TAIWAN UNIVERSITY

## DOCTORAL DISSERTATION

# Transport in biological systems. Monolithic method for fluid–structure interaction

By : **Chen-Yu CHIANG**

Advisors : **Tony W. H. SHEU**, Ph.D. and **Marc THIRIET**, M.D., Ph.D.
Counselor : **Olivier PIRONNEAU**, Ph.D.

Submitted in partial fulfillment of the requirement for
the degree of Doctor of Philosophy
specialized in Engineering Science
at National Taiwan University
and
the degree of Doctor of science,
specialized in Applied Mathematics
at Sorbonne Université

Chen-Yu CHIANG :

Sorbonne Universités, UPMC Univ Paris 06, UMR 7598, Laboratoire Jacques-Louis Lions, F-75005, Paris, France.
Adresse électronique: chiang@ljll.math.upmc.fr, f01525007@ntu.edu.tw

Publications

- 2014, Numerical investigation of chemotaxic phenomenon in incompressible viscous fluid flow.
- 2016, Numerical study of plume patterns in a chemotaxis–diffusion–convection coupling system.
- 2017, Numerical Study of a 3D Eulerian Monolithic Formulation for Incompressible Fluid–Structures Systems.
- 2018, 3D Compressible Structure Immersed in Newtonian Fluid with Eulerian Monolithic Formulation.
- 2018, Computational contact using Eulerian Monolithic Formulation.

Presentation

- 2017, 2nd Symposium du Réseau de Biologie des Systèmes de Sorbonne Université.
- 2017, The 9th tutorial and Workshop on FreeFem++.
- 2018, Invited speaker at 2nd International Conference on Digital Medicine.

Laboratoire Jacques-Louis Lions
Sorbonne Universités, UPMC Univ Paris 06, UMR 7598
Boîte courrier 187
75252 Paris Cedex 05 France

École Doctorale de Sciences Mathématiques de Paris Centre (ED 386)
Sorbonne Universités
Boîte courrier 290
4, Place Jussieu
75252 Paris Cedex 05
France

Scientific Computing and Cardiovascular Simulation Laboratory
Department of Engineering Science and Ocean Engineering
National Taiwan University
No. 1, Sec. 4, Roosevelt Rd., Daan District, Taipei City 106
Taiwan

# Contents

# Objectives

This work is aimed at developing a numerical solver in finite element method with monolithic formulation to solve fluid–structure interaction problems and implementing it on studying transport phenomenon in biological system. The major objectives of this study are to:

1. conceive a monolithic fluid–structure interaction solver;
2. design and implement a proper scheme related to fluid–structure interaction with possible contact;
3. verify and validate;
4. apply to blood flow in deformable veins, that is, investigate coupling of blood dynamics with veins mechanics (Navier–Stokes equations coupled with wall mechanics), focusing on venous valve motion.

It is divided into 6 chapters.

1. Introduction and state of the art
2. Numerical analysis of a monolithic formulation
3. Implementation of a monolithic method in FreeFEM++
4. Verification and validation
5. Computational contact mechanism
6. Flow in valved veins of inferior limbs

# Chapter 1

# Introduction and state of the art

## Contents

**NOMENCLATURE**

| | | | |
|---|---|---|---|
| $f_c$ | heart rate | $q$ | blood flow rate |
| $\mu$ | dynamic viscosity | $R_h$ | hydraulic radius of the blood vessel |
| $p$ | transmural pressure | $\xi$ | the head loss coefficients |
| $\delta$ | boundary layer thickness | $\delta_S$ | stokes boundary layer thickness |
| $\omega$ | angular frequency of periodic flow | $V_{\text{inf}}$ | free stream velocity |
| $Le$ | entry length | $L$ | distance from the tube entry |
| $R$ | vessel radius | $V_{ax}(L)$ | axial velocity varied with respect to $L$ |
| $\nu_T(\mathbf{x},t)$ | eddy viscosity | $T$ | cycle period |
| $\kappa_{vp}$ | ratio between vessel bore and cell size | $\gamma$ | shear rate |
| $\nu$ | kinematic viscosity ($\nu = \mu/\rho$) | $\rho$ | mass density |
| $\mathbf{v}$ | velocity vector | $\sigma$ | stress tensor |
| $\mathbf{d}$ | displacement vector | $J$ | the Jacobian of the deformation |
| $p_i, p_e$ | the internal/external pressure | $\mathbf{f}$ | volumic force |
| $g$ | the gravity constant | $R_c$ | curvature radius |
| Re | Reynolds number (Re= $VL/\nu$) | Sto | Stokes number (Sto= $R/\delta_S$) |
| St | Strouhal number (St= $\omega L/V$) | De | Dean number (De= $\left(\frac{R_h}{R_c}\right)^{1/2}$ ×Re) |

This chapter yields biological and mechanical information on blood circulation as well as introduces some computational aspect of blood flow in deformable vessels. Sect. 1.1 provides the fundamental features of blood and vascular wall composition. Blood circulatory circuits are briefly described in Sect. 1.2. The literature survey related to blood flow mechanics in deformable vessels is split into a fluid (Sect. 1.3.1) and structure part (Sect. 1.3.2). Fluid–structure interaction (FSI) is introduced in Sect. 1.4 with the governing equations of fluid and structure, tube law of vascular deformation, formulation of discretized system equations, and corresponding numerical approaches of interface tracking. At the end of this chapter, Sect. 1.5 collects literature survey of modeling and simulation methods used in blood circulatory circuit.

## 1.1 Biological materials

Veins contain about 70% blood. These blood vessels are both distensible, serving as blood buffer, and collapsible, when the transmural pressure decays below zero, that is, the reference pressure that determines the unstressed configuration.

### 1.1.1 Blood — A flowing biological tissue

The blood performs three major functions: (1) transport of nutrient and waste throughout the body; (2) regulation of bulk equilibria (homeostasis); and (3) body immune defense against foreign bodies. Blood supplies oxygen and removes carbon dioxide and products of cell metabolisms toward lungs and purification organs (liver, kidneys, and skin). Blood transmits metabolism factors and messengers. Blood volume and electrolyte concentrations are regulated by a set of hormones. Blood maintains the body temperature

($36.4 - 37.1\,^{\circ}$C) and $H^+$ concentration, controlling blood pH, which remains in the range 7.35 to 7.45. The blood is involved in the body defense against infection, transporting immune cells and antibodies, and in repair processes after injury. It limits blood losses by clotting.

Blood contains cells and plasma (Table 1.1). Blood cells include red blood capsules (RBC), leukocytes, and platelets. Blood rheology is introduced in Sect. 1.3.2; some blood mechanical properties are collected in Table 1.13.

Table 1.1: Blood composition and main characteristics in healthy adult man. The blood cells include erythrocytes (red blood cells), leukocytes (white blood cells) and platelets. Leukocytes are divided into five classes based on morphological and tinctorial characteristics. Neutrophils, eosinophils, and basophils are known as granulocytes due to granules in the cytoplasm. Monocytes and lymphocytes are involved in the body scavenging and defense. The blood plasma consists of water (90 %), the remainder being electrolytes (sodium ($Na^+$), 142 mmol per liter, chloride ($Cl^-$), 102 mmol/l, and potassium ($K^+$ ), 5 mmol/l ), carbohydrates, lipids, and amino acids, etc.

| | |
|---|---|
| Erythrocytes | $4.5 - 5.2 \times 10^6\,/mm^3$ |
| Hematocrit | $41 - 47\,\%$ |
| Leukocytes | $4 - 10 \times 10^3\,/mm^3$ |
| Neutrophils | $40 - 70\,\%$ |
| Eosinophils | $1 - 2\,\%$ |
| Basophils | $0.5 - 1\,\%$ |
| Lymphocytes | $20 - 40\,\%$ |
| Monocytes | $2 - 10\,\%$ |
| Platelets | $2 - 4 \times 10^5\,/mm^3$ |
| ions | $295 - 310\,mEq/l$ |
| peptides | $70 - 80\,g/l$ |
| Lipids | $5 - 7\,g/l$ |
| Glucids | $0.8 - 1.1\,g/l$ |
| Osmotic pressure | $280 - 300\,mosm$ |
| pH | $7.39 - 7.41$ |

### Plasma

Plasma represents approximately *55 % of the blood volume*. Hematocrit (Ht) is the amount in percent of packed cells (Ht $38 - 46\,\%$ in women, $42 - 53\,\%$ in men). Plasma is mainly composed of water, a suspending fluid (or solvent) for various solutes (Table 1.2). Plasma contains 92 % water, 7 % proteins (7 g/dl), 0.9 % electrolytes, and other substances.

Table 1.2: Plasma approximate composition (%).

| | |
|---|---|
| Water | 92 |
| Proteins | 7 |
| Electrolytes | 0.9 |
| Lipids | 0.6 |
| Glucids | 0.1 |

### Electrolytes

Electrolytes, or ions, contribute to the *osmotic pressure* and hence transport from microvasculature to tissue and conversely. Their concentrations is mainly regulated by the kidneys. Major electrolytes are cations $Na^+$, $K^+$, $Ca^{++}$, $Mg^{++}$, and anions $HCO_3^-$, $Cl^-$, $HPO_4^{2-}$, and $SO_4^{2-}$. Cations and anions are unevenly distributed in body fluid compartments. Sodium ion ($Na^+$) is the major cation and chloride ($Cl^-$) the major anion outside the cell. Inside the cell, potassium ion ($K^+$) is the major cation and phosphate ($HPO_4^{2-}$) the major anion. At physiological pH, proteins are negatively charged.

Ion transport through the cell membrane between the body fluid compartments require specialized plasmalemmal proteins. Ion displacements in different body's compartments affect *blood volume*.

### Proteins

Serum is plasma without *fibrinogen* (195 – 365 mg/dl) and other clotting factors. Fibrinogen acts on *RBC aggregation*, hence in blood rheology and coagulation. Serum proteins are composed of *albumin* and *globulins*. Albumin is the main plasma protein (3.3 – 4.5 g/dl) synthetized in the liver. It binds many small molecules for transport through the blood and participates in blood colloidal osmotic pressure, which keeps fluids within the vascular circuit. As does fibrinogen, globulins induce *reversible RBC aggregation* in stagnant blood regions.

### Plasma lipids and lipoproteins

Lipoproteins carry water-insoluble triglycerides and cholesteryl esters. However, core lipids can move between lipoproteins. The four main types of circulating lipoproteins, which differ in size, density, and content, include chylomicrons, very-low–density (VLDL), low-density (LDL), and high-density lipoproteins (HDL).

### Glucids

Glycemia ($\sim$1 g/l),the blood glucose concentration, depends on the exogenous supply and degradation of hepatic glycogen. Glycemia is controlled by two pancreatic hormones, insulin and glucagon. Insulin decreases glucose level by cell uptake and storage, especially in the liver and muscles. Glucagon increases glucose concentration.

### Blood gas

Blood circulation is aimed at carrying dissolved, transformed, and attached gas molecules, oxygen and carbon dioxide. Coupling between breathing and blood flow is aimed at conveying $O_2$ from atmosphere to blood and removes $CO_2$ from cells to ambient air. Oxygen binds to a suitable transporter in erythrocytes, hemoglobin. Oxygen-carrying capacity is related to the quantity of oxygen transported by hemoglobin.

### Blood cells

RBCs, leukocytes, and platelets constitute the pool of circulating cells and pseudo-cells (Table 1.3). Red blood capsules (RBCs) are mainly devoted to *blood gas transport*, especially oxygen. When the demand for oxygen changes, signals are detected and transmitted so that the supply of oxygen by the cardiorespiratory system varies to match the demand.

Leukocytes coordinate the immune response. Platelets are cell fragments that participate in blood coagulation and inflammation.

### Leukocytes

Leukocytes, or white blood cells (WBC), play a role in immune defense. Five major types of leukocytes exist, three types of granulocytes, which have about the same size, neutrophils, eosinophils and basophils, and two types of agranular leukocytes, lymphocytes and monocytes. Granulocytes are innate immune cells that contain granules involved in immune defense. WBC life span in blood is several days.

### Platelets

Platelets (size $2--4\mu$m) are cell fragments involved in coagulation. The average life time is 10 days. Platelet activation can be affected by hemodynamic forces. The usual concentration is equal to $250-500\times 10^3\,/mm^3$.

### Red blood capsules

Red blood capsule (nonnucleated cell) is a hemoglobin (Hb) solution bounded by a flexible membrane. In its undeformed state, it has a biconcave disc shape with a greater thickness in its outer ring (diameter $7.7\pm 0.7\mu$m, central and peripheral thickness $1.4\pm 0.5\mu$m and $2.8\pm 0.5\mu$m, aspect ratio $\sim 0.4$, surface $\sim 140\mu\text{m}^2$, volume $\sim 90\mu\text{m}^3$, membrane thickness $\sim 0.02\mu$m). It deforms with a negligable bending resistance, taking a parachute shape in tiny capillaries. Its mass density is equal to about 1100 kg/m$^3$. It lives an average of 120 days. The RBC number depends on age and gender ($4.2-5.5\times 10^6\,/\text{mm}^3$ in women and $4.5-6.2\times 10^6\,/\text{mm}^3$ in men).

Blood rheology is influenced by RBCs due to their amount (97% of total blood cell volume). For a healthy person, that is, in the absence of stagnant flow region, it is reasonable to consider blood as a Newtonian fluid as well as homogeneous in large blood vessels because the size of blood cells is negligible compared to the radius of vessels. In present study, blood circulation of healthy people is studied; selection of model for blood flow is shown in section 1.4.1.

Table 1.3: Blood cell approximated geometry and relative concentration.

| Blood cell | Quantity (/mm$^3$) | Relative proportion | Size ($\mu$m) | Cell volume percentage |
|---|---|---|---|---|
| RBC | $5 \times 10^6$ | 1 | $\sim 8$ | 97% |
| Leukocyte | $5 \times 10^3$ | $10^{-3}$ | $\sim 15$ | 2% |
| Platelet | $3 \times 10^5$ | $6 \times 10^{-2}$ | $\sim 3$ | 1% |

### 1.1.2 Vascular wall composition

The wall structure of large blood vessels (macrociculation), the target of the present study, is composed of three layers and two laminae.

- The vascular lumen is covered by a monolayer of endothelial cells (ECs) that form the internal tunica of *intima*. The endothelium is supported at its abluminal surface by a basal lamina, that separates it form the thin subendothelial layer of connective tissue in normal conditions, that is, in the absence of intimal hyperplasia and atherosclerosis. The endothelium modulates wall structure and function. Endothelial cells have a shear-dependent shape ($50-100 \times 10 \times 0.5-2\mu$m).

- The *internal elastic lamina* (IEL) delimits the intima from the media. The fenestrated internal elastic lamina, through pores of which moves water and solutes and ECs contact adjoining medial smooth myocytes (SMCs). Cells thus communicate and possibly migrate through these pores. The number of fenestrations is greater at branching points.

- The middle layer—*media*— contains bands of smooth muscle cells (SMCs) separated by elastic lamellae. Action potentials from advential nerve endings trigger SMC contraction after a delay ranging from 80 to 100 ms that lasts from 10 to 15 s.

- The *external elastic lamina* (EEL) is located between the media and adventitia. The external elastic lamina is not always well-defined.

- The thick outermost layer, *adventitia*, is made of connective tissue. In large vessels, the adventitia contains nerves, vasa vasorum, which irrigate internal part of the vascular wall, and lymphatic vessels.

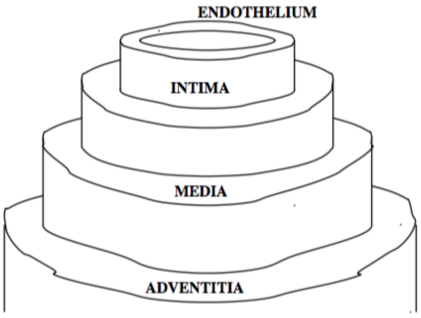

Figure 1.1: Wall tunicae. The media (intermediate layer) is bounded by the internal and external elastic lamina from the intima (inner layer) and adventitia (outer layer), respectively.

In general, vein walls have nearly the same thickness than artery walls for a given branch order, but the veinous and arterial cross section are elliptical and circular, respectively. The venous intima is very thin. The internal and external elastic laminae are either absent or very thin. The venous media is thinner than the adventitia.

To summarize, the difference between a vein and its associated artery walls is listed in the Table 1.4.

Table 1.4: Comparison between a vein and its associated artery walls.

| | Artery | Vein |
|---|---|---|
| Shape | Circular | Elliptical |
| Wall | Thick | Thin |
| Intima | | Very thin |
| Media | Prominent | Weak |
| IEL | | Quasi–absent |

Some selected properties of veins (superficial, deep, and perforating veins) and arteries (aortic arch and posterior tibial artery) are collected in Tables 1.5 and 1.6 from literature data [1–9]. Quantifying properties of vessels is not a trivial task, as they depend on numerous factors, such as age, gender, height, and weight. Cumulative pressure difference in arteries is about 10% and in arterioles 40–60%, whereas in veins it is about 15% and venules 8-10%.

## 1.2 Blood circulatory circuit

Blood circulation (Fig. 1.2) is composed of two serial circuits, systemic and pulmonary, irriagated by two apposed synchronous pumps, the left and right heart, respectively.

In the systemic circulation, the one targeted by the present study, blood flows from the left ventricle to aorta, arteries, arterioles, and capillaries, and come back to the right atrium

Table 1.5: Material data of veins [8, 9]

| | superficial vein (great saphenous vein) | deep vein (femoral vein) | perforating vein |
|---|---|---|---|
| diameter (cm) | 0.776 | 1.36 | 0.35 |
| length (cm) | 32 | 18.9 | |
| elasticity (dyn/cm$^2$) | 4.0 | 2.0 | |
| area (cm$^2$) | 0.473 | 1.453 | |
| thickness (cm) | 0.01 | 0.025 | |

Table 1.6: Material data of arteries [8]

| | aortic arch | popliteal artery |
|---|---|---|
| diameter (cm) | 1.095 | 0.202 |
| length (cm) | 2.95 | 9.5 |
| elasticity (dyn/cm$^2$) | 4.0 | 4.0 |
| area (cm$^2$) | 3.764 | 0.138 |
| thickness (cm) | 0.219 | 0.047 |

through venules and veins.

### 1.2.1 Heart

Two cardiac pumps propel blood into the pulmonary and systemic circulation. They are combined into a single muscular organ to synchronously beat. Due to pressure differences between the vascular entry and exit, atria are auxiliary chambers that allow rapid ventricle filling, especially at rest when the cardiac frequency is low.

*Cardiac output* (CO) is the blood volume that crosses the aortic valve per unit of time. In a healthy person at rest, cardiac output ranges from 5 to 6 $l/min$. Cardiac output is quantified by multiplying the *stroke volume*, the difference between the end-diastolic volume (EDV) and end-systolic volume (ESV; Table 1.7), by the heart rate (CO=SV$\times f_c$).

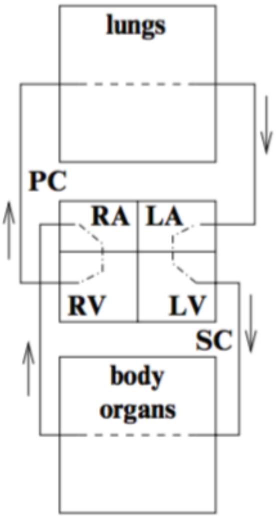

Figure 1.2: Pulmonary (PC) and systemic (SC) circulation. The blood is conveyed from the drainage veins of the systemic circulation to the right atrium (RA). It is then convected into the right ventricle (RV) and expelled into the arteries of the pulmonary circulation for oxygenation into the lungs. The oxygenated blood is sent to the left atrium (LA) via the pulmonary veins. It then enters into the left ventricle (LV) to be propelled into the arteries of the systemic circulation, which distribute blood to every body organ (including heart and lungs) for energy and nutrient supply and waste removal.

The stroke volume is related to myocardial contraction force and venous return. The stroke volume is the difference between the end–diastolic volume (EDV) and end–systolic volume (ESV; Table 1.7). The ratios of blood volume to SV in the serial compartments of both systemic and pulmonary circulations are shown in Table 1.8.

Table 1.7: Physiological quantities at rest in healthy subjects: $f_c$ decreases and then increases with aging; SV decreases with aging ($q \sim$6.5 l/min at 30 years old and $q \sim$ 4 l/mn at 70 years old).

| | |
|---|---|
| EDV | 70–150 ml |
| ESV | 20–50 ml |
| SEV | 50–100 ml |
| $f_c$ | 60–80 beats/min, 1–1.3 Hz |
| $q$ | 4–7 l/min (70–120 ml/s) |
| ejection fraction | 60–80 % |

Various factors determine cardiac output. *Preload* corresponds to a stretching force exerted on the myocardium at the end of diastole imposed by the ventricular blood volume. *Afterload* is the force that needs to be overcome for ventricular ejection. Myocardial contractility is affected by different molecules. As $f_c$ increases, cardiac output rises until a

Table 1.8: Approximative blood compartment volume relative to SEV (%) with SEV of 80 ml and total volume 4.4 l.

| Pulmonary circulation | 16.3 |
|---|---|
| Arteries | 5 |
| Capillaries | 0.8 |
| Veins | 10.5 |
| Systemic circulation | 38.7 |
| Aorta | 1.3 |
| Arteries | 5.6 |
| Capillaries | 3.7 |
| Veins | 28.7 |

critical $f_c$ is reached; then it decreases.

The heart has a chaotic behavior. Its non-periodic behavior characterizes a pump able to quickly react to any changes of the body's environment. The normal heartbeat indeed exhibits complex nonlinear dynamics. At the opposite, stable, periodic cardiac dynamics gives a bad prognosis. A decay in random variability over time, which is associated with a weaker form of chaos, is indicative of congestive heart failure [10]. This feature, positive with respect to heart function, is a handicap in signal and image processing, that is, for ensemble averaging used to improve the signal-to-noise ratio. Variantions of pressure and flow rate during the cardiac cycles are plotted in Fig. 1.3.

### 1.2.2 Windkessel effect

Windkessel effect accounts for the interaction between the stroke volume and the compliance of the aorta and large elastic arteries, the distensibility of large elastic arteries operating as a capacitor. Elastic arteries distend when blood pressure rises during systole and recoil when blood pressure falls during diastole. Blood stored in elastic arteries during systole is restituted during diastole in both direction; the coronary arterial flow is larger during diastole than systole.

The windkessel effect enables transition from a starting–stopping flow to a permanent pulsatile flow during the entire acrdiac cycle. Otto Frank developed the concept and provided a firm mathematical f oundation [11].

### 1.2.3 Macrocirculation

The blood pressure maintains a suitable blood flow, which is distributed among the different parts of the body. Blood irrigates the heart pump, brain (control center), endocrine organ (remote regulation), bone marrow (source of blood cells), lungs (site of gas exchange), kidneys (blood filter), liver (purifier), digestive tract (food processor), muscles (body motion), etc.

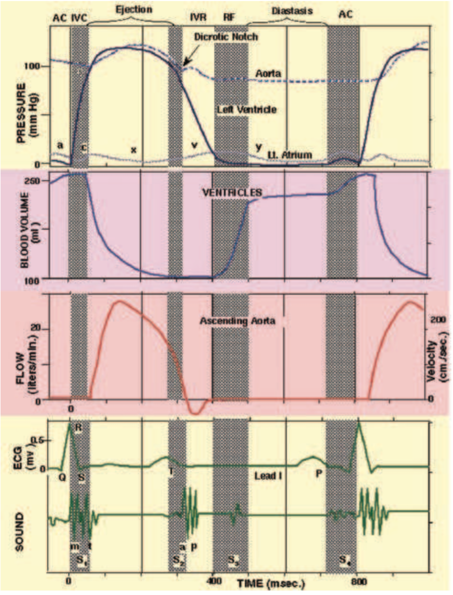

Figure 1.3: Cardiac cycle. Evolution of the pressure in the left cardiac cavities and aorta (top), of left ventricle volume (second row), aortic flow (third row), and ECG trace and phonocardiogram (bottom; from [**?**]).

Beyond large arteries, blood pressure abruptly drops and the systolodiastolic pressure difference decays. The major pressure drop occurs mostly in small arteries and arterioles (resistance vessels). In the venous bed, most of the pressure decrease is observed in venules with little further drop in large veins. Therefore, a small pressure difference suffices to fill the right atrium.

Blood velocity decreases from the arteries, with a peak of $O(10 \text{ cm/s})$, to capillaries with a magnitude of $O(0.1 \text{ mm/s})$.

The pressure in the pulmonary circulation is much lower than that in systemic circulation. Therefore, the right ventricular myocardial is much weaker than the left one. Nonetheless, the mass conservation principle states that the flow rate in the pulmonary circulation is identical to that in the systemic one, the pulmonary resistances being smaller in normal conditions.

### 1.2.4 Microcirculation

Microcirculation contains four main compartments: arterioles, capillaries, venules, and terminal lymphatic vessels. It regulates blood flow distribution within the organs, transcapillary exchanges, and removal of cell wastes.

Arterioles are small precapillary resistance vessels. They are innervated by sympathetic adrenergic fibers and highly responsive to sympathetic $\alpha 1$ and $\alpha 2$ postjunctional receptor stimulation that causes vasoconstriction. They are thus a major site for systemic vascular resistance (SVR). The primary function is nutrient delivery and catabolite washout according to organ needs. Precapillary sphincters can regulate the number of perfused capillaries.

Venules are collecting vessels. Sympathetic innervation of larger venules can affect venular tone and regulate capillary hydrostatic pressure.

The capillary circulation is characterized by: (1) a particle flow, the flowing cell size being similar to that of capillary bore; (2) a low flow velocity; (3) existence of a lubrifiaction layer and plasma skimming; and (4) a short distance between the capillary lumen and cells. It is adapted to molecular exchanges (Table 1.9). Capillaries indeed are the primary site of exchange for fluid, electrolytes, gases, and macromolecules by para- and transcellular transfer.

Table 1.9: Main features of the capillary circulation.

| | |
|---|---|
| Length | $0.2-0.4$ mm |
| Radius | 4 $\mu$m |
| Transient time | $0.6-3$ s |
| Pressure | $3.5-4$ kPa (arteriolar side)<br>$1.5-2.9$ kPa (venular side) |
| Mean velocity | $\leq 1$ mm |
| Viscosity | $\mu=\mu(\mathrm{R}_h,\mathrm{Ht})$ (Fahraeus–Lindqvist effect) |

A computational model of deformable RBCs (bioconcave particles) in blood (Newtonian fluid) is considered in study [12].

## 1.3 Mechanical aspects

Blood flow in large vessels is unsteady developing laminar 3D process, due to the succession of bends, branching and merging points and unsteady conditions set by the left ventricle, that is, at the arterial entry station, as well as breathing and right ventricle, that is, at the venous exit station.

### 1.3.1 Main blood flow properties

Due to wall friction, the near–wall fluid particles slow down, whereas the fluid particles in the core accelerate. Viscous forces are dominant in the boundary layer, whereas inertia forces are greater in the core. In the boundary layer, the fluid particles then respond to the pressure time changes with a phase lag with respect to those in the core flow (Table 1.10).

The vasculature is made of successive geometrical singularities characterized by a more or less strong curvature angles, sespecially large in the aortic arch and intracranial segment of the internal carotid artery. Bend represents the most simple basic unit of the circulatory circuit.

Energy dissipation is generated by fluid shearing within the vessel lumen. In addition, kinetic energy changes result from bend, taper, branching, merging, with possible flow separation.

Table 1.10: Flow response to the imposed pressure difference ($p(t)$).

| | |
|---|---|
| Near wall | Viscosity–dominant pattern<br>Important phase lag |
| Boundary layer | Inertia balances viscosity<br>Moderate phase lag |
| Core | Inertia-dominant pattern<br>Quick response<br>Small phase lag |

The pressure loss in bends, embranchments, and confluences depends on: (1) vessel caliber, (2) respective flow rates, (3) curvature angle and branching/merging angles, (4) wall roughness, and (5) fluid physical properties.

The influence agents can be combined into dimensionless ratios (curvature ratio, area ratio, flow distribution, head loss/friction coefficient, Reynolds number, Dean number, etc.). Values of the head loss coefficient $\zeta$ in various types of singular vessel geometries in steady flow can be found in Idel'cik's textbook [13].

In addition to bends, embranchments, and junctions, changes in cross-section along the vessel length, such as those as in straight transition zones of planar symmetrical vessel bifurcation and straight collapsed segments, also generates 3D flows. However, the types of the local velocity fields projected in the cross–section plane, the so–called virtual *secondary motion*, differs whether they are produced by vessel curvature or gradual change in transverse shape.

### Unsteady flow–pulsatile

In pulsatile flow, two boundary layer thicknesses $\delta_S$ and $\delta$ are assessed either from the balance between the inertia forces associated with the local acceleration in the core flow $\propto \rho^f \omega V_\infty$ and the viscous forces in the boundary layer $\propto \mu V_\infty/\delta_1^2$ ($\mu$: fluid dynamic viscosity, $V_\infty$: free stream velocity) or from the balance between the inertia forces due to the convective acceleration in the boundary layer and the viscous forces respectively: $\delta_S \propto (\nu/\omega)^{1/2}$ and $\delta \propto (\nu L/V_\infty)^{1/2}$. $\delta_1 = \delta_2$ when $z \equiv L_+ = 2.64\, V_\infty/\omega$. When $z < L_+$, the temporal inertia forces are dominant; when $z > L_+$, the convective inertia forces are greater.

### Cardiac cycle

The heart beat is a two-stage pumping over a period of about 1 second or less: a longer diastole and systole. More precisely, the heart rhythm focuses on left ventricle activity, which consists of four main phases: (1) isovolumetric relaxation (IR), with closed atrioventricular and ventriculoarterial valves, which reduces the ventricular pressure below the atrial one to enable filling; (2) ventricular filling (VF), with open atrioventricular valves and closed ventriculoarterial valves; (3) isovolumetric contraction (IC), with closed atrioventricular and ventriculoarterial valves, which raises the ventricular pressure above the aortic one, preparing blood ejection; and (4) systolic ejection (SE), with closed atrioventricular valves and open ventriculoarterial valves. Both VF and SE can be subdivided into rapid and reduced subperiods (rapid [RVF] and slow ventricular filling [SVF] and rapid [RSE] and slow systolic ejection [SSE]). With possible atrial contraction (AC), mechanical events are divided into seven phases. Durations of these four phases of the cardiac cycle are given in Table 1.11.

Table 1.11: Duration (ms) of the four main phases of the cardiac (left ventricle) cycle ($f_c$ = 1.25 Hz, i.e., 75 beats/mn).

| Phase | Cycle time | Duration | Starting event |
|---|---|---|---|
| IC | 0–50 | 50 | Mitral valve closure<br>ECG R wave peak |
| SE | 50–300 | 250 | Aortic valve opening |
| IR | 300–400 | 100 | Aortic valve closure |
| VF | 400–800 | 400 | Mitral valve opening |

### Upstream and downstream effect

Blood conveyed in bends affects the flow pattern upstream and downstream. Therefore, boundary conditions should be set at distance from the computational fluid domain. Moreover, a transverse pressure gradient created by vessel curvature is not compatible with a stress-free condition.

### Developing flow – entry length

In straight pipes conveying a steady flow of a Newtonian fluid, two flow regions can be defined: (1) a developing flow region in a tube length equal to the entry length (Le), where the pressure drop nonlinearly, and (2) a fully developed flow region characterized by an invariant velocity distribution in the cross–section and a constant pressure drop.

In entry steady flows, the boundary layer of thickness $\delta \propto (\nu L/V)^{1/2}$ ($L$: distance from the tube entry) grows. In fully developed flows, the boundary layer spreads across the whole pipe lumen.

The entry length in pulsatile flow in a straight rigid cylindrical pipe of circular cross–section has been found to have similar expression as for the steady flow, using $\mathrm{Le}/\delta\mathrm{Re}(\delta)$ rather than $\mathrm{Le}/R\mathrm{Re}(R)$ when $\mathrm{Sto} \leq 14$ [14].

The entry length in a straight tube conveying a steady flow can be defined by $(v_{ax}(\infty) - v_{ax}(\mathrm{Le})/v_{ax}(\infty) \leq 0.01$. Similarly, the entry length in any periodic flow of amplitude $V_q$ can be defined by the centerline velocity, whatever the time $t$, using the proposed ratio $(v_{ax}(\infty,t) - v_{ax}(\mathrm{Le},t))/V_q$ [15]. Expressions of $\mathrm{Le}/(R\mathrm{Re}R)$ with respect to Sto have been proposed, knowing that, for a given Sto, the value of $\mathrm{Le}/(R\mathrm{Re}R)$ can vary according to the cycle phase [16].

### Flow stability

A stable flow is one in which any small disturbance is spontaneously eliminated. Strong local pressure gradients, velocity profile inflections, and shear reversals affect the flow stability. A major source of instabilities is vortex production. Vortices arise from concentrated–vorticity regions.

A disturbed flow is characterized by transient instabilities, which decay as they propagate downstream, due to the dissipative action of the viscous forces. The development of velocity/vorticity perturbations in the flow, with a characteristic magnitude $\varepsilon V*$, can lead to a transitional flow. Transitional flow is defined by preserved perturbations.

Turbulent motions are characterizd by a nonlinear highly dissipative process associated with random motions, 3D fluctuation velocities, and high diffusivity, which is accounted for by an eddy viscosity $\nu_T(\mathbf{x},t)$.

The phase difference between the response of the boundary layer flow and the core flow to the time–dependent pressure gradient produces a velocity profile characterized by an inflection point, which is considered an instability source. When Sto is high (small flow modulation period), the inflection point of the inflectional velocity profile is ineffective in producing instabilities [17]. When the inflection point is neither very close to the wall nor far away from it, its importance is reduced [18]. The flow in a channel that is suddenly blocked off (at a quicker rate than the aortic flow, the aortic valve beginning to close after the peak transvalvular flow) gives an estimate of the available time for instability occurrence ($0.023\nu/R^2$), where $R^2/\nu$ is the damping time scale by viscous effects [19]. A critical dimensionless parameter is a ratio of destabilizing to stabilizing forces. When the threshold is exceeded at any point of the fluid domain, the flow destabilization is not counterbalanced by restoring forces and the disturbances grow.

The Reynolds number, the ratio of convective inertia forces to viscous forces, is adapted to steady flows. The critical Reynolds number ($\mathrm{Re}_{\mathrm{crit}}$) is the threshold below which the flow is stable to infinitesimal disturbances, but transition from laminar pattern occurs. In experimental not perfectly handled, its value in straigth pipes equals 2200 [20, 21]. This threshold reaches values of about $10^5$ when extreme care is done to reduce disturbances. A simple threshold is not suitable because it is strongly related to the flow conditions from which it is determined.

Because the blood flows with a 3D pulsatile nature in deformable vessels under a pressure difference which has a given harmonic content, the standard $\mathrm{Re}_{\mathrm{crit}}$ is not a reliable index of transition from laminar flow for the blood circulation.

The transition Reynolds number for a pulsatile flow in straight ducts has been defined by the value of Re at which the slope of the isoSto St–Re relationships changes [22]. The peak Reynolds number for a pulsatile flow is more appropriate.

In addition, flow modulations affect the values of $\mathrm{Re}_{\mathrm{crit}}$ [23]. $\mathrm{Re}_{\mathrm{crit}}$ is lower for non–harmonic (piston driven by a slider–crank mechanism $L/L' = 4$) than for harmonic (piston driven by a scotch–yoke mechanism) pulsations, the latter providing, for the same mean pressure gradient, a more stable flow than the steady flow.

Like steady flows, time-varying flows are stable if any disturbance decays continuously.

Periodic flows become unstable when the disturbance grows during each period from the decelerating phase onset. Periodic flow patterns have thus been classified into four main types [24]. *Type 1* corresponds to a laminar flow, the flow remaining undisturbed throughout the flow cycle. *Type 2* is a disturbed laminar flow with small amplitude perturbations. *Type 3* is an intermittently turbulent flow in which high-frequency velocity fluctuations occur at the beginning of the deceleration phase, increase, and dissipate prior to or during the subsequent acceleration phase. *Type 4* is a fully developed turbulent flow, high-frequency velocity fluctuations existing during the whole flow cycle. Additional types have been proposed [25, 26]. *Subpattern 1* is defined by small-amplitude perturbations occurring in the early stage of acceleration phase in the flow core. *Subpattern 2* is characterized by small-amplitude perturbations during the whole acceleration phase.

The simplest quantity to consider is the available time for disturbance growth and spreading. A dimensionless relaxation time has been proposed, that is, the product of the ratio of the time available for perturbation growth (the duration of the acceleration phase) to the momentum diffusion time scale ($R^2/\nu$) by the ratio between convective inertia and viscous effects (Re) [27].

The higher the Sto, the lower the time available for disturbance growth. The growth rate increases with Re, when the flow unsteadiness acts as a simple modulation factor. The value of the Strouhal number (St) can then be taken into account. When $\mathrm{St} \ll 1 (\mathrm{St} \propto T_{\mathrm{conv}}/T)$ and $Re \ll 1 (Re \propto T_{\mathrm{diff}}/T_{\mathrm{conv}})$, the convective time scale for vortex development inside the vessel lumen ($R/\widehat{V}$ , $\delta_S/\nu$ inside the boundary layer) is lower than both the momentum diffusion time scale ($R^2/\nu, \delta_S^2/\nu$ inside the boundary layer) and the cycle period $T$ (even shorter than the duration of the decelerating phase). Destabilization–stabilization of a pulsatile flow depends thus on the frequency and magnitude of flow modulation. A critical Strouhal number, based on the unsteady boundary layer thickness ($(R/\delta_S)^2/(\widehat{V}\delta_S/\nu) = R^2\nu/\delta_S^3\widehat{V}$) has been proposed for time–dependent flows.

A single index being insufficient, diagrams based on the main involved dimensionless parameters are used. The Stokes number, which ressembles Re, the convective inertia being replaced by the unsteady inertia in the force ratio, is a frequency parameter. A combination of Sto and Re, with suitable scales, has been defined to provide critical conditions [28]. These authors observed turbulent bursts in the dog aorta after peak flow when $\widehat{\mathrm{Re}} > 250$ Sto, which disappear before the cycle end. However, such disturbances can have been generated by the measurement sensors. Similar orders of magnitude have been found in pipe flows using the same measurement technique (hotfilm velocimetry) [29]. Demarcation of the flow patterns is commonly made on Sto–Re diagrams.

The instability limit $\mathrm{Re}_\delta = \mathrm{Re/Sto}$ has been estimated to be about 100 in a plane boundary layer of thickness $\delta \propto (\nu/\omega)^{1/2}$ as well as in the aorta, from in vivo measurements that strongly disturbs the flow [30]. Some explanations attribute the turbulence to the stability of the oscillating boundary layer [31].

Overestimation of flow instabilities has been shown in experiments carried out on artificial heart valves compared with the values obtained from a spectral analysis of LDV data and determination of the main frequency modes [32].

In summary, several features affect flow stability: vessel curvature according to disturbance amplitude, wall distensibility, flow period, and the frequency content of the pressure signal. Laminar flow in blood vessels is a weak assumption.

### 1.3.2 Blood rheology

Blood behaves like a concentrated RBC suspension in plasma, which contains proteins that bridge RBCs. Hence, interactions between conveyed plasma molecules and RBCs govern partly the blood rheological behavior. *Aggregation of RBC* is the reversible clumping of these blood elements under low shear forces or at stasis. RBC aggregation can be evaluated by optical techniques based on reflected and transmitted light energy by blood samples subjected to shear [33].

Several factors affect the blood rheology (Table 1.12). The rheological properties of nonNewtonian blood is dictated by the flow-dependent evolution of the blood internal microstructure, that is, possible aggregation and deformation of flowing cells with their given time constants.

In the macrocirculation, the ratio between vessel bore and cell size ($\kappa_{vp} >\sim 50$) is such that blood is considered as a continuous homogeneous medium. In the microcirculation, $\kappa_{vp} < 1$ and the blood is heterogeneous, transporting deformed cells in a Newtonian plasma.

Table 1.12: Factors affecting the blood viscosity

| Plasma | Cell | Vessel | Flow |
|---|---|---|---|
| Temperature | Cell concentration | Vessel bore | Shear field |
| Protein concentration | Cell aggregability | | |
| | Cell deformability | | |

Biological application of this study focuses on large veins of inferior limbs. In the absence of flow stagnant regions, where the local flow time scale may be larger than the RBC aggregation rate, the flow is supposed to be Newtonian (Table 1.13).

Table 1.13: Blood ($\mathrm{Ht} = 45\,\%$, $\mathrm{T} = 37\,^{\circ}\mathrm{C}$) and water ($\mathrm{T} = 37\,^{\circ}\mathrm{C}$) physical properties.

| | $\mu$<br>$( \times 10^{-3}\mathrm{Pl} )$ | $\rho^f$<br>$( \times 10^{3}\ \mathrm{kg/m^3} )$ | $\nu$<br>$\times 10^{-6}\ \mathrm{m^2/s}$ |
|---|---|---|---|
| Blood | 3–4 | 1.055 | $2.8 - 3.8$ |
| Plasma | 1.2 | $\sim 1.03$ | $\sim 1.2$ |
| Water | 0.692 | 0.993 | 0.696 |

Shear-step experiments (steady state after a short transient regime) show that blood has a shear–thinning behavior [34]. This set of experiments do not represent the reality, as it works on a fully aggregated blood that is sheared in a stepwise fashion, measurements being done in the steady regime.

Furthermore, blood is viscoelastic and thixotropic. Thixotropic behavior is explained by changes in blood internal structure, that is, by the kinetics of both reversible RBC aggregation and deformation, with their time scales. Furthermore, blood rheology depends on the loading history. A model based on the generalized Newtonian behavior, as the one mostly used in the literature, is thus not suitable.

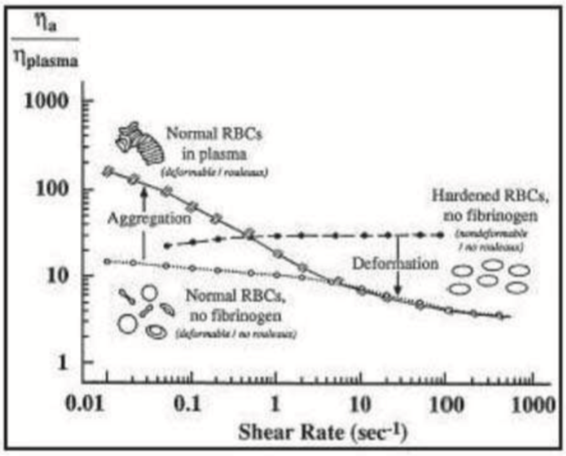

Figure 1.4: Blood shear rate–relative viscosity relationships with its shear–thinning behavior in static conditions (from [34]). The relation depends upon the kinetic of formation and rupture of RBC aggregates at low shear rates and kinetics of RBC deformation and RBC orientation at high shear rates. Two ratios are involved: (1) the ratio between RBC size and flow length scale (vessel radius), and (2) the ratio between aggregation time constant and flow time scale (convection characteristic time for macrocirculation, transit time for microcirculation) in the explored vessel segment. Kinetics are governed by relaxation phenomena. Blood rheology is thus governed by variation in RBC suspension structure (thixotropic medium with viscoelastic behavior). The value at low shear rates is questionable because of the resolution limit of measurements. A between–subject variability exists, in particular in slope and curve inflection point values ($\dot{\gamma}(1/2)$)

There are many nonNewtonian blood models, such as shear–thinning model [35–38], blood aggregation model [39], and other particular models [40–43] applied in some specific conditions.

## 1.4 Fluid–structure interactions (FSI)

More than 70% of Earth surface is covered by ocean, and earth is surrounded by atmosphere. Naturally, physical body moves in fluid (gas and liquid) and interact with fluid on the surface of body. A problems needs to couple fluid dynamics to solid mechanics, which is so called fluid–structure interaction (FSI) problem.

Among applications of FSI, computer-aided design of prosthetic heart valves is analyzed in [44]. Flow pattern and stress distribution of parachute opening is studied in [45, 46]. Studies focus on animal motion [47–49], especially on flapping wings [47, 50].

Mechanically, consideration of FSI becomes gradually essential thanks to application of elastic materials, such as macromolecular substance and cables, rather than solid mediums, like concrete and metal. Failing to consider the effects of interactions can be catastrophic, especially in structures comprising materials susceptible to fatigue. Tacoma Narrows Bridge (1940), the first Tacoma Narrows Bridge, is probably one of the most infamous examples of large-scale failure.

FSI-based development of artificial organs and vessels shortened the overall design time frame from an order of years to months [51–53]. Additionally, it provided detailed, three–dimensional predictions of fluid flow, and it reduced the expense of prototype manufacture and testing.

Mathematically, Lagrangian and Eulerian depictions for objects and fluid respectively are mixed in FSI problems. The problem of combined depictions occurs on prescribing boundary condition of moving objects [54]. Displacement on the surface of objects also changes fluid domain, and this displacement field has no connection to the fluid velocity field.

A transformation of the current fluid domain and corresponding governing equations to some fixed reference domain is developped in the pseudo-solid mapping method.

Numerically, there are two critical issues of FSI application. First, stability of numerically solving coupled system must be warranted; a discussion is summarized in 1.4.1. Second, the moving and deformable interface between fluid and structure must be tracked. A proper scheme to track interface is essential and necessary for FSI problems.

Most of numerical approaches could be roughly separated into body-fitted meshes and mathematical approaches. Body-fitted mesh approaches are defined as generation and moving of meshes along the interface between fluid and structure. Deformation and motion of interface is mathematically assessed by a well-posed function or artificial forces. Many approaches to track the interface are summarized and compared in section 1.4.4.

### 1.4.1 Fluid mechanics – Navier–Stokes equations

The main blood variables, the velocity vector $\mathbf{v}$ and the stress tensor $\sigma$, use the Eulerian formulation. The set of conservation equations is closed by the relationships between the transmural pressure $p = p_i - p_e$, where the external pressure $p_e$, the distribution of which is currently supposed to be uniform, is assumed to be equal to zero for superficial blood vessels.

The governing equations for an unsteady flow (mass density $\rho^f$, dynamic viscosity $\mu$, and kinematic viscosity $\nu = \mu/\rho^f$) of an incompressible fluid are derived from the mass and momentum conservation (Eq. 1.1 and 1.2).

$$\nabla \cdot \mathbf{v} = 0 \tag{1.1}$$

$$\rho^f \left( \frac{\partial \mathbf{v}}{\partial t} + \mathbf{v} \cdot (\nabla \mathbf{v}) \right) = \nabla \cdot (\sigma) + \mathbf{f} \tag{1.2}$$

where $\sigma = -p\mathbf{I} + 2\mu D$ and $D = \frac{1}{2}\left(\nabla\mathbf{v} + \nabla\mathbf{v}^T\right)$ in the case of a Newtonian fluid. The volumic force term $\mathbf{f}$ in this study indicates the gravitational force $\mathbf{f} = -\rho^f g\hat{e}_z$ ($g$ the gravity).

### Governing parameters

The formulation of the dimensionless equations depends on the choice of the variable scales ($\bullet^*$). The dimensionless equations exhibit a set of dimensionless parameters.

The *Reynolds number* $\mathrm{Re} = V^*L^*/\nu (V^* \equiv V_q$ : cross–sectional average velocity, $L^* \equiv R$ : vessel radius) is the ratio between convective inertia and viscous effects.

When flow depends on time, both mean $\widehat{\mathrm{Re}} = Re(\widehat{V}_q)$ and peak Reynolds numbers $Re = Re(V_q)$, proportional to mean and peak $V_q$ respectively, can be calculated. $\mathrm{Re}_{\delta_S} = \mathrm{Re/Sto}$ is used for flow stability study ($\mathrm{Sto} = R/\delta_S$, $\delta_S$: *Stokes boundary layer thickness*).

The *Stokes number* $\mathrm{Sto} = L^*(\omega/\nu)^{1/2}$ is the square root of the ratio between time inertia and viscous effects.

The *Strouhal number* $\mathrm{St} = \omega L^*/V^*$ is the ratio between time inertia and convective inertia ($\mathrm{St} = \mathrm{Sto}^2/\mathrm{Re}$).

The *Dean number* $\mathrm{De} = (R/R_c)^{1/2}\mathrm{Re}$, for laminar flow in planar curved vessels with a single curvature radius, is the product of the square root of the vessel curvature ratio by the Reynolds number. The Dean number is calculated in phantom tests but not in image–based flow models because of the complex curvature of the vessel axis which varies continually in every direction.

The *modulation rate* (or amplitude ratio), easily determined when the blood flow is approximated by a sinusoidal component, of amplitude $V_\sim$, superimposed on a steady one, $\gamma_\nu = V_\sim/\overline{V}$ plays a role in flow behavior.

An unsteady Reynolds number has been identified for a nonzero-mean sinusoidal flow: $\mathrm{Re}_\omega = \mathrm{Re}^2_\sim(\delta)/\gamma_\nu = \overline{V}V_\sim/(\omega\nu)$ [55]. A flow waveform dimensionless parameter has been proposed $\kappa_{(-)}\mathrm{Sto}(\,\mathrm{Re}/\,(\mathrm{Re}_{\max} - \mathrm{Re}_{\min}\,)\,))$, where $\kappa_{(-)}$ is the number of negative flow portions during the flow cycle [56].

## 1.4.2 Vascular wall dynamics

Vascular dilation and collape can take place during each cardiac cycle. Among 5 different layers (section 1.1.2), the *media* layer is vital to consider, because stiffness of blood vessels mainly depends on the state of medial smooth muscle cells.

Venous walls and valves are treated as the same material to simplify venous model and avoid coupling error between different materials. Bileaflet valves in veins undergo large deformation upon muscular activity. Therefore, an isotropic hyperelastic model is implemented to precisely capture motion of valves instead of linear elasticity model.

A Mooney–Rivlin material is chosen to model vasular walls and valves. Conservation of momentum and mass is summarized below:

$$\rho_s \frac{\partial^2 \mathbf{d}}{\partial t^2} = \nabla \cdot \sigma_s + \mathbf{f}, \quad \frac{d}{dt}(J\rho_s), \quad J\rho_s = \rho_s^0 \tag{1.3}$$

Table 1.14: Comparison of veins and arteries.

| | Arteries | Veins |
|---|---|---|
| **Oxygen concentration** | Arteries carry oxygenated blood (with the exception of the pulmonary artery and umbilical artery). | Veins carry deoxygenated blood (with the exception of pulmonary veins and umbilical vein). |
| **Types** | Pulmonary and systemic arteries. | Superficial veins, deep veins, pulmonary veins and systemic veins |
| **Direction of blood flow** | From the heart to various parts of the body. | From various parts of the body to the heart. |
| **Overview** | Arteries carry blood away from the heart.<br>Upstream very distensible arteries<br>Downstream resistance arteries | Veins carry blood towards the heart.<br>Capacitance vessels<br>Collapsible vessels |
| **Cross section** | Circular section | Elliptic section |
| **Valves** | not present (except for semi–lunar valves) | present, especially in limbs |
| **Disease** | Atherosclerosis<br>Stenosis<br>Ischemia | Venous insufficiency<br>Deep vein thrombosis<br>Thrombophlebitis |

where $J$ is the Jacobian of the deformation. Stress tensor of an incompressible hyperelastic mateiral can be writen as

$$\sigma_s = -p_s\mathbf{I} + \partial_{\mathbf{F}}\Psi_{\mathrm{MR}}\,\mathbf{F}^T$$

where $\Psi_{\mathrm{MR}}$ indicates Helmholtz potential, $\Psi_{\mathrm{MR}}(\mathbf{F}) = c_1\mathrm{tr}_{\mathbf{F}^T\mathbf{F}} + c_2\left(\mathrm{tr}_{(\mathbf{F}^T\mathbf{F})^2} - \mathrm{tr}^2_{\mathbf{F}^T\mathbf{F}}\right)$, and $\mathbf{F}$ stands for the transposed gradient of the deformation. Detailed description and derivation can be found at chapter 2.

### 1.4.3 Tube law

A uniform elastic tube will collapse while transmural pressure, $p = p_i - p_e$ (internal minus external pressure), is applied. The cross–sectional shape and area, $A$, will vary with different levels of $p$ as sketched in Figure 1.5. When $p$ is large and positive, the cross–section will be circular and rather stiff because the perimeter must be stretched in order to increase $A$. As $p$ is lowered, a critical value is passed at which the circular cross–section buckles, becoming at first elliptical and then more significantly deformed. During this phase a thin–walled tube is very *compliant (large area change for small pressure change)* because only wall bending is required for a change of shape and hence area. Additionally, bifurcation happens if cross–section is circular [57]. At very low values of $A$ the tube is almost totally collapsed and becomes stiff again. During the compliant phase, even the small pressure changes associated with flow through the tube (viscous or inertial) can be enough to cause collapse.

Collapse of compressed elastic tubes conveying a flow occurs naturally. Blood flow in veins, either above the level of the heart where the internal pressure may be subatmospheric

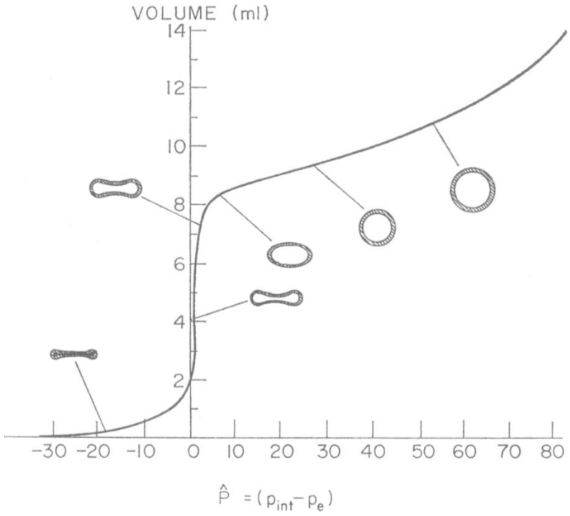

Figure 1.5: Volume in a collapsible tube as a function of transmural pressure. Typical transverse cross–sections are shown at various points on the curve [58].

because of the effect of gravity is illustrated by the jugular vein of the giraffe [59]) and the muscle pump [60–62]. Collapse of large intrathoracic airways during forced expiration has been extensively explored [63–66].

Stability problem comes from large deformation of objects, poor description of boundary, weakly coupled systems, etc. Two numerical approaches to solve coupled systems include monolithic and partitioned formulation. The monolithic formulation treats the problem as one continuum within different material coefficients and stress tensors [54, 67–72]. On the other hand, fluid and structure are solved individually with partitioned formulation [73, 74].

Most FSI studies utilize partitioned formulations. Widely used and validated fluid and structure solvers are coupled using a master software and considering coupling conditions. In practice, fluid and structure systems are solved in different time step, fluid being solved first then structure for each time step. Interaction between fluid and structure is considered as kinematic boundary conditions for structure. Furthermore, partitioned formulation solves two comparatively small systems separately rather than solving fully coupled system simultaneously (monolithic formulation). However, it takes longer time to get results because the system is relatively unstable with respect to monolithic formulation.

Although partitioned formulation has many advantages, it may neglect some detailed procedure of interface deformation. This flaw introduces instability.

Recently, more and more studies focus on monolithic formulation because of stability issues in partitioned formulation. In the monolithic formulation, the entire variable fields are solved simultaneously in one time step. Kinematic boundary conditions of interaction between fluid and structure are embedded in monolithic formulation at interface of two different materials, meaning that interaction of fluid and structure is automatically considered in monolithic formulation.

### 1.4.4 Numerical approaches of FSI problems

Many methods developed track the surface, such as arbitrary Lagrangian–Eulerian (ALEM), immersed boundary (IBM), level set (LSM), volume of fluid (VOFM), and particle methods (PM). The following paragraphs introduce these five methods. Advantages and drawbacks of each method are summarized in Table 1.15.

#### Arbitrary Lagrangian-Eulerian method

Moving mesh methods use meshes following domains occupied by fluid and structure respectively. The mesh is then given exactly at boundary to fit fluid and structure surface. The ALE formulation was proposed first by Donea in 1982 [75]. Briefly, the ALE framework is an arbitrary depiction between Lagrangian and Eulerian description. The ALE framework is mathematically rigorous to describe transport phenomena in time. However, it raises some implementation questions on the interface tracking with time discretization. Yet, every body–fitted approaches will encounter overtaken and skew meshes while large deformation happens, but this problem is avoided by regenerating meshes and redistributing mesh nodes (adaptive meshing).

#### Immersed boundary method

The IBM was first proposed by Peskin [76]. This mathematical approach prescribes artificial forces and conditions, avoiding remeshing to fit structure surface. Therefore, it simplifies discretization of spatial derivatives and saves time in generating quality meshes.

Studies were dedicated to prescription of artificial force [77–80] and their distribution [81–83]. Many similar algorithms are developed for different purposes [84, 85]. However, for IBM, mass conservation around structure and stability of coupled system are questionable.

#### Level set method

The LSM was introduced in Osher and Sethian [86]. It relies on an implicit representation of the interface, equation of its motion being numerically approximated using schemes built from those for hyperbolic conservation laws [87].

The technique handles problems in which the speed of the evolving interface may depend on local properties such as curvature and normal direction, as well as jump. LSMs are particularly designed for problems in multiple space dimensions in which the topology of the evolving interface changes during the course of events and for problems in which sharp corners and cusps are present [88–90].

Numerically, LSM suffers severe issues of phase error from solving hyperbolic equation and distance error of level set function. Choice of Heaviside function also affects simulation results.

### Volume of fluid method

The VOFM was introduced by Noh and Woodward in 1976 [91]. It is dedicated in smoothed void fraction function which represents fluid and structure ratio in one mesh. The VOF method satisfies mass conservation extremely well [92], since VOF methods are proper to two–phase flow simulation [93,94]. The disadvantage of VOF method deals with difficulty with which the geometric properties (interface normal and curvature) are captured from the VOF function, spatial derivatives od which are not continuous near interface [95].

### Particle method

The PM is a mesh-free Lagrangian technique that was first applied in chemistry, quantum mechanics, as well as astrophysics by Monaghan and Lucy in 1977 [96]. The method has been used in many other fields, such as ballistics, volcanology, and oceanography.

The PM indicates the coordinate movement with the fluid. Validation can be found in [97, 98]. The particle method is very popular because of: (1) exact treatment of advection, (2) particles on behalf of material, (3) bridge of gap between the continuum and fragmentation in a natural way, and (4) resolution depending on position and time.

Nevertheless, numerically, particle method is stained with errors of order $O(1)$ [96,99] or even worse. Additionally, treatment of boundary conditions sometimes is tricky.

Two studies [100, 101] utilize lattice Boltzmann method (LBM) to solve numerically fluid flow coupled with a lattice spring model for structure mechanics. The LBM is classified in particle methods, it solves collision and streaming models rather than conservation equations of macroscopic properties (i.e. mass, momentum, and energy).

## 1.5 Computational aspects of blood flow

### 1.5.1 Modeling and simulation methods in distensible vessels

Blood flow in distensible arteries is associated with pressure wave propagation and accompanying lumen dilation and related effects such as the windkessel effect. Most studies of blood flow in distensible arteries are based on partitioned formulation, projection methods [73, 74, 102], a single monolithic formulation being proposed [72]. In space, finite volume-based software is utilized to solve governing equations with projection method in [102]. The ALEM applied on partitioned FSI formulation are studied at [73, 74], and numerical analysis for stability of scheme is presented in [73]. Space–time finite element method is applied on monolithic formulation in [72].

The distribution of atherogenic low–density lipoproteins (LDLs) is calculated by modeling and simulating blood flow coupled with mass transport equation in aortic arch [102]. The study points out importance of aortic taper and torsion with different models of aorta. The helical flow induced by aortic torsion may stabilize blood flow in the aorta and lessen deposit of LDLs in the aortic arch wall. The taper of the aorta can further stabilize blood

Table 1.15: Comparisons of FSI numerical approaches.

| Approach | Advantages | Drawbacks |
|---|---|---|
| ALEM | 1.body–fitted approach<br>2.mathematically rigorous method | 1.twisted meshes<br>2.interface tracking with time discretization |
| IBM | 1.no need of remeshing<br>2.calculation on Cartesian coordinates<br>3. easy application to original code | 1.stability issue<br>2.mass conservation around structure |
| LSM | 1.evolving interface<br>2.clear indication of interface location | 1.choice of Heaviside function<br>2.phase error of hyperbolic equation<br>3.error of distant function |
| VOFM | 1.mass conservation<br>2.two phase flow | 1.implicit interface position<br>2.discontinuous derivatives around interface |
| PM | 1.exact treatment of advection<br>2.particles on behalf of material<br>3.resolution depending on position and time | 1.errors with order of 1, $O(1)$<br>2.treatment of boundary conditions |

flow. Helical flow generated in the ascending aorta can remain down to the entrance segment of the descending aorta.

A technique to optimize material properties by comparing cross sections with MR images of aortic arch is proposed by [74]. Combination of FSI models and image segmentation provide a powerful tool for in vivo analysis of arterial tissue properties.

Aneurysm is a localized balloon-like bulge of blood vessel walls [103, 104]. The oscillatory shear index (OSI= $\frac{1}{2}(1-\tau_{mean}/\tau_{abs})$) is largest in the aneurysm region, especially along the posterior wall, suggesting that wall shear stress is highly oscillatory due to the recirculating flow [72]. Low time–averaged wall shear stress, in combination with high shear stress temporal oscillations, as measured by the OSI, are indicators of the regions of high probability of occurrence of atherosclerosis.

### 1.5.2 Modeling and simulation methods in collapsible vessels

Input parameters derive at best from in vivo measurements. Some properties of material are assessed and incorporated in artificial valvular veins [105–107]. Velocity distribution within given stations in the greater saphenous vein was measured [108].

Difficulty of modeling and simulation in collapsible veins results from prescription of adequate transmural pressure and valvular motion. Detailed information on flow in collapsible tubes is given in appendix A. Valves closure means leaflet contact over the coaptation zone to avoid defective functioning. Numerical contact is an artificial approach to deal with valvular closure. Another issue is linked to material properties distribution. Most studies assume homogeneous vessel walls and valves instead of multilayered structures made up from a composite material.

ALEM, IBM, LSM, and PM are often used to simulate FSI problems with complicated geometries. In [109], commercial software FEM- and ALE-based ANSYS-CFX and LS-DYNA are compared. Numerical modeling and simulation of valvular veins is considered in [100, 109, 110]. A coupled system of linear elasticity model of solid mechanics and Newtonian fluid is considered as venous blood flow model in [100]. Flow rate and valvular opening area are varied with respect to pressure difference. Self-exited oscillation of blood vessels are studied in [101].

### 1.5.3 Modeling and simulation methods in aortic valves

Orifices between the cardiac chambers are endowed with tricuspid valves, except the mitral valve. Whereas tricuspid nventriculoarterial valves have a large copatation zone (between-leaflet contact region) to resist diastolic back flow, atrioventricular valves are attached to the myocardium by cordages, thus taking a parachute-like shape that maintains bloodtightness and thus prevents blood reflux.

Some works investigated stress distribution on valves [44,111,112], to assist in designing and optimizing artificial valves [51].

Combined ALEM and IBM to track interface between fluid and structure and monolithic formulation is utilized to solve FSI systems [44]. In [111], a partitioned formulation is applied with FEM to connect fluid and structure by a continuous stress distribution along the interface. Combination of ALEM and fictitious domain has also been used [112].

A realistic aortic valve model should contain the following properties [112]: (1) three-dimensionality, (2) fully coupled fluid–structure interaction, (3) combined fictitious domain and arbitrary Lagrangian–Eulerian method, (4) fiber-reinforced leaflets, and (5) compliant aortic root.

A computater-aided analysis of velocity and stress fields in artificial aortic valves is studied in [51]. It is cheaper to use computational simulations than producing a prototype and measuring. However, it is not trivial to develop a stable and general software to solve FSI problems.

# Chapter 2

# Numerical analysis of a monolithic formulation for fluid–structure interaction

## Contents

The aim of this chapter is to provide a fundamental basis for the modelling and numerical analysis. In this study, *Actualized Lagrangian method* (ALM) [113, 114] is adopted for structures, which is first proposed by Thomas Dunne and Rolf Rannacher in [113]. To be able to describe the deformations in the Eulerian description, points in the solid are transported with the structure velocity in each time step. Like particle methods (PM), there is no nonlinear advection terms in the solid. The ALM takes the advantages of the nature of Lagrangian description in solid, and it still follows previous numerical studies with Eulerian description in fluid.

We propose a fully Eulerian monolithic formulation to solve fluid–structure interaction problems in this study. To construct a monolithic formulation in Eulerian depiction, solid stress tensor is recast into Eulerian depiction from Lagrangian depiction. With the characteristic Galerkin method [115] for total derivative terms, it yields a consistent approximation with first order accuracy in time.

Governing equations of fluid and structure are shown in section 2.1 with derivation of solid stress tensor in fully Eulerian expression. A monolithic weak formulation of fluid-structure interaction problem is shown in section 2.2. A consistent approximation with first order accuracy in time is derived in section 2.3 with characteristic-Galerkin method and spatial discretization, and then we can get a solution algorithm at each time step. At the end, stability analysis the of proposed monolithic formulation is carried out in section 2.4.

To shorten the content, we only show the derivation and results for incompressible Newtonian fluid coupled with Mooney–Rivlin model in 3D from sections 2.2 to 2.4, and the detailed derivation with other material models can be found in [116–118]. Consistent approximations of variational problems with different material models with first order accuracy in time can be found in appendix B.

## Notations

$\Omega^t$ denotes the time dependent domain which is the union of the fluid part $\Omega^t_f$ and the solid part $\Omega^t_s$. Technically, $\Omega^t$ must be an open set and we denote it by $\overline{\Omega}^t$ for closure. The following requirements are needed

$$\overline{\Omega}^t = \overline{\Omega}^t_f \cup \overline{\Omega}^t_s, \quad \Omega^t_f \cap \Omega^t_s = \emptyset \text{ at any times } t \in (0,T).$$

$\Omega^0_f$ and $\Omega^0_s$ are initially prescribed. Let $\Sigma^t = \overline{\Omega}^t_f \cap \overline{\Omega}^t_s$ be the fluid–structure interface , $\partial\Omega^t$ be the boundary of $\Omega^t$, and $\Gamma$ be the part of $\partial\Omega^t$. The structure can be either clamped or the fluid is not allowed to slip.
The following standard notations are used:

- $\mathbf{X}$: $\Omega^0 \times (0,T) \mapsto \Omega^t$ : $\mathbf{X}\left(x^0,t\right)$, the Lagrangian position at $t$ of $x^0$,
- $\mathbf{d} = \mathbf{X}\left(x^0,t\right) - x^0$, the displacement,
- $\mathbf{v}(X(x^0,t)) = \partial_t \mathbf{X}(x^0,t)$, the Eulerian velocity of the deformation,
- $\mathbf{F}_{ji} = \partial_{x^0_i}\mathbf{X}_j$, the transposed gradient of the deformation,
- $J = \det_{\mathbf{F}}$, the Jacobian of the deformation.

Let the density/stress tensor for fluid be $\rho_f/\sigma_f$ and for solid be $\rho_s/\sigma_s$. It is convenient to define a unique density and stress tensor by using the set function indicators $\mathbf{1}_{\Omega^t_f}$ and $\mathbf{1}_{\Omega^t_s}$:

- $\rho(x,t) = \mathbf{1}_{\Omega_f^t}\rho_f(x,t) + \mathbf{1}_{\Omega_s^t}\rho_s(x,t)$ , the density,
- $\sigma(x,t) = \mathbf{1}_{\Omega_f^t}\sigma_f(x,t) + \mathbf{1}_{\Omega_s^t}\sigma_s(x,t)$ , the stress tensor,

For readability, vector, tensor and matrix are noted in bold, except $x$ and $x^0$. Unless specified, otherwise, all spatial derivatives are with respect to $x \in \Omega^t$ and not with respect to $x^0 \in \Omega^0$. If $\phi$ is a function of $x = \mathbf{X}\left(x^0,t\right)$, $x^0 \in \Omega^0$,

$$\nabla_{x^0}\phi = \left[\partial_{x_i^0}\phi\right] = \left[\partial_{x_i^0}\mathbf{X}_j\partial_{x_j}\phi\right] = \mathbf{F}^T\nabla\phi \tag{2.1}$$

When $\mathbf{X}$ is an one–to–one and invertible mapping, $\mathbf{d}$ and $\mathbf{F}$ can be seen as the functions of $(x,t)$ instead of $(x^0,t)$. They are related by

$$\mathbf{F}^T = \nabla_{x^0}\mathbf{X} = \nabla_{x^0}\left(\mathbf{d}+x^0\right) = \nabla_{x^0}\mathbf{d}+\mathbf{I} = \mathbf{F}^T\nabla\mathbf{d}+\mathbf{I} \quad \Rightarrow \quad \mathbf{F} = \left(\mathbf{I}-\nabla\mathbf{d}\right)^{-T} \tag{2.2}$$

Time derivatives are related by

$$\mathbb{D}_t\phi(x,t) := \frac{d}{dt}\phi\left(\mathbf{X}\left(x^0,t\right),t\right)\Big|_{x=\mathbf{X}\left(x^0,t\right)} = \partial_t\phi(x,t) + \mathbf{v}\cdot\nabla\phi(x,t). \tag{2.3}$$

It is convenient to introduce a notation

$$\mathbf{D}\mathbf{v} = \nabla\mathbf{v} + \nabla^T\mathbf{v}$$

## 2.1 Fluid dynamics and solid mechanics equations

Conservation of momentum and mass take the same form for the fluid and the solid. With $\mathbf{f}(x,t)$ the volumic force, the system is

$$\rho\mathbb{D}_t\mathbf{v} = \mathbf{f} + \nabla\cdot\sigma, \quad \frac{d}{dt}(J\rho), \quad J\rho = \rho^0$$

with the continuity of $\mathbf{v}$ and of $\sigma\cdot\mathbf{n}$ at the fluid–structure interface $\Sigma^t$ in absence of external surface force, like surface tension. The incompressibility implies $J = 1$ thus $\rho = \rho^0$ along the Lagrangian trajectories.

We consider Newtonian incompressible fluid in this study. For solid, Mooney-Rivlin (MR) and S$^{\mathrm{t}}$–Venant–Kirchhoff (STVK) model, the hyperelastic models, are considered as the representatives of incompressible and compressible materials.

- For a Newtonian incompressible fluid, $\sigma_f = -p_f\mathbf{I} + \mu\mathbf{D}\mathbf{v}$
- For a hyperelastic incompressible material, $\sigma_s = -p_s\mathbf{I} + \partial_{\mathbf{F}}\Psi_{\mathrm{MR}}\mathbf{F}^T$
- For a hyperelastic compressible material, $\sigma_s = J^{-1}\partial_{\mathbf{F}}\Psi_{\mathrm{STVK}}\mathbf{F}^T$

where $\Psi_{\square}$ indicates Helmholtz potential for the chosen models such as

$$\Psi_{\mathrm{MR}}\left(\mathbf{F}\right) = c_1 \mathrm{tr}_{\mathbf{F}^T\mathbf{F}} + c_2 \left(\mathrm{tr}_{\left(\mathbf{F}^T\mathbf{F}\right)^2} - \mathrm{tr}^2_{\mathbf{F}^T\mathbf{F}}\right) \tag{2.4}$$

$$\Psi_{\mathrm{STVK}}\left(\mathbf{F}\right) = \frac{\lambda_s}{2}\mathrm{tr}^2_{\mathbf{E}} + \mu_s \mathrm{tr}_{\mathbf{E}^2}, \quad \mathbf{E} = \frac{1}{2}\left(\mathbf{F}^T\mathbf{F} - \mathbf{I}\right) \tag{2.5}$$

In the above equations, $c_1$ and $c_2$ are the coefficients for the MR model which can be determined only by experimental data, such as uniaxial tensile load–displacement test.

For homogeneous isotropic linear elastic materials, its elastic properties are uniquely determined by two coefficients. Two descriptions can be used: either the Young's modulus $E_s$ and the Poisson ratio $\nu_s$ or Lamé coefficients $\lambda_s$ and $\mu_s$. Conversion between these two sets of coefficients is shown below

$$\begin{cases} \lambda_s = \frac{\nu_s E_s}{(1+\nu_s)(1-2\nu_s)} \\ \mu_s = \frac{E_s}{2(1+\nu_s)} \end{cases}, \qquad \begin{cases} E_s = \frac{\mu_s(2\mu_s+3\lambda_s)}{\mu_s+\lambda_s} \\ \nu_s = \frac{\lambda_s}{2(\mu_s+\lambda_s)} \end{cases} \tag{2.6}$$

### 2.1.1 Fully Eulerian description

In most of studies, stress tensor for solid $\sigma_s$ is expressed as a function of $\mathbf{F}$ ( or $\mathbf{B} = \mathbf{F}\mathbf{F}^T$). In order to compute the tensors at Eulerian points $(x,t)$ rather than at Lagrangian points $\left(x^0,t\right)$, it is more practical to compute $x \to \mathbf{d}\left(x,t\right)$ in terms of $\Psi$. This treatment leads to a more complicated formulation, but the $\sigma_s$ derived in following sections becomes a fully Eulerian description in displacement with comprehensive consideration of deformation. With (2.2), the following equation holds:

$$\mathbf{B}^{-1} = \mathbf{F}^{-T}\mathbf{F}^{-1} = \left(\mathbf{I} - \nabla\mathbf{d}\right)\left(\mathbf{I} - \nabla\mathbf{d}\right)^T = \mathbf{I} - \mathbf{D}\mathbf{d} + \nabla\mathbf{d}\nabla^T\mathbf{d} = \mathbf{I} - \mathbf{C} \tag{2.7}$$

with $\mathbf{C} = \mathbf{D}\mathbf{d} - \nabla\mathbf{d}\nabla^T\mathbf{d}$. Additionally, Cayley–Hamilton theorem states that an $n \times n$ invertible matrix $B$ satisfies its own characteristic equation, and $n$ stands for dimension in this study. The characteristic equations for $B$ when $n = 2$ and 3 are

$$n = 2, \qquad \mathbf{B}^2 - \mathrm{tr}_{\mathbf{B}}\mathbf{B} + \det{}_{\mathbf{B}}\mathbf{I} = 0, \tag{2.8}$$

$$n = 3, \quad \mathbf{B}^3 - \mathrm{tr}_{\mathbf{B}}\mathbf{B}^2 + \gamma\mathbf{B} - \det{}_{\mathbf{B}}\mathbf{I} = 0 \ \text{ with } \ \gamma = \tfrac{1}{2}(\mathrm{tr}^2_{\mathbf{B}} - \mathrm{tr}_{\mathbf{B}^2}). \tag{2.9}$$

With the help of (2.7), (2.8) in 2D, or (2.9) in 3D, different solid material models can be rewritten into their fully Eulerian descriptions.

### 2.1.2 Solid mechanics equations – incompressible material

**The Mooney–Rivlin stress tensor** $\boldsymbol{\Psi}_{\mathbf{MR}}\left(\mathbf{F}\right) = c_1 \mathbf{tr}_{\mathbf{F}^T\mathbf{F}} + c_2 \left(\mathbf{tr}_{\left(\mathbf{F}^T\mathbf{F}\right)^2} - \mathbf{tr}^2_{\mathbf{F}^T\mathbf{F}}\right)$

Note that $\partial_{\mathbf{F}}\mathrm{tr}_{\mathbf{F}^T\mathbf{F}} = 2\mathbf{F}$ and $\partial_{\mathbf{F}}\mathrm{tr}_{\left(\mathbf{F}^T\mathbf{F}\right)^2} = 4\mathbf{F}\mathbf{F}^T\mathbf{F}$. Hence

$$\partial_{\mathbf{F}}\Psi_{\mathrm{MR}}\mathbf{F}^T = \left(2c_1 - 4c_2\mathrm{tr}_{\mathbf{B}}\right)\mathbf{B} + 4c_2\mathbf{B}^2. \tag{2.10}$$

The incompressibility implies $J = 1$ and $\det_{\mathbf{B}} = J^2 = 1$.

### 2D formulation [118]

According to (2.8) and with $\det_{\mathbf{B}} = 1$, $\mathbf{B}$ and $\mathbf{B}^2$ can be rewritten as:

$$\mathbf{B} = \mathrm{tr}_{\mathbf{B}}\mathbf{I} - \mathbf{B}^{-1}, \qquad \mathbf{B}^2 = \mathrm{tr}_{\mathbf{B}}\mathbf{B} - \mathbf{I} = \left(\mathrm{tr}_{\mathbf{B}}^2 - 1\right)\mathbf{I} - \mathrm{tr}_{\mathbf{B}}\mathbf{B}^{-1} \tag{2.11}$$

With the help of (2.11), (2.10) becomes

$$\begin{aligned} \partial_{\mathbf{F}}\Psi_{\mathrm{MR}}\mathbf{F}^T &= (2c_1 - 4c_2\mathrm{tr}_{\mathbf{B}})\,\mathbf{B} + 4c_2\mathbf{B}^2 \\ &= (2c_1 - 4c_2\mathrm{tr}_{\mathbf{B}})\left(\mathrm{tr}_{\mathbf{B}}\mathbf{I} - \mathbf{B}^{-1}\right) + 4c_2\left(\left(\mathrm{tr}_{\mathbf{B}}^2 - 1\right)\mathbf{I} - \mathrm{tr}_{\mathbf{B}}\mathbf{B}^{-1}\right) \\ &= -2c_1\mathbf{B}^{-1} + (2c_1\mathrm{tr}_{\mathbf{B}} - 4c_2)\,\mathbf{I} \end{aligned} \tag{2.12}$$

Then, using (2.7), one has

$$\begin{aligned} \partial_{\mathbf{F}}\Psi_{\mathrm{MR}}\mathbf{F}^T &= -2c_1\left(\mathbf{I} - \mathbf{Dd} + \nabla\mathbf{d}\nabla^T\mathbf{d}\right) + (2c_1\mathrm{tr}_{\mathbf{B}} - 4c_2)\,\mathbf{I} \\ &= 2c_1\left(\mathbf{Dd} - \nabla\mathbf{d}\nabla\mathbf{d}^T\right) + (2c_1\mathrm{tr}_{\mathbf{B}} - 2c_2)\,\mathbf{I}. \end{aligned} \tag{2.13}$$

### 3D formulation [116]

According to (2.9) and with $\det_{\mathbf{B}} = 1$, $\mathbf{B}$ and $\mathbf{B}^2$ can be rewriten as:

$$\begin{aligned} &\mathbf{B} = \mathrm{tr}_{\mathbf{B}}\mathbf{I} - \gamma\mathbf{B}^{-1} + \mathbf{B}^{-2} \\ &\mathbf{B}^2 = \mathrm{tr}_{\mathbf{B}}\mathbf{B} - \gamma\mathbf{I} + \mathbf{B}^{-1} = \left(\mathrm{tr}_{\mathbf{B}}^2 - \gamma\right)\mathbf{I} + (1 - \mathrm{tr}_{\mathbf{B}}\gamma)\,\mathbf{B}^{-1} + \mathrm{tr}_{\mathbf{B}}\mathbf{B}^{-2} \end{aligned} \tag{2.14}$$

With the help of (2.14), (2.10) becomes

$$\begin{aligned} \partial_{\mathbf{F}}\Psi_{\mathrm{MR}}\mathbf{F}^T =& (2c_1 - 4c_2\mathrm{tr}_{\mathbf{B}})\,\mathbf{B} + 4c_2\mathbf{B}^2 \\ =& (2c_1 - 4c_2\mathrm{tr}_{\mathbf{B}})\left(\mathrm{tr}_{\mathbf{B}}\mathbf{I} - \gamma\mathbf{B}^{-1} + \det_{\mathbf{B}}\mathbf{B}^{-2}\right) \\ &+ 4c_2\left[\left(\mathrm{tr}_{\mathbf{B}}^2 - \gamma\right)\mathbf{I} + (1 - \mathrm{tr}_{\mathbf{B}}\gamma)\,\mathbf{B}^{-1} + \mathrm{tr}_{\mathbf{B}}\mathbf{B}^{-2}\right] \\ =& 2c_1\mathbf{B}^{-2} + (4c_2 - 2c_1\gamma)\,\mathbf{B}^{-1} + (2c_1\mathrm{tr}_{\mathbf{B}} - 4c_2\gamma)\,\mathbf{I} \end{aligned} \tag{2.15}$$

Then, using (2.7), the 3D Mooney–Rivlin stress tensor as a function of $\mathbf{d}$ is recast into

$$\begin{aligned} \partial_{\mathbf{F}}\Psi_{\mathrm{MR}}\mathbf{F}^T =& 2c_1\,(\mathbf{I} - \mathbf{C})^2 + (4c_2 - 2c_1\gamma)\,(\mathbf{I} - \mathbf{C}) + (2c_1\mathrm{tr}_{\mathbf{B}} - 4c_2\gamma)\,\mathbf{I} \\ =& 2a_1\left(\mathbf{Dd} - \nabla\mathbf{d}\nabla^T\mathbf{d}\right)^2 + 2a_2\left(\mathbf{Dd} - \nabla\mathbf{d}\nabla^T\mathbf{d}\right) + \alpha'_{3d}\mathbf{I}, \end{aligned} \tag{2.16}$$

with the coefficients

$$\begin{cases} a_1 = c_1, \quad a_2 = \frac{c_1}{2}\left(\mathrm{tr}_{\mathbf{B}}^2 - \mathrm{tr}_{\mathbf{B}^2} - 4\right) - 2c_2 \\ \alpha'_{3d} = \left(2 - \mathrm{tr}_{\mathbf{B}}^2 + \mathrm{tr}_{\mathbf{B}^2}\right)(c_1 + 2c_2) + 2c_1\mathrm{tr}_{\mathbf{B}}. \end{cases} \tag{2.17}$$

Comparison between the 2D and 3D MR model with the same $\Psi$ is shown below:

$$\partial_{\mathbf{F}}\Psi_{\mathrm{MR}}\mathbf{F}^T = \begin{cases} 2c_1\left(\mathbf{Dd} - \nabla\mathbf{d}\nabla^T\mathbf{d}\right) + (2c_1\mathrm{tr}_{\mathbf{B}} - 2c_2)\,\mathbf{I}, & \text{2D model.} \\ 2a_1\left(\mathbf{Dd} - \nabla\mathbf{d}\nabla^T\mathbf{d}\right)^2 + 2a_2\left(\mathbf{Dd} - \nabla\mathbf{d}\nabla^T\mathbf{d}\right) + \alpha'_{3d}\mathbf{I}, & \text{3D model.} \end{cases}$$

where $a_1$, $a_2$, and $\alpha'_{3d}$ are given in (2.17).

**Derivation from 3D to 2D**

For the 3D model, $a_2$ varies with the structural rheology ($\mathrm{tr}_{\mathbf{B}}$ and $\mathrm{tr}_{\mathbf{B}^2}$) instead of being constant like $c_1$ in 2D model. The way to calculate $a_2$ is to compute directly $\mathrm{tr}_{\mathbf{B}}$ and $\mathrm{tr}_{\mathbf{B}^2}$ by (2.7) which involves a 3 by 3 matrix inverse at each considering point.

The 3D model degenerates into a 2D system when the geometry and variables are invariant with respect to one coordinate like a translation invariance with respect to $z$, for instance, in a Cartesian coordinate system or a rotation invariance in $\theta$ in a cylindrical coordinate system.

Assume invariance with respect to the third coordinate, and one has

$$\mathbf{F} = \begin{pmatrix} \mathbf{I} - \nabla_2 \mathbf{d} & 0 \\ 0 & 1 \end{pmatrix}^{-T} = \begin{pmatrix} \tilde{\mathbf{F}} & 0 \\ \mathbf{0} & 1 \end{pmatrix} \text{ with } \tilde{\mathbf{F}} = (\mathbf{I} - \nabla_2 \mathbf{d})^{-T}, \quad \nabla_2 \mathbf{d} = \begin{pmatrix} \partial_1 d_1 & \partial_1 d_2 \\ \partial_2 d_1 & \partial_2 d_2 \end{pmatrix}.$$

Consequently, $\mathrm{tr}_{(\mathbf{F}^T\mathbf{F})^j} = \mathrm{tr}_{(\tilde{\mathbf{F}}^T\tilde{\mathbf{F}})^j} + 1,\ j = 1,2,\ (\mathrm{tr}_{\mathbf{F}^T\mathbf{F}})^2 = (\mathrm{tr}_{\tilde{\mathbf{F}}^T\tilde{\mathbf{F}}})^2 + 2\mathrm{tr}_{\tilde{\mathbf{F}}^T\tilde{\mathbf{F}}} + 1$,

$$\begin{aligned} \Psi_{\mathrm{MR}}(\mathbf{F}) &= c_1 \mathrm{tr}_{\mathbf{F}^T\mathbf{F}} + c_2 \left( \mathrm{tr}_{(\mathbf{F}^T\mathbf{F})^2} - \mathrm{tr}^2_{\mathbf{F}^T\mathbf{F}} \right) \\ &= c_1 (\mathrm{tr}_{\tilde{\mathbf{F}}^T\tilde{\mathbf{F}}} + 1) + c_2 \left( \mathrm{tr}_{\left(\tilde{\mathbf{F}}^T\tilde{\mathbf{F}}\right)^2} + 1 - \left( (\mathrm{tr}_{\tilde{\mathbf{F}}^T\tilde{\mathbf{F}}})^2 + 2\mathrm{tr}_{\tilde{\mathbf{F}}^T\tilde{\mathbf{F}}} + 1 \right) \right) \\ &= (c_1 - 2c_2) \mathrm{tr}_{\tilde{\mathbf{F}}^T\tilde{\mathbf{F}}} + c_2 \left( \mathrm{tr}_{\left(\tilde{\mathbf{F}}^T\tilde{\mathbf{F}}\right)^2} - (\mathrm{tr}_{\tilde{\mathbf{F}}^T\tilde{\mathbf{F}}})^2 \right) + \text{constant} \end{aligned} \tag{2.18}$$

Hence, a comparison between the 2D model and the 3D model on a 2D configuration requires to replace the $c_1$ in the 2D Helmholtz potential by $c_1 - 2c_2$ from the 3D Helmholtz potential.

### 2.1.3 Solid mechanics equations – compressible material

**The S$^{\mathrm{t}}$–Venant–Kirchhoff stress tensor** $\quad \Psi_{\mathbf{STVK}}(\mathbf{F}) = {}^{\lambda_s}/_2 \mathbf{tr}^2_{\mathbf{E}} + \mu_s \mathbf{tr}_{\mathbf{E}^2}$

It is obvious to see that $\mathrm{tr}_{\mathbf{E}} = \frac{1}{2}(\mathrm{tr}_{\mathbf{F}^T\mathbf{F}} - \mathrm{tr}_{\mathbf{I}})$ , $\mathrm{tr}_{\mathbf{F}^T\mathbf{F}} = \mathrm{tr}_{\mathbf{F}\mathbf{F}^T}$, and their differential with respect to $\mathbf{F}$

$$\begin{cases} \partial_{\mathbf{F}} \mathrm{tr}_{\mathbf{F}^T\mathbf{F}} = 2\mathbf{F} & \Rightarrow \quad \partial_{\mathbf{F}} \mathrm{tr}_{\mathbf{E}} = \mathbf{F} \\ \partial_{\mathbf{F}} \mathrm{tr}_{(\mathbf{F}^T\mathbf{F})^2} = 4\mathbf{F}\mathbf{F}^T\mathbf{F} & \Rightarrow \quad \partial_{\mathbf{F}} \mathrm{tr}_{\mathbf{E}^2} = 2\mathbf{F}\mathbf{E} \end{cases} \tag{2.19}$$

Therefore

$$\partial_{\mathbf{F}} \Psi_{\mathrm{STVK}} \mathbf{F}^T = \mathbf{F}(\lambda_s \mathrm{tr}_{\mathbf{E}} + 2\mu_s \mathbf{E}) \mathbf{F}^T = \left[ \frac{\lambda_s}{2} (\mathrm{tr}_{\mathbf{B}} - \mathrm{tr}_{\mathbf{I}}) - \mu_s \right] \mathbf{B} + \mu_s \mathbf{B}^2 \tag{2.20}$$

**2D formulation [119]**

According to (2.8) and with $\det_{\mathbf{B}} = J^2$, $\mathbf{B}$ and $\mathbf{B}^2$ can be rewriten as:

$$\begin{aligned} \mathbf{B} &= \mathrm{tr}_{\mathbf{B}} \mathbf{I} - J^2 \mathbf{B}^{-1}, \\ \mathbf{B}^2 &= \mathrm{tr}_{\mathbf{B}} \mathbf{B} - J^2 \mathbf{I} = \left( \mathrm{tr}^2_{\mathbf{B}} - J^2 \right) \mathbf{I} - \mathrm{tr}_{\mathbf{B}} J^2 \mathbf{B}^{-1} \end{aligned} \tag{2.21}$$

Furthermore, equation (2.21) can be recast with $\mathbf{C} = \mathbf{I} - \mathbf{B}^{-1} = \mathbf{Dd} - \nabla\mathbf{d}\nabla^T\mathbf{d}$. Then,

$$\begin{aligned} \mathbf{B} &= \left(\mathrm{tr}_{\mathbf{B}} - J^2\right)\mathbf{I} + J^2\mathbf{C} \\ \mathbf{B}^2 &= \left[\mathrm{tr}_{\mathbf{B}}^2 - (1+\mathrm{tr}_{\mathbf{B}})J^2\right]\mathbf{I} + \mathrm{tr}_{\mathbf{B}}J^2\mathbf{C} \end{aligned} \tag{2.22}$$

With the help of (2.22) and $\mathrm{tr}_{\mathbf{I}} = 2$, (2.20) yields

$$\begin{aligned} \partial_{\mathbf{F}}\Psi_{\mathrm{STVK}}\mathbf{F}^T &= \left[\frac{\lambda_s}{2}(\mathrm{tr}_{\mathbf{B}} - 2) - \mu_s\right]\mathbf{B} + \mu_s\mathbf{B}^2 \\ &= \left[\frac{\lambda_s}{2}(\mathrm{tr}_{\mathbf{B}} - 2) - \mu_s\right]\left[\left(\mathrm{tr}_{\mathbf{B}} - J^2\right)\mathbf{I} + J^2\mathbf{C}\right] + \mu_s\left\{\left[\mathrm{tr}_{\mathbf{B}}^2 - (1+\mathrm{tr}_{\mathbf{B}})J^2\right]\mathbf{I} + \mathrm{tr}_{\mathbf{B}}J^2\mathbf{C}\right\} \\ &= \alpha\mathbf{I} + \beta\mathbf{C} = \alpha\mathbf{I} + \beta\left(\mathbf{Dd} - \nabla\mathbf{d}\nabla^T\mathbf{d}\right) \end{aligned} \tag{2.23}$$

with

$$\begin{cases} \alpha = \frac{\lambda_s}{2}(\mathrm{tr}_{\mathbf{B}} - 2)\left(\mathrm{tr}_{\mathbf{B}} - J^2\right) + \mu_s\mathrm{tr}_{\mathbf{B}}\left(\mathrm{tr}_{\mathbf{B}} - J^2 - 1\right) \\ \beta = \frac{\lambda_2}{2}(\mathrm{tr}_{\mathbf{B}} - 2) + \mu_s(\mathrm{tr}_{\mathbf{B}} - 1)J^2 \end{cases} \tag{2.24}$$

### 3D formulation

According to (2.9) and with $J^2 = \det_{\mathbf{B}}$, $\mathbf{B}$ and $\mathbf{B}^2$ can be rewriten as:

$$\begin{aligned} \mathbf{B} &= \mathrm{tr}_{\mathbf{B}}\mathbf{I} - \gamma\mathbf{B}^{-1} + J^2\mathbf{B}^{-2} \\ \mathbf{B}^2 &= \mathrm{tr}_{\mathbf{B}}\mathbf{B} - \gamma\mathbf{I} + J^2\mathbf{B}^{-1} = \left(\mathrm{tr}_{\mathbf{B}}^2 - \gamma\right)\mathbf{I} + \left(J^2 - \mathrm{tr}_{\mathbf{B}}\gamma\right)\mathbf{B}^{-1} + \mathrm{tr}_{\mathbf{B}}J^2\mathbf{B}^{-2} \end{aligned} \tag{2.25}$$

To make the content neat, we denote $t_1 = \mathrm{tr}_{\mathbf{B}}$ and $t_2 = \mathrm{tr}_{\mathbf{B}^2}$, and then $\mathbf{B}$ and $\mathbf{B}^2$ can be rewritten as :

$$\begin{aligned} \mathbf{B} &= t_1\mathbf{I} - \frac{1}{2}(t_1^2 - t_2)\mathbf{B}^{-1} + J^2\mathbf{B}^{-2}, \\ \mathbf{B}^2 &= \frac{1}{2}\left(t_1^2 + t_2\right)\mathbf{I} + \left[J^2 - \frac{1}{2}\left(t_1^3 - t_1t_2\right)\right]\mathbf{B}^{-1} + t_1J^2\mathbf{B}^{-2} \end{aligned} \tag{2.26}$$

Futhermore, equation (2.26) can be recast as $\mathbf{C} = \mathbf{I} - \mathbf{B}^{-1} = \mathbf{Dd} - \nabla\mathbf{d}\nabla^T\mathbf{d}$. Then,

$$\begin{aligned} \mathbf{B} &= \left[t_1 - \frac{1}{2}\left(t_1^2 - t_2\right) + J^2\right]\mathbf{I} + \left[\frac{1}{2}\left(t_1^2 - t_2\right) - 2J^2\right]\mathbf{C} + J^2\mathbf{C}^2, \\ \mathbf{B}^2 &= \left[\frac{1}{2}\left(t_1^2 + t_2\right) + J^2 - \frac{1}{2}\left(t_1^3 - t_1t_2\right) + t_1J^2\right]\mathbf{I} + \left[\frac{1}{2}\left(t_1^3 - t_1t_2\right) - J^2 - 2t_1J^2\right]\mathbf{C} + t_1J^2\mathbf{C} \end{aligned} \tag{2.27}$$

With the help of (2.27), (2.20) becomes

$$\begin{aligned}
\partial_{\mathbf{F}}\Psi_{\mathrm{STVK}}\mathbf{F}^T =& \left[\lambda_s\left(\frac{\mathrm{tr}_{\mathbf{B}}}{2}-\frac{3}{2}\right)-\mu_s\right]\mathbf{B}+\mu_s\mathbf{B}^2\\
=& \left[\lambda_s\left(\frac{\mathrm{tr}_{\mathbf{B}}}{2}-\frac{3}{2}\right)-\mu_s\right]\left[\left[t_1-\frac{1}{2}\left(t_1^2-t_2\right)+J^2\right]\mathbf{I}+\left[\frac{1}{2}\left(t_1^2-t_2\right)-2J^2\right]\mathbf{C}+J^2\mathbf{C}^2\right]\\
&+\mu_s\left[\left[\frac{1}{2}\left(t_1^2+t_2\right)+J^2-\frac{1}{2}\left(t_1^3-t_1t_2\right)+t_1J^2\right]\mathbf{I}+\left[\frac{1}{2}\left(t_1^3-t_1t_2\right)-J^2-2t_1J^2\right]\mathbf{C}+t_1J^2\mathbf{C}^2\right]\\
=&\alpha\mathbf{I}+\beta\mathbf{C}+\gamma\mathbf{C}^2\\
=&\alpha\mathbf{I}+\beta\left(\mathbf{Dd}-\nabla\mathbf{d}\nabla^T\mathbf{d}\right)+\gamma\left(\mathbf{Dd}-\nabla\mathbf{d}\nabla^T\mathbf{d}\right)^2
\end{aligned} \tag{2.28}$$

with

$$\begin{cases}
\alpha=\frac{\lambda_s}{4}\left(\mathrm{tr}_{\mathbf{B}}-3\right)\left(2\mathrm{tr}_{\mathbf{B}}-\mathrm{tr}_{\mathbf{B}}^2+\mathrm{tr}_{\mathbf{B}^2}+2J^2\right)+\frac{\mu_s}{2}\mathrm{tr}_{\mathbf{B}}\left(2\mathrm{tr}_{\mathbf{B}}+\mathrm{tr}_{\mathbf{B}^2}-\mathrm{tr}_{\mathbf{B}}^2-2+2J^2\right)\\
\beta=\frac{\lambda_s}{4}\left(\mathrm{tr}_{\mathbf{B}}-3\right)\left(\mathrm{tr}_{\mathbf{B}}^2-\mathrm{tr}_{\mathbf{B}^2}-4J^2\right)+\frac{\mu_s}{2}\left(\mathrm{tr}_{\mathbf{B}}^3-\mathrm{tr}_{\mathbf{B}}\mathrm{tr}_{\mathbf{B}^2}-\mathrm{tr}_{\mathbf{B}}^2+\mathrm{tr}_{\mathbf{B}^2}+2J^2-4\mathrm{tr}_{\mathbf{B}}J^2\right)\\
\gamma=\frac{\lambda_s}{2}\left(\mathrm{tr}_{\mathbf{B}}-3\right)J^2+\mu_s\left(\mathrm{tr}_{\mathbf{B}}-1\right)J^2
\end{cases} \tag{2.29}$$

3D fully Eulerian description (2.28) can be compared with 2D description (2.23) derived in previous section.

## 2.2 Monolithic formulation

### 2.2.1 Variational Formulation

For simplicity, we only consider the case of homogeneous boundary conditions on $\Gamma\subset\partial\Omega$, i.e. clamped or no–slip, and homogeneous Neumann conditions on $\partial\Omega^t\setminus\Gamma$.

So, given $\Omega_f^0$, $\Omega_s^0$, $\mathbf{d}$, and $\mathbf{v}$ at $t=0$, one must find $\left(\mathbf{v},p,\mathbf{d},\Omega_f^t,\Omega_s^t\right)$ with $\mathbf{v}_{|\Gamma}=0$ and

$$\int_{\Omega^t}\left(\rho\mathbb{D}_t\mathbf{v}\cdot\hat{\mathbf{v}}-p\nabla\cdot\hat{\mathbf{v}}-\hat{p}\nabla\cdot\mathbf{v}\right)+\frac{\mu}{2}\int_{\Omega_f^t}\mathbf{Dv}:\mathbf{D}\hat{\mathbf{v}}+\frac{1}{2}\int_{\Omega_s^t}\sigma_s:\mathbf{D}\hat{\mathbf{v}}=\int_{\Omega^t}\mathbf{f}\cdot\hat{\mathbf{v}} \tag{2.30}$$

$$\mathbb{D}_t\mathbf{d}=\mathbf{v}, \tag{2.31}$$

for all $(\hat{\mathbf{v}},\hat{p})$ with $\hat{\mathbf{v}}_{|\Gamma}=0$. Note that $\Omega_s^t$ and $\Omega_f^t$ are defined by

$$\frac{d\chi}{d\tau}=\mathbf{v}\left(\chi\left(\tau\right),\tau\right),\ \ \chi\left(t\right)\in\Omega_r^t\quad\Rightarrow\quad\chi\left(\tau\right)\in\Omega_r^\tau\ \ \forall\tau\in\left(0,T\right),\ \ r=s,f$$

In equation (2.30), solid part is written in a general form, because solid stress tensor $\sigma_s$ has different expressions for various models given in equations (2.13), (2.16), (2.23), and (2.28).

## 2.3 Numerical schemes and computational algorithm

### 2.3.1 Characteristic–Galerkin derivatives

Characteristics–Galerkin method is applied to (2.30) to discretize the total derivatives. Let $\Omega \subset \mathbb{R}^3$ , $\mathbf{v} \in \mathbf{H}_0^1(\Omega) := \{\mathbf{v} \in \left(H^1(\Omega)\right)^3 \ : \ v|_\Gamma = 0\}$ , $t \in (0,T)$ and $x \in \Omega$. Then, let $\chi^t_{\mathbf{v},x}(\tau)$ be the solution at time $\tau$ of

$$\dot{\chi}(\tau) = \mathbf{v}(\chi(\tau),\tau) \ \text{ with } \chi(t) = x.$$

If **u** is Lipschitz in space and continuous in time, the solution exists. The characteristic–Galerkin [115] method relies on the concept of total derivative:

$$\mathbb{D}_t\mathbf{u}(x,t) := \frac{d}{d\tau}\mathbf{u}(\chi(\tau),\tau)|_{\tau=t} = \partial_t\mathbf{u} + \mathbf{v}\cdot\nabla\mathbf{u} \tag{2.32}$$

Given a time step $\delta t$, let us approximate $\chi$ by $\mathbb{Y}$:

$$\chi^{(n+1)\delta t}_{\mathbf{v}^{n+1},x}(n\delta t) \approx \mathbb{Y}^{n+1}(x) := x - \mathbf{v}^{n+1}(x)\,\delta t$$

$$\mathbb{D}_t\mathbf{u}(x,t) \approx \frac{1}{\delta t}\left(\mathbf{u}^{n+1}(x) - \mathbf{u}^n\left(\mathbb{Y}^{n+1}(x)\right)\right)$$

### 2.3.2 A monolithic time–discrete variational formulation

Let $L_0^2(\Omega) = \{q \in L^2(\Omega) \ : \ \int_\Omega q = 0\}$.

**Theorem 1.** *The following variational problem is a consistent approximation with first order accuracy in time of (2.30)(2.31):*

*Find,* $\Omega^{n+1}$, $\mathbf{v}^{n+1} \in \boldsymbol{H}_0^1(\Omega^{n+1})$, $p^{n+1} \in L_0^2(\Omega^{n+1})$ *such that for all* $\hat{\mathbf{v}}^{n+1} \in \boldsymbol{H}_0^1(\Omega^{n+1})$, $\hat{p}^{n+1} \in L_0^2(\Omega^{n+1})$,

$$\begin{aligned}
&\int_{\Omega^{n+1}}\left(\rho^{n+1}\frac{\mathbf{v}^{n+1}-\mathbf{v}^n\circ\mathbb{Y}^{n+1}}{\delta t}\cdot\hat{\mathbf{v}} - p^{n+1}\nabla\cdot\hat{\mathbf{v}} - \hat{p}\nabla\cdot\mathbf{v}\right) + \int_{\Omega_f^{n+1}}\frac{\mu}{2}\mathbf{D}\mathbf{v}^{n+1} : \mathbf{D}\hat{\mathbf{v}}\\
&\quad + \delta t\int_{\Omega_s^{n+1}}\left[2a_1\left(\mathbf{D}\mathbf{v}^{n+1} - \nabla\mathbf{v}^{n+1}\nabla^T\tilde{\mathbf{d}}^n - \nabla\tilde{\mathbf{d}}^n\nabla^T\mathbf{v}^{n+1}\right)\left(\mathbf{D}\tilde{\mathbf{d}}^n - \nabla\tilde{\mathbf{d}}^n\nabla^T\tilde{\mathbf{d}}^n\right)\right.\\
&\quad + \qquad \left. a_2^{n+1}\left(\mathbf{D}\mathbf{v}^{n+1} - \nabla\mathbf{v}^{n+1}\nabla^T\tilde{\mathbf{d}}^n - \nabla\tilde{\mathbf{d}}^n\nabla^T\mathbf{v}^{n+1}\right)\right] : \mathbf{D}\hat{\mathbf{v}}\\
&\quad + \int_{\Omega_s^{n+1}}\left[a_1\left(\mathbf{D}\tilde{\mathbf{d}}^n - \nabla\tilde{\mathbf{d}}^n\nabla^T\tilde{\mathbf{d}}^n\right)^2 + a_2^{n+1}\left(\mathbf{D}\tilde{\mathbf{d}}^n - \nabla\tilde{\mathbf{d}}^n\nabla^T\tilde{\mathbf{d}}^n\right)\right] : \mathbf{D}\hat{\mathbf{v}} = \int_{\Omega^t}\mathbf{f}\cdot\hat{\mathbf{v}}
\end{aligned} \tag{2.33}$$

*where* $\tilde{\mathbf{d}}^n$ *stands for* $\mathbf{d}^n(\mathbb{Y}^{n+1})$ *and* $\mathbf{d}^{n+1}$ *is updated by*

$$\mathbf{d}^{n+1} = \mathbf{d}^n\circ\mathbb{Y}^{n+1} + \delta t\mathbf{v}^{n+1} \tag{2.34}$$

**Remark 1.** *One may wonder why the scheme is applied to* $\mathbf{v}$ *and not to* $\rho\mathbf{v}$*? Note that* $\rho = \rho_f \mathbf{1}_{\Omega_f^t} + \rho_s \mathbf{1}_{\Omega_s^t}$ *is convected by the velocity* $\mathbf{v}$*. Hence,* $\rho^{n+1}(x) = \rho^n \circ \mathbb{Y}^{n+1}(x)$*. This shows that discretizing the total derivative of* $\mathbf{v}$ *or the total derivative of* $\rho\mathbf{v}$ *gives the same scheme:*

$$\frac{1}{\delta t}\left(\mathbf{w}^{n+1}(x) - \mathbf{w}\left(\mathbb{Y}^{n+1}(x)\right)\right) = \left(\partial_t \mathbf{w} + \mathbf{v}\cdot\nabla\mathbf{w}\right)|_{x,t^{n+1}} + O(\delta t)\, \textit{with}\ \ \mathbf{w} = \mathbf{v}\ \textit{or}\ \ \mathbf{w} = \rho\mathbf{v} \tag{2.35}$$

**Proof of Theorem 1** With the characteristic Galerkin method, a consistent time discretization of (2.30) would be that at each time step:

Find $\mathbf{v}^{n+1} \in \mathbf{H}_0^1\left(\Omega^{n+1}\right)$, $p \in L_0^2\left(\Omega^{n+1}\right)$, $\Omega^{n+1} = \Omega_f^{n+1} \cup \Omega_s^{n+1}$, such that $\forall \hat{\mathbf{v}} \in \mathbf{H}_0^1\left(\Omega^{n+1}\right)$, $\forall \hat{p} \in L_0^2\left(\Omega^{n+1}\right)$; the three relations given below hold:

$$\begin{aligned} &\int_{\Omega^{n+1}} \left(\rho^{n+1}\frac{\mathbf{v}^{n+1} - \mathbf{v}^n \circ \mathbb{Y}^{n+1}}{\delta t}\cdot\hat{\mathbf{v}} - p^{n+1}\nabla\cdot\hat{\mathbf{v}} - \hat{p}\nabla\cdot\mathbf{v}\right) + \int_{\Omega_f^{n+1}} \frac{\mu}{2}\mathbf{D}\mathbf{v}^{n+1} : \mathbf{D}\hat{\mathbf{v}} \\ &+ \int_{\Omega_s^{n+1}} \left[a_1\left(\mathbf{D}\mathbf{d}^{n+1} - \nabla\mathbf{d}^{n+1}\nabla^T\mathbf{d}^{n+1}\right)^2 + a_2^{n+1}\left(\mathbf{D}\mathbf{d}^{n+1} - \nabla\mathbf{d}^{n+1}\nabla^T\mathbf{d}^{n+1}\right)\right] : \mathbf{D}\hat{\mathbf{v}} = \int_{\Omega^t} \mathbf{f}\cdot\hat{\mathbf{v}} \end{aligned} \tag{2.36}$$

$$\mathbf{d}^{n+1} = \tilde{\mathbf{d}}^n + \delta\mathbf{v}^{n+1} \quad \text{where } \tilde{\mathbf{d}}^n = \mathbf{d}^n \circ \mathbb{Y}^{n+1} \tag{2.37}$$

$$\Omega^{n+1} = \left(\mathbb{Y}^{n+1}\right)^{-1}\left(\Omega^n\right) = \left\{x\colon\ \mathbb{Y}^{n+1}(x) := x - \delta t\mathbf{v}^{n+1}(x) \in \Omega^n\right\} \tag{2.38}$$

A fully implicit monolithic formulation with variables $\left(\mathbf{v}^{n+1}, p^{n+1}\right)$ can be derived by substituting $\mathbf{d}^{n+1}$ into (2.36) with (2.37):

$$\begin{aligned} &\int_{\Omega^{n+1}} \left(\rho^{n+1}\frac{\mathbf{v}^{n+1} - \mathbf{v}^n \circ \mathbb{Y}^{n+1}}{\delta t}\cdot\hat{\mathbf{v}} - p^{n+1}\nabla\cdot\hat{\mathbf{v}} - \hat{p}\nabla\cdot\mathbf{v}^{n+1}\right) + \int_{\Omega_f^{n+1}} \frac{\mu}{2}\mathbf{D}\mathbf{v}^{n+1} : \mathbf{D}\hat{\mathbf{v}} \\ &\quad + \int_{\Omega_s^{n+1}} \left[a_1\left(\mathbf{D}\left(\tilde{\mathbf{d}}^n + \delta t\mathbf{v}^{n+1}\right) - \nabla\left(\tilde{\mathbf{d}}^n + \delta t\mathbf{v}^{n+1}\right)\nabla^T\left(\tilde{\mathbf{d}}^n + \delta t\mathbf{v}^{n+1}\right)\right)^2\right. \\ &\quad \left. + a_2^{n+1}\left(\mathbf{D}\left(\tilde{\mathbf{d}}^n + \delta t\mathbf{v}^{n+1}\right) - \nabla\left(\tilde{\mathbf{d}}^n + \delta t\mathbf{v}^{n+1}\right)\nabla^T\left(\tilde{\mathbf{d}}^n + \delta t\mathbf{v}^{n+1}\right)\right)\right] : \mathbf{D}\hat{\mathbf{v}} = \int_{\Omega^t} \mathbf{f}\cdot\hat{\mathbf{v}} \end{aligned} \tag{2.39}$$

By expanding $\tilde{\mathbf{d}}^n + \delta t\mathbf{v}^{n+1}$ in (2.39) and considering only the terms of order one in $\delta t$, the formulation can be linearized with the error of $O\left(\delta t^2\right)$. Then, we can get (2.33).

**Remark 2.** *Most studies [75, 120] keep their formulations with* $\mathbf{d}^{n+1}$ *or* $\mathbf{F}^{n+1}$ *like (2.36) which are easy to change them into an efficient steady solvers. However, this study is aimed to develop a numerical solver with Eulerian monolithic formulation to simulate a fluid–structure interaction problem with respect to time, such as blood flow in valved veins. It does take a long time to reach steady state when solving a stationary problem. However, this fully implicit monolithic formulation performs well for transient problems.*

### 2.3.3 Spacial discretization with finite elements

Let $\mathcal{T}_h^0$ be a triangulation of the initial domain. Spatial discretization can be done for the most popular finite elements for fluids: the Lagrangian triangular elements with the degree 2 for the space $V_h$ of velocities and displacements and the Lagrangian triangular elements of degree 1 for the pressure space $Q_h$ provided that the pressure is different in the structure and the fluid because the pressure is discontinuous at the interface $\Sigma$; therefore, $Q_h$ is the space of piecewise linear functions on the triangulations and continuous in $\Omega_r^{n+1}$, $r = s,\ f$. A penalization parameter $\varepsilon$ must be added to impose the uniqueness of the pressure, when $L_0^2$ is replaced by $Q_h \approx L^2$.

This leads us to find $\mathbf{v}_h^{n+1} \in V_{0h}$, $p_h^{n+1} \in Q_h$, $\Omega^{n+1}$ such that for all $\hat{\mathbf{v}}_h$, $\hat{p}_h \in V_{0h} \times Q_h$ with

$$\tilde{\mathbf{d}}_h^n := \mathbf{d}_h^n \circ \mathbb{Y}^{n+1}, \quad \text{where } \mathbb{Y}^{n+1}(x) = x - \mathbf{v}_h^{n+1}(x)\,\delta t,$$

the following holds:

$$\begin{aligned}
&\int_{\Omega^{n+1}} \left( \rho^{n+1} \frac{\mathbf{v}_h^{n+1} - \mathbf{v}_h^n \circ \mathbb{Y}^{n+1}}{\delta t} \cdot \hat{\mathbf{v}}_h - p_h^{n+1} \nabla \cdot \hat{\mathbf{v}}_h - \hat{p}_h \nabla \cdot \mathbf{v}_h^{n+1} \right) + \int_{\Omega_f^{n+1}} \frac{\mu}{2} \mathbf{D}\mathbf{v}_h^{n+1} : \mathbf{D}\hat{\mathbf{v}}_h \\
&\quad + \delta t \int_{\Omega_s^{n+1}} \left[ 2a_1 \left( \mathbf{D}\mathbf{v}_h^{n+1} - \nabla \mathbf{v}_h^{n+1} \nabla^T \tilde{\mathbf{d}}_h^n - \nabla \tilde{\mathbf{d}}_h^n \nabla^T \mathbf{v}_h^{n+1} \right) \left( \mathbf{D}\tilde{\mathbf{d}}_h^n - \nabla \tilde{\mathbf{d}}_h^n \nabla^T \tilde{\mathbf{d}}_h^n \right) \right. \\
&\qquad\qquad \left. + a_2^{n+1} \left( \mathbf{D}\mathbf{v}_h^{n+1} - \nabla \mathbf{v}_h^{n+1} \nabla^T \tilde{\mathbf{d}}_h^n - \nabla \tilde{\mathbf{d}}_h^n \nabla^T \mathbf{v}_h^{n+1} \right) \right] : \mathbf{D}\hat{\mathbf{v}}_h \\
&\quad + \int_{\Omega_s^{n+1}} \left[ a_1 \left( \mathbf{D}\tilde{\mathbf{d}}_h^{n+1} - \nabla \tilde{\mathbf{d}}_h^n \nabla^T \tilde{\mathbf{d}}_h^n \right)^2 + a_2^{n+1} \left( \mathbf{D}\tilde{\mathbf{d}}_h^n - \nabla \tilde{\mathbf{d}}_h^n \nabla^T \tilde{\mathbf{d}}_h^n \right) \right] : \mathbf{D}\hat{\mathbf{v}}_h = \int_{\Omega^t} \mathbf{f} \cdot \hat{\mathbf{v}}_h \\
&\quad \Omega^{n+1} = \left( \mathbb{Y}^{n+1} \right)^{-1} (\Omega^n) = \left\{ x \colon \mathbb{Y}^{n+1}(x) \in \Omega^n \right\}. \\
&\quad \mathbf{d}_h^{n+1} = \tilde{\mathbf{d}}_h^n + \delta t\, \mathbf{v}_h^{n+1}
\end{aligned} \tag{2.40}$$

### 2.3.4 Solution algorithm

Equation (2.40) must be solved iteratively because $\Omega^{n+1}$ is updated by (2.38). The most natural method is to freeze some coefficients, such as $a_2$, to obtain a well posed linear problem and iterate at each time step $n$:

1. Set $\rho = \rho^n$, $a_2 = a_2^n$, $\Omega = \Omega^n$, $\mathbf{v} = \mathbf{v}_h^n$, $\mathbb{Y}(x) = x - \mathbf{v}\delta t$,
2. Solve equation (2.40),
3. Set $\mathbf{v} = \mathbf{v}_h^{n+1}$, $\mathbb{Y}(x) = x - \mathbf{v}\delta t$, $\Omega_r = \mathbb{Y}^{-1}(\Omega_r^n)$, $r = s,\ f$, update the value of $a_2$ and $\rho$.
4. If not converged, return to step 2.

**Remark 3.** *To update $\Omega^{n+1}$, we move the vertices $q^j$ in the solid part by its velocity $\mathbf{v}(q^j)$, and it is more practical to shift the vertices $q^j$ in the fluid part by the distributed velocity*

$\mathbf{v}_d\left(q^j\right)$ *compatible with the new position of the interface* $\Sigma$ *and fluid boundary* $\partial\Omega_f^{n+1}$*. The distributed velocity can be determined by solving a Laplace equation with its boundary condition [121].*

$$-\nabla^2\mathbf{v}_d = 0, \quad \mathbf{v}_d|_\Sigma = \mathbf{v}, \quad \mathbf{v}_d|_{\partial\Omega_f^{n+1}} = \mathbf{0} \tag{2.41}$$

## 2.4 Stability analysis of monolithic formulation

### 2.4.1 Conservation of energy

**Proposition 1.** *In the continuous case, the following statement holds :*

$$\frac{d}{dt}\int_{\Omega^t}\frac{\rho}{2}|\mathbf{v}|^2 + \frac{\mu_f}{2}\int_{\Omega_f^t}|\mathbf{Dv}|^2 + \frac{d}{dt}\int_{\Omega_s^0}\Psi\left(\mathbf{I}+\nabla_{x^0}\mathbf{d}^T\right) = \int_{\Omega^t}\mathbf{f}\cdot\mathbf{v} \tag{2.42}$$

*Proof.* Choosing $\hat{\mathbf{v}} = \mathbf{v}$, $\hat{p} = -p$ in equation (2.30) and solid stress tensor $\sigma_s = \partial_{\mathbf{F}}\Psi\mathbf{F}^T$, it results in:

$$\int_{\Omega^t}\rho\mathbb{D}_t\mathbf{v}\cdot\mathbf{v} + \frac{\mu}{2}\int_{\Omega_f^t}\mathbf{Dv}\colon\mathbf{Dv}\int_{\Omega_s^t}\partial_{\mathbf{F}}\Psi\mathbf{F}^T : \nabla\mathbf{v} = \int_{\Omega^t}\mathbf{f}\cdot\mathbf{v} \tag{2.43}$$

Now, $\frac{d}{dt}\Psi(\mathbf{F}) = \partial_{\mathbf{F}}\Psi(\mathbf{F}) : \partial_t\mathbf{F}$ and $\mathbf{F}^T\nabla\mathbf{v} = \nabla_{x^0}\mathbf{v}\left(x^0\right) = \partial_t\nabla_{x^0}\mathbf{d}\left(x^0\right) = \partial_t\mathbf{F}^T\left(x^0\right)$, so conservation of the Helmholtz potential $\Psi$ can be derived as follows:

$$\begin{aligned}\int_{\Omega_s^t}\partial_{\mathbf{F}}\Psi\mathbf{F}^T : \nabla\mathbf{v} &= \int_{\Omega_s^0}\partial_{\mathbf{F}}\Psi\colon\mathbf{D}_{x^0}\mathbf{v} = \int_{\Omega_s^0}\partial_{\mathbf{F}}\Psi\colon\partial_t\mathbf{D}_{x^0}\mathbf{d} = \int_{\Omega_s^0}\partial_{\mathbf{F}}\Psi\colon\partial_t\mathbf{F}^T \\ &= \int_{\Omega_s^0}\frac{d}{dt}\Psi(\mathbf{F}) = \frac{d}{dt}\int_{\Omega_s^0}\Psi(\mathbf{F}) = \frac{d}{dt}\int_{\Omega_s^0}\Psi\left(\mathbf{I}+\nabla_{x^0}\mathbf{d}^T\right)\end{aligned} \tag{2.44}$$

With sufficient regularity on $\Omega^t$, the first term in (2.43) yields

$$\int_{\Omega^t}\rho\mathbb{D}_t\mathbf{v}\cdot\mathbf{v} = \int_{\Omega^t}\frac{d}{dt}\frac{|\mathbf{v}|^2}{2} = \frac{d}{dt}\int_{\Omega^t}\frac{|\mathbf{v}|^2}{2} \tag{2.45}$$

Therefore, one can combine (2.43), (2.44), and (2.45) to yield

$$\frac{d}{dt}\int_{\Omega^t}\frac{\rho}{2}|\mathbf{v}|^2 + \frac{\mu_f}{2}\int_{\Omega_f^t}|\mathbf{Dv}|^2 + \frac{d}{dt}\int_{\Omega_s^0}\Psi\left(\mathbf{I}+\nabla_{x^0}\mathbf{d}^T\right) = \int_{\Omega^t}\mathbf{f}\cdot\mathbf{v}$$

□

**Remark 4.** *When is* $\Psi$ *convex, additional regularity can be gained from this energy conservation which can lead to the existence of solution up to time* $T$*. Loosely speaking, in an optimistic prospective, the first time of contact of two boundaries which were not in contact initially (see [122–124] etc).*

### 2.4.2 Stability of the scheme discretized in time

**Proposition 2.** *When (2.36) is used and if* $f = 0$ *and* $\rho_r$ *is constant in each domain* $\Omega_r^n$, $r = s, f$*, one has*

$$\int_{\Omega^{n+1}} \frac{\rho^{n+1}}{2}\left|\mathbf{v}^{n+1}\right|^2 + \delta t \int_{\Omega_f^{n+1}} \frac{\mu}{2}\left|\mathbf{D}\mathbf{v}^{n+1}\right|^2 + \int_{\Omega_s^0} \Psi\left(\mathbf{F}^{n+1}\right) \leq \int_{\Omega^n} \frac{\rho^n}{2}\left|\mathbf{v}^n\right|^2 + \int_{\Omega_s^0} \Psi\left(\mathbf{F}^n\right) \tag{2.46}$$

*Proof.* With the selection of $\hat{\mathbf{v}} = \mathbf{v}^{n+1}$, $\hat{p} = -p^{n+1}$, $f = 0$ in equation (2.36), one has

$$\begin{aligned}
&\int_{\Omega^{n+1}} \left(\rho^{n+1}\frac{\mathbf{v}^{n+1} - \mathbf{v}^n \circ \mathbb{Y}^{n+1}}{\delta t}\cdot \mathbf{v}^{n+1}\right) + \frac{\mu}{2}\int_{\Omega_f^{n+1}} \left|\mathbf{D}\mathbf{v}^{n+1}\right|^2 \\
&+ \int_{\Omega_s^{n+1}} \left[a_1\left(\mathbf{D}\mathbf{d}^{n+1} - \nabla\mathbf{d}^{n+1}\nabla^T\mathbf{d}^{n+1}\right)^2 + a_2^{n+1}\left(\mathbf{D}\mathbf{d}^{n+1} - \nabla\mathbf{d}^{n+1}\nabla^T\mathbf{d}^{n+1}\right)\right] : \mathbf{D}\mathbf{v}^{n+1} = 0
\end{aligned} \tag{2.47}$$

Note that $\rho_r^{n+1}(x) = \rho_r^n \circ \mathbb{Y}^{n+1}(x)$, $x \in \Omega_r^{n+1}$, so the second term of time discretization yields

$$\int_{\Omega_r^{n+1}} \rho_r^{n+1}\mathbf{v}^n \circ \mathbb{Y}^{n+1} \cdot \mathbf{v}^{n+1} = \int_{\Omega_r^{n+1}} \left(\sqrt{\rho_r^n}\mathbf{v}^n\right) \circ \mathbb{Y}^{n+1}\left(\sqrt{\rho_r^{n+1}}\mathbf{v}^{n+1}\right)$$

By applying the Schwartz inequality on the right side, the following inequality is derived

$$\int_{\Omega_r^{n+1}} \left(\sqrt{\rho_r^n}\mathbf{v}^n\right) \circ \mathbb{Y}^{n+1}\left(\sqrt{\rho_r^{n+1}}\mathbf{v}^{n+1}\right) \leq \left(\int_{\Omega_r^{n+1}} \left(\sqrt{\rho_r^n}\mathbf{v}^n\right)^2 \circ \mathbb{Y}^{n+1}\right)^{\frac{1}{2}} \left(\int_{\Omega_r^{n+1}} \rho_r^{n+1}\left(\mathbf{v}^{n+1}\right)^2\right)^{\frac{1}{2}}$$

Then using the Young's inequality $ab \leq \frac{1}{2}a^2 + \frac{1}{2}b^2$, one can get

$$\left(\int_{\Omega_r^{n+1}} \left(\sqrt{\rho_r^n}\mathbf{v}^n\right)^2 \circ \mathbb{Y}^{n+1}\right)^{\frac{1}{2}} \left(\int_{\Omega_r^{n+1}} \rho_r^{n+1}\left(\mathbf{v}^{n+1}\right)^2\right)^{\frac{1}{2}} \leq \frac{1}{2}\int_{\Omega_r^{n+1}} \rho_r^{n+1}\left|\mathbf{v}^{n+1}\right|^2 + \frac{1}{2}\int_{\Omega_r^n} \rho_r^n\left|\mathbf{v}^n\right|^2$$

Note that the first term of (2.47) can be rewritten as

$$\frac{1}{2\delta t}\int_{\Omega_r^{n+1}} \rho_r^{n+1}\left|\mathbf{v}^{n+1}\right|^2 - \frac{1}{2\delta t}\int_{\Omega_r^n} \rho_r^n\left|\mathbf{v}^n\right|^2 \leq 0 \tag{2.48}$$

Recall that the fully Eulerian description of Mooney–Rivlin 3D model in equation (2.13) is

$$\partial_{\mathbf{F}}\Psi\mathbf{F}^T\Big|^{n+1} = \left[2a_1\left(\mathbf{D}\mathbf{d}^{n+1} - \nabla\mathbf{d}^{n+1}\nabla^T\mathbf{d}^{n+1}\right)^2 + 2a_2^{n+1}\left(\mathbf{D}\mathbf{d}^{n+1} - \nabla\mathbf{d}^{n+1}\nabla^T\mathbf{d}^{n+1}\right)\right]$$

The third term in (2.47) can be rewritten as:

$$\begin{aligned}
\int_{\Omega_s^{n+1}} \partial_{\mathbf{F}}\Psi\mathbf{F}^T\Big|^{n+1} : \nabla\mathbf{v}^{n+1} &= \int_{\Omega_s^{n+1}} \partial_{\mathbf{F}}\Psi\mathbf{F}^T\Big|^{n+1} : \nabla\left(\frac{\mathbf{d}^{n+1} - \mathbf{d}^n \circ \mathbb{Y}^{n+1}}{\delta t}\right) \\
&= \frac{1}{\delta t}\int_{\Omega_s^0} \partial_{\mathbf{F}}\Psi\left(\mathbf{F}^{n+1}\right) : \nabla_{x^0}\left(\mathbf{d}^{n+1} - \mathbf{d}^n\right) \\
&= \frac{1}{\delta t}\int_{\Omega_s^0} \partial_{\mathbf{F}}\Psi\left(\mathbf{F}^{n+1}\right) : \left(\mathbf{F}^{n+1} - \mathbf{F}^n\right)
\end{aligned} \tag{2.49}$$

By the convexity of $\Psi$, one has

$$\int_{\Omega_s^0} \partial_{\mathbf{F}}\Psi\left(\mathbf{F}^{n+1}\right) : \left(\mathbf{F}^{n+1}-\mathbf{F}^{n}\right) \geq \int_{\Omega_s^0} \Psi\left(\mathbf{F}^{n+1}\right) - \int_{\Omega_s^0} \Psi\left(\mathbf{F}^{n}\right)$$

Finally, the final inequality yields

$$\int_{\Omega^{n+1}} \frac{\rho^{n+1}}{2}\left|\mathbf{v}^{n+1}\right|^2 + \delta t \int_{\Omega_f^{n+1}} \frac{\mu}{2}\left|\mathbf{D}\mathbf{v}^{n+1}\right|^2 + \int_{\Omega_s^0} \Psi\left(\mathbf{F}^{n+1}\right) \leq \int_{\Omega^{n}} \frac{\rho^{n}}{2}\left|\mathbf{v}^{n}\right|^2 + \int_{\Omega_s^0} \Psi\left(\mathbf{F}^{n}\right) \tag{2.50}$$

□

### 2.4.3 Energy inequality for the fully discrete scheme

From the solution algorithm in section 2.3.4, a general mapping of $\hat{\mathbb{Y}}^{n+1}(\mathbf{x})$ can be defined as :

$$\hat{\mathbb{Y}}^{n+1}(\mathbf{x}) = \mathbf{x} - \delta t \begin{cases} \mathbf{v}_h^{n+1}(\mathbf{x}), & \mathbf{x} \in \Omega_s \\ \mathbf{v}_d(\mathbf{x}), & \mathbf{x} \in \Omega_f \end{cases} \tag{2.51}$$

where $\mathbf{v}_d$ is distributed velocity to move vertices in the fluid domain $\Omega_f$. The detailed description of $\mathbf{v}_d$ can be found in Equation (2.41). Then, the connection of position at $n+1$ and $n$ can be written as

$$\mathbf{X}^n = \mathbf{X}^{n+1} \circ \hat{\mathbb{Y}}^{n+1}. \tag{2.52}$$

For $(\mathbb{P}1, \mathbb{P}1)$ linear velocity–pressure element, velocity and pressure are continuous and piecewise linear on the triangulation of $\Omega^t$. The proof of proposition 2 can be adapted for the continuous case, as long as $\mathbf{X}^{n+1} \circ \hat{\mathbb{Y}}^{n+1}$ mapping remains linear. In other words, proposition 2 holds when the mapping remains linear, because whole variables are just transposed to a new position $\mathbf{X}^{n+1}$ by the mapping $\left(\hat{\mathbb{Y}}^{n+1}\right)^{-1}$.

For $(\mathbb{P}1b, \mathbb{P}1)$ velocity–pressure element, the previous statements holds, because each triangle (tetrahedron) can be separated into 3 subdivided triangle (4 subdivided tetrahedra) by the interior bubble point. On this subdivided triangulation, the velocity is chosen continuous and piecewise linear.

# Chapter 3

# Implementation of a monolithic formulation in FreeFEM++

## Contents

All simulation results in this study are carried out with software *FreeFem++*. This chapter briefly presents *FreeFem++* with some examples and scripts. In section 3.1, background and history of *FreeFem++* is introduced. In section 3.2, basic syntax and adhere tools are presented with examples and results mainly focused on building computational domain, and constructing linear system from variational formulation. In section 3.3, two distinct problems are considered, namely, the evolution problem and the problem governed by the incompressible Navier–Stokes equation.

## 3.1 Introduction

*FreeFem++* [125] is an open source partial differential equation solver developed by Frédéric Hecht, in collaboration with Olivier Pironneau, , Antoine Le Hyaric, Domique Bernardi and Kohji Ohtsuka, in the Laboratory Jacques-Louis Lions (LJLL) of Sorbonne Université (Paris, France). As a highly adaptive software developed to solve problems, *FreeFem++*

includes the following modules: triangular finite element spaces, composing of discontinuous FE spaces; automatic mesh generator; mesh adaptation; fast linear solvers; MPI (Message Passing Interface) tools for parallel computing. Users can write their own algorithms in *FreeFem++* scripts to solve PDEs and visualize the computed results within the software. For advanced users, *FreeFem++* provides a robust developing environment, so that it's feasible to implement user-defined finite elements and user-developed linear solvers.

## 3.2 FreeFem++ and its interpreted language

### 3.2.1 The syntax

*FreeFem++* language, an interpreted language based on C++, aims to numerically solve partial differential equations (PDEs) based on finite element method. *FreeFem++* syntax partially follows C++ syntex. In *FreeFem++*, the basic data types *int, real, complex, bool* correspond in C++ to *long, double, complex<double>, bool* respectively. The syntax for loops *for* and *while* or the conditional statements *if / else* is the same as C++ with the use of the brackets { } to define blocks. The declared variables can be manipulated with most of the usual C++ operators.

A special feature of the *FreeFem++* language is that some variable types are relevant to the finite element method, such as the mesh type *mesh*, the finite element space type *fespace*, or the variational formulation type *varf*. Examples of these types used in *FreeFem++* are given in script 3.1.

---

```
x, y, z //Cartesian coordinates
N.x, N.y, N.z // Normal vector components

int N = 10; //integer
real T=2.3; //real
bool bb = ( T > 0.0 );  //boolean

real[int] A(N); // array of N real values
// numbering from 0 to N-1
A(2) = 1; // Set 3rd value equals to 1

mesh th;      // 2d mesh
mesh3 th3;    // 3d mesh

fespace Vh(th,P1);  // finite element space
Vh uu=x^2+1;     // finite element function
uu[];         // array associated to FE function uu
uu[].max;     // max of the array uu
uu[].min;     // min of the array uu
```

```
uu[].sum;     // sum of all elements of uu
uu[].l1;      // L1 norm of uu
uu[].l2;      // L2 norm of uu
uu[].linfty;// L.infinity norm of uu

fespace Wh(th,[P1b,P1b,P1]);
Wh [u,v,p]; // a vectorial finite element function or array

// Definition of macro
macro div(u,v) ( dx(u) + dy(v) ) //EOM

func f=x+y; //function only depends on global varibles

// regular function declaration
func real g ( real a, int b ){
    return a + b;
}

// Weak formulation
varf a([var1,var2,...],[vh1,vh2,...])
    = int2d(...) + on(...);

// Stiffness matrix of the problem
matrix Am=a(Vh,Vh,solver=sparsesolver);
real[int] B=a(0,Vh);     // right hand side term

u[]=Am^-1*b;      // Solve u=A^-1*b
```

Script 3.1: Exemples of variable types, function declarations, and operators

### 3.2.2 Meshing tools

The first step to perform any kind of numerical simulations is to discretize a geometry $\Omega$ into the associated mesh. In *FreeFem++*, that is a triangulation $\mathcal{T}_h$, and mesh generation in two and three dimensions can be done by *FreeFem++* built-in tools. Mesh generated by third-party software such as Gmsh or TetGen can be used by FreeFem with tools **readmesh**.

#### 2D meshing – border

The geometry can be defined by closed boundaries which are described analytically. Each boundary is described by its parametric equation and is declared with a **border** type. The keyword **label** labels one curve or a group of curves of the boundary. The **label** type can be either an integer or a name. A tool **buildmesh** can automatically generate Delaunay triangulation from a set of boundary points (see scrip 3.2). An example of the generation mesh is in Figure 3.1.

Note that the orientation of the curve is essential to define the domain at the correct side of curve. In the **buildmesh** command, how many points on each piece of boundary must be explicit. These numbers are positive or negative, and the sign indicates the orientation of the curve (see script 3.6 and Figures 3.3(a) and 3.3(b)). It should also be noted that boundaries can only intersect at their end points.

```
int NN = 10, fix = 31;

// Build 2d mesh from connected borders
border c1( t = 0, 1 ){  x = 1 - t;   y = t;   label = fix;}
border c2( t = 0, 1 ){  x = -t;  y = 1 - t;   label = fix;}
border c3( t = 0, 1 ){  x = t - 1;   y = -t;  label = fix;}
border c4( t = 0, 1 ){  x = t;   y = t - 1;   label = fix;}
mesh th0 = buildmesh( c1(NN) + c2(NN) + c3(NN) + c4(NN) );
plot( th0, ps="Border.eps");
```

Script 3.2: Script to build the mesh plotted in Figure 3.1.

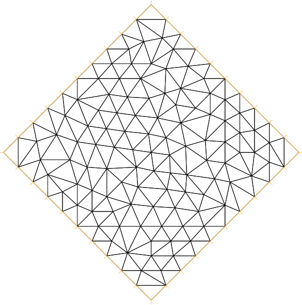

Figure 3.1: Mesh is surrounded by connected borders

To simplify and extend usage of **border**, we can summarize and recast script 3.2 into script 3.3 with multiple borders embedded a local loop of an index variable *i* to use values of array. Script 3.3 also comes to the similar mesh in Figure 3.1. A further implementation of multiple borders can be seen in later chapters. Most meshes generation in 2D can be generated in this way.

```
int NN = 10, fix = 31;

// Advanced way to use border with similar formulation
int[int] NCON(4);    NCON=NN;
real[int] XC=[ 1.0, 0.0, -1.0, 0.0 ];
```

```
real[int] YC=[ 0.0, 1.0, 0.0, -1.0 ];
border CON( t = 0, 1 ; i ){
    int ii = i+1;   if( i == 3 ) ii = 0;
    x = ( 1.0 - t )*XC(i) + t*XC(ii);
    y = ( 1.0 - t )*YC(i) + t*YC(ii);
    label = fix;
}
mesh th1 = buildmesh( CON( NCON ) );
plot( th1, ps="MultiBorder.eps");
```

Script 3.3: Script with multi-borders to build the mesh plotted in Figure 3.1.

### 2D meshing – square

Since rectangular geometry is widely used in numerical simulation, there is a useful and simple command **square** in *FreeFem++*. By prescribing numbers of boundary points along horizontal and vertical direction in order, uniform triangulation of a unit square geometry in Figure 3.2(a) can be automatically made by command **square** (see script 3.4).

By adding one expression in script 3.5, we can extend unit square geometry into rectangular geometry $[X_s, X_e] \times [Y_s, Y_e]$.

```
int NN = 10, fix = 31;

// Build unit square mesh
mesh th2 = square(NN,NN);
plot( th2, ps="square.eps");
```

Script 3.4: Script to build the mesh plotted in Figure 3.2(a).

```
int NN = 10, fix = 31;

// Build retangular mesh [Xs,Xe]*[Ys,Ye]
real Xs = 0.0, Xe = 2.0;
real Ys = 0.0, Ye = 1.0;
mesh th3 = square( 2*NN, NN, [ Xs + x*( Xe-Xs ), Ys + y*( Ye-Ys )] );
plot( th3, ps="square2.eps");
```

Script 3.5: Script to build the mesh plotted in Figure 3.2(b).

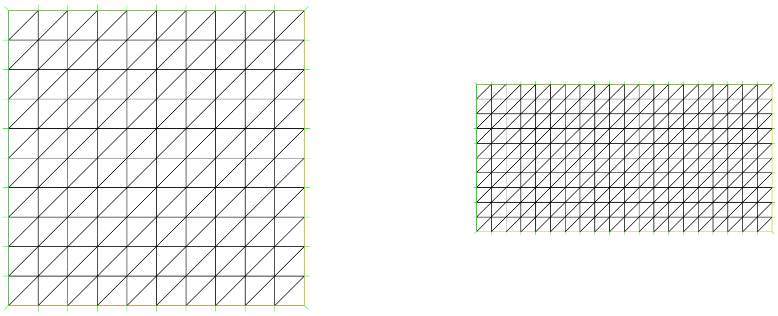

(a) (b)

Figure 3.2: Uniform square and rectangle meshes generated by the scripts 3.4 and 3.5, respectively.

### Manipulation of mesh

Commands in this section can be applied both to two-dimensional mesh and three-dimensional mesh.

**Change, region, and label** In previous section, each piece of boundary can be given different labels by **label** command. After triangulation, **buildmesh** in this case, different codes are automatically assigned by built-in tool to tell each closed district of mesh. We can get this code for each closed district of mesh with one interior point (line 33 and 34 in script 3.6). To change **label** and **region**, we can use **change** command to change (line 38 and 42 in script 3.6). More details are given in script 3.6.

**Truncating and adding** Extractng a specific district from a mesh can be accomplished by a function **trunc**. In script 3.6, we provide an example of truncating a specific district with its own **region** code, see Figure 3.4(a) and 3.4(b). This function **trunc** and command **region** are quite helpful when dealing with heterogeneous materials.

To add or collate two meshes together, one can simply use the + operator ( line 50 in script 3.6). Note that to collate two meshes, the vertices on the adjoining boundary must correspond.

```
1 int NN = 10, lab1 = 31, lab2 = 32, lab3 = 33;
2 int[int] LABs = [ 41, 42, 43 ];
3
4 // A [0,2]*[0,2] square geometry
5 int[int] NCON(4);     NCON=NN;
6 real[int] XC=[ 0.0, 2.0, 2.0, 0.0 ];
7 real[int] YC=[ 0.0, 0.0, 2.0, 2.0 ];
8 border CON( t = 0, 1 ; i ){
9     int ii = i+1;    if( i == 3 ) ii = 0;
```

```
    x = ( 1.0 - t )*XC(i) + t*XC(ii);
    y = ( 1.0 - t )*YC(i) + t*YC(ii);
    label = lab1;
}

// A circle geometry with rad 0.5 and center (1.0,1.0)
real RAD = 0.5;
real[int] CEN(2);   CEN = [ 1.0, 1.0];
border Cir( t = 0, 2.0*pi ){
    x = CEN(0) + RAD*cos( t );
    y = CEN(1) + RAD*sin( t );
    label = lab2;
}

// Orientation of Circle is counter clockwise
mesh th0 = buildmesh( CON( NCON ) + Cir(2*NN) );
plot( th0, ps="OM1.eps");

// Orientation of Circle is clockwise
mesh th1 = buildmesh( CON( NCON ) + Cir(-2*NN) );
plot( th1, ps="OM2.eps");

// Get code for separate region
int Rc = th0( CEN(0), CEN(1) ).region;
int Rs = th0( 0.01, 0.01 ).region;
cout<<" Rc = "<<Rc<<", Rs = "<<Rs<<endl;

// Change label with array [ old_L1, new_L1, old_L2, nwe_L2, ... ]
int[int] CC=[ lab1, LABs(0), lab2, LABs(1) ];
th0 = change( th0, label=CC );

// Change region with array [ old_R1, new_R1, old_R2, nwe_R2, ... ]
CC = [ Rc, 70, Rs, 71 ];
th0 = change( th0, region=CC );

// Truncation of mesh
mesh th2 = trunc( th0,region==70);  plot( th2, ps="TR1.eps");
mesh th3 = trunc( th0,region==71);  plot( th3, ps="TR2.eps");

```

```
// Add 2 meshes into 1
th0 = th2 + th3;    plot( th0, ps="ADD.eps");
```

Script 3.6: Script to show command **change, region, label, and trunc**.

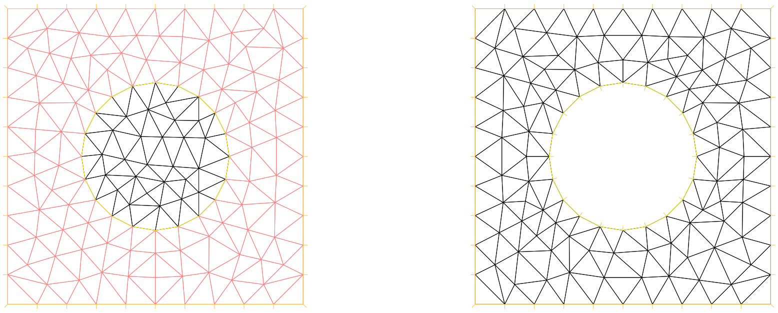

(a) (b)

Figure 3.3: Meshes generated by the script 3.6. (a) *OM1.eps*; (b) *OM2.eps* show different meshes with two orientations of circular curve.

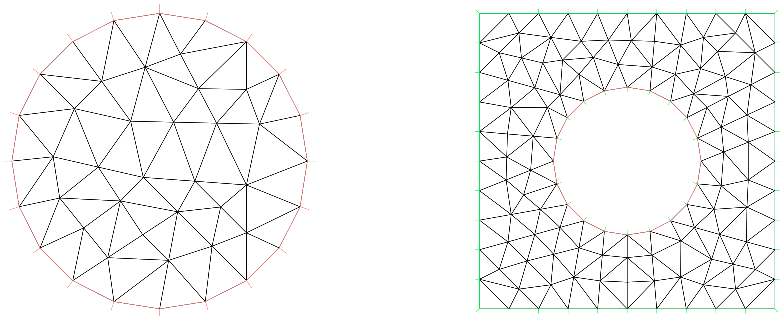

(a) (b)

Figure 3.4: Meshes generated by the script 3.6. (a) and (b) indicate two separated regions, 70 and 71, truncated by command **trunc**.

### Adapt mesh

A straightforward tool for mesh adaptation is the function **splitmesh**. This function divides each triangle by the value at the center of the triangle of a spatial function. An example of function **splitmesh** is schematic in script 3.7 and is shown in Figure 3.5.

```
border b(t=0,4.0*pi){ x = -0.5*cos(t)+cos( -0.5*t )+1.5;
y =-sin(-0.5*t); label =1;}
```

```
mesh Th=buildmesh ( b(70) ) ;
plot( Th, ps="Geometry.eps");

mesh Sh = splitmesh(Th,1+x*x); //split in int(1+x*x) triangles
plot( Sh, ps="Split.eps" ); // figure in the middle

mesh Qh=splitmesh(Th,5); // all triangles are split in 5
plot( Qh, ps="Split5.eps" ); // figure right
```

Script 3.7: Script to adapt mesh with the **splitmesh** function.

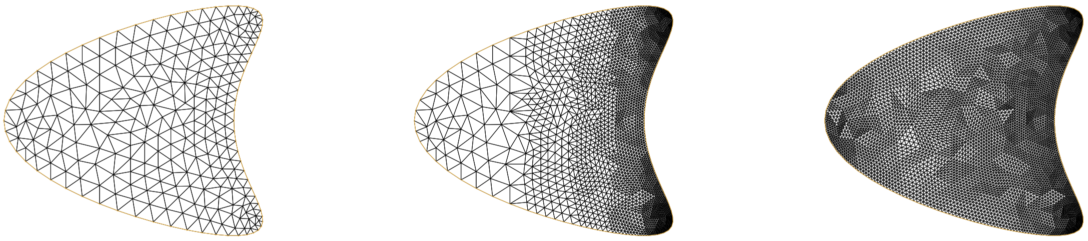

(a) (b) (c)

Figure 3.5: Meshes generated by the script 3.7, (a) original mesh gererated by **buildmesh**, (b) split original triangles in *int* $(1+x^2)$ triangles, (c) split original triangles in 5 triangles.

The function **adaptmesh** is the one built-in tool to adapt two dimensional mesh with ample arguments. It's based on a variable metric/Delaunay automatic meshing algorithm. There are abundant arguments of **adaptmesh**, including the required precision **err**, the minimum **hmin** or maximum **hmax** edge size of the triangles, or the maximum number of vertices **nbvx**. See the full documentation for the details of arguments. As an example of *adaptmesh* in script 3.8, mesh adaptation is performed with respect to the function $u$, and the results are illustrated in Figure 3.6.

```
border b(t=0,4.0*pi){ x = -0.5*cos(t)+cos( -0.5*t )+1.5;
y =-sin(-0.5*t); label =1;}
mesh Th=buildmesh ( b(70) ) ;

fespace Vh(Th,P1);
func f= 10.0*exp( -50.0*square(x-1.0) - 50.0*square(y) );
Vh u=f; //u is the projection of f to Vh
Vh u0;

plot( Th, u, fill=1, ps="Adapt0.eps");
```

```
plot( Th, ps="MAdapt0.eps");
for(int it=0; it<5; ++it) {
    Th = adaptmesh( Th, u, err=1.0e-3 ); //meshad
    u = f;  plot( Th, u, fill=1, ps="Adapt"+(it+1)+".eps");
     plot( Th, ps="MAdapt"+(it+1)+".eps");
}
```

Script 3.8: Script to adapt mesh with the **adaptmesh** function.

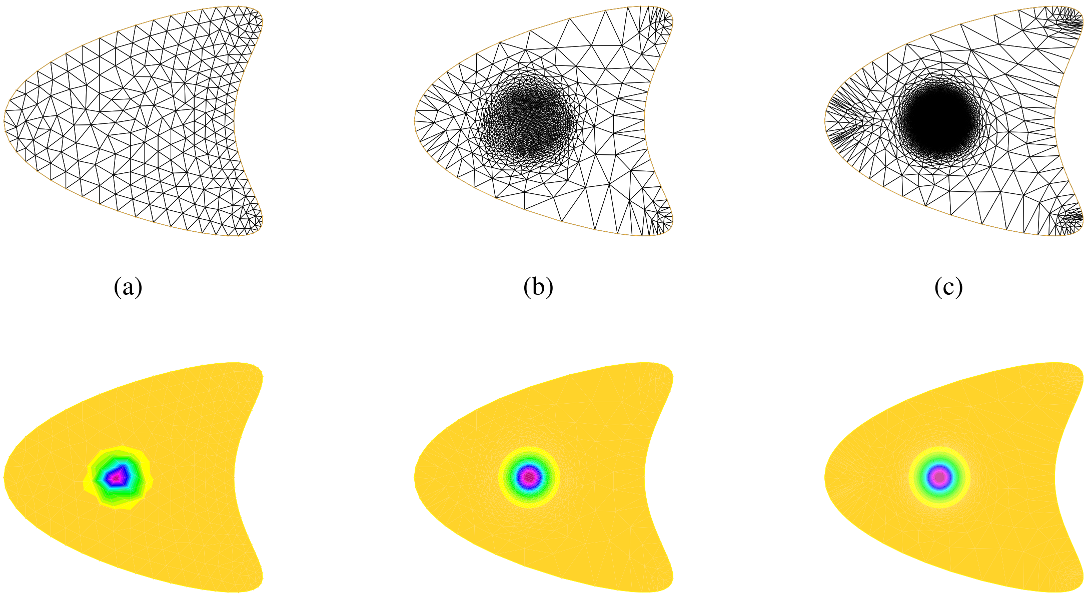

(a) (b) (c)

(d) (e) (f)

Figure 3.6: Meshes generated by the script 3.8, (a) original mesh generated by **buildmesh**, (b) adapt mesh with respect to function $u$ after one iteration, (c) mesh adapted after five iterations, (d) to (f) are corresponding variable $u$ at each mesh.

### 3.2.3 Finite element method

#### Finite element space

The software *FreeFem++* is mainly developed to numerically solve partial differential equations with finite element methods. It has an extra package *FreeVol* for finite volume methods. Therefore, except manual construction of stiffness matrix, problems must be expressed in their weak form. The weak formulation consists of multiplying the equation by a test function and integrating it over the computational domain $\Omega$. Then, time discretization scheme needs to be chosen, and the final finite element formulation can be expressed as: find $\omega \in V_\omega(\Omega)$

$$a(\omega,\varphi) - l(\varphi) = 0, \qquad \forall \varphi \in V_\varphi(\Omega). \tag{3.1}$$

*FreeFem++* uses a penalty method to impose Dirichlet boundary conditions. For Neumann boundary conditions, it's directly implemented into the weak formulation without any derivation error.

*FreeFem++* contains classical finite elements such as the Lagragian finite elements ($\mathbb{P}_0$, $\mathbb{P}_1$, $\mathbb{P}_2$, $\mathbb{P}_3$, $\mathbb{P}_4$), bubble elements ($\mathbb{P}_{1b}$, $\mathbb{P}_{2b}$), discontinuous $\mathbb{P}_1$ finite elements, and Raviart–Thomas elements. A full list of finite elements available in *FreeFem++* can be referred to the documentation, and it is convenient to include a user–defined finite elements in a C++ extension file. which can also find one example in documentation.

Let $V_h$ be a space embedded in the continuous space $H^1(\Omega)$. The $\mathbb{P}_1$ finite element discretization of $V_h$ on triangulation $\mathcal{T}_h$ of $\Omega$ corresponds to the space of continuous piecewise polynomial of degree one defined as follows

$$V_h = \left\{\omega_h \in H^1(\Omega), \omega_h \in \mathcal{C}(\Omega), \omega_{h|_K} \in P^1(K), \forall K \in \mathcal{T}_h\right\}. \tag{3.2}$$

The type **fespace** is to define the discrete finite element space for the unknowns and test functions. The declaration of a finite element space on any mesh $\mathcal{T}_h$ can be written as follows.

```
fespace Vh(th,P1);          //scalar space
fespace Wh(th,[P1b,P1b,P1]);          //vectorial space
```

Script 3.9: Declaration of finite element spaces.

The trial function $u$ and the test function $v$ can then be declared in the finite element space $V_h$ accordingly.

```
Vh u, v;      //unknown and test function
Vh w = x;
Wh [u,v,p] = [ 1.0, X + y, 1 - y^2 ];
```

Script 3.10: Declaration of finite element functions in the space $V_h$.

### Weak formulation

In *FreeFem++*, partial differential equations are solved in their weak forms within the context of finite element method. Problem is defined by the keywords **solve, problem**, or **varf**, and the problem should be well–posed, non–singular and linear. For a nonlinear problem, *FreeFem++* lets users implement their own linearization schemes. *FreeFem++* provides many direct and iterative solvers, such as conjugate gradient CG, GMRES, the multifrontal solver UPFPACK, the superLU, the MUMPS, and domain decomposition method HPDDM.

In scripts 3.11, the Poisson's equation is solved as an example to demonstrate the use of the keyword **solve, problem** or **varf**.

```
int NN=50;  int[int] LAB(4);    LAB=1;
mesh th=square( NN, NN, label=LAB );    //mesh
fespace Vh(th,P1b); //P1b FE space
Vh u, v;     //unknown and test function
func f=1;    //right hand side function
func g=0;    //boundary condition function

// Weak form of Poisson equation in macro
macro PE(th,u,v,f,g)
int2d(th)( dx(u)*dx(v) + dy(u)*dy(v) )  /* bilinear form $\int_{\mathcal{T}_h}\nabla u\cdot\nabla v$ */
- int2d( th )( f*v )     /* right hand side $\int_{\mathcal{T}_h} fv$ */
+ on( 1, u=g )           /* bondary conditions */
//EOM

solve Pdef1(u,v) = PE(th,u,v,f,g);   // declare and solve the problem

problem Pdef2(u,v) = PE(th,u,v,f,g);// declare the problem
Pdef2;       //solve the problem

varf Pdef3(u,v) = PE(th,u,v,f,g);    // bilinear form
matrix A = Pdef3(Vh,Vh);             //construct stiffness matrix
Vh F;   F[] = Pdef3(0,Vh);        //construct RHS vector
u[] = A^-1*F[];                      //solve the problem
```

Script 3.11: Solving the Poisson's equation in 2d with the keyword **solve, problem**, and **varf**.

In spite of the complexity of usage, the keyword **varf** is normally faster than others, so it is suggested to solve a large problem with the keyword **varf**.

## 3.3 Solving problems in FreeFem++

### 3.3.1 Evolution problem

To solve an evolution problem with finite element methods, time differential terms are discretized with a finite difference scheme, and then a stationary problem is solved at each time step.

In this section, the heat equation is regarded as an example, and it takes only few lines of code in *FreeFem++* to solve and display results. A general form of the reaction–diffusion problem is: find a function $u \in \mathcal{C}([0,T])$, for $T > 0$, such that

$$\begin{aligned} \frac{\partial u}{\partial t} - \mathcal{D}\nabla^2 u = f \qquad & \text{in } ]0,T] \times \Omega, \\ u = g_D \qquad & \text{on } ]0,T] \times \Gamma_D, \\ \nabla u \cdot \mathbf{n} = g_N \qquad & \text{on } ]0,T] \times \Gamma_N, \\ u(0,x) = u_0(x) \qquad & \text{in } \Omega. \end{aligned} \tag{3.3}$$

$u_0 \in L^2$ is the initial condition to the problem, $f$ the reaction term, $\mathbf{n}$ the normal, and $g_D/g_N$ the value of Dirichlet/Neumann boundary condition. For any $g \in H^{1/2}(\Gamma_D)$, let $V_g = \left\{v \in H^1(\Omega),\ v = g \text{ on } \Gamma_D\right\}$. The weak formulation of (3.3) is to find $u \in L^2(]0,T[, V_{g_D}) \cup \mathcal{C}\left([0,T], L^2(\Omega)\right)$ such that, $\forall t \in ]0,T[$,

$$\begin{aligned} \forall v \in V_0, \int_\Omega \left(\frac{\partial u}{\partial t} v + \mathcal{D}\nabla u \cdot \nabla v\right) - \int_{\Gamma_N} \mathcal{D}\nabla u \cdot \mathbf{n} v = \int_\Omega f v, \\ u(0,x) = u_0(x). \end{aligned} \tag{3.4}$$

To begin with, implicit Euler scheme is implemented to discretize $\frac{\partial u}{\partial t}$ term. The equation (3.4), in its semi-discrete form, reads as : find $u^{n+1} \in V_{g_D}$ such that

$$\forall v \in V_0, \int_\Omega \left(\frac{u^{n+1} - u^n}{\delta t} v + \mathcal{D}\nabla u^{n+1} \cdot \nabla v\right) - \int_{\Gamma_N} \mathcal{D}\nabla u^{n+1} \cdot \mathbf{n} v = \int_\Omega f v, \quad \forall n \in \mathbb{N} \tag{3.5}$$

Let $V_{h,g}$ be the finite element approximation of the space $V_g$ on the triangulation $\mathcal{T}_h$. The weak formulation sets into a finite dimensional linear system: find $u^{n+1} \in V_{h,g_D}$ such that

$$\forall v \in V_0, \int_{\mathcal{T}_h} \left(\frac{u^{n+1} - u^n}{\delta t} v + \mathcal{D}\nabla u^{n+1} \cdot \nabla v\right) - \int_{\Gamma_N} \mathcal{D}\nabla u^{n+1} \cdot \mathbf{n} v = \int_{\mathcal{T}_h} f v, \quad \forall n \in \mathbb{N} \tag{3.6}$$

In the following script 3.12, the keywords *varf* and $A^{-1}$ introduced in the previous section allows to write the problem in a variational formulation and solves it at each time step.

---

```

int BCD=1, BCN=2;    int NN=20;// label of boundary
int[int] LL=[BCN,BCN,BCN,BCN];
// [0,1]*[0,1] square mesh
mesh th = square(NN,NN,[x,y],label=LL);
// trick to remove a tiny square [0.4,0.6]*[0.4,0.6]
th = trunc( th, x>0.6 || y>0.6 || x<0.4 || y<0.4, label=BCD
  );
```

```
plot(th,ps="Domain.eps");

int NT=5; real dt = 0.2, time=0; // time parameters
real D=0.1; // thermal conductivity

//finite element space and variables
fespace V2h(th,P2); V2h u, u0;
macro dd(u) [dx(u),dy(u)]//EOM

// iso valu for output plot
real[int] color(40);    for( int i=0;i<40;i++) color(i)=i*0.01;

// weak formulation of problem
varf heat(u,v) = int2d(th)(u*v/dt + D*dd(u)'*dd(v) )
               + int2d(th)( u0*v/dt )
               + on( BCD, u=(x*y)*time );
// time loop
for( int nt=0 ; nt < NT ; nt++ ){
    time = time + dt;   u0=u;
    matrix A = heat(V2h,V2h);   real[int] b=heat(0,V2h);
    u[] = A^-1*b; // solving linear system
    plot(u,viso=color,cmm="time="+time, fill=1,ps="EV"+nt+".eps");
}
```

Script 3.12: *FreeFem++* code to solve heat conductivity.

### 3.3.2 Incompressible Navier–Stokes equation

The incompressible Navier–Stokes equation is composed of the following equations

$$\begin{aligned} \frac{\partial \mathbf{v}}{\partial t} + \mathbf{v}\cdot\nabla\mathbf{v} - \nu\nabla^2\mathbf{v} + \nabla p = \mathbf{f} \quad & \text{in } \Omega \\ \nabla\cdot\mathbf{v} = 0 \quad & \text{in } \Omega \end{aligned} \tag{3.7}$$

for the primitive variables $\mathbf{v}$ and $p$.

The incompressible Navier–Stokes equations (3.7) are solved using the charateristic Galerkin method [115], in section 2.3.1, together with the Euler implicit scheme for the time discretization. The term $\mathbf{v}^n \circ \mathbf{X}^n$ is computed by the interpolation operator *convect*$(\mathbf{a}^n, -\delta t, \phi)$, where $\mathbf{a}$ is the convective velocity and $\phi$ is the interpolated variable. The Navier–Stokes equations can be approximated through the pseudo-compressible approxi-

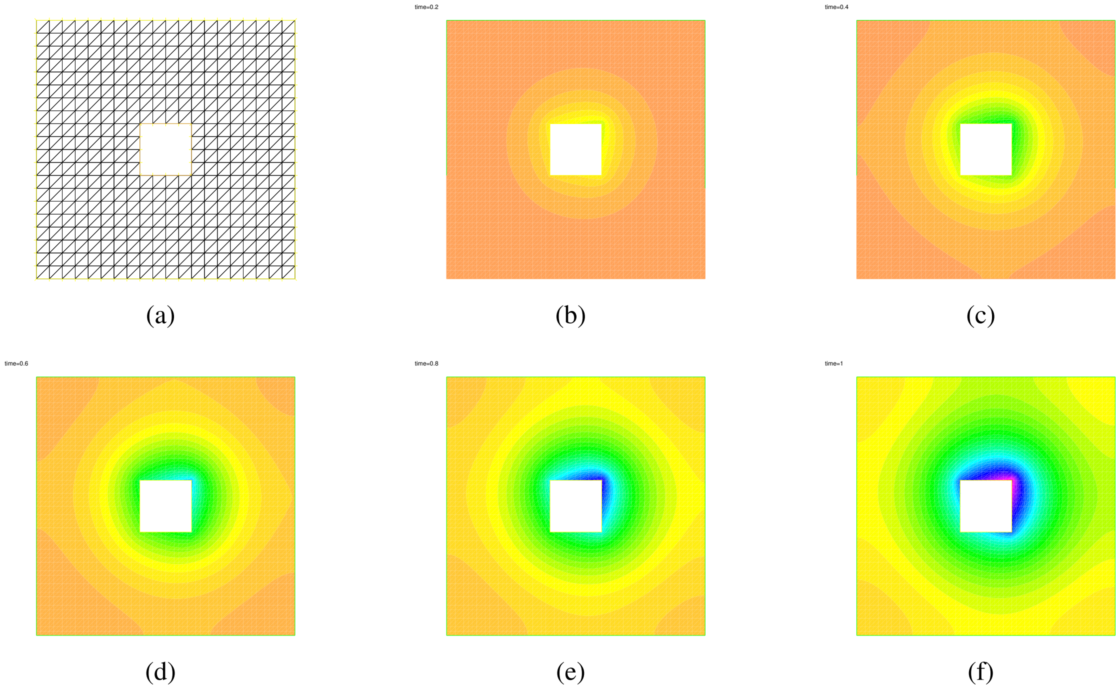

(a) (b) (c)

(d) (e) (f)

Figure 3.7: (a) Computational domain and mesh generated by script 3.12. The contours of simulation results are plotted at (b) $t = 0.2$, (c) $t = 0.4$, (d) $t = 0.6$, (e) $t = 0.8$, (f) $t = 1.0$.

mation

$$\begin{aligned} \frac{\mathbf{v}^{n+1} - \mathbf{v}^n \circ \mathbf{X}^n}{\Delta t} - \nu \nabla^2 \mathbf{v}^{n+1} + \nabla p^{n+1} = \mathbf{f}^{n+1} \quad \text{in } \Omega \\ \nabla \cdot \mathbf{v}^{n+1} + \varepsilon p^{n+1} = 0 \quad \text{in } \Omega \end{aligned} \tag{3.8}$$

where $\varepsilon$ is a small parameter. The formulation (3.8) with the artificial compressibility method is introduced by Chorine [126] and Témam [127]. The pseudo compressibility term is not only essential to achieve the V-ellipticity property of the bilinear form in the discretized system (3.8), but also works as a numerical stabilizer.

Let us consider the product space

$$V = \left\{ (\mathbf{w}, q) \in \left[ H^1(\Omega) \right]^2 \times L^2(\Omega), \mathbf{w} = 0 \text{ on } \Gamma \right\}$$

Considering boundary conditions, the weak formulation of (3.8) is as follows: find $\left( \mathbf{v}^{n+1}, p^{n+1} \right) \in V$ such that

$$\begin{aligned} \int_\Omega \left( \frac{\mathbf{v}^{n+1} - \mathbf{v}^n \circ \mathbf{X}^n}{\Delta t} \right) \cdot \hat{\mathbf{v}} + \nu \int_\Omega \nabla \mathbf{v}^{n+1} \cdot \nabla \hat{\mathbf{v}} - \int_\Omega p^{n+1} \nabla \cdot \hat{\mathbf{v}} = \int_\Omega \mathbf{f}^{n+1} \cdot \hat{\mathbf{v}} \\ \int_\Omega q \nabla \cdot \mathbf{v}^{n+1} + \varepsilon \int_\Omega p^{n+1} q = 0 \end{aligned} \tag{3.9}$$

for all $(\hat{\mathbf{v}}, p) \in V$. As $\varepsilon \to 0$, the solution of (3.9) tends to be the solution of the problem:

find $\left(\mathbf{v}^{n+1}, p^{n+1}\right) \in V$ such that

$$\begin{aligned}\int_\Omega \left(\frac{\mathbf{v}^{n+1}-\mathbf{v}^n\circ\mathbf{X}^n}{\Delta t}\right)\cdot\hat{\mathbf{v}} + \nu\int_\Omega \nabla\mathbf{v}^{n+1}\cdot\nabla\hat{\mathbf{v}} - \int_\Omega p^{n+1}\nabla\cdot\hat{\mathbf{v}} &= \int_\Omega \mathbf{f}^{n+1}\cdot\hat{\mathbf{v}} \\ \int_\Omega q\nabla\cdot\mathbf{v}^{n+1} &= 0\end{aligned} \tag{3.10}$$

for all $(\hat{\mathbf{v}}, p) \in V$, and it has been proven in [128] as

$$||\mathbf{v}'^{n+1}-\mathbf{v}^{n+1}||_{[H_0^1]^2} + ||p'^{n+1}-p^{n+1}||_{L^2} < C\varepsilon, \tag{3.11}$$

where $C$ is a constant and is independent of $\varepsilon$. In this study, $\varepsilon = 10^{-10}$ is chosen. $\mathbb{P}_1$ bubble - $\mathbb{P}_1$ elements are adopted to satisfy the LBB stability condition [129–132].

The incompressible Navier–Stokes equations (3.7) are solved with the boundary conditions

$$\begin{aligned}\mathbf{v} &= 0 && \text{on } \Gamma_{fix}\cup\Gamma_{fix2}, \\ \mathbf{v} &= \mathbf{U}_{in} && \text{on } \Gamma_{Inlet}, \\ -p\mathbf{n}+\nu\nabla\mathbf{v}\cdot\mathbf{n} &= 0 && \text{on } \Gamma_{Outlet},\end{aligned} \tag{3.12}$$

and the initial condition

$$\mathbf{v}_{|t=0} = \mathbf{v}_0 \text{ in } \Omega. \tag{3.13}$$

The linear system at each time step is given in *FreeFem++* script 3.13. The simulated results are shown in section 4.1.2.

```
load "MUMPS"; load "Curvature"; load "isoline";
load "iovtk"; include "Function.edp";
include "Contact.edp"; include "getARGV.idp"
verbosity=0;

// Time step and delta t
int NN=getARGV("-NN", 4000);
real T=200.0, dt=T/NN, time=0.0;

// fluid coefficients
real gravity = 0, rhof=1.0, penal=1e-20;
real Re=getARGV("-RE", 200.0), nu=1.0/Re;

int fix=21, fix2=22, Inlet=31, Outlet=41;
int Ns = 1, m=getARGV("-b", 100);
int[int] Np(Ns);      Np=-m;

real[int] XCEN(Ns), YCEN(Ns), RAD(Ns);
XCEN(0)=9.5; YCEN(0)=0.0; RAD(0)=0.5;

```

```
border Cir( t=0,1; i){
x = XCEN[i]+RAD[i]*cos(2*pi*t);
y = YCEN[i]+RAD[i]*sin(2*pi*t);
label = fix2;
}

int n=getARGV("-m", 20);
real maxX=40.0, minX=0.0, maxY=10.0, minY=-10.0;

/* size of Rectangular Domain */
int[int] Nrec(4);  Nrec=[2*n,n,2*n,n];
real[int] Xrec=[minX,maxX,maxX,minX];
real[int] Yrec=[minY,minY,maxY,maxY];

/* Border of Rectangle */
border Rectangle( t=0,1; i ){
  int ii=(i+1)%4; real t1 = 1-t;
  x = Xrec[i]*t1 + Xrec[ii]*t;
  y = Yrec[i]*t1 + Yrec[ii]*t;

  if( i == 1 )label = Outlet;
  else if( i == 3 )label = Inlet;
  else label = fix;
}
mesh th=buildmesh( Rectangle(Nrec) + Cir(Np) );
int fluid=th(0.0,0.0).region;

// finite element variables
fespace Vh(th,P1);  Vh p;
fespace V2h(th,P1b);    V2h u,v, uold=0, vold=0.0;

// function for inlet boundary conditions
int seed = 123456789;   randinit ( seed );
func real UIN( real TIME, real Uin ){
    if( TIME > 2.0 )return Uin;
    else return Uin*( 1 - 0.2*randreal1() );
}

// macro for equations
macro div(u,v) ( dx(u)+dy(v) ) // EOM
macro DD(u,v)  [[2*dx(u),div(v,u)],[div(v,u),2*dy(v)]] // EOM
macro Grad(u,v)[[dx(u),dy(u)],[dx(v),dy(v)]] // EOM
```

```
macro D(u) [dx(u),dy(u)] // EOM
macro CONV(Vx,Vy,a,b,dt)[convect([Vx,Vy],dt,a),convect([Vx,Vy],dt,b)]//EOM

// weak formulation of incompressible Navier stokes equation
varf NS([u,v,p],[uh,vh,ph]) =
    int2d(th,fluid)( rhof*[u,v]' *[uh,vh]/dt
        + nu*0.5*trace( DD(uh,vh)' *DD(u,v) )
        - div(uh,vh)*p - div(u,v)*ph
        + penal*p*ph
    )
    + on(fix,fix2,u=0,v=0) + on(Inlet,u=UIN(time,Uin),v=0);

varf RHS([u,v,p],[uh,vh,ph]) =
    int2d(th,fluid)(
        rhof*CONV(uold,vold,uold,vold,-dt)' *[uh,vh]/dt
    )
    + on(fix,fix2,u=0,v=0) + on(Inlet,u=UIN(time,Uin),v=0);

fespace Wh(th,[P1b,P1b,P1]);

// time loop
for(int n=0;n<NN;n++){
    time+=dt;

    Wh [uc,vc,pc];
    // construct linear system
    matrix AA=NS(Wh,Wh,solver=sparsesolver);
    real[int] bb=RHS(0,Wh); //source of linear problem
    uc[] = AA^-1*bb;        //solve the linear system
    u=uc;   v=vc;   p=pc;
    uold = u;   vold = v; //update variables
}
```

Script 3.13: Freefem++ code to solve flow pass a fixed cylinder with Navier Stokes equations.

## 3.4 Concluding remarks

*FreeFem++* consists of numerous tools as presented in this chapter, which makes it easy to be applied to solve partial differential equations with finite element method. It is a straightforward programming language, and it is easy to learn it from examples. Furthermore, it is feasible to link external tools and software with *FreeFem++* to deal with more complex tasks, especially in three dimensions and parallel computing.

Unlike most commercial softwares which pack all solving procedure into several options to set up numerical methods and solution algorithms, *FreeFem++* allows users to define their own weak formulation and solving algorithms in the script. Main task of *FreeFem++* is to automatically assemble stiffness matrix and the right hand side vector for the discretized problem of weak formulation defined in the script within the framework of the finite element method. Furthermore, *FreeFem++* is embedded and possibly linked with numerous packages such as MMG3d, finite element spaces, sequential and parallel linear solvers, etc.

Finally, while all the tasks presented in this chapter are sequential, they can be parallelized by calling different processes simultaneously. One powerful library *HPDDM* is regarded as an example, which utilizes domain decomposition as the preconditioners. The detailed introduction can be found in Appendix C.

# Chapter 4

# Verification and validation

## Contents

This chapter is aimed at verifying and validating the proposed finite element solver with Eulerian monolithic formulation with benchmark problems in 2D and 3D respectively. Validation of numerical solvers can be separated into three parts with the consideration of fluid, structure, and coupling of fluid and structure, respectively. For two dimensional problems, vorticity $\omega$ is defined as $\omega = v_x - u_y$ with velocity tensor $\mathbf{u} = (u, v)$.

The fluid solver with the viscous incompressible Navier Stokes equations is validated with some well–known CFD benchmark problems, namely, the lid–driven cavity flow [133–137] and the flow pass a cylinder. [138–149]. For the structural solver with hyperelastic model, it is validated with analytical solutions and numerical results of a cantilever beam bending under variant loadings [150]. The proposed FSI solver with Eulerian monolithic formulation is verified with two similar numerical simulations given in [54,68,113,151–154] and validated with an experiments of a structural model immersed in fluid [155–159]. At last, three dimensional monolithic formulation is validated with a thin plate in steady cross flow [160,161] and with an elastic structure in merging flow from two inlets [162].

## 4.1 Validation of Navier Stokes equations

### 4.1.1 Lid–driven cavity flow

Viscous fluid is contained in a unit square cavity with a sliding upper wall, as shown in Figure 4.1. This problem is so called lid–driven cavity flow, which is a benchmark problem

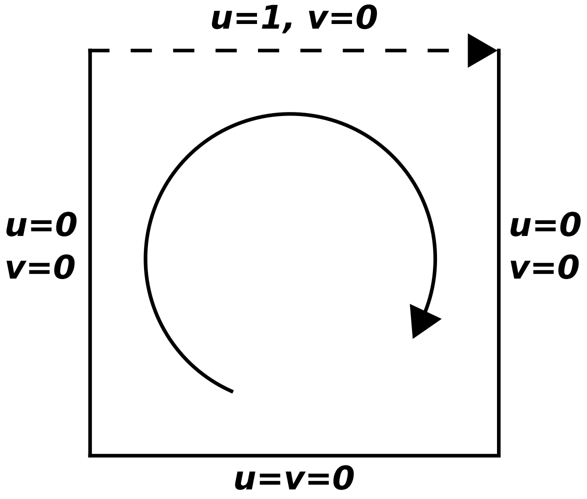

Figure 4.1: Schematic of lid–driven cavity flow

for viscous incompressible fluid flow, and the simulation results are carried out by solving a steady and linearized weak formulation of Navier Stokes equation at $k+1$ iteration.

$$\int_{\Omega}\left(\left(\left(\mathbf{v}^{k}\cdot\nabla\right)\mathbf{v}^{k+1}\right)\cdot\hat{\mathbf{v}}+\frac{1}{2Re}\mathbf{D}\mathbf{v}^{k+1}:\mathbf{D}\hat{\mathbf{v}}-p^{k+1}\nabla\cdot\hat{\mathbf{v}}-\hat{p}\nabla\cdot\mathbf{v}^{k+1}\right)=0 \tag{4.1}$$

The whole computational domain is homogeneously discreized into 12000 Taylor–Hood $(\mathbb{P}_2-\mathbb{P}_1)$ elements. The simulation is carried out with velocity Dirichlet boundary conditions as illustrated in Figure 4.1 without any special treatment on corners' discontinuity. To speed up computation, numerical results obtained from lower Reynolds number are considered as initial conditions, and the calculation stops after 2000 iterations.

A clockwise rotating primary vortex is developed due to friction from the upper wall sliding from left to right. When Reynolds number increases, novel vortices are generated at bottom right, bottom left and top left corners of cavity. It can be observed from the streamlines colored with the velocity magnitude in Figure 4.2 with Reynolds number from 400 to 10000. Furthermore, the boundary layer becomes thinner as Reynolds number increases, and velocity sharply changes around walls.

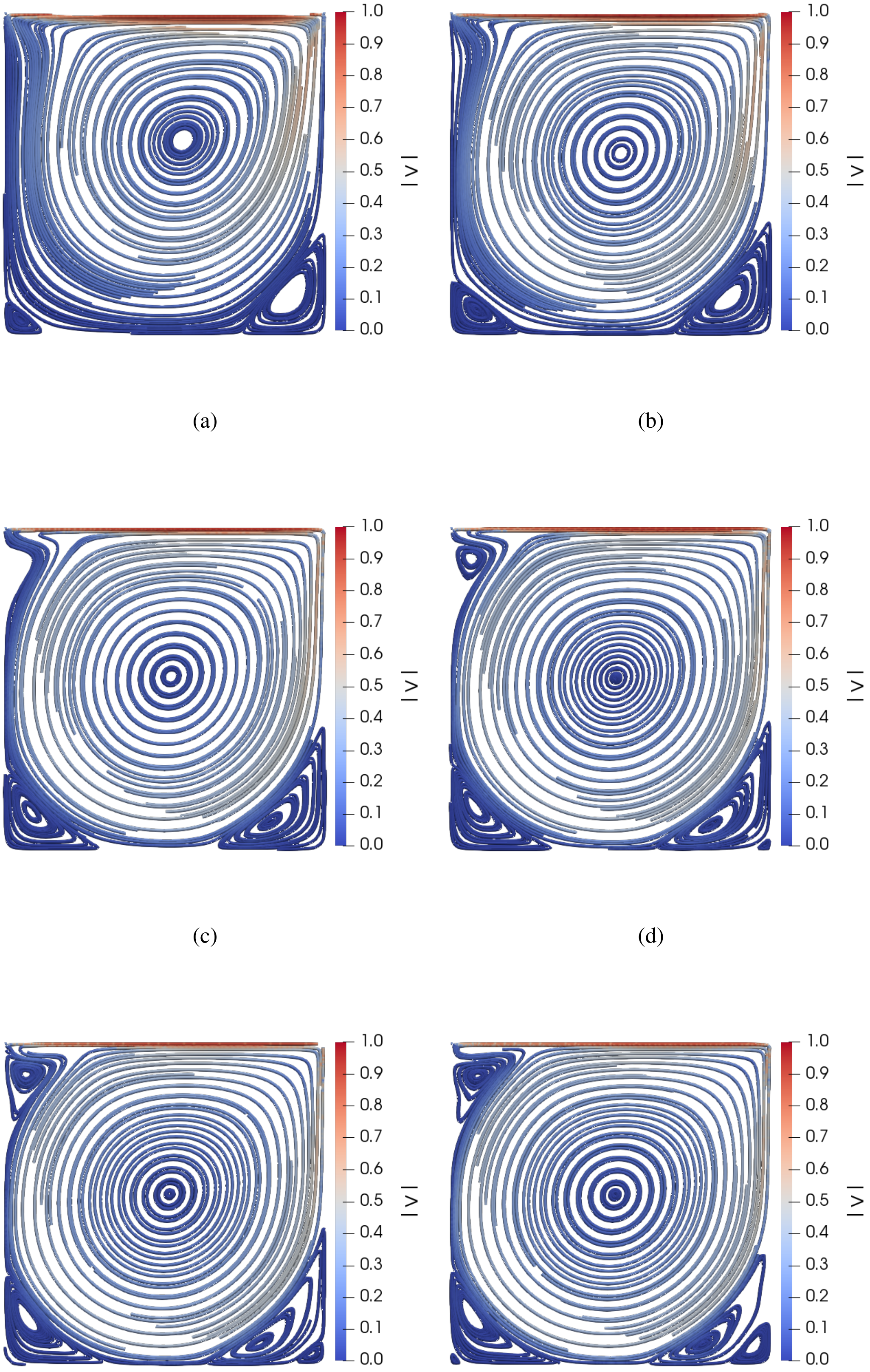

(a) (b)

(c) (d)

(e) (f)

Figure 4.2: Streamlines of the lid–driven cavity flow with different Reynolds numbers: (a) $Re = 400$; (b) $Re = 1000$; (c) $Re = 3200$; (d) $Re = 5000$; (e) $Re = 7500$; (f) $Re = 10000$.

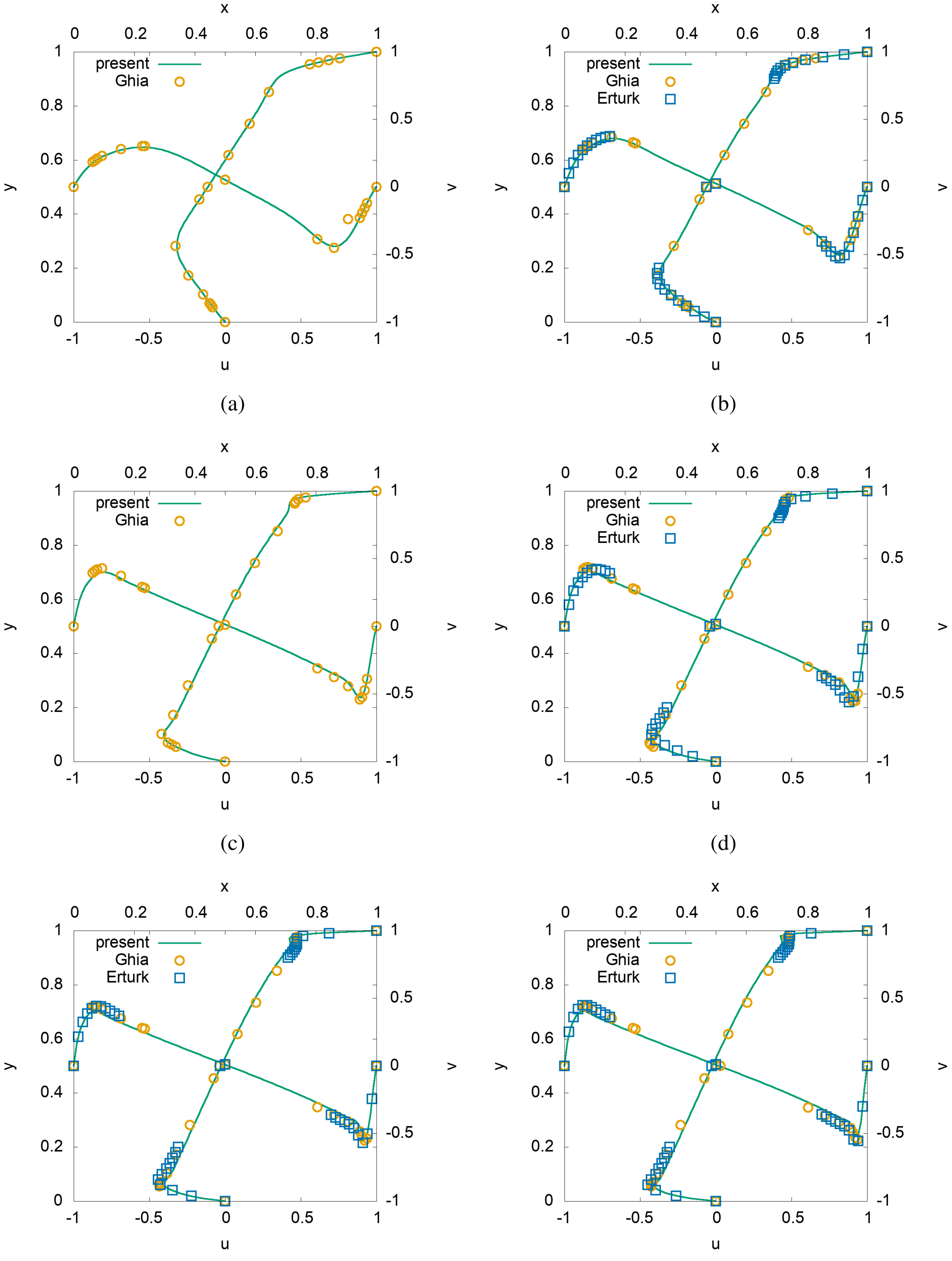

(a) (b)

(c) (d)

(e) (f)

Figure 4.3: Velocity profiles of the lid–driven cavity flow with different Reynolds numbers: (a) $Re = 400$; (b) $Re = 1000$; (c) $Re = 3200$; (d) $Re = 5000$; (e) $Re = 7500$; (f) $Re = 10000$.

Following two benchmarks of Erturk [136] and Ghia [135], velocity profiles are plotted along centerlines to compare $v$ along $x = 0.5$ and $u$ along $y = 0.5$. Figure 4.3 shows a nice agreement between the present results and those in literature. For high Reynolds numbers $Re = 7500$ and 10000, Figure 4.3(e) and 4.3(f), present results still can capture the velocity changes around boundaries with homogeneously distributed elements.

According to the literature survey, Hopf bifurcation occurs at $Re = 8000$, and we can also observe this bifurcation in the current results. The previous results are only shown and compared at final time step $t = 20$ in the Figure 4.2(f) and 4.3(f).

### 4.1.2 Flow past a cylinder

Under uniform inflow $u_\infty$, flow past a fixed cylinder with diameter $D$, and vortices is generated due to cylinder wall's friction. The center of a fixed cylinder is located at $(x_c, y_c) = (9.5, 0.0)$ in a rectangular domain $[0,40] \times [-10,10]$. A schematic of this problem is in Figure 4.4.

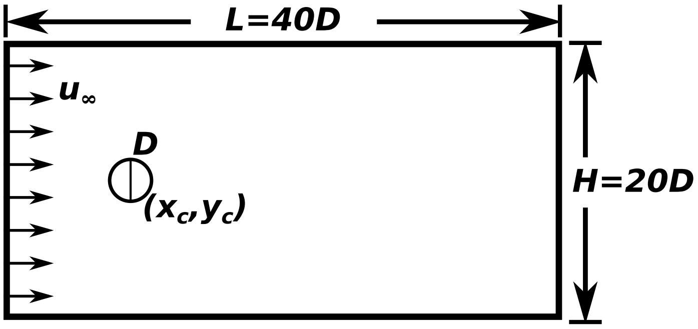

Figure 4.4: Computational domain of the flow passing a cylinder.

The flow field is changed from steady to transient flow field while Reynolds numbers $Re$ increasing. At lower value of $Re$, two symmetric and steady vortices are seen to attach behind the cylinder. As $Re$ increases, the vortices become stretched and the flow will be distorted and broke apart, leading to an alternating vortex shedding (or Kármán vortex street) in the wake. Flow transition is observed at $Re \approx 47$. Additionally, it is not sufficient to determine the bifurcation point with first order characteristic method. However, this study was not primarily aimed at precisely locating the bifurcation point of the problem.

To study two different flow patterns, our simulations were carried out at three different Reynolds numbers ($Re = 40, 100, 200$). Drag and lift coefficients and Strouhal number are calculated for the purpose of making a quantitative comparison with other numerical and experimental results. Drag and lift coefficients are defined as $C_D = {}^{F_x}/_{\frac{1}{2}u_\infty^2 D}$ and $C_L = {}^{F_y}/_{\frac{1}{2}u_\infty^2 D}$, respectively, where $F_x$ and $F_y$ are hydrodynamic forces applied on the cylinder along $x$ and $y$ direction and defined as $(F_x, F_y) = \int_{\partial\Omega_s} \left(-p\mathbf{I} + \mu_f \mathbf{D}\mathbf{v}\right) \cdot \mathbf{n} d\Gamma$. Strouhal number is defined as $S_t = \frac{f_q}{u_\infty D}$, and $f_q$ stands for shedding frequency of Kármán vortex street.

For numerical simulation, $\delta t$ is set to 0.015. Minimum element size $h_{min}$ is $\pi/100$, and 13000 $(\mathbb{P}_2 - \mathbb{P}_1)$ elements are considered. A constant velocity profile $u_\infty = 1$ is prescribed

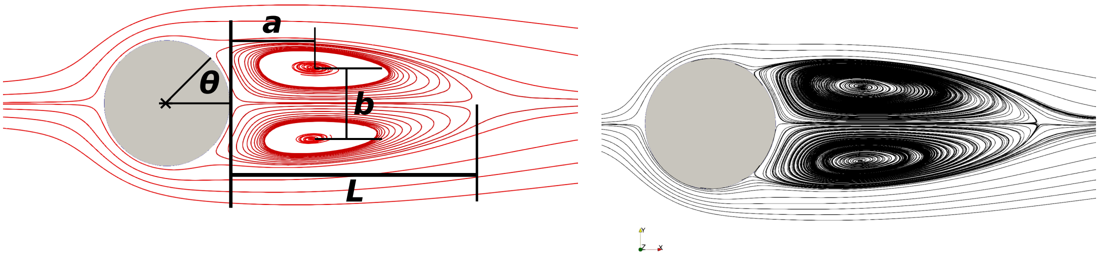

(a) (b)

Figure 4.5: Numerical results of flow past a cylinder when $Re = 40$ : (a) streamline contours and the chosen characteristic lengths; (b) vorticity contours.

at the inlet, and the Neumann boundary condition $\nabla \mathbf{v} \cdot \mathbf{n} = 0$ is prescribed along the outlet and the lateral boundaries, where $\mathbf{n}$ is the outward normal vector.

For the case with $Re = 40$, the drag coefficients and measures of steady wake are compared with well-established studies [84, 138, 143, 163–166]. Schematic of different measures for steady wake is shown in Figure 4.5(a) ( $L$ : length of bubble recirculation; $b$ : gap between two wake vortex centers; $a$ : horizontal distance between cylinder and vortex center; and $\theta$ : separating angle;). Streamlines and vorticity contours at $T = 200$ are plotted in Figure 4.5. The numerical results in Table 4.1 show good agreement with the referenced numerical and experimental results, and the corresponding methods are listed at last column for reference.

Table 4.1: Comparison of $C_D$ and characteristic lengths of vortices $L$, $a$, $b$, and $\theta$ at $Re = 40$

| Authors | $C_D$ | $L$ | $a$ | $b$ | $\theta$ | Method |
|---|---|---|---|---|---|---|
| Present | 1.584 | 2.02 | 0.66 | 0.56 | 51.41 | $2^{nd}$ FEM |
| Tritton [143] | 1.59 | - | - | - | - | Experiment |
| Coutanceau [165] | - | 2.13 | 0.75 | 0.59 | 53.8 | Experiment |
| Russel [166] | 1.6 | 2.29 | - | - | 53.8 | $4^{th}$ FDM |
| Linnick [84] | 1.54 | 2.28 | 0.72 | 0.60 | 53.6 | $4^{th}$ FDM |
| Taira [163] | 1.54 | 23.0 | 0.73 | 0.60 | 53.7 | $2^{nd}$ FVM |
| Chiu [138] | 1.52 | 2.27 | 0.73 | 0.60 | 53.6 | $2^{nd}$ FDM |
| Choi [164] | 1.52 | 2.25 | - | - | 51.0 | $2^{nd}$ FVM |

For the case with $Re = 100$ and 200, comparison of $C_D$, $C_L$, and $S_t$ is presented in Table 4.2, and the present results are in good agreement with the referenced numerical results [138, 164, 166–169]. Figure 4.6 plots streamlines and vorticity contours at $T = 200$ for $Re = 100$ and 200.

Additionally, we compare Strouhal numbers for the cases investigated at $Re = 75$, 100, 150, 200, 300, 400, and 500. A functional relationship between the Strouhal and the

Table 4.2: Comparison of $C_D$, $C_L$, and $S_t$ at $Re = 100$ and 200

| Author | Re=100 | | | Re=200 | | | Method |
|---|---|---|---|---|---|---|---|
| | $C_D$ | $C_L$ | $St$ | $C_D$ | $C_L$ | $St$ | |
| Present | $1.30 \pm 0.010$ | $\pm 0.33$ | 0.168 | $1.30 \pm 0.04$ | $\pm 0.62$ | 0.188 | $2^{nd}$ FEM |
| Stalberg [167] | $1.32 \pm 0.009$ | $\pm 0.33$ | 0.166 | - | - | - | $4^{th}$ FDM |
| Russell [166] | $1.38 \pm 0.007$ | $\pm 0.322$ | 0.169 | $1.29 \pm 0.022$ | $\pm 0.50$ | 0.195 | $4^{th}$ FDM |
| Chiu [138] | $1.35 \pm 0.012$ | $\pm 0.303$ | 0.167 | $1.37 \pm 0.051$ | $\pm 0.71$ | 0.198 | $2^{nd}$ FDM |
| Calhoun [168] | $1.35 \pm 0.014$ | $\pm 0.3$ | 0.175 | $1.17 \pm 0.058$ | $\pm 0.67$ | 0.202 | $2^{nd}$ FDM |
| Choi [164] | $1.34 \pm 0.011$ | $\pm 0.315$ | 0.164 | $1.36 \pm 0.048$ | $\pm 0.64$ | 0.191 | $2^{nd}$ FVM |
| Wright [169] | - | - | - | $1.33 \pm 0.04$ | $\pm 0.68$ | 0.196 | $2^{nd}$ FVM |

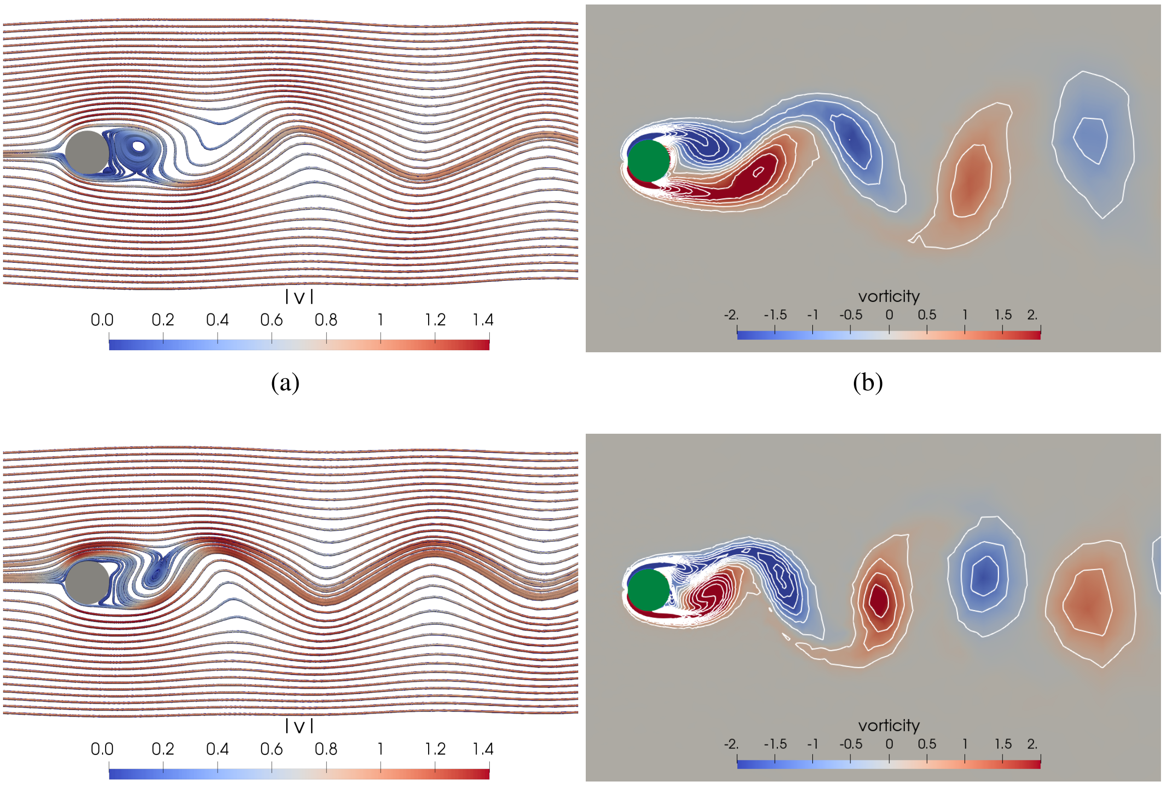

(a) (b)

(c) (d)

Figure 4.6: The simulation results in the near wake of the investigated circular cylinder at $T = 200$ : (a) streamlines at $Re = 100$; (b) vorticity contours at $Re = 100$; (c) streamlines at $Re = 200$; (d) vorticity contours at $Re = 200$.

Reynolds number up to $Re = 1000$ has been given by Willamsona and Brown [170]. The comparison among the current results and numerical results by Stålberg [167] is plotted in Figure 4.7.

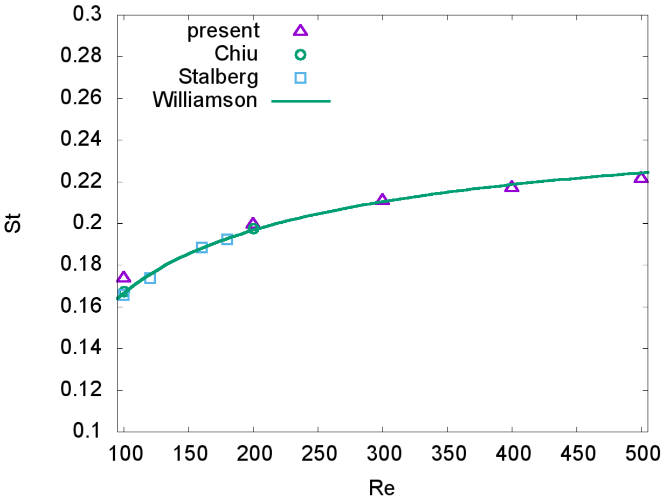

Figure 4.7: Comparison on Strouhal number

## 4.2 Validation of structural equations

### 4.2.1 Bending beam

The proposed solid solver with a fully Eulerian description in previous chapter can be validated with the analytical solution [171] and the simulation results [150] in the study of an elastic beam bending under an uniformly distributed load $P_{in}$, and it is modelled by linear elasticity model.

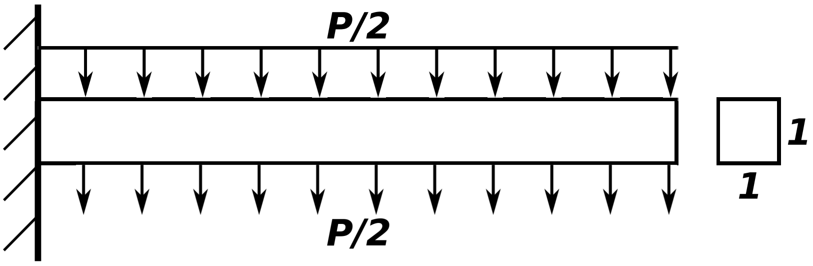

Figure 4.8: Simulation results of free falling beam with variant elastic models.

The beam with unit cross section area and length of 10 $in$ along $y$-direction, $[0,1] \times [0,10] \times [0,1]$, is considered to be clamped at $y = 0$ plane. The domain is discretized into 4000 elements. The uniform distributed load $\frac{P_{in}}{2}$ $lb/in$ is applied along $z$ direction on the top and the bottom of surface as shown in Figure 4.8. The density of the beam is $\rho_s = 10^{-6}$ $lb\ sec^2/in^4$. Young's modules $E$ and Poisson ratio $\nu_s$ of the beam are chosen as $1.2 \times 10^4$ $lb/in^2$ and 0.2. Simulation is carried out in fully Eulerian description using three dimensional Mooney–Rivlin and $\mathrm{S^t}$–Venant–Kirchhoff model.

Deflection is predicted under various loads $P_{in}$. Analytical solutions and simulation results are shown in Figure 4.9. There are three inferences to be drawn from the comparison

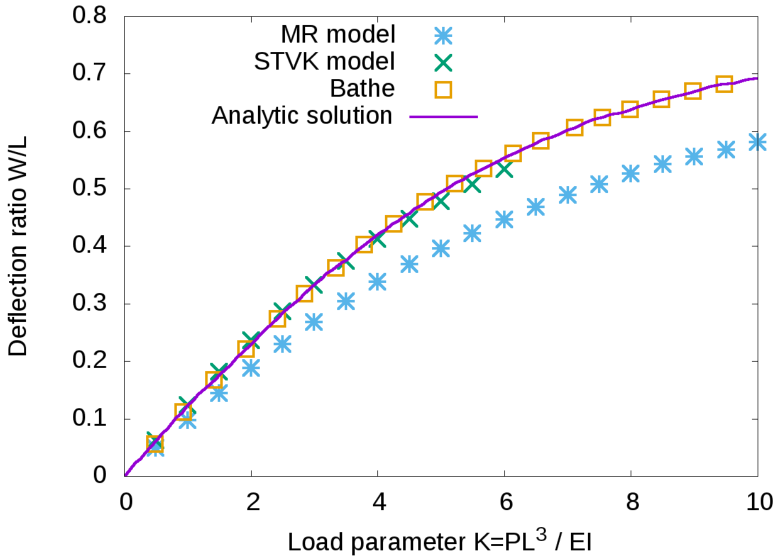

Figure 4.9: Simulation results for the free falling beam with different elastic models.

of results. First, all kinds of models display consistent response while the deflection is small enough. The approximation of hyperelastic model is also confirmed. Second, results of compressible STVK model are closer to analytical solutions than incompressible MR model, because Poisson ratio $\nu_s$ is far from 0.5. Third, with optimized coefficients for Mooney–Rivlin model, it's possible to conduct numerical results with a better agreement to the analytical solution, because coefficients $c_1$ and $c_2$ of Mooney–Rivlin model are simply chosen as $c_1 = \frac{\mu_s}{2}$ and $c_2 = 0$ in this numerical study. An overestimation of the coefficients makes the beam harder than expected which can be also observed in Figure 4.9.

## 4.3 Validation of 2D monolithic formulation

### 4.3.1 A thin elastic plate clamped into a small rigid square body immersed in a flowing fluid

According to [68, 153], under a constant inflow $U_{in}$, flow past through an elastic plate $[0,4] \times [-0.03, 0.03]$ attached to a fixed rigid square $[-1,0] \times [-0.5, 0.5]$ placed in a rectangular pipe $[-6.5, 14.5] \times [-6, 6]$, an schematic in Figure 4.10, is simulated. Due to alternating vortex shedding in the wake, the attached elastic plate oscillates with a shedding frequency of Kármán vortex street.

By setting the computational settings as thos in the original study [68], material properties are listed in Table 4.3, and the governing equations are incompressible Navier–Stokes equation for fluid and STVK hyperelastic model for solid. Besides the constant inflow $U_{in}$, Neumen type boundary condition $\frac{\partial u}{\partial x} = \frac{\partial v}{\partial x} = 0$ is prescribed at outlet, and the applied lateral

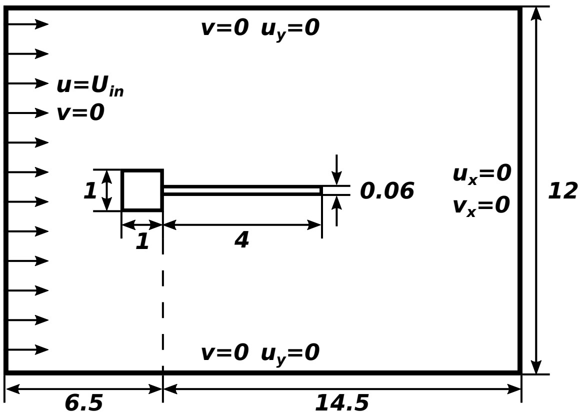

Figure 4.10: Schematic of problem

boundary conditions $\frac{\partial u}{\partial y} = 0,\ v = 0$ assure that flow can not cross lateral border. Simulation results were carried out with $\delta t = 0.0025$ and the minimum size of elements as $h_{min} = 0.02$ around the elastic plate. There are roughly 10000 elements, for which they are refined at the surface of the plate during computation. Simulation were carried out with two different solid models, MR and STVK model.

Table 4.3: Material parameters

| $\rho_f\ [g\ cm^{-3}]$ | $\nu_f\ [g\ cm^{-1} s^{-1}]$ | $\rho_s\ [g\ cm^{-3}]$ | $E\ [g\ cm^{-1} s^{-2}]$ | $\nu_s$ | $U_{in}\ [cm\ s^{-1}]$ |
|---|---|---|---|---|---|
| $1.18 \times 10^{-3}$ | $1.82 \times 10^{-4}$ | 2 | $2 \times 10^{6}$ | 0.35 | 31.5 |

Alternating vortex shedding and oscillation of the elastic plate are observed in Figure 4.11 with velocity contours at time $t = 12.5$ and 13.0. The simulation results compared with Hubner [68] in Table 4.4 show good agreement in the magnitude of oscillation, with the difference less than 6% for both models Both models exhibit the same mode of oscillations with quite a close magnitude under different frequency.

Table 4.4: Comparison of simulation results

| | present, STVK | present, MR | Hubner [68] |
|---|---|---|---|
| Magnitude | 2.05 | 1.94 | 2.0 |
| Frequency | 1.02 | 1.2 | 0.8 |

### 4.3.2 A thin elastic plate clamped to a rigid cylinder immersed in a flowing fluid

In the study [151], a thin elastic plate with the thickness of $h = 0.02$ and the length of $l = 0.6$ is clamped to a fixed cylinder with diameter 0.1, and it is immersed in a rectangular

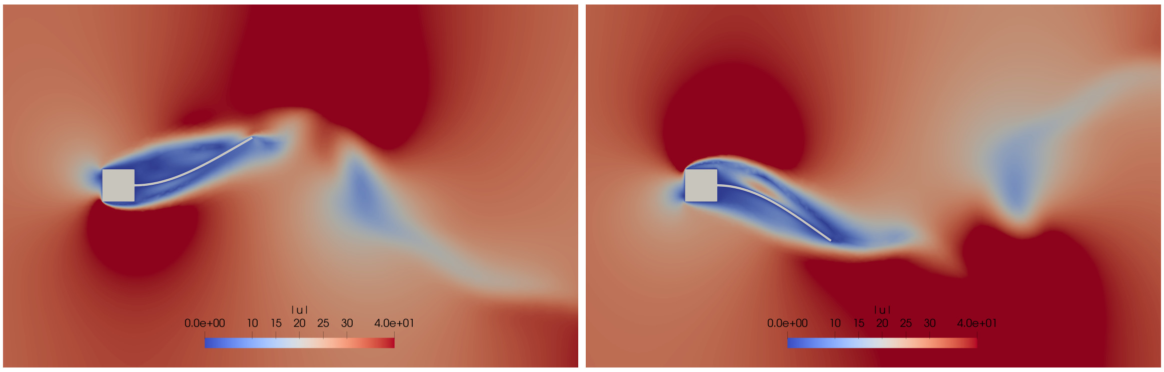

(a)

(b)

Figure 4.11: Contours of velocity magnitude at (a) $t = 12.5$ and (b) $t = 13.0$.

pipe $[-0.2, 2.3] \times [-0.205, 0.205]$ filled with fluid, as the schematic shown in Figure 4.12. Two different types of problems are studied, which are computational structural mechanics, CSM2 and CSM4, and fluid–structure interaction problems, FSI2 and FSI3.

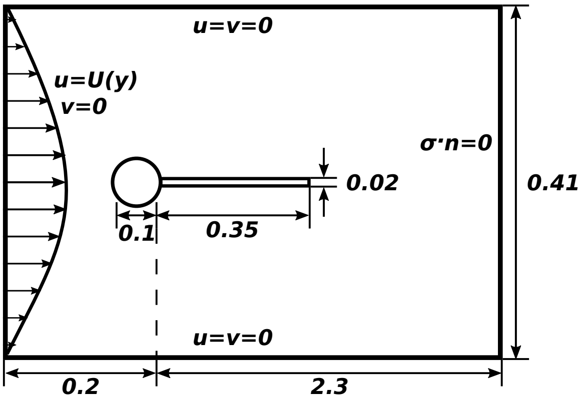

Figure 4.12: Schematic of bechmark problems proposed by Turek [151]

The properties of fluid and solid material for each problem are listed in table 4.5, and the Poisson ratio of solid is $\nu_s = 0.4$. In referenced paper [151], fluid is considered as viscous incompressible Newtonian fluid, and the plate is modelled by $S^t$–Venant–Kirchhoff model. For comparison, the simulations with Mooney–Rivlin model are also carried out. Apart from the inlet boundary condition, Neumann boundary condition is prescribed at outlet to achieve stress–free at outlet, and no–slip boundary conditions $u = v = 0$ are prescribed on lateral boundaries. The computational domain is decomposed into 10000 elements with $h_{min}\,(= 0.008)$ being refined at the surface of the elastic plate. Additionally, the measure point $A$ is placed at the center of the plate's end to track motion.

Table 4.5: Material parameters used in Turek's benchmark problems

| | $\rho_f\left[kg\,m^{-3}\right]$ | $\nu_f\left[m^2s^{-1}\right]$ | $\rho_s\left[kg\,m^{-3}\right]$ | $\mu_s\left[kg\,m^{-1}s^{-2}\right]$ | $g_s\left[ms^{-2}\right]$ | $U_{in}\left[ms^{-1}\right]$ |
|---|---|---|---|---|---|---|
| CSM2 | 1000 | 0.001 | 1000 | $5\times10^5$ | 2 | 0 |
| CSM4 | | | 1000 | $5\times10^5$ | 4 | 0 |
| FSI2 | | | 10000 | $5\times10^5$ | 0 | 1 |
| FSI3 | | | 1000 | $2\times10^6$ | 0 | 2 |

### Computational structure mechanics problem

In the two steady problems, CSM2 and CSM4, the elastic plate bends under a vertical gravitational force $g_s$ applied the solid part. The comparison of the $x$ and $y$ displacements at point $A$ between the present results and referenced results [54, 113, 151, 152] is shown in table 4.6. Good agreement is observed in coarse meshes. The $x-$ and $y-$ displacements at point $A$ are plotted with respect to time in Figure 4.13(a), and the centerline positions of plate under different values of $g_s$ were plotted in Figure 4.13(b). Besides STVK model in the original study,comparison between the simulation results with MR model can infer that an overestimation on coefficient of $c_1$, selected as $\frac{\mu_s}{2}$, makes that elastic plate to react harder than our expectation.

Table 4.6: Comparison of the numerical results for $g = 2$ and $g = 4$

| | $g_s$=2 | | $g_s$=4 | |
|---|---|---|---|---|
| | $d_x$ | $d_y$ | $d_x$ | $d_y$ |
| Present, MR model | 3.845 | 48.23 | 17.31 | 101.86 |
| Present, STVK model | 6.827 | 64.41 | 21.62 | 113.76 |
| Dunne [113] | 7.187 | 66.10 | - | - |
| Hron and Turek [151] | 7.187 | 66.10 | - | - |
| Richter [152] | 7.149 | 66.07 | 25.10 | 122.16 |
| Wick [154] | 7.150 | 64.90 | 25.33 | 122.30 |

### Fluid–structure interaction problem

FSI2 and FSI3 study self-excited oscillation of the attached pate under different magnitudes $U_{in}$ of Poiseuille inflow $U\left(y\right)$ prescribed at inlet $\Gamma_{in}$.

$$U\left(y\right) = 1.5U_{in}\frac{y\left(H-y\right)}{\left(0.5H\right)^2}$$

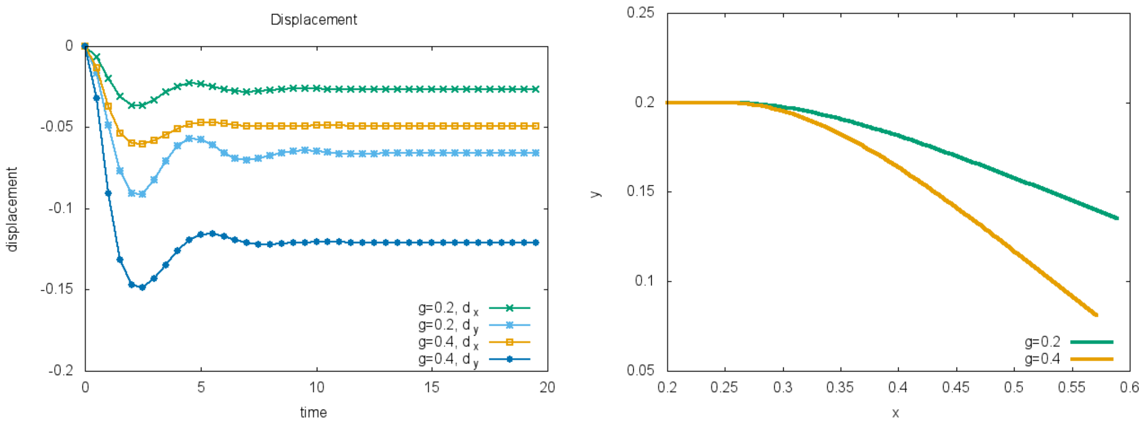

(a) (b)

Figure 4.13: Computational structure mechanics results: (a) displacements at point $A$ on $x$ and $y$ with respect to time; (b) centerline positions with $g = 0.2$ and $g = 0.4$.

The attached elastic plate oscillates at a certain frequency due to alternating vortex shedding in the wake. Velocity contours of the simulation results at different time steps are shown in Figure 4.14 and Figure 4.15 for the case of FSI2 and FSI3, respectively It is clear to observe oscillating pattern for the elastic plate in Figure 4.14 in one periodic cycle.

After the development of alternating vortex, the elastic plate reached to periodic oscillation. Periodic trajectory at measure point $A$ is recorded in Figure 4.16 to trace the motion of the elastic plate. The amplitude and frequency of periodic oscillation are compared with those in [54, 113, 151] , as shown in table 4.7. For both test cases, the present results are in good agreement with others.

Table 4.7: Comparison of numerical results for FSI2 and FSI3

| | FSI2 | | FSI3 | |
|---|---|---|---|---|
| | amplitude | frequency | amplitude | frequency |
| Present, MR model | $7.54 \times 10^{-2}$ | $2.02\ s^{-1}$ | $3.17 \times 10^{-2}$ | $5.32\ s^{-1}$ |
| Present, STVK model | $8.05 \times 10^{-2}$ | $1.92\ s^{-1}$ | $3.27 \times 10^{-2}$ | $5.21\ s^{-1}$ |
| Turek [151] | $8.06 \times 10^{-2}$ | - | $3.44 \times 10^{-2}$ | - |
| Dune [113] | $8.00 \times 10^{-2}$ | $1.953\ s^{-1}$ | $3.00 \times 10^{-2}$ | $5.04\ s^{-1}$ |
| Thomas [154] | $8.06 \times 10^{-2}$ | $1.93\ s^{-1}$ | - | - |

As mentioned in previous section, overestimation of coefficients $c_1$ makes elastic plate to react harder than what under expectation. This error has a tiny inflection in these two FSI problems, because the deformation of plate is comparatively small. The predicted stress tensors of the hyperelastic models are practically equal.

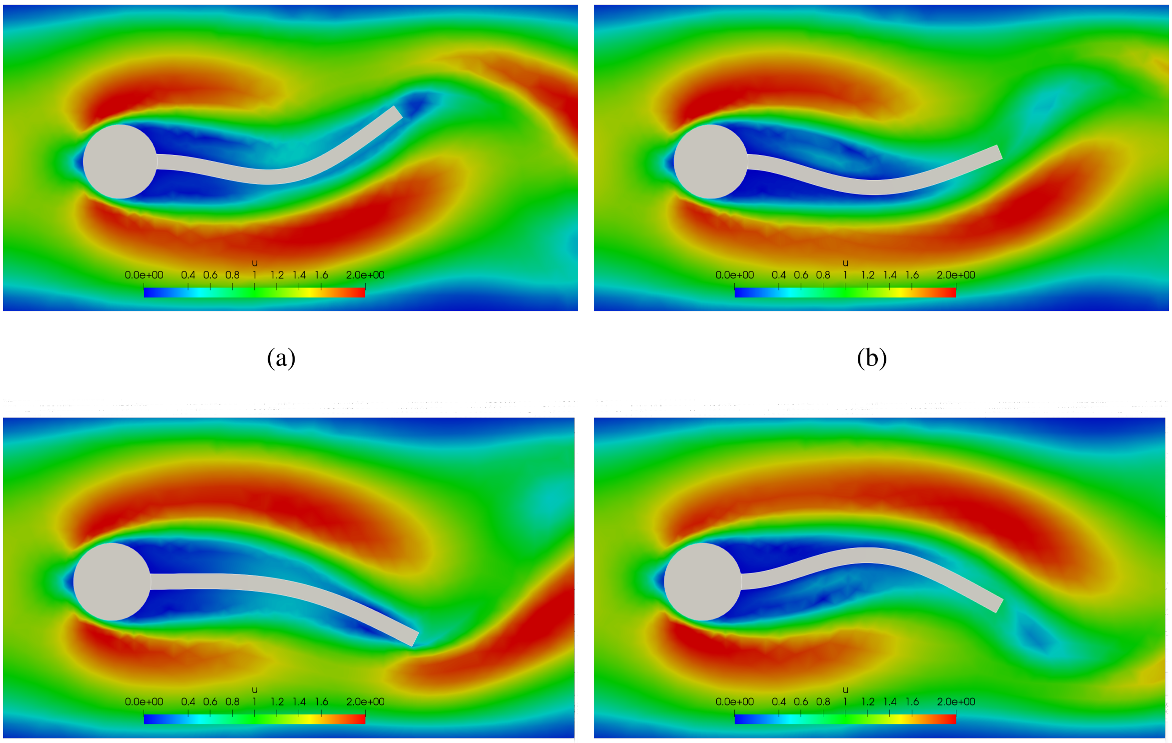

(a) (b)

(c) (d)

Figure 4.14: Velocity contours of FSI2 at (a) $t = 12.00$; (b) $t = 12.08$; (c) $t = 12.20$; (d) $t = 12.32$.

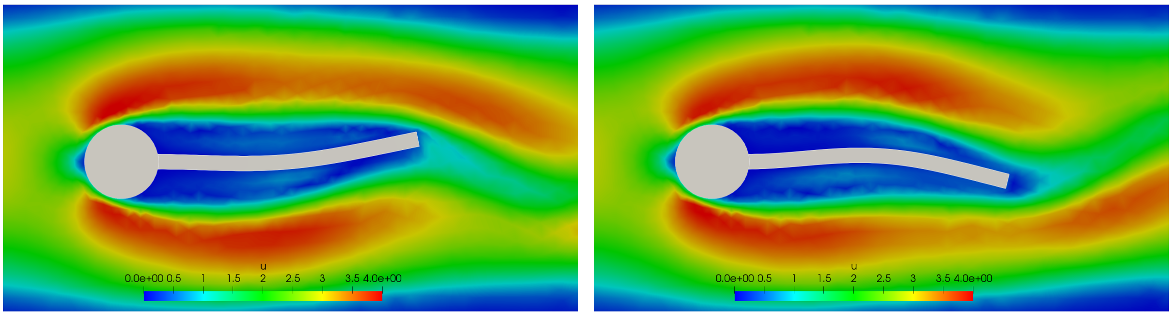

(a) (b)

Figure 4.15: Velocity contours of FSI3 at (a) $t = 15.12$ and (b) $t = 15.4$.

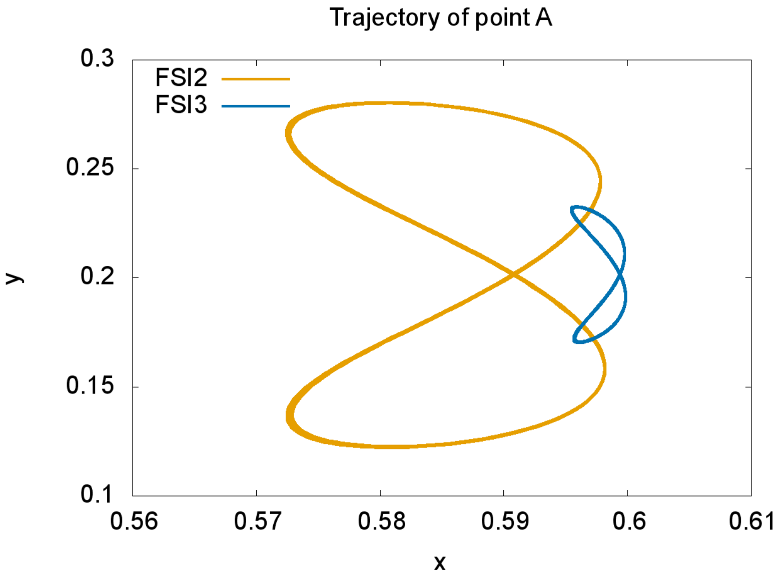

Figure 4.16: Trajectory at the monitor point $A$.

### 4.3.3 Flow past a flexible sheet with a rear mass attached to a rotatable cylinder

An experiment designed by Gome and Lienhart [155, 159, 172] for studying fluid–structure interaction deals with the self-excited swinging motion of a flexible structure immersed in a laminar flow $Re \approx 140$. The structure is composed of three connected objects: a rotatable cylinder, a flexible sheet, and a rectangular rear mass. The center of the rotatable cylinder with the diameter of 0.022 is located at $(0,0)$. The flexible sheet has a length of 0.05 and a width of 0.00004 The rear mass has a length of 0.01 and a width of 0.004. The structure is immersed in a rectangular pipe $[-0.155, 0.593] \times [-0.12, 0.12]$. The simulation setup is schematic in Figure 4.17. Velocity measurement of the fluid surrounding the flexible structure is executed by a two dimensional particle image velocimetry (PIV) system with a measurement uncertainty less than 1.5% of the undisturbed flow. The swivelling frequency experimentally determined is 6.38 Hz.

Following the experimental setup [155], the density of structural objects are taken to be $\rho_{\text{cylinder}} = 2828\, kg\, m^{-3}$, $\rho_{\text{flexible sheet}} = 7855\, kg\, m^{-3}$, and $\rho_{\text{rear mass}} = 7800\, kg\, m^{-3}$. The Young's module of the flexible sheet under investigation is $E_{\text{flexible sheet}} = 2 \times 10^{11}\, N\, m^{-2}$, and the Poisson ratio is $\nu_s = 0.305$.

For fluid, the density is $\rho_f = 1050\, kg\, m^{-3}$, and kinematic viscosity is $\nu_f = 1.64 \times 10^{-4}\, m^2\, s^{-1}$. In this study, gravity is considered as $g = 9.81\, m\, s^{-2}$ along $x$ direction, and the inflow velocity is $U_{\text{in}} = 1.07\, m\, s^{-1}$ and $v = 0$. The stress–free boundary condition $\frac{\partial u}{\partial x} = \frac{\partial v}{\partial x} = 0$ is prescribed at outlet, and no–slip boundary condition $u = v = 0$ is prescribed at the lateral boundary.

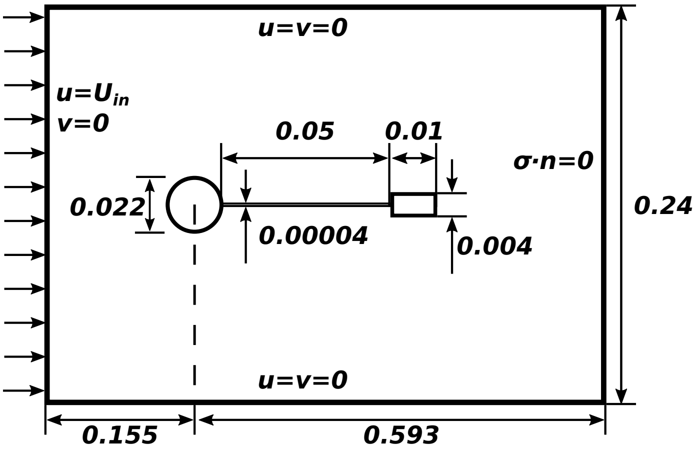

Figure 4.17: Schematic of problem (out-of-proportion)

The measurement of time phase angle $\mathrm{tpa}_j$ is defined as

$$\mathrm{tpa}_j = \frac{t_{ij} - t_i'}{T_i} \times 360$$

where $T_i = t_{i+1}' - t_i'$ is the period of the swinging cycle in which the measurement $t_{ij}$ takes place. To measure flow field, the monitor point $A$ is placed right behind the flexible structure, $(0.082, 0.0)$, and the monitor point $B$ is placed above point $A$ at $(0.082, 0.04)$. The simulation is carried out with 30000 ($\mathbb{P}1b$,$\mathbb{P}1$) elements with mesh being refined at the surface of the flexible string. Time increment is chosen as $\delta t = 0.001$.

The comparison between numerical results and expermental data [155, 159] plotted in Figures 4.18 shows a relatively good agreement. At each periodic cycle, the centerline of the elastic string swings at a bounded region between the purple symbols in Figure 4.18(a). The present numerical scheme yields a good agreement with experimental data [155] in comparatively coarse mesh. Additionally, rotating angle of the front body, the rotatable cylinder, is compared within one cycle and shown in Figure 4.18(b). To compare the flow field at the downstream of the swinging structure, flow velocity at two monitor points $A$ and $B$ are plotted with respect to the time-phase angle in Figure 4.18(c) and 4.18(d), respectively. There are two inferences to be drawn from the comparison of results. First, due to the different deforming configuration in Figure 4.18(a) at each periodic cycle, it is expected to see the difference of velocity profiles at point $A$ between numerical results and experimental data in Figure 4.18(c). Second, the disturbance on velocity of the swinging structure becomes less from point $A$ to $B$, which is related to the distance from downstream region. A better agreement of results on velocity profiles can be observed in Figure 4.18(d).

Figure 4.19 shows the trajectories of trailing edge in $x$-$y$ with experimental and numerical results, and the present numerical scheme yields a good agreement with experimental data [155] in comparatively coarse mesh.

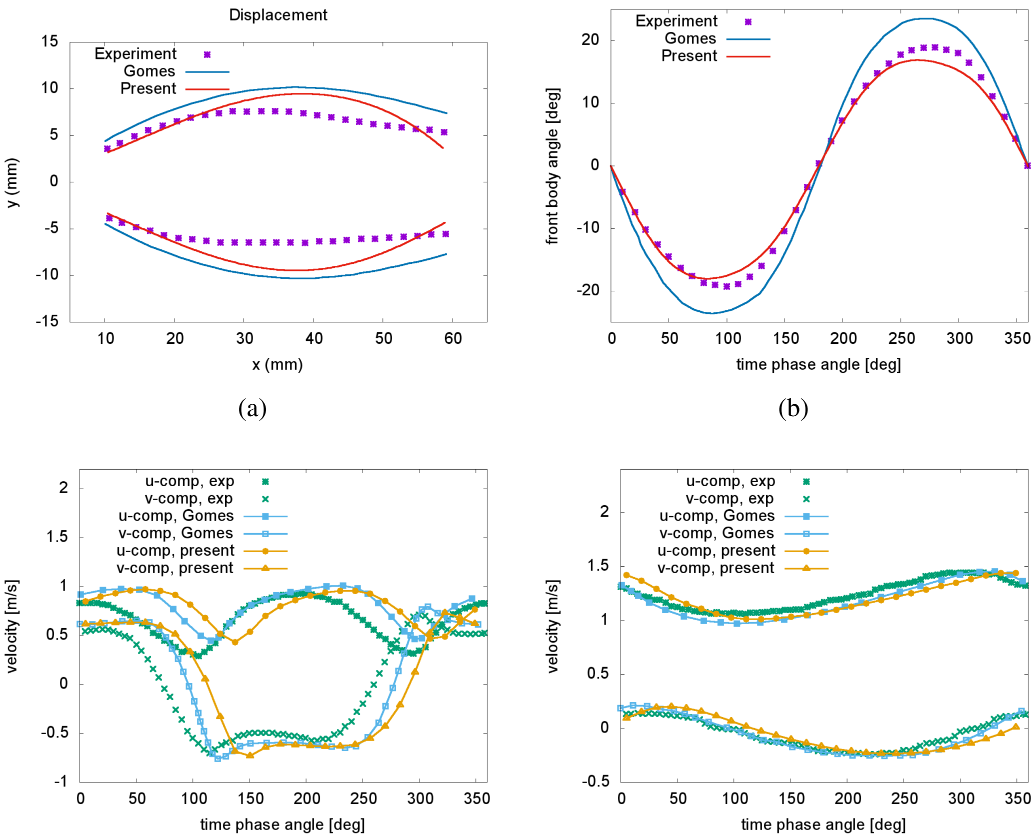

(a) (b)

(c) (d)

Figure 4.18: Comparison of (a) the structure deformations for time - phase angles of 90 and 270; (b) front body angle for one period; (c) flow velocity at the monitor point $A$ for one period; (d) flow velocity at the monitor point $B$ for one period.

## 4.4 Validation of 3D monolithic formulation

### 4.4.1 Bending of a flexible plate in cross flow

A uniform flow of velocity $U_0$ along the positive $x$ direction is prescribed on $\Gamma_{in}$, as shown in Figure 4.20(a). An elastic plate is defined in $\frac{-h}{2} \leq x \leq \frac{h}{2}$, $\frac{-b}{2} \leq y \leq \frac{b}{2}$, and $0 \leq z \leq L$. By choosing $b$ as the characteristic length, we have $h = 0.2b$ and $L = 5b$. The plate is clamped at the bottom $z = 0$ of the rectangular tube ($-5b \leq x \leq 16b$, $-8b \leq y \leq 8b$, and $0 \leq z \leq 17b$), as shown in Figure 4.20.

Dimensionless properties follow the experimental setup given in Luhar [160]: $Re = U_0 b/\nu = 1600$, $\rho_f^* = \rho_f/\rho_f = 1$, $\rho_s^* = \rho_s/\rho_f = 0.678$, $E^* = E/\rho_f U_0^2 = 19054.9$, and $\nu_s = 0.4$. The buoyancy force, $f_b^* = \left(\rho_f - \rho_s\right) gh/\left(\rho_f U_0^2\right) = 0.2465$, is applied only on the solid part. The flexible plate bends due to the drag force and the pressure difference induced by uniform inflow The deformation, as a result, follows inflow direction

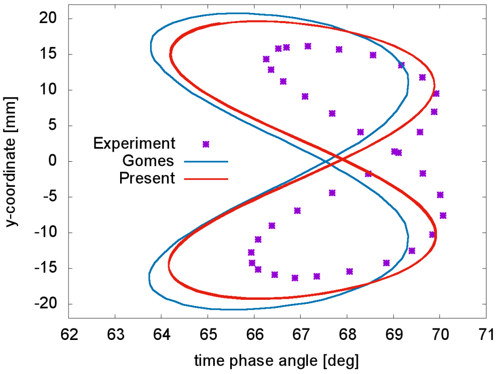

Figure 4.19: Comparison of $x$-$y$ position at monitor point at the end of the solid throughout one period.

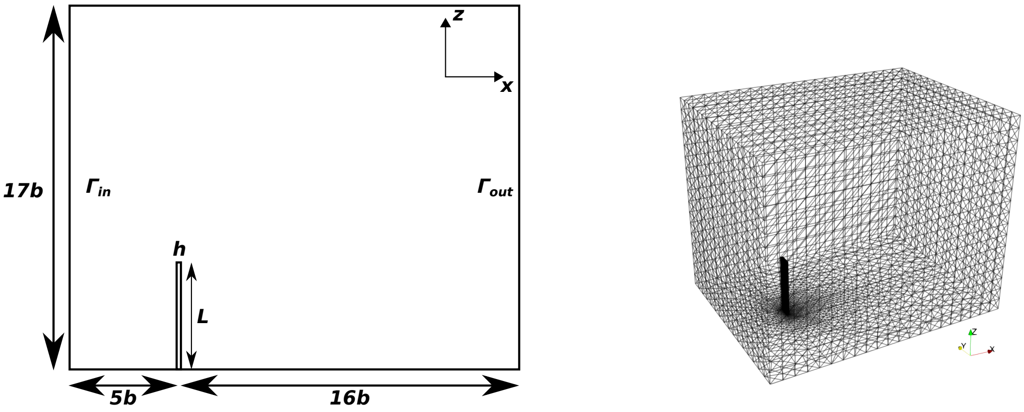

(a) (b)

Figure 4.20: Schematic of computational domain $[-5b,16b] \times [-8b,8b] \times [0,17b]$ with $h/b = 0.2$ and $L/b = 5$. (a) Cross section along $y = 0$; (b) top view of domain and surface mesh.

with one clamp–mounted end of the plate. By following the experimental setup given in Luhar [160], bending of the flexible plate would achieve a steady pattern. The snapshot of the experimental results are shown in Figure 4.21(a) and the present simulation results are displayed Figure 4.21(b).

The quantitative comparison between the experimental and simulation results is summarized in Table 4.8: drag coefficient $C_D$, and deflection in $x-$ and $z-$ direction of the center of free end, $\mathbf{D}_x$ and $\mathbf{D}_z$. The drag coefficients, $C_D$, of the flexible plate is defined as $C_D = F_x/\left(\frac{1}{2}\rho_f U_0^2 bL\right)$, where $F_x$ is the total hydrodynamic force $\mathbf{F} = (F_x, F_y, F_z) = \int_{\partial\Omega_s}\left(-p\mathbf{I} + \mu_f \mathbf{D}\mathbf{v}\right) \cdot \mathbf{n} d\Gamma$ in the $x$-direction. Considering 10% error of the drag coefficient in experimental observation [160], these three measures from the present simulation are in good agreement with the experimental data.

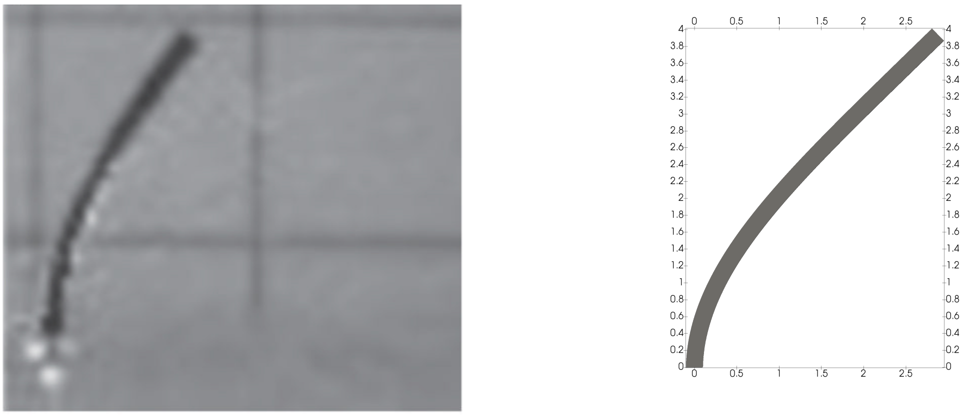

(a) (b)

Figure 4.21: Bending of a flexible plate in cross flow. (a) Experimental results [160], and (b) computational results.

| | $C_D$ | $\mathbf{D}_x/b$ | $\mathbf{D}_z/b$ |
|---|---|---|---|
| Present | 1.03 | 2.13 | 0.54 |
| Luhar and Nepf [160] | 1.15 (with 10% error) | 2.14 | 0.59 |
| Tian and Dai etc [161] | 1.03 | 2.12 | 0.54 |

Table 4.8: Comparison of the drag coefficients $C_D$ and the deflections in $x-$ and $z-$ directions among the referenced data.

### 4.4.2 Elastic structure in merging flow from two inlets

A silicon filament is clamped on the junction center between two inlet and one outlet pipes. A variant of inlet conditions establish different patterns of flow field and deformed silicon filament, stable and constant inflow at phase I and the transient peak velocity of Poiseuille profile flow at phase II. This experiment designed by Hessenthaler et al. [162] is chosen to validate transient FSI algorithms, as the work done in Larma [173].

Due to the implicit description of geometrical setting in experiments [162], we consider a similar problem with a simpler connection between inlet and outlet pipes. Although it is expected to have influence on flow field and shape of silicone filament because of the presence of different junctions, computational results still can demonstrate some key dynamics observed in original experiments, especially at the upstream of merging flow where the silicone filament is located.

The geometry is a cylindrical chamber with the length of 200 *mm*, diameter 76.2 *mm*, and the axis parallel to $x = y = 0$. Two inlet circular wholes are on the left $z = 0$ wall, one with the center at $(0, -27.15, 0)$, the other at $(0, 27.15, 0)$. The diameter of both chambers is 21.9 *mm* and the inlet pipes are 20 *mm* long. A silicon filament clamped on the $z = 0$ plane is 2 *mm* thick, 11 *mm* wide, and 65 *mm* long, and the center of the connected surface is located at $(0,0,0)$. Geometric schematic is shown in Figure 4.22. The computational domain is discretized into $10^4$ vertices and refined at the surface of the silicone filament to decrease error during its motion.

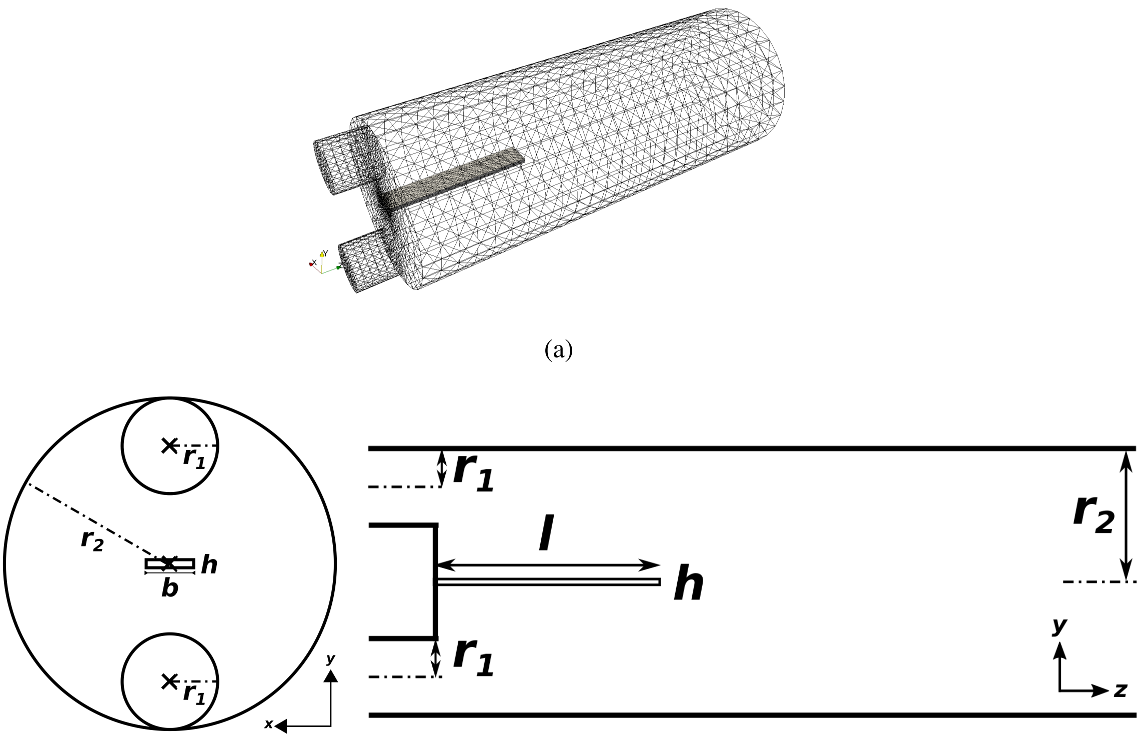

(a)

(b) (c)

Figure 4.22: Schematic of the computational domain with $r_1 = 10.95\ mm$, $r_2 = 38.1\ mm$, $h = 2\ mm$, $b = 11\ mm$, and $l = 65\ mm$. (a) top view; (b) viewed from the negative $z$ direction; (c) viewed from the symmetric plane along $x = 0$.

As experimental setup [162], the density of the silicone filament is $\rho_s = 1.0583 \times 10^{-3}\ g/mm^3$. Coefficients of solid are determined by curve–fitting to uni–axial tensile–load displacement test data. In [173], solid material properties are chosen as Young's modulus $E_s = 216260\ Pa$, Poisson ratio $\nu_s = 0.315$, Lamé parameters $\mu_s = \frac{\nu_s E_s}{(1+\nu_s)(1-2\nu_s)}$ and $\lambda_s = \frac{E_s}{2(1+\nu_s)}$. Gravity $g$ is $-9810\ mm/s^2$ along the $y$–direction. Two numerical tests are performed, which involve a steady phase I, and transient phase II. Table 4.9 tabulates the fluid physical parameters $\rho_f$ and $\mu_f$ for two different phases.

### Initial configuration

Under the experimental setup in [162], the silicone filament will be finally settled down to a steady configuration due to the buoyancy force in the rested fluid. The experimental and

| | $\rho_f$ | $\mu_f$ |
|---|---|---|
| Phase I | $1.1633 \times 10^{-3}\ g\ mm^{-3}$ | $12.5 \times 10^{-3}\ g\ mm^{-1}\ s^{-1}$ |
| Phase II | $1.164 \times 10^{-3}\ g\ mm^{-3}$ | $13.37 \times 10^{-3}\ g\ mm^{-1}\ s^{-1}$ |

Table 4.9: Fluid physical parameters under consideration [162].

simulated configurations of the silicone filament along the centerline are plotted in Figure 4.23.

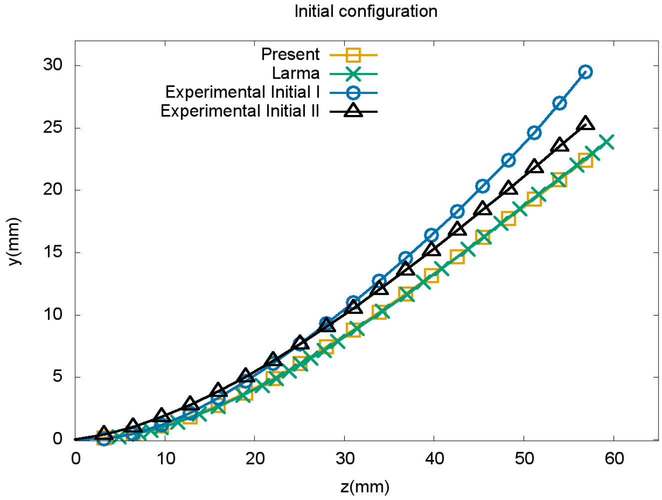

Figure 4.23: Initial configuration of the silicone filament.

The figure shows that the current result is in a very good agreement with the numerical result done by Larma [173], but the obvious difference is observed between the experimental data [162] and simulated results. A less deflected silicone filament than the experimental data is observed. Accordingly, we can only infer that the overestimation of Young's modulus results from by the uniaxial tensile–load displacement test in [162] so that the modelled material is stiffer than expected.

Additionally, there is one suspicious point in experimental data. According to the experimental data in Table 4.9, the fluid density $\rho_f$ changes with an amount less than 1% from $1.1633 \times 10^{-3}\ g\ mm^{-3}$ in phase I to $1.164 \times 10^{-3}\ g\ mm^{-3}$ in phase II. However, the 1% change of the fluid density causes the steady deflection of the silicone filament to have a roughly 13% variance, which is physically unusual.

### Phase I

A stable constant inflow is prescribed on two inlet pipes in phase I. The $z$-component of the inlet velocity can be described by Poiseuille profile with its peak velocity of 630 $mm\ s^{-1}$ and 615 $mm\ s^{-1}$ for upper and lower inlets, respectively. The other components are set to zero.

By following the experimental setup, the silicone filament will be finally settled down to a steady configuration (Figure 4.24) from the initial configuration (Figure 4.23). The experimental and simulated configurations of the silicone filament along the centerline are plotted in Figure 4.24(a), and the contours of velocity magnitude are displayed at the symmetric plane $x = 0$ in Figure 4.24(b). In spite of the difference between initial and predicted configurations observed in Figure 4.23, Figure 4.24(a) shows the comparison, which demonstrates that very good agreement has been achieved among the current result, the numerical result of Larma [173], and the experimental data [162].

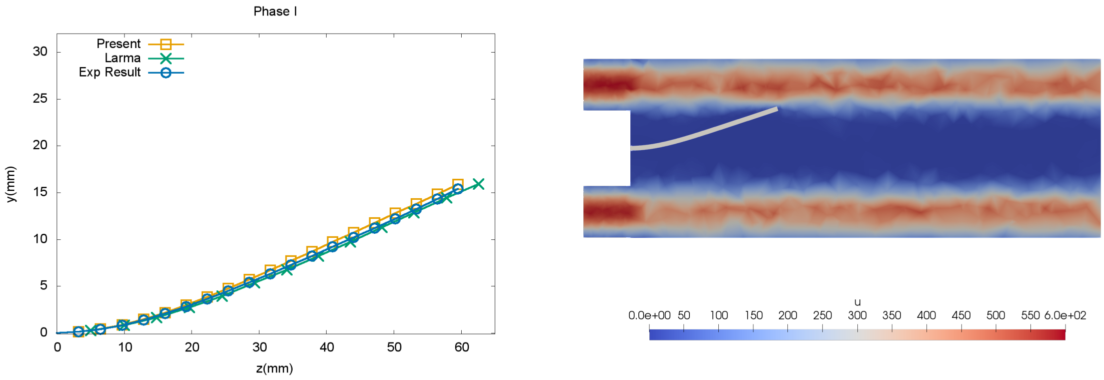

(a) (b)

Figure 4.24: Computational results in phase I. (a) Position of the center line of the plate along $z$ direction; (b) velocity contours at the symmetric plane $x = 0$.

### Phase II

On the upper inlet, the Poiseuille flow has a transient maximum velocity $\hat{v}_k(t)$, $k \in [x,y,z]$, as shown in Figure 4.25. The maximum velocity $\hat{v}_k(t)$ can be approximated as $\hat{v}_k(t) \approx \Sigma_{i=1}^{3} n_i t^i / \Sigma_{j=0}^{4} b_j t^j$ with the coefficients in Table 4.10. On the lower inlet, the same velocity profile is prescribed except $y$–component which is set to zero.

The fluid and solid parts are rested at $t = 0$. The simulation stops at $t = 5$ after 1600 time steps with $\delta t = 0.003125$. By following the experimental setup, the silicone filament is deformed with respect to time.

Figure 4.26(a) to 4.26(f) show the comparison among the current results, the experimental data [162], and the simulated configurations by Larma [173] of the silicone filament

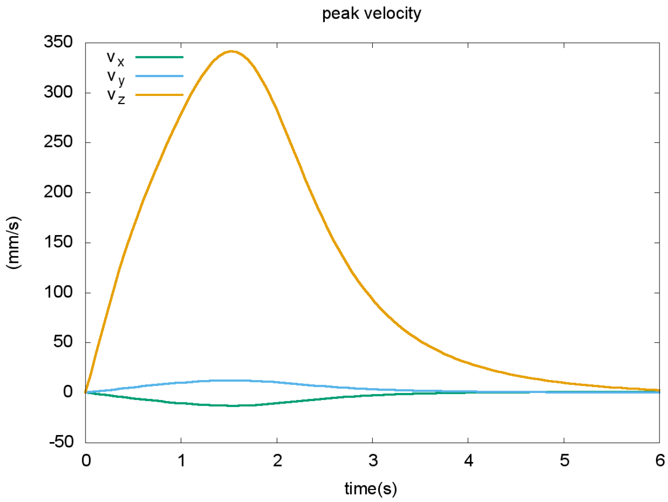

Figure 4.25: The peak inflow experimental velocities [162].

| | $n_1$ | $n_2$ | $n_3$ | $b_0$ | $b_1$ | $b_2$ | $b_3$ | $b_4$ | $\hat{\mathrm{I}}_k$ |
|---|---|---|---|---|---|---|---|---|---|
| $\hat{v}_x$ | -11.37 | -28.99 | 7.73 | 1.38 | 0.24 | 3.59 | -3.14 | 1 | $[0,4.07]$ |
| $\hat{v}_y$ | 14.95 | 11.88 | -2.17 | 2.06 | -2.0 | 4.95 | -3.50 | 1 | $[0,5.51]$ |
| $\hat{v}_z$ | 367.10 | 363.40 | -62.24 | 1.21 | -0.38 | 3.76 | -3.19 | 1 | $[0,5.27]$ |

Table 4.10: In phase II, curve–fitting coefficients in the inlet peak velocity $\hat{v}_k(t) \approx \Sigma_{i=1}^{3} n_i t^i / \Sigma_{j=0}^{4} b_j t^j$ with $\hat{v}_k = 0$ for $t \in \mathrm{I}\backslash\mathrm{I}_k$. Note that flow in $y$-direction is applied only at the upper inlet.

along the centerline at $t = 0.073$, 0.721, 1.153, 1.585, 2.017, and 4.781. The comparison in Figure 4.26 shows that the current results obtained in coarse mesh have comparatively good agreement with experimental data [162] and the simulation results [173]. In addition to the error mentioned in section 4.4.2, the difference is possible due to an improper determination of the material model coefficients.

Figure 4.27 shows the comparison of velocity profiles $u_z$ at $x = 0\ mm$ midplane for four different $z$ cross section $z \approx 0.20l$, $0.51l$, $0.82l$, $1.21l$ and at $t = 0.073$, 0.721, 1.153, 1.585 $s$. A referenced length scale $l$ is selected as the length $l = 65\ mm$ of the silicon filament. In Figure 4.27(a), an excellent agreement has been achieved in the comparison between the current results and the experimental data [162]. However, the comparison in Figure 4.27(b) and 4.27(c) demonstrates that the current results still can capture the trends of the experimental velocity profiles [162] with roughly16% and 25% difference, respectively. Furthermore, the velocity profiles $u_z$ of the current results and the experimental data [162] become totally different.

The reason of why the difference gradually increases from $z \approx 0.20l$ to $z \approx 1.21l$ is discussed in the following paragraph. In this numerical calculation, we consider a similar

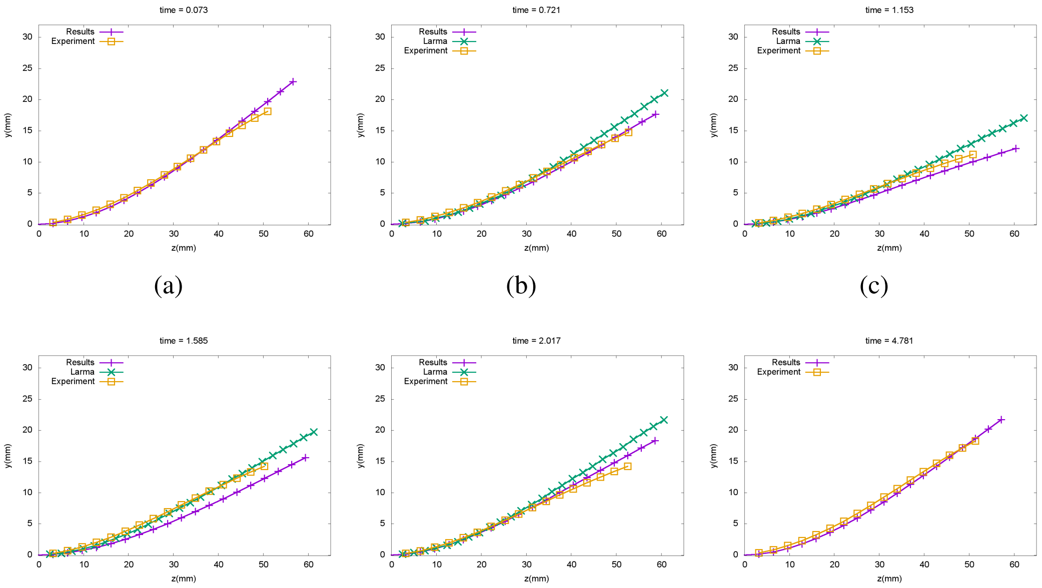

(a) (b) (c)

(d) (e) (f)

Figure 4.26: Deflection of the silicone filament in phase II. (a) $t = 0.073$; (b) $t = 0.721$; (c) $t = 1.153$; (d) $t = 1.585$; (e) $t = 2.017$; (f) $t = 4.781$.

problem with a simpler junction as mentioned in the previous section. The predictable influence of junction increases from the upstream to the downstream of the merging inlet flow. Also, we can observe the same effect from the comparison in Figures 4.27. Additionally, sparse and scattered elements are applied to discretize the fluid domain.

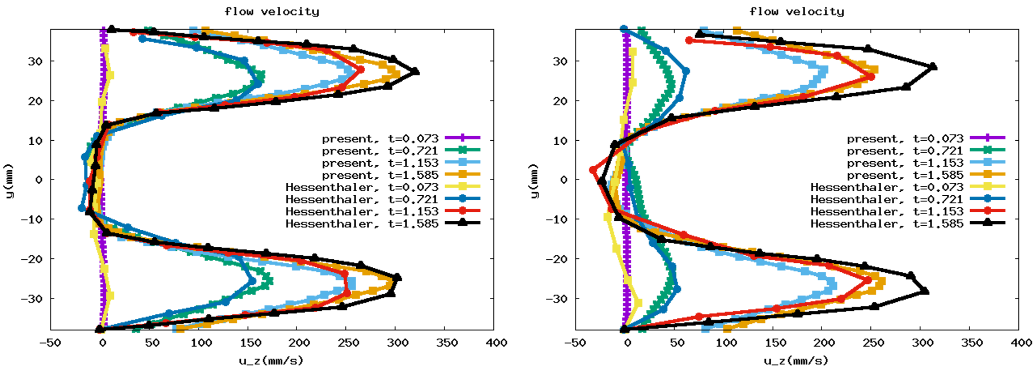

(a) $z \approx 0.20l$; (b) $z \approx 0.51l$;

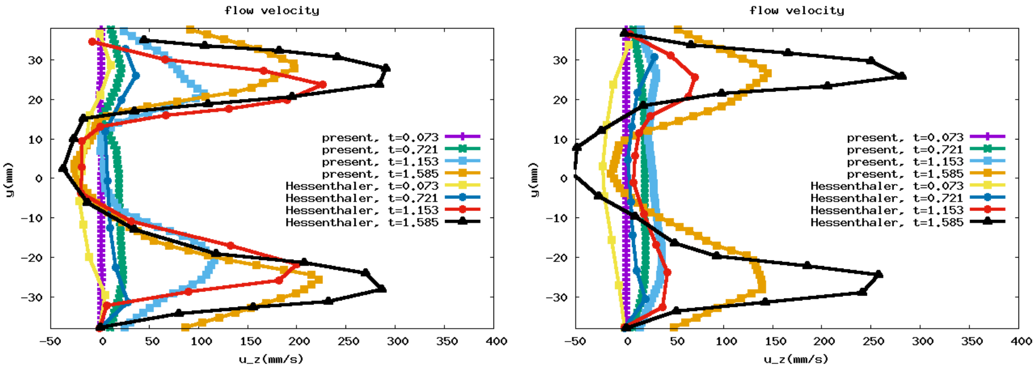

(c) $z \approx 0.82l$; (d) $z \approx 1.21l$;

Figure 4.27: Velocity profiles of $u_z$ component at the midplane $x = 0\,mm$ ($l = 65\,mm$ is the length of the silicon filament).

# Chapter 5

# Computational contact mechanism

## Contents

Many problems in mechanics and engineering involve contact. Furthermore, these problems can be coupled with heat transfer due to temperature difference at contact points [174]. Mathematically, boundary conditions or constraints for contact are naturally nonlinear. Various studies investigated the accuracy, efficiency, and robustness of numerical contact algorithms.

A huge number of articles are related to computational contact algorithms. Most algorithms can be implemented with the Lagrange multiplier or penalty method. Contact algorithms can be categorized into three groups. First, the rigid approach is based on geometrical constraints [174] without deformation [175]. Second, the regularized approach, the so-called penalty or force-based formulation, is based on the evaluation of contact forces. Third, the linear complementarity problem (LCP), one of the most popular techniques, assumes rigid colliding bodies and contact using a nonsmooth dynamics formulation [176].

The proposed contact scheme considers geometrical constraints of colliding bodies Rather than displacements, velocities are considered as variables to conform Eulerian monolithic formulation. Similar treatments of contact can be also found in [152] and [177]. An Eulerian finite element method was used in these studies. Utilizing the characteristic

Galerkin method to discretize total derivatives [115], the stability analysis was previously demonstrated [116–118]. A contact constraint is to be implemented with Eulerian formulations. Main features of contact treatment with Eulerian formulation comprise the absence of (1) added variables during contact and (2) dependency of results on some selected numerical coefficients.

Table 5.1: Comparison of three different computational contact schemes.

| | **Rigid body formulation** | **Forced-based formulation** | **LCP** |
|---|---|---|---|
| **Based on** | Geometrical constrain | Resolution of contacted force | Modelling of contact with nonlinear dynamics equation |
| **Advantage** | Same primitive variables<br>Stable and consistent | Easy to implement | Realistic consideration of contact mechanism |
| **Drawback** | Rigid contacted objects | Variant numerical results with user defined parameters | Additional governing equations and variables |

Two computational contact schemes are addressed at section 5.1, penalty method and Lagrange multiplier, respectively. For the sake of stability, contact scheme with Lagrange multiplier is implemented in the following simulation. In section 5.2, numerical verification and validation are carried out for the 2D problems available in the literature.

## 5.1 Numerical schemes

This section introduces two schemes for contact problems based on a penalty method and a Lagrange multiplier method. The corresponding computation results are shown at the end of this section. For a further and detailed study of computational contact, [174] introduces computational contact problem and the corresponding constitutive equations for solid. It collects various computational schemes to prescribe contact between two physical bodies and summarize them into a general algorithm for three–dimensional contact problem which contains searching, penalty method and construct of local Mortar elements.

### 5.1.1 Penalty method: non–penetration method

The penalty method has been widely applied to simulate contact problems [174, 177–183] because of its conceptual simplicity and straightforward implementation.

Additional enforcement of structural non–penetration is considered to model contact between surfaces with penalty method. The following contact scheme is based on [179] with some correction.

Consider two surfaces $S_1$ and $S_2$ to be smooth parametric surfaces in $\Re^3$. For $\mathbf{x}_1 \in S_1$, with surface outward normal $\mathbf{n}_1$, we could find a possible contact point (closest point) $\mathbf{x}_2 \in S_2$. Distance between two points can defined as $d = h - |\mathbf{d}| = h - |\mathbf{x}_1 - \mathbf{x}_2|$, where $h$ is the gap to commence contact force. The reaction force on $\mathbf{x}_1$ is $\mathbf{f}_1 = -wP_k(d)\frac{\mathbf{d}}{|\mathbf{d}|}$ and the force on $\mathbf{x}_2$ is $\mathbf{f}_2 = -\mathbf{f}_1$, where $w$ is a weighting coefficients associated with $\mathbf{x}_1$ and $P_k(d)$ penalizes non-penetration. For non-penetration method, penalty function $P_k(d)$ is defined as below

$$P_k(d) = \begin{cases} \frac{k}{2h}(d+h)^2 & ,d \in (-h, 0) \\ \frac{kh}{2} + kd & ,d \geq 0 \\ 0 & ,otherwise \end{cases} \tag{5.1}$$

where $k$ determines the strength of position penalty. The behaviour of $P_k(d)$ on the interval $-2 < d/h < 1$, illustrated in Fig. 5.1, ensures that the penalty activates smoothly as contact starts, helping us to resolve the nonlinearity through Newton's iteration process.

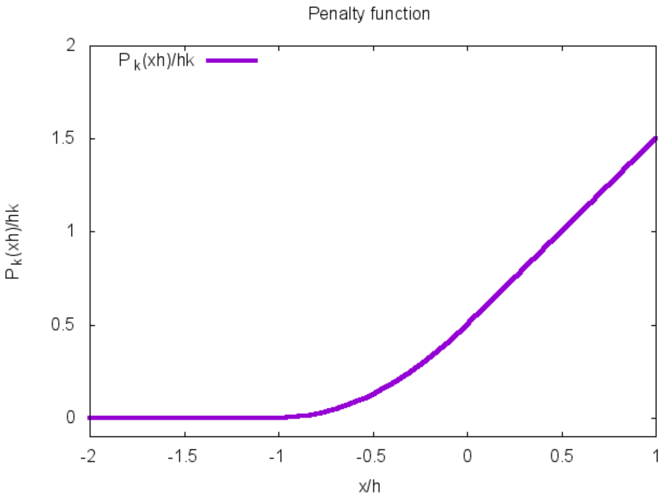

Figure 5.1: Penalty function $P_k(x)$.

In general, the contact parameters are chosen as

$$k = c_1 E/\Delta x$$

$$h = \varepsilon_{cont} = c_2 \Delta x$$

where $\Delta x$ is the size of structural element.

### 5.1.2 Lagrange multiplier

A classical method is the use of Lagrange multipliers to add contact constraints on contacted interface in a weak form. Like penalty method in previous section, the non–penetration is imposed as the contacted constrain in this study. For each simply connected disjointed part $S_i^t$, $i = 1 \cdots n_s$ of $\Sigma^t$ or $\Gamma^t$, a signed distance function $\mathbf{x} \mapsto d_{S_i^t}(\mathbf{x})$ measures the Euclidian distance of $\mathbf{x}$ to $S_i^t$, and the sign indicates whether $\mathbf{x}$ is in the structure ( $d_{S_i^t}(\mathbf{x}) < 0$ ) or in the fluid ( $d_{S_i^t}(\mathbf{x}) > 0$ ). When $d_{S_i^t} = 0$ for some $\mathbf{x} \in \partial\Omega \setminus S_i^t$, there is a contact. Note that contact between points on the same part $S_i^t$ is not apprehended by this framework.

Considering a general variational problem of fluid–structure interaction system $A(\mathbf{u}_h, \hat{\mathbf{u}}_h)$ and the right hand side term $b(\hat{\mathbf{u}}_h)$, the problem in this study can refer to equation (2.30).

$$A(\mathbf{u}_h, \hat{\mathbf{u}}_h) = b(\hat{\mathbf{u}}_h)$$

After discretizing time differential term at time step $n+1$ and with nonlinear iteration $k$ times, it yields

$$\tilde{A}\left(\mathbf{u}_h^{n+1,k+1}, \hat{\mathbf{u}}_h\right) = \tilde{b}^{n+1,k}(\mathbf{u}_h^n, \hat{\mathbf{u}}_h)$$

The problem $\tilde{A}$ and $\tilde{b}$ in this study can refer to equation (2.33).

As discussed before, contact points are located where $d_{S_i^n} = 0$ for some $\mathbf{x^n} \in \partial\Omega \setminus S_i^n$. With non–penetration constrains, the distance functions $d_{S_i^n}(\mathbf{x}^n)$ of potential contact points are constrained to be positive $d_{S_i^n}(\mathbf{x^n}) \leq 0$ at every time step $n$. Regarding to the moving of surface, the distance function at next time step $n+1$ can be predicted and calculated with backward Euler method and time increment $\delta t$:

$$d_{S_i^n}\left(\mathbf{x^n} + \delta t \mathbf{u}^{n+1}\right) \leq 0$$

Practically, there is a small gap $\delta_{ck}$ between any two contacted surfaces to reduce the complexity in mesh generation and in moving mesh.

$$d_{S_i^n}\left(\mathbf{x^n} + \delta t \mathbf{u}^{n+1}\right) \leq \delta_{ck} \tag{5.2}$$

The system is modelled by a variational inequality with Largrange multiplier $\lambda$ along normal direction on the contacted surface:

$$\tilde{A}\left(\mathbf{u}_h^{n+1,k+1}, \hat{\mathbf{u}}_h\right) + \int_{\partial\Omega^{n+1,k}} \lambda^{n+1,k} \mathbf{n} \cdot \hat{\mathbf{u}}_h = \tilde{b}^{n+1,k}(\mathbf{u}_h^n, \hat{\mathbf{u}}_h) \tag{5.3}$$

To solve the problem, we apply the discretization described above and the semi–smooth Newton method proposed by Ito and Kunisch [184], which replaces the inequality constraints by the equality constraints at time step $n$:

$$\lambda^{n+1,k+1}(\mathbf{x}) - \min\left\{0, \lambda^{n+1,k}(\mathbf{x}) + c_0\left(d_{S_i^n}\left(\mathbf{x^n} + \delta t \mathbf{u}^{n+1}\right) - \delta_{ck}\right)\right\} = 0 \quad \forall \mathbf{x} \in S_i^{n,k+1} \tag{5.4}$$

where $c_0$ is any positive constant related to the sensitivity of contact. These equality constraints are only left and right differentiable, but it is enough for a Newton–type algorithm to converge. To the end, one needs to solve iteratively in $k^{th}$ iteration for each time step $n$ through

$$\begin{aligned} & A\left(\mathbf{u}_h^{n+1,k+1}, \hat{\mathbf{u}}_h\right) - b^{n+1,k}(\hat{\mathbf{u}}_h) \qquad (5.5) \\ + & \sum_{i=1}^{n_s} \sum_{\substack{j=1 \\ j \neq i}}^{n_s} \int_{S_j^{n+1,k} \cap \left\{\mathbf{x}:\, \lambda^k + c_0\left(d_{S_i^{n+1,k}} - \delta_{ck}\right) < 0\right\}} c_L \left(\mathbf{u}_h^{n+1,k+1} - \mathbf{u}_R\right) \cdot \hat{\mathbf{u}}_h = 0 \end{aligned}$$

where $n_s$ is the number of closed and separated surfaces, $\mathbf{u}_R$ is rebound velocity to ensure separation, and $c_L$ is a very large constant to impose $\mathbf{u}_h^{n+1,k+1} - \mathbf{u}_R = \mathbf{0}$ on the surface $S_j$ where the constraint is almost active. For one dimensional contact problem, velocity constraints can be simplified as $u_h^{n+1,k+1} - u_R = 0$. Furthermore, it is straightforward to extend the proposed contact scheme from one dimension to multi dimensions along the normal direction, which yields $\mathbf{u}_R - u_R\mathbf{n}_i = \mathbf{0}$ with the outward normal direction $\mathbf{n}_i$ at the referenced surface $S_i$.

It is shown that Eulerian formulations are well adapted to an easy treatment of contacts as observed by Richter [152]. The argument above shows also that semi-smooth Newton fits very well the Eulerian framework: it is simply an additional surface integral. Moreover the iteration index $k$ can be combined with the fixed point iterations required by the algorithm.

Practically, the rebound velocity $u_R$ should be explicitly defined. The Rebound velocity $u_R$ could be defined as a function of distance or velocity. The following continuous function of the relative velocity $u_{re}$ is chosen in this study (see Figure 5.2).

$$u_R - \mathbf{u}_i \cdot \mathbf{n}_i = \begin{cases} u_{re} & \text{if } u_{re} > \varepsilon_{ck} \\ \varepsilon_{ck} & \text{if } u_{re} \leq \varepsilon_{ck} \end{cases} \tag{5.6}$$

The relative velocity $u_{re}$ between the contacted surface $S_j$ and the referenced surface $S_i$ is determined by $u_{re} = \left(\mathbf{u}_j - \mathbf{u}_i\right) \cdot \mathbf{n}_i$. When it's going to contact $u_{re} < 0$, rebound velocity on $S_j$ is defined as $u_R = \mathbf{u}_i \cdot \mathbf{n}_i + \varepsilon_{ck}$. Here, a positive value $\varepsilon_{ck}$ is introduced to guarantee separation at next time step. Additionally, another way to determine rebound velocity is also shown in Figure 5.2, which introduces one coefficient $\beta$ to fit different types of contacted reaction.

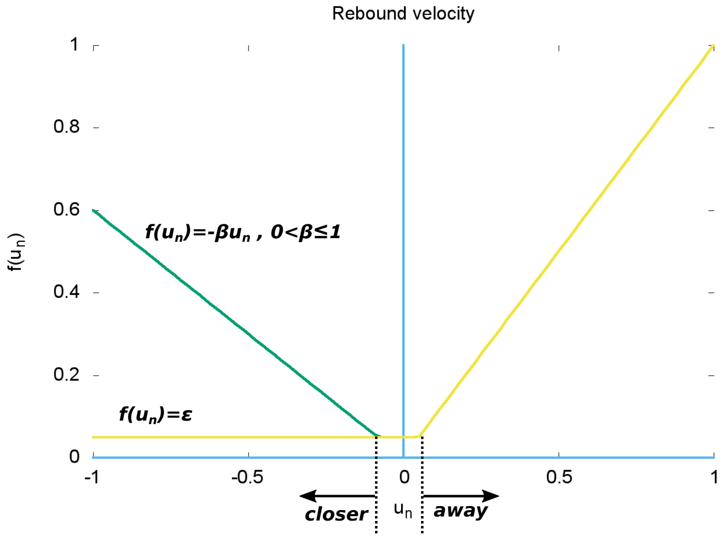

Figure 5.2: Rebound velocity $u_R - \mathbf{u}_i \cdot \mathbf{n}_i = f\left(u_n\right)$ to ensure boundaries separate.

One–dimensional contact scheme is proposed in this work. The extension of the proposed scheme to multi–dimension is along normal direction of referenced surface $S_i$. However, there is no extra velocity constraint on tangential direction of contacted surface. In other words, two colliding bodies are frictionless at the contacted surface. We can also observe that from the following simulation results. The contact coefficients $\delta_{ck}$ and $\varepsilon_{ck}$ are normally defined as:

$$\delta_{ck} = 2h_{min}, \quad \varepsilon_{ck} = 0.001 \sim 0.1 \tag{5.7}$$

where $h_{min}$ is the minimum size of elements. The $\delta_{ck}$ is about the small gap to simplify the mesh generation. The $\varepsilon_{ck}$ is to ensure the separation among contacted objects.

## 5.2 Computational results

Distinct numerical tests are discussed in this section to validate and verify the proposed contact schemes. First, different numerical tests about dynamical contact of objects are chosen to demonstrate the capability of proposed contact scheme. Second, sections 5.2.2 and 5.2.3, two similar numerical tests, a freely falling disc on a horizontal plane and stairs–shaped geometry respectively, are studied to verify the proposed contact scheme with the referenced article [177]. Third, in sections 5.2.4 and 5.2.5, two more numerical tests are carried out to examine symmetry of the proposed contacted scheme and the applicability to simulate multiple objects contact problems.

### 5.2.1 Simulations of contact problems

The contact between elastic discs is tested to show the numerical results of the proposed contact algorithm before considering fluid–structure interaction problems. All elastic discs have radius $r = 0.4$, density $\rho_s = 1.0$, and Lamé coefficients $\mu_s = 2000$ and $\lambda_s = 8000$. Four numerical test cases are considered : falling disc on a slope, horizontal projection of a disc, and collapsing moving discs from two different directions, and simulation results are plotted in Figures 5.3.

The elastic balls start from rest, and they move under the gravity force or the force along the direction of arrow in Figures 5.3. Trajectories of moving balls for each numerical test are separately plotted in Figures 5.3. Observation of simulation results can exhibit some features of proposed scheme. First, the proposed contact scheme is capable of dealing with multidimensional contact problems. Second, rebound velocity is inclined to the tangential direction compared to the elastic collision. Third, there is an emphasis on the proposed contact scheme that velocity constraint is implemented on the normal direction of the referenced surface, and it is frictionless on contacted surface.

### 5.2.2 Validation: free falling disc

Free falling elastic disc with radius 0.4 centered at $(x_c, y_c) = (1,1)$ hits the bottom of a rectangular cavity $[0,2] \times [0,1.5]$ filled with fluid of density $\rho^f = 1000$ and viscosity

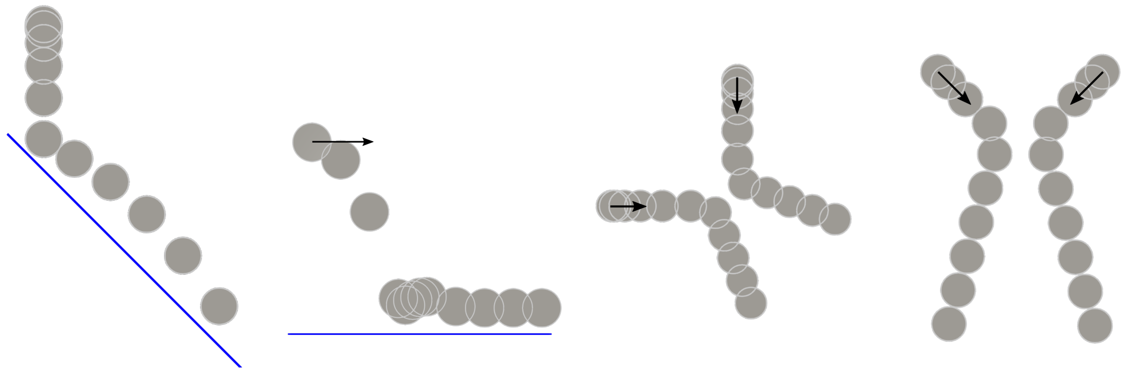
(a) (b) (c) (d)

Figure 5.3: Trajectories of moving objects for the simulation contact problems without fluid : (a) free falling disc on a slop; (b) horizontal projection of a disc; (c) and (d) two collapsible discs from different directions.

$\mu^f = 1.0$. For solid, the density is $\rho^s = 1000$ and the Lamé parameters are chosen as $\mu_s = 2 \cdot 10^5$ and $\lambda_s = 8 \cdot 10^5$.

Traction–free condition is imposed at the lateral and top walls of the cavity. No–slip boundary condition is prescribed at the bottom wall. The structure is subject to a gravity $g = -1$ along the vertical direction ($y$), but the fluid is not. Simulation results are carried out with the minimum size of element $h_{min} = 0.0008$ with the mesh being refined at the surface of the falling disc and near the bottom The time step is chosen as $\delta t = 0.001$. For the proposed contact model, parameters are chosen as $C_L = 1.0 \times 10^5$, $\varepsilon_{ck} = 0.01$, and the gap is $\delta_{ck} = 0.002$.

Velocity contours of $y$-component are shown in Figures 5.4 a t$t = 1.25$, 1.875, 2.5, 3.0, 3.25, 4.0. We can observe four repeating motions, which are falling, rebound, ascending, and floating, until energy dissipates in fluid. From Figure 5.4(a) to 5.4(f), it is obvious to observe some difficulties to simulate contacted problems: steep change in velocity and large deformation at contacted region.

Three different measures of the numerical test are introduced to analyze and verify the simulation results. To trace the position of the falling disc, the location of the disc's lowest point is recorded with respect to time, as shown in Figure 5.5(a). The distance between the highest and lowest point and the averaged velocity of elastic disc are plotted in Figure 5.5(b) with respect to time to have better insights of the falling disc during contact. Obviously, the present results showed a perfect agreement before the second contact, and this difference is acceptable owing to numerical error and distinct contact models. During contact, steep change in velocity (see figure 5.5(b)) occurs in a very short time period. The vibration of elastic disc is observed after each collision, as shown in Figure 5.5(b). Additionally, it's much clear to see the repeating procedures of falling, rebound, ascending, and floating in Figure 5.5(a) and 5.5(b).

Different numerical tests with various parameters $\varepsilon_{ck}$ or $\mu_f$ are considered to verify

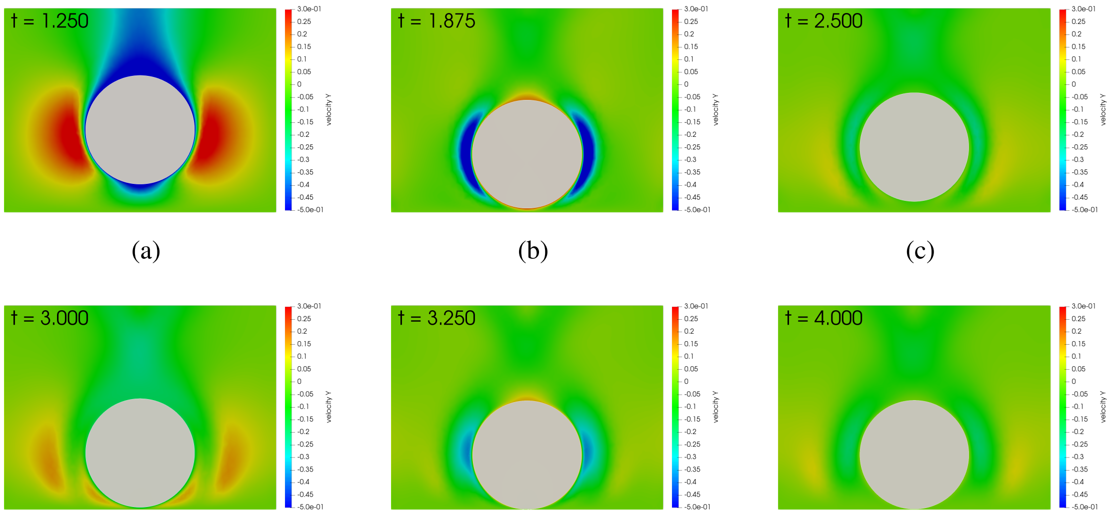

(a) (b) (c)

(d) (e) (f)

Figure 5.4: Velocity contours of $y$ component at (a) $t = 1.25$; (b) $t = 1.875$; (c) $t = 2.5$; (d) $t = 3.0$; (e) $t = 3.25$; (f) $t = 4.0$.

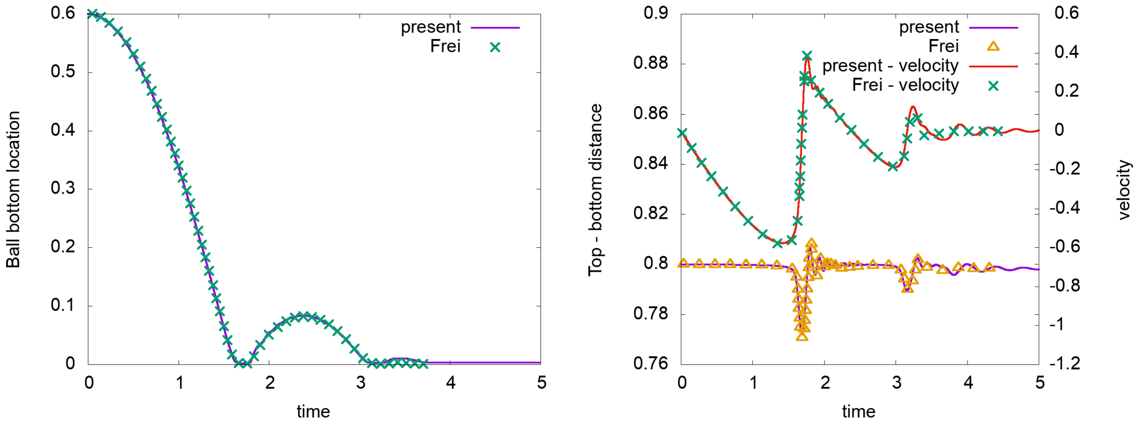

(a) (b)

Figure 5.5: Comparison of simulation results with Frei [177] : (a) lowest point of disc; (b) distance between the top and the bottom points; (c) averaged velocity.

the proposed contact scheme. First, rebound velocity $\varepsilon_{ck}$ is tested for the consistency of simulation results. Results with four values $\varepsilon_{ck} = 0.001$ to $0.01$ show 10 times difference between maximum and minimum value, as shown in Figure 5.5(a)0. A perfect consistency is observed. Second, simulations with various $\mu_f = 1$, 2, and 4 are tested to show the whole fluid–structure interaction. The smaller viscosity $\mu_f$ is, the higher rebound can be observed. Simulation results also show this phenomena in Figure 5.6(b).

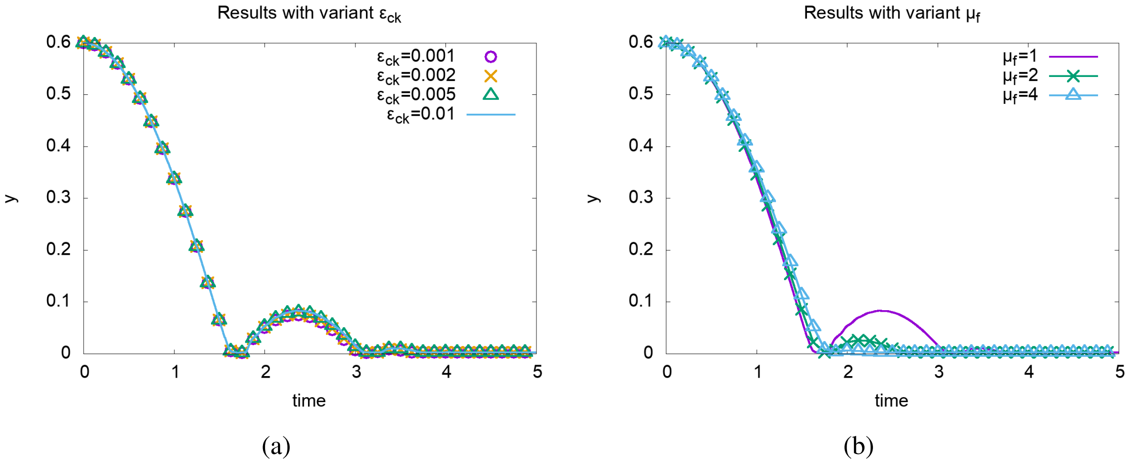

(a) (b)

Figure 5.6: The position of disc's lowest point with (a) different $\varepsilon_{ck}$; (b) different $\mu_f$.

### 5.2.3 Validation: free falling disc on stairs

A disc freely falling on a slope and stairs, as shown in Figure 5.7(a), is designed as a test by Frei [177] to valid numerical contact scheme with a complex geometry. To remove the discontinuity around stairs' corners, they are connected with circular arc of a small enough radius, $r_c = 0.02$ in this case.

No slip boundary conditions are prescribed on low, left, and right walls, and *traction-free* boundary condition is applied on the top. All material parameters are identical to those in section 5.2.2. The computational domain is discretized into 4000 elements, being refined at the surface of the falling ball and the bottom with the minimum size of element $h_{min} = 0.008$ The time difference is chosen as $\delta t = 0.001$. Trajectories of solid surface at different time steps is shown in Figure 5.7(b) to display the whole falling process.

Contours of velocity along $y$ direction at 9 time steps $t = 1.0$, 1.4, 1.6, 2.0, 2.4, 2.6, 3.0, 3.4, and 4.0 are shown at Figure 5.8 to show flow fields during falling, contact, and rebound processes. It is interesting to observe that the change in velocity around the ball during contact, such as in Figure 5.8(c) and 5.8(f) at $t = 1.6$ and 2.6. Additionally, as mentioned before, there is no extra velocity constraint on the tangential direction, meaning that the contact surfaces are considered as frictionless in the present contact problem. The sliding on contact surface with simulation results are plotted in Figure 5.8.

Two different measures of the numerical test are introduced to analyze and verify the simulation results, the lowest position of the falling ball and the averaged velocity of the ball. The trajectory of the falling ball can be traced by following the lowest position of the falling ball, as shown in Figure 5.9(a). The elastic disc first rebounds on slope at $t \approx 1.6$ and hits two stair on the corners at $t \approx 2.6$ and 4.0, respectively, in Figure 5.9(b).

Some inferences can be seen from the comparison between the present and the referenced [177] results in Figure 5.9. First, in consideration of distinct methologies of contacted schemes and numerical error, it is expected to see the difference between numerical

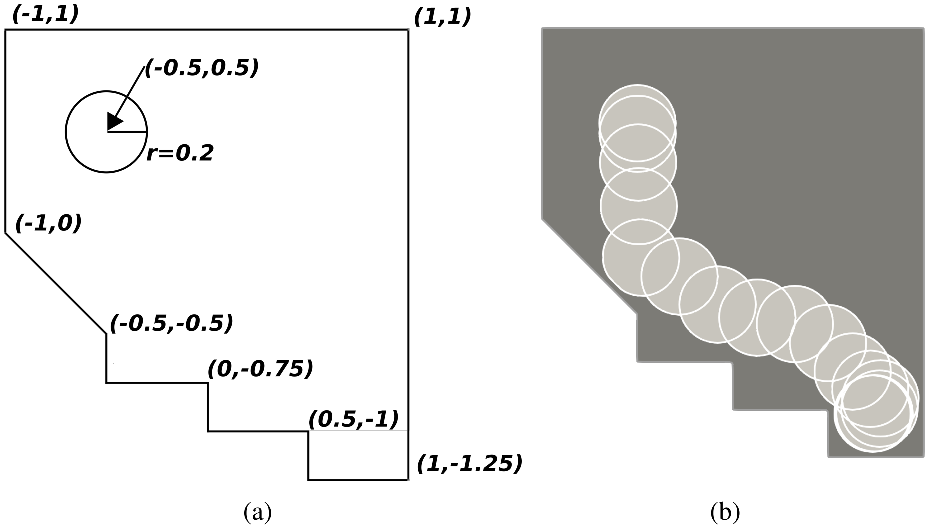

Figure 5.7: (a) Schematic of the problem and (b) trajectory of the solid surface.

results of the present and the referenced study [177]. Second, as mentioned before, the proposed contact scheme neglects the friction at the contact surface, so the angle of rebound would become larger than expected, which conforms to the simulation results in Figure 5.9(a).

To test the consistency of the proposed contact scheme, simulation results with various $\varepsilon_{ck}$ are carried out and shown in Figure 5.10(a), and the consistent results are observed. Simulation results are also carried out with various $\rho_f$ from 100 to 1000 and plotted in Figure 5.10(b), which also follow the physics.

### 5.2.4 Falling ball hitting a fixed and rigid ball

A free falling elastic ball hits a fixed and solid ball in a rectangular container filled with fluid. This simple numerical test is proposed to test the rebound direction of the proposed scheme. The line connecting two circular centers is along the gravity direction, and the elastic ball and fluid are still in the beginning. Predictably, falling ball is going to hit the fixed ball, rebounds along the gravity direction, and repeats for few times. Then, it is going to descend right/left side of the fixed ball since the stationary point on the fixed ball is unstable.

Material properties are chosen as $\rho_f = 100$ and $\mu = 2.0$ for fluid, and $\rho_s = 200$, $\mu_s = 2 \times 10^5$, and $\lambda_s = 8 \times 10^5$ for solid. Gravity force is acting only on the structure $g = -1$.

The velocity contours of $y$-component at different time steps are shown in Figures 5.11. The trajectories of the falling ball can be observed through Figure 5.11(a) to 5.11(f). After several rebounds and descendings, the falling ball slides upon the fixed ball and falls because of an unstable balance on the stationary point. The position of the lowest point of the falling ball and the averaged velocity are plotted in Figures 5.12 with respect to time. First, slight oscillation on the horizontal position is observed in Figure 5.12(a), because colliding

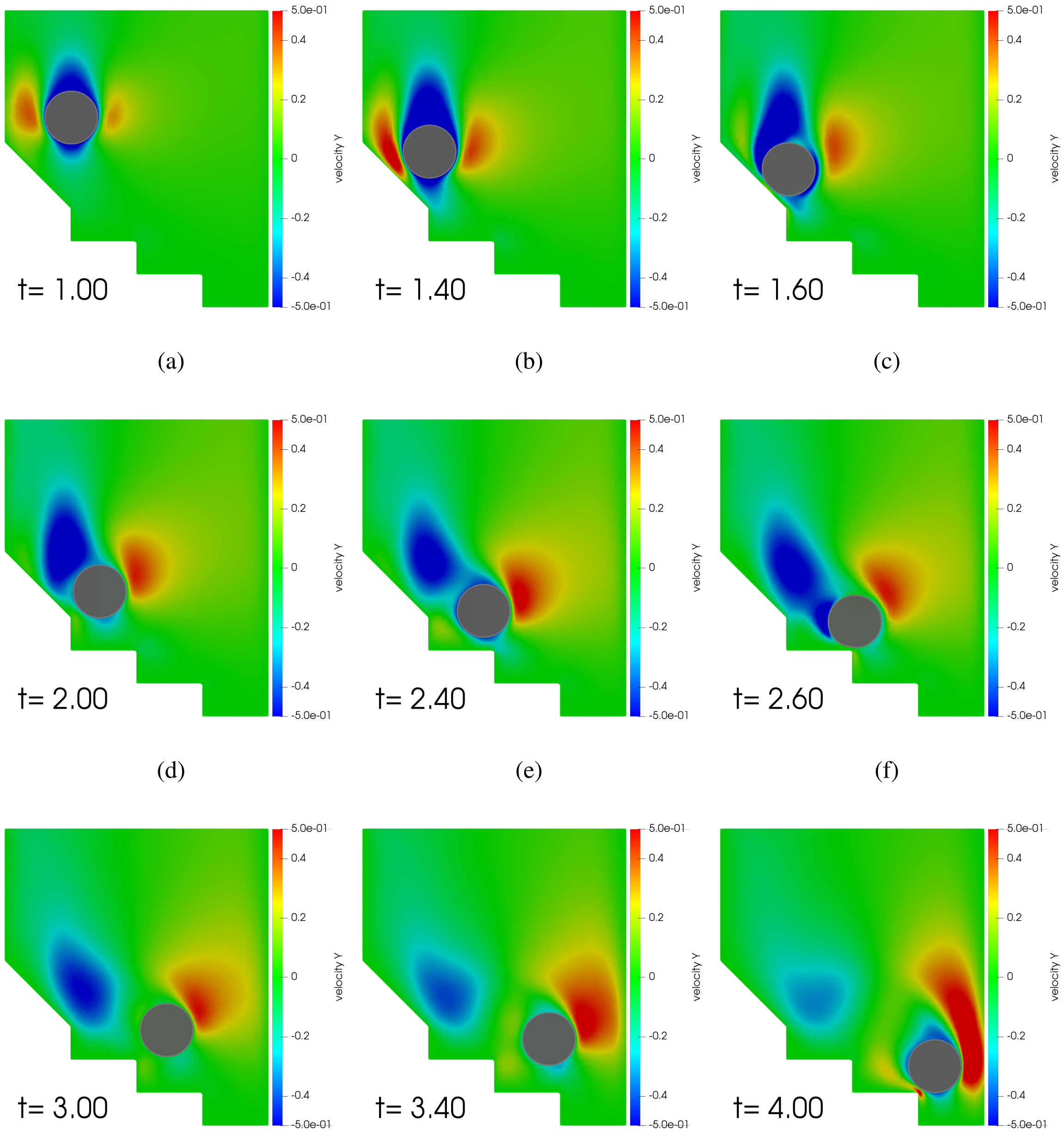

(a) (b) (c)

(d) (e) (f)

(g) (h) (i)

Figure 5.8: Velocity contours of $y$ component at (a) $t = 1.0$; (b) $t = 1.4$; (c) $t = 1.6$; (d) $t = 2.0$; (e) $t = 2.4$; (f) $t = 2.6$; (g) $t = 3.0$; (h) $t = 3.4$; (i) $t = 4.0$.

makes the falling ball to deform into a concave shape at the contact surface. Second, a series of bouncings on the fixed ball can be clearly seen in Figure 5.12(b) through repeating a shift of $y$-component velocity between positive and negative value, which represents ascending and descending.

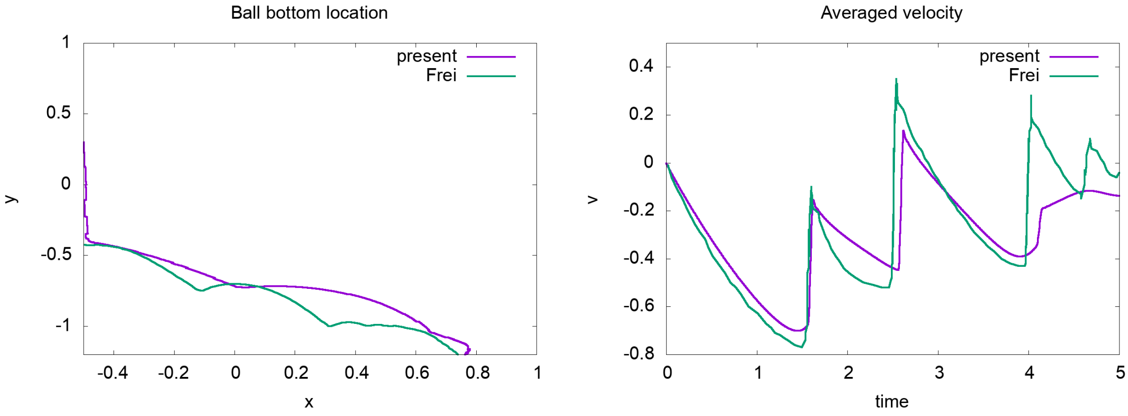

(a) (b)

Figure 5.9: (a) Position of the ball's bottom and (b) the averaged velocity with respect to time.

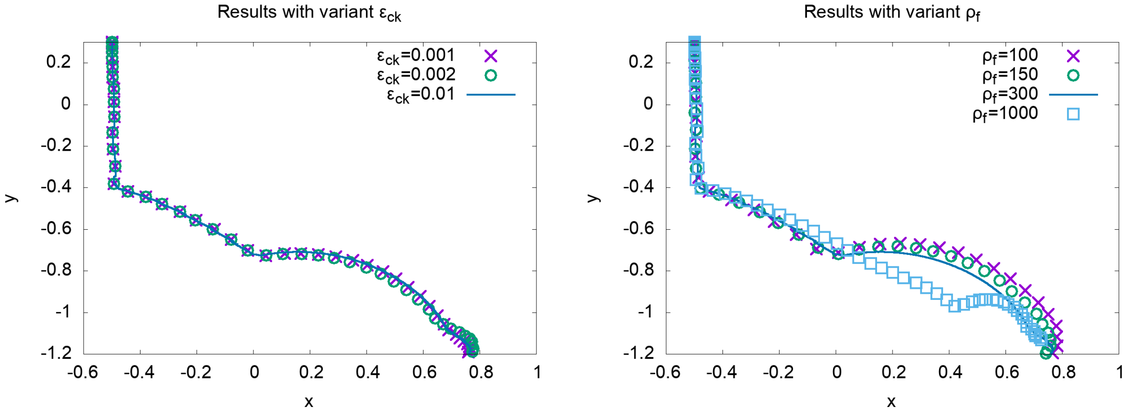

(a) (b)

Figure 5.10: The simulation results with (a) variant $\varepsilon_{ck}$ and (b) fluid densities.

Physically speaking, falling from which side of the fixed ball is unpredictable, and it should not have any preference for a computational contact scheme. Therefore, a little change of the contact scheme coefficients possibly leads to totally different results, falling from another side of the fixed ball in this numerical case in Figure 5.12(c).

### 5.2.5 Falling discs in a container

According to the formulation (5.5) with the proposed contact scheme, it is easy to implement on multiple objects' contact problem while the distance function $d_{S_i^{n+1,k}}$ is determined at each iteration on each connected surface $S_i$. For the last 2D numerical test, we consider

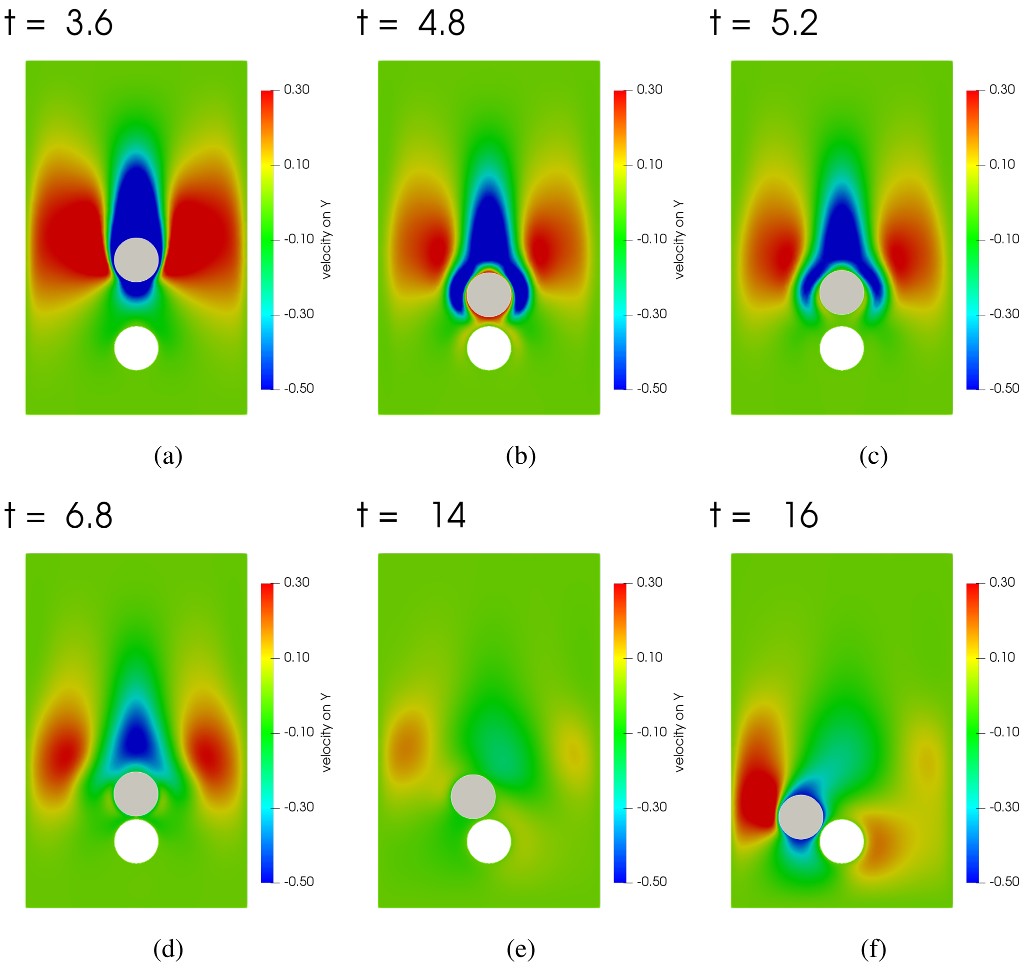

Figure 5.11: A free falling elastic ball hits a fixed solid ball at (a) $t = 3.6$; (b) $t = 4.8$; (c) $t = 5.2$; (d) $t = 6.8$; (e) $t = 14.0$; (f) $t = 16.0$.

multiple discs falling to a circular–arc shaped bottom. The centers of three identical discs are placed at $(2.2, 2.0)$, $(2.4, 3.2)$, and $(2.0, 4.5)$, and they fall under gravity force $g = -1.0$ along $y$ direction. The center of circular arc is located at $(2, 3.5)$ and with radius of 3.5, and we only consider the arc with $x \in [-1, 5]$.

The Dirichlet boundary condition $u = v = 0$ is prescribed on the circular arc, and *traction-free* boundary condition is prescribed on the rest of computational domain. Computation domain is discretized into 7000 elements with the mesh being refined at interfaces of discs and the circular–arc with the minimum size of element $h_{min} = 0.02$. The time difference is chosen as $\delta t = 0.0016$. Simulation results at 6 time steps are plotted in Figure 5.13.

There are two distinct interactions among these falling balls, which are the contact with the container and other balls. In the previous sections, numerical tests mainly focus on one moving object hitting another object which is fixed and rigid, and these are similar

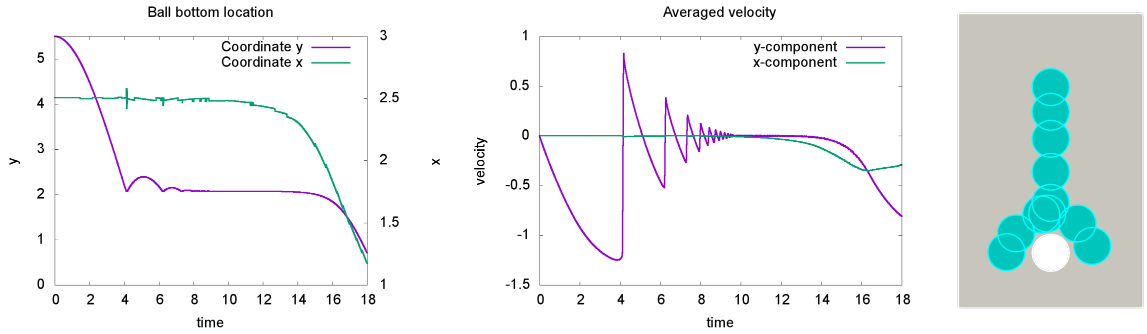

(a) (b) (c)

Figure 5.12: (a) Position of the ball bottom, (b) averaged velocity, and (c) trajectory of the solid surface.

to contact with container in this section. Few obstacles occur while multiple objects move and deform. First, it is not easy to calculate distance between each objects. Thanks to *Freefem++*, there is one library available to carry out the distance function to specified regions and borders. Second, it requires stricter selection of the contact parameter $\varepsilon_{ck}$ to get convergent results. Third, in order to compute relative velocity between two contacted interfaces, it is necessary to estimate local velocity around the contact interfaces, especially, when large deformation happens at a small region. Accordingly, averaged velocity around contact interfaces is chosen to be carried out relative velocity locally.

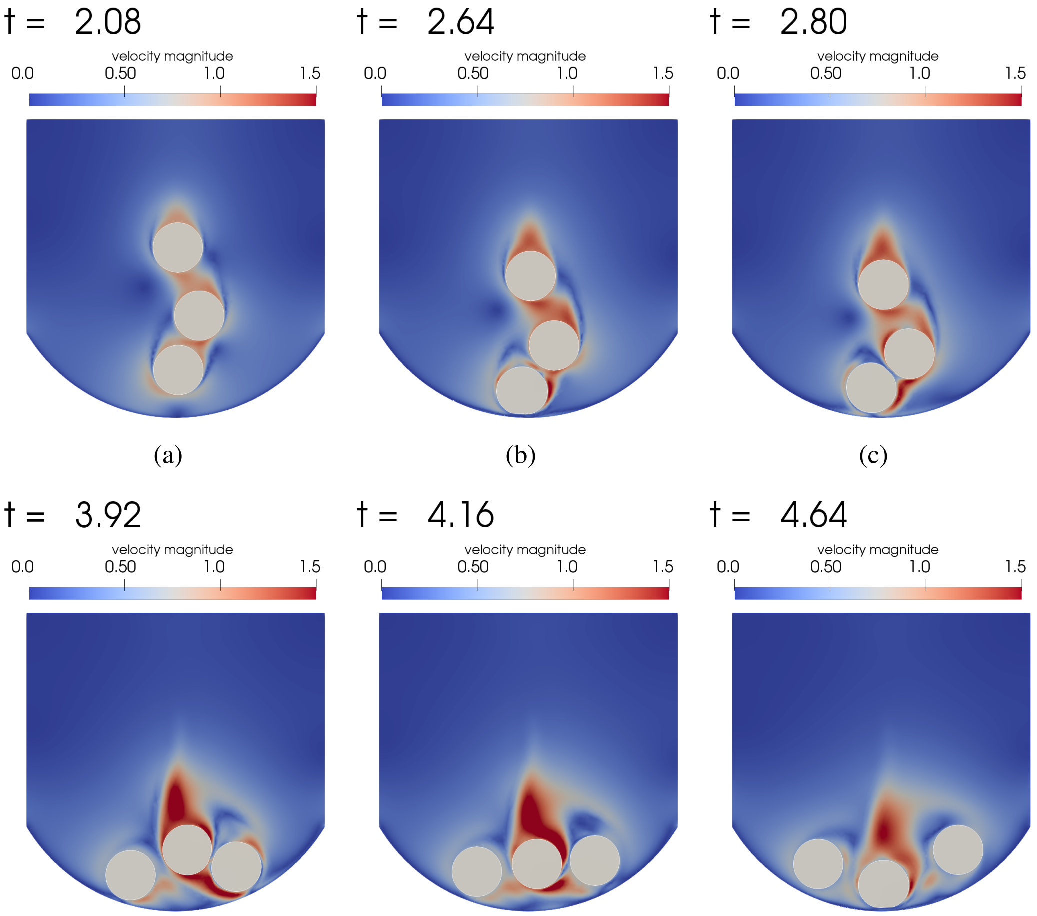

(a) (b) (c)

(d) (e) (f)

Figure 5.13: Elastic balls fall to a fixed arc-shaped container at (a) $t = 2.08$; (b) $t = 2.64$; (c) $t = 2.8$; (d) $t = 3.92$; (e) $t = 4.16$; (f) $t = 4.64$.

# Chapter 6

# Blood flow in valved veins of inferior limbs

Contents

## 6.1 Introduction of venous blood flow

### 6.1.1 Vein architecture (anatomy–geometry)

In the circulatory system, veins are blood vessels that carry blood toward the heart. Except the pulmonary and umbilical veins, veins carry deoxygenated blood. Veins are volume buffers because of the elasticity of vessels. Veins, which are the major blood storage compartments, accommodate volume changes by shrinking to possible collapse. There are two different kinds of veins that define a compartment within the pulmonary and systemic circulation. The limbs have superficial and deep veins.

For example, for driving the blood circulation in the body, arteries and veins are under various pressure at each cardiac cycle phase. During each cardiac cycle, arteries are supplied by a blood bolus ejected by the heart and dilate upon the passage of the pressure wave. In the limbs, veins, which collect blood from capillaries, undergo compression–decompression cycles due to contraction and relaxation of the neighboring skeletal muscles that assist in blood to return to the heart. Furthermore, the following Table 1.14 makes a detailed comparison between veins and arteries.

One of the main objectives in this study is to understand the cause and consequence of venous diseases using mathematical models and conducting numerical simulations. Chronic venous insufficiency (CVI) is caused by superficial venous reflux related to aging, hormone progesterone level, obesity, prolonged sitting or standing, etc. Varicose veins are enlarged and twisted. Ultimately, an improper functioning of veins generates venous ulcers. However, there are still many disagreements from mechanical aspects. By solving the mathematical model equations for valved veins, comprehension of details for varicose veins assists us to propose an explanation to disease with numerical evidence. Characteristics developed to adjust venous functions are categorized into anatomy and histology. Additionally, the valved vein is a main target.

### Anatomy of veins–venous circuit in the lower limbs

Venous structure and geometry is introduced in this section. Cross section of veins is close to an ellipse (Fig. 6.1), and the elliptic cross section has the unique collapse pattern. During the collapse, the original elliptic cross section would stretch along the major axial direction and shrink along minor axial direction. The detailed literature survey of collapsible tubes such as veins is in section A.1.

Inferior limb veins are endowed with bicuspid valves to prevent transient back flow during muscular compression (Fig. 6.2).

The limb venous network is composed of a superficial and a deep compartment (Fig. 6.3). The main superficial veins of the lower limbs are the short (SSV or saphena interna) and the long saphenous vein (LSV or saphena externa), which runs from foot to knee (saphenopopliteal junction) and from foot to groin (saphenofemoral junction), respectively. Venous blood also moves from the superficial to the deep venous network via perforating or communicating veins that cross the deep fascia.

The popliteal vein (PoV) is formed by the union of the anterior tibial vein (ATiV) and the trunk formed by the confluence of the posterior tibial (PTiV) and peroneal (PeV) veins. The popliteal vein becomes the femoral vein. The small saphenous vein (SSaV) crosses the popliteal fossa and drains into the popliteal vein. The great saphenous vein (GSaV), the longest vein, ascends from the foot to the groin to enter into the femoral vein. The femoral vein (FV) becomes the external iliac vein (EIV).

To simplify the venous network in inferior limbs for the sake of modelling the simu-

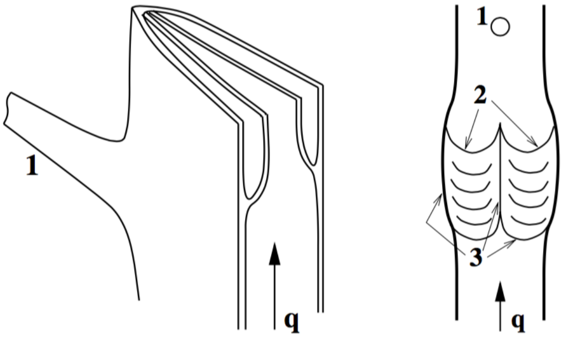

Figure 6.1: Bicuspid venous valves. (Left) cross and axial cut of a vein (1: orifice of communication vein at the vein edge; 2: cusp free border in front of the vein face; 3: valve insertion lines). (Right) open and spread vein after axial incision of a wall edge. The valvular sinuses are behind the cusps. The luminal face is smooth; the parietal face is rough.

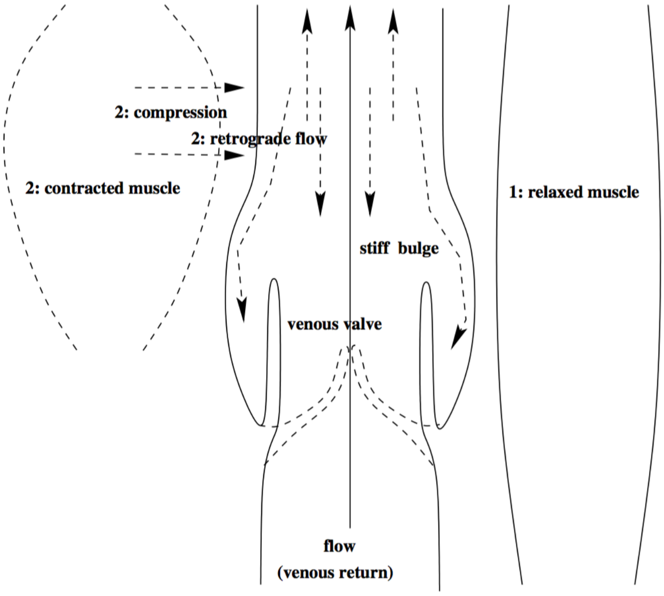

Figure 6.2: Venous valves and neighbour muscles.

lation, the structure in Fig. 6.4 is taken into consideration. Superficial and deep veins are connected by perforating veins (Fig. 6.1 and 6.4). The blood flow in this connected venous structure is from superficial to deep vein through the perforating vein and from distal to proximal segments. Generally, deep veins are stiffer than superficial veins so that CVI on superficial segments will be comparatively easy to occur.

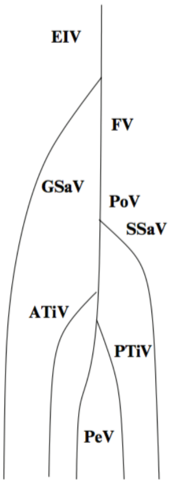

Figure 6.3: Veins of the lower limbs. The venous network is composed of a superficial (great and small saphenous veins) and a deep circuit (femoral and popliteal veins).

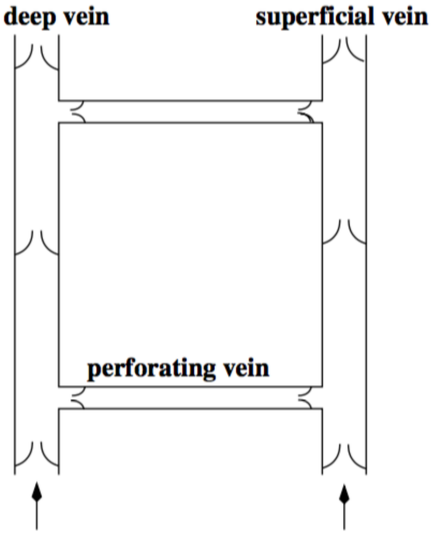

Figure 6.4: Limb valved vein network, with a superficial vein and a deep vein anastomosed by a communicating vein equipped with ostial valves for the one–way circulation from superficial to deep vein.

### Valvular anatomy and histology

Venous valves prevent reflux during various cardiac cycle phases. Therefore, possible to observe long–period opening valves at some conditions. Bicuspid venous valves are attached to veins along the major axial direction (Fig. 6.1). The valve orifice is elliptic in nature, with an opening area about 35 % of the full luminal area [185]. Valve motion is driven by pressure gradients [106, 185] and flow direction [186].

In [185, 186], authors proposed a new mechanism and procedure for valvular closure and validated it by observation and experimental data. Earlier studies believed flow directions mainly drive valvular motion, opening and closure, but the study in [186] showed there is no direct relationship between valvular closure and flow direction. They pointed out the difference in size and dimension for venous sinus segments has connection with pressure increase.

Physiologically, valves are capable of withstanding very high proximal pressure gradients with minimal leakage, and opening at very low distal pressure gradients. The thickness of valvular leaflets ranges from 20 to 50 $\mu$m. Leaflets are composed of collagenous fibers covered with two unicellular endothelialized layers. There are some ridges on parietal side facing proximally towards valve sinus. The other side, luminal side, is generally smooth [187]. The leaflets are parabolic in shape, and connect to the vein wall via the valvular agger. The agger, a thickened protrusion of the vein wall, acts as a stiffening collar to prevent excessive vein dilation at the site of the leaflets (Fig. 6.5) [187]. This helps to limit vein distension to the sinus region. Thinner media layer in sinus region, only 20 to 25 % of normal venous wall [188], allows local sinus expansion. This mechanism plays a key role of correcting valvular opening and closing.

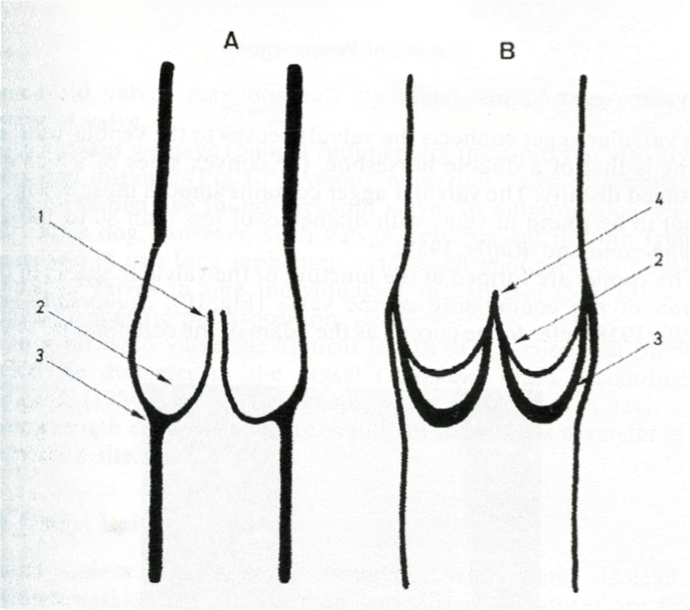

Figure 6.5: Anatomy of bi-leaflet vein valve [187]. 1) orifice 2) sinus pocket 3) valvular agger 4) valvular commissure

As shown in Figure 6.2, venous valves are fully open when neighboring skeletal muscles are relaxed. Adjoining muscle contraction deforms much more the avalvular segments of veins than the valvular parts, which are slightly dilated and stiffer. Consequently, venous return is favored, but it is associated with retrograde flow. The latter is impeded by valve closure due to blood stream between the vein wall and the valve.

### 6.1.2 Governing equations for blood flow

Modelling of blood flow involves several features like vessel bore, blood velocity, and blood aggregation. Selection of the blood model has been discussed in section 1.4.1, and the current study is dedicated to large veins of inferior limbs. The blood flow is modelled as incompressible Newtonian fluid. The governing equations for a unsteady blood flow (with mass density $\rho^f$, dynamic viscosity $\mu$, and kinematic viscosity $\nu = \mu/\rho^f$) of an incompressible blood are the following mass and momentum conservation equations (Eq. 6.1 and 6.2).

$$\nabla \cdot \mathbf{v} = 0 \tag{6.1}$$

$$\rho_f \left( \frac{\partial \mathbf{v}}{\partial t} + \mathbf{v} \cdot (\nabla \mathbf{v}) \right) = \nabla \cdot (\sigma) + \mathbf{f} \tag{6.2}$$

where $\sigma = -p\mathbf{I} + \mu_f D$ and $D = \left( \nabla \mathbf{v} + \nabla \mathbf{v}^T \right)$ in the case of a Newtonian fluid. The volumatic force term $\mathbf{f}$ in this study indicates the gravitational force $\mathbf{f} = -\rho_f g \hat{e}_z$ ($g$ the gravity).

### 6.1.3 Governing equations for venous wall and valves

Vascular dilation and collapsing take place during each cardiac cycle. To model the motion of vascular wall, it is essential to consider the construction of wall. Among five different layers (section 1.1.2), the *media* layer is vital to be considered, because the elasticity of blood vessels is mainly established by smooth muscle cells (SMC) in *media* layer. Regarding the orientation and arrangement of smooth muscle cells, some studies treat vascular wall as anisotropic material. According to Table 1.4, *media* layer is prominent in the artery and is weak in the vein. Therefore, it is substantial to regard the artery as an anisotropic material, but it is not required for veins.

This study focuses on valved veins and venous circuit in lower limbs. Furthermore, venous wall and valves are treated as the same material to simplify venous model and avoid coupling error between different materials. Bileaflet valves in veins are driven by blood flow, and large deformation can be observed between each opening and closure of valves throughout the cardiac cycle. Therefore, hyperelastic model is necessarily implemented to precisely capture the motion of valves instead of by a linear elasticity model. To conclude, an isotropic hyperelastic material is utilized to model venous wall and valve in this study.

Mooney–Rivlin model is chosen to model vascular walls and valves in this study. Conservation of momentum and mass is given below:

$$\rho_s \mathbb{D}_t^2 \mathbf{d} = \nabla \cdot \sigma_s + \mathbf{f}, \quad \frac{d}{dt}(J\rho_s), \quad J\rho_s = \rho_s^0 \tag{6.3}$$

where $J$ is the Jacobian of the deformation. The stress tensor of an incompressible hyperelastic material can be derived as

$$\sigma_s = -p_s \mathbf{I} + \partial_{\mathbf{F}} \Psi_{\mathrm{MR}} \, \mathbf{F}^T$$

where $\Psi_{\mathrm{MR}}$ indicates Helmholtz potential, $\Psi_{\mathrm{MR}}(\mathbf{F}) = c_1 \mathrm{tr}_{\mathbf{F}^T\mathbf{F}} + c_2 \left(\mathrm{tr}_{(\mathbf{F}^T\mathbf{F})^2} - \mathrm{tr}^2_{\mathbf{F}^T\mathbf{F}}\right)$ , and $\mathbf{F}$ stands for the transposed gradient of the deformation. Detailed description and derivation can be seen at chapter 2.

## 6.2 Modelling aspects

### 6.2.1 Computational domain – 2D geometry

Geometrical model of valved veins is defined and prescribed in this section. Every measure is dimensionalized with the bore of vein ($d$). Schematic description is shown in Figure 6.6. The shape of enlarged segment is prescribed by a Gaussian function with respect to $y$.

$$x = x_c + d + \left(w - {}^{d}/_{2}\right) \times e^{-\left(\frac{y-y_{cs}}{\sigma}\right)^2}$$

In the above equation, $x_c$ is the $x$ coordinate of venous segment's geometric center, and $y_{cs}$ is the $y$ coordinate of enlarged segment's center. This two center points can be co-located to simplify the venous geometric model. The *variance* $\sigma$ is related to the height from enlarged segment's center, and it is differently chosen for the upper and the lower partition (rate between upper and lower variance 1 : 1.6). To ensure that the whole computational domain is smooth, a transition/connection between vascular wall and valve is introduced to take care of the steep change of geometry and resolve the difficulty of meshing.

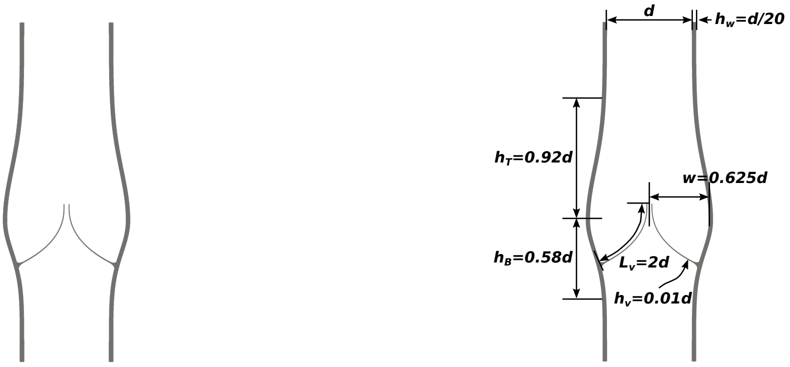

(a) (b)

Figure 6.6: Shape and size of one valved vein

The venous network, as shown in Figure 6.4, can be modelled as connection of venous segments in Figure 6.6 with different bores. In this way, complicated architecture of venous circuit can be simplified into venous segments and connection. In venous circuit, material coefficients are different for superficial, deep, and perforating veins.

### 6.2.2 Computational domain – meshing

It is required to develop an algorithm to deal with moving mesh and mesh refinement for any body–fitted methods. With the help of *FreeFem++*, a strategy of mesh refinement is presented to reduce computational time and enhance solution resolution at specified regions or borders. First, mesh refinement around specified borders utilizes the Heaviside function of distance to the border, and distance is carried out with *FreeFem++* inherent library *distance*, which can calculate signed distance with the interface of value 0 defined by Phi in scrip 6.1. A simple implementation on *FreeFem++* with *macro* is shown in scrip 6.1.

```

// Set 0 at border with label=fix
varf AdaptDist(Phi,Phih) = int2d(th)( Phi*Phih ) + on( fix,
    Phi=0 );
varf RHSAdapt(Phi,Phih) = int2d(th)( Phih ) + on( fix, Phi=0
     );

macro AdaptmeshCY( AdaptDist, RHSAdapt, Vh, b, Msize ){
    Vh Phi, Hevi, DIST;
    for( int add=0 ; add<3 ; add++ ){
        Phi=0;  SolveProblem( AdaptDist, RHSAdapt, Vh, Phi )
    ;
        /* Compute distance to border and Heviside function
    */
        DIST=0; distance(th,Phi,DIST[],distmax=1.0);
        real epsH=b;    Hevi=0;
        for( int i=0 ; i<Vh.ndof ; i++ ){
            Hevi[][i] = Heaviside( DIST[][i], 2*epsH );
        }

        /* Adapt with function of Hevi */
        th = adaptmesh( th, Hevi, hmin=epsH, hmax=Msize
            , nbvx=80000, ratio=ratio );

        /* This way is faster but don't gurantee quality
        th = adaptmesh( th, Phi, hmin=epsH, hmax=Msize
            , nbvx=80000, ratio=ratio );
        */
    }
} //EOM
```

Script 6.1: Macro to do mesh adaptation on specific borders.

Second, the mesh refinement at different regions is discussed. Venous geometrical model is regarded as an example in the following paragraph. In this study, computational domain can be divided into three connected regions (walls, valves, and fluid). The element size of fluid region is determined by the required resolution of solution, and the element sizes of walls and vales can be easily chosen as the thickness divided by the demanded layers. A part of *FreeFem++* code is attached in script 6.2.

```

macro AdaptmeshCY( Vh, FSLab, b, Msize, Reg ){
    Vh Phi, Hevi;
    for( int add=0 ; add<3 ; add++ ){
        Vh m1, m2, m3, m11, m22, m33;
        /* generate Adaptmesh matrix m1, m2, m3 for each
   region*/
        for( int Ireg=0 ; Ireg<Reg.n ; Ireg++ ){
            /* At region Reg(Ireg) */
            FSLab = (region==Reg(Ireg) - (region!=Reg(Ireg))
   ;
            Phi=0;  distance(th,FSLab,Phi[],distmax=1.0);
            real epsH=b(Ireg);  Hevi=0;
            for( int i=0 ; i<Vh.ndof ; i++ )
                Hevi[][i] = Heaviside( Phi[][i], 2*epsH );

            adaptmesh( th, Hevi, metric=[m1[],m3[],m2[]]
                , hmin=epsH, hmax=Msize, nbvx=800000
                , ratio=ratio , nomeshgeneration=1 );
            /* Substitute to total matrix */
            for( int i=0 ; i<Vh.ndof ; i++ ){
                if( Phi[][i] > -0.1*epsH )continue;
                m11[][i]=m1[][i];
                m22[][i]=m2[][i];
                m33[][i]=m3[][i];
            }

        }

        th=adaptmesh( th, metric=[m11[],m33[],m22[]]
                , hmin=epsH, hmax=Msize
                , ratio=ratio , nbvx=80000 );
    }
} //EOM
```

Script 6.2: Macro to do mesh adaptation in different regions with the specified sizes.

The generated mesh is shown in Figure 6.7. It is clear to see three different element sizes in three connected regions. Furthermore, it is feasible to establish a general and powerful mesh refinement algorithm by combining these two strategies.

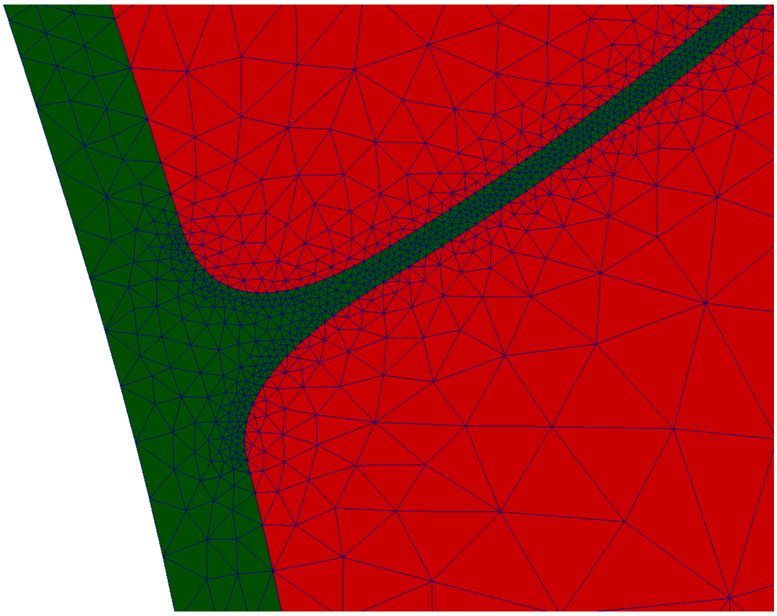

Figure 6.7: Mesh after adaptation

To sum up, this section introduces an algorithm to perform mesh refinement to the specified borders and regions. It is a widely applicable algorithm to solve the problem with complicated boundary conditions, but it practically takes a much longer time to construct matrix for each region. That is a vital defect of the proposed algorithm. Therefore, from an efficient point of view, it is better to develop an effective extension of library with C++ syntax. It is now an acceptable expense at the present moment, since mesh regeneration is not adopted in each iteration.

### 6.2.3 Modelling and assumption from 3D to 2D

In the present study, focus is on the two dimensional simulation of the blood flow in valved veins. The computational domain is defined as the cross section along the minor axis of three dimensional geometry. It is assumed that the computational results in three dimensions are symmetric at this selected cross section. To save computational efforts, simulation are only carried out on this symmetric plane. In other words, influence on symmetry plane can be neglected or replaced with $2D$ treatments.

It is reasonable to neglect the effect from symmetric direction in the fluid and wall region, because the magnitude and the first derivative of the considered variables are approximately equal to zero.

For valves, the stress along the symmetric direction is related to the closure of valves. Without the stress along symmetric direction, which is related to the support from the connected border, valves in two dimensional model would just attach to each other and then descend towards the opposite direction. We assume that valves can only move in a constrained region which is bounded by the geometrical limit of the real three dimensional valves, and constrained region is shown in Figure 6.8.

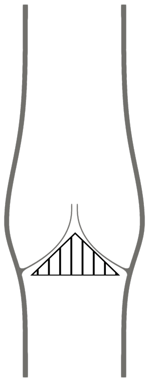

Figure 6.8: Constrained region of valves.

### 6.2.4 Boundary conditions

Appropriate selection of inlet/outlet boundary conditions is significant to model and simulate blood flow in valved veins. Two different types of inlet/outlet boundary conditions are implemented. First, a periodic velocity (pressure) function is prescribed as the inlet or outlet boundary condition. It is a common treatment to simulate blood flow in arteries with periodic velocity function as inlet/outlet boundary conditions [102, 112, 190–192]. For periodic function of pressure, it is usually applied to the simulation of blood flow in heart or veins which are with valves [112, 192]. Second, the solution of cardiac cycle model is prescribed as the inlet/outlet boundary condition. The ardiac cycle is generally modelled by the ordinary differential equations of time and $1D$ partial differential equations, and the corresponding primitive variable is pressure [193] or flow rate [11, 194–196]. However, the blood flow is normally modelled in $2D$ or $3D$, so the difficulty arises in coupling systems with different dimensions. As an example, if the flow rate is the primitive variable of the cardiac cycle model, the flow rate on inlet/outlet border has to be converted to the distribution of velocity such as the Poiseuille profile. However, it is only suitable when considering partition is far from any other disturbance like connection and bending. To sum up, this type of boundary conditions is more general and realistic, but the coupling boundary conditions among different dimensions is still a problem.

In this study, periodic pressure function is adopted as boundary conditions. The blood flow is driven by pressure difference between inlet and outlet, and valves open/close when pressure difference is positive/negative. The attractive advantages of periodic pressure function as boundary conditions are simple to implement and insensitive to the smoothness of pressure. Unlike the pressure boundary conditions, it takes enormous efforts to numerically capture steep change of velocity. Practically speaking, experimented measures display rugged velocity and pressure profiles. It is easier to directly implement the pressure rugged profiles as boundary conditions. For the velocity type boundary conditions, it is required to smoothen the velocity profiles from experiments with filters. Periodic function $f(t)$ is plotted in Figure 6.9, and the pressure boundary condition can be expressed as

$$p = p_{amp} f(t) + p_{mean} \tag{6.4}$$

where $p_{amp}$ is the amplitude of pressure function, and $p_{mean}$ is the mean pressure.

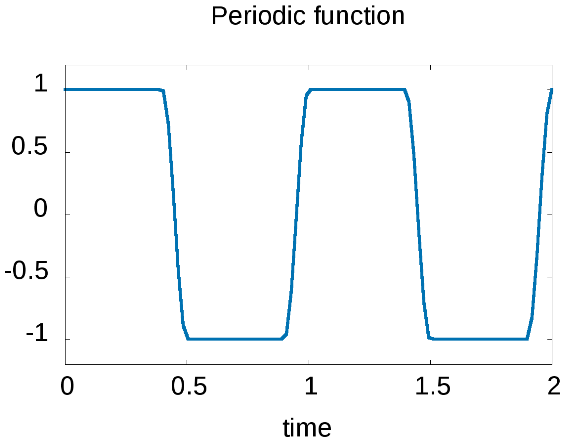

Figure 6.9: Periodic function for pressure.

## 6.3 Tube law

The unstressed cross–sectional shape of physiological vessels is commonly assumed to be elliptic. A uniform elastic vessel will collapse under the transmural pressure $\hat{p} = p_i - p_e$, internal $p_i$ and external $p_e$ pressure. This phenomena has been discussed in Section 1.4.3, and the details of the computation and approximation are summarized in Appendix A.3.

In this section, a simple 2D numerical test is proposed to examine and validate the proposed Eulerian monolithic formulation. Material properties of vascular wall are chosen as Youngs' modulus $E = 1 \times 10^5$ and Poisson ratio $\nu_s = 0.4$, and the density is $\rho_s = 1.0$ Unstressed cross–sectional shape is elliptic with semi–major axes $a = 1.0$ and semi–minor axes $b = 0.8$ and the thickness of vascular wall is $h_w = 0.025$. The area encircled by the centerline of vascular wall is 2.44268.

Transmural pressure $\hat{p}$ is varied from $-3$ to 2, and the change of cross–sectional area and shape are plotted in Figure 6.10(a) and 6.10(b), respectively. The changing cross section is similar to that shown in Figure 1.5. It studies the collapsing region rather than the radial dilation and totally collapsed regions. There is no bifurcation due to initial elliptic shape [57]. We can also say that blood vessel becomes compliant (large area change for small pressure change) when vessel collapsing starts.

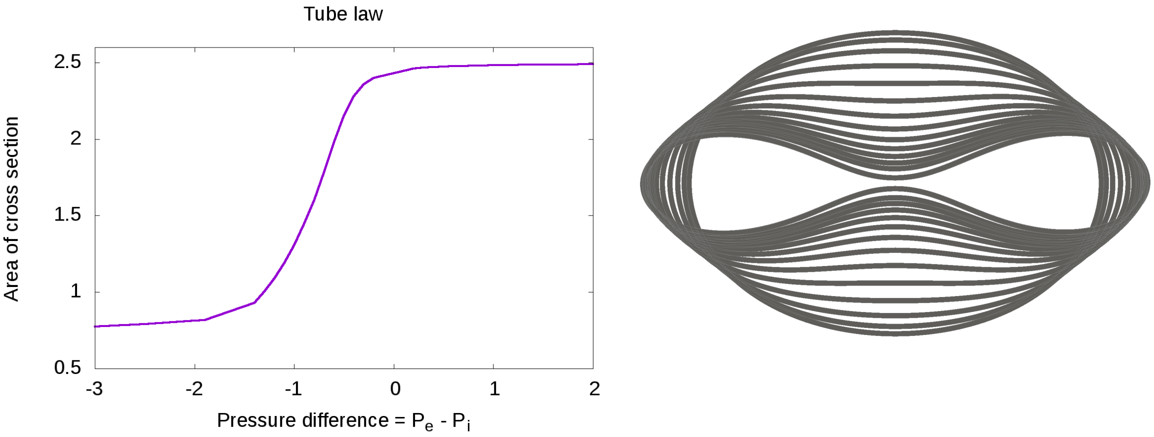

(a) (b)

Figure 6.10: Tube law with hyperelastic material and shape of cross section.

This numerical test also displays a large deformation of vascular wall, and it provides more reliability of numerical computation about vascular deformation in the following sections.

## 6.4 Numerical results

This section shows the simulation results of the blood flow in valved veins The blood flow is driven by the pressure difference between inlet and outlet boundary conditions discussed in section 6.2.4. Target of this chapter is to model and simulate blood flow in venous circuit which includes superficial, deep and perforating veins. The material properties, such as stiffness, varies with different veins. As an example, the deep veins are embedded at muscles so that the vascular walls are almost fixed and solid.

In sections 6.4.1 and 6.4.2, the simulations of the blood flow in one and two venous segments are carried out for the case with soft and solid walls. In section 6.4.3, the simulation of blood flow in venous circuit are presented.

Except periodic pressure functions prescribed at inlets and outlets, material properties are the same in the following sections. After nondimensionalizing, the density of blood is $\rho_f = 1.0$, and the Reynolds number $Re$ is 100. The venous wall and valve have density $\rho_s = 1.1$, Young's modules $E = 250000$, and Poisson ratio $\nu_s = 0.5$, and Mooney–Rivlin model is adopted.

### 6.4.1 One valved vein

The blood flow in one venous segment is discussed in this section, and the simulation results are carried out with deformable and rigid wall, respectively. To utilize periodic function of pressure as boundary conditions, the equation 6.4 is adopted, and the amplitude and mean pressure are selected as $p_{amp} = 50$ and $p_{mean} = 0$ in this section. The computational domain is discretized into 14000 $(\mathbb{P}1b, \mathbb{P}1)$ elements, and time increment is chosen as $\delta t = 0.002$.

Simulation results of velocity magnitude and vorticity contours are shown in Figure 6.11 throughout one cardiac cycle $t \in [1,2]$. Valves open while the pressure difference is positive, and they close to prevent backflow of blood when the pressure difference turns to be negative. For the simulation results with deformable walls, the slight collapsion and dilation of vascular walls can be seen.

In this study, the focus is not on modelling of blood cells and aggregation, but it's worth to discuss it over here. According to [197], the vortex in blood flow is one reason leading to clotting. The contours of vorticity in Figure 6.11 show that dual vortex are generated by the friction of valves during the closure of valves. However, the time for clotting is around 5 to 10 seconds. Since one cardiac cycle is roughly 1 second, there is no sufficient time for blood to clot.

The simulation of the blood flow in valved veins is carried out with soft and rigid walls. Two different measures of the simulation results, the inlet flow rate and the flow rate difference between inlet and outlet, are shown in the Figure 6.12(a) and 6.12(b) throughout one cardiac cycle $t \in [1,2]$. There are two inferences to be drawn from the comparison of results in Figure 6.12. First, although the backflow is blocked by the closure of the valves, the tiny leakage of backflow still can be observed in Figure 6.12(a) from $t = 1.7$ to 1.8. It's because the proposed contact scheme imposes a small gap $\delta_{ck}$ between contact surfaces of valves during contact. Second, the valved veins' deformable walls vibrate at $t \approx 1.4$ and 1.8, and it is related to the pressure change and the closure of valves. It is clear to observe this phenomena in Figure 6.12(b).

### 6.4.2 Two connected valved veins

The blood flow in two connected venous segments is simulated with deformable and harder walls , respectively. The amplitude and mean pressure are selected as $p_{amp} = 50$ and $p_{mean} = 0$ in this section. In Figures 6.13, the contours of velocity magnitude and vorticity of simulation results are shown throughout one cardiac cycle $t \in [1,2]$. The computational domain is discretized into 30000 $(\mathbb{P}1b, \mathbb{P}1)$ elements, and time increment is chosen as $\delta t = 0.002$.

In addition to the inference in the previous section, we still place emphasis on the vortex generated by the friction of valves during the closure of valves. After the first cardiac cycle $t \in [0,1]$, the first dual vortex was generated and driven by the blood flow towards downstream, as shown in Figure 6.13. The magnitude of vorticity gradually decreased with respect to time, which stands for the energy dissipation of the vortex. Therefore, it is

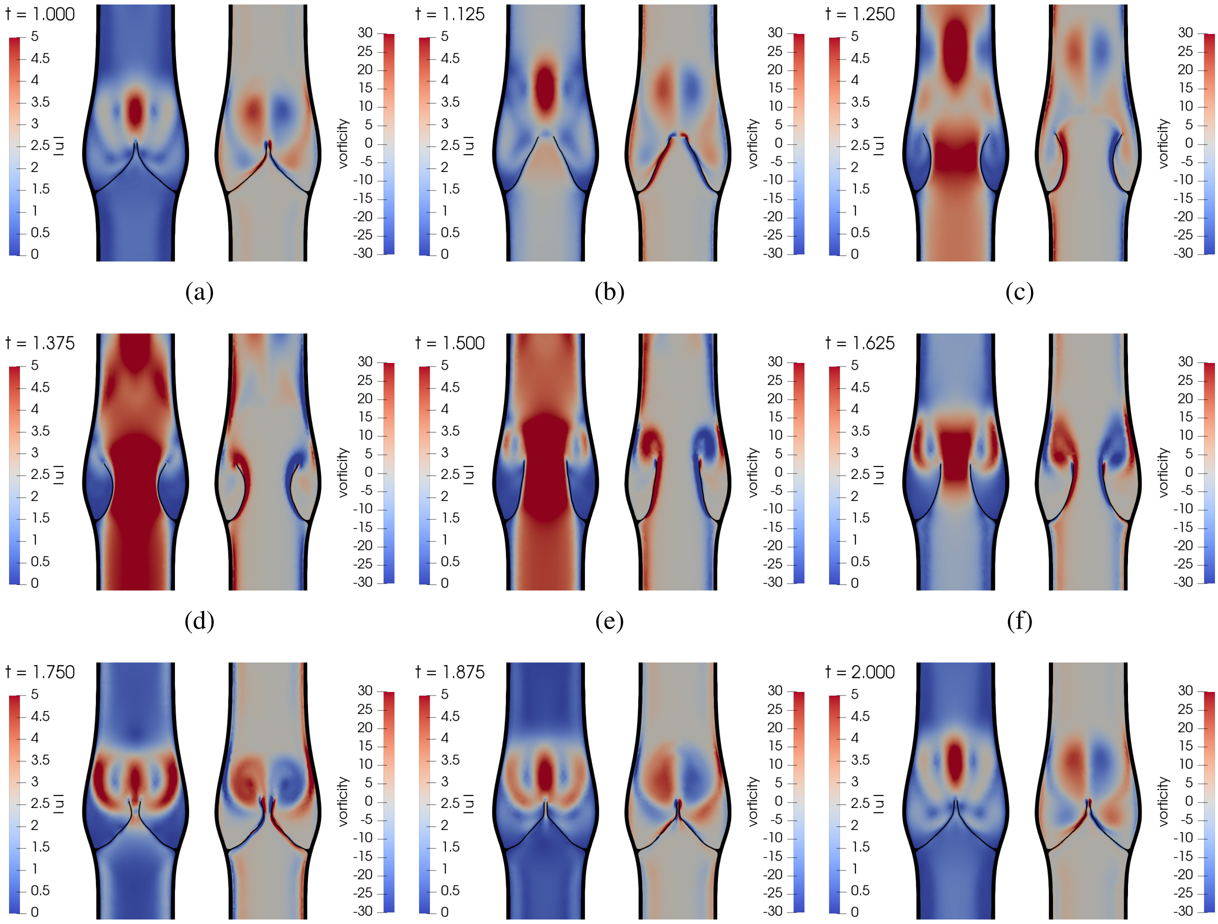

(a) (b) (c)

(d) (e) (f)

(g) (h) (i)

Figure 6.11: Velocity magnitude (left) and vorticity contours (right) of the simulation results in venous circuit are shown at (a) $t = 1.0$; (b) $t = 1.125$; (c) $t = 1.25$; (d) $t = 1.375$; (e) $t = 1.5$; (f) $t = 1.625$; (d) $t = 1.75$; (e) $t = 1.875$; (f) $t = 2.0$.

predictable to see the disappearance of the first dual vortex within few cardiac cycles.

In this numerical simulation case, the upper and lower valves simultaneously close to prevent reflux of blood, but it is possible to see the lag between the closure of upper and lower valves.

In this numerical test, we also carry out the numerical calculation with harder vascular walls, which is 10 times harder than the previous. As mentioned in the previous section, two different measures of the simulation results, the inlet flow rate and the flow rate difference between inlet and outlet, are shown in the Figure 6.14(a) and 6.14(b) throughout one cardiac cycle $t \in [1,2]$. We still can get the same inference from the comparison of results in Figure 6.14 : the tiny leakage of backflow and the vibration of the vascular wall due to the pressure change. Furthermore, the dilation and collapsion of vascular wall is almost absent in the case with harder wall.

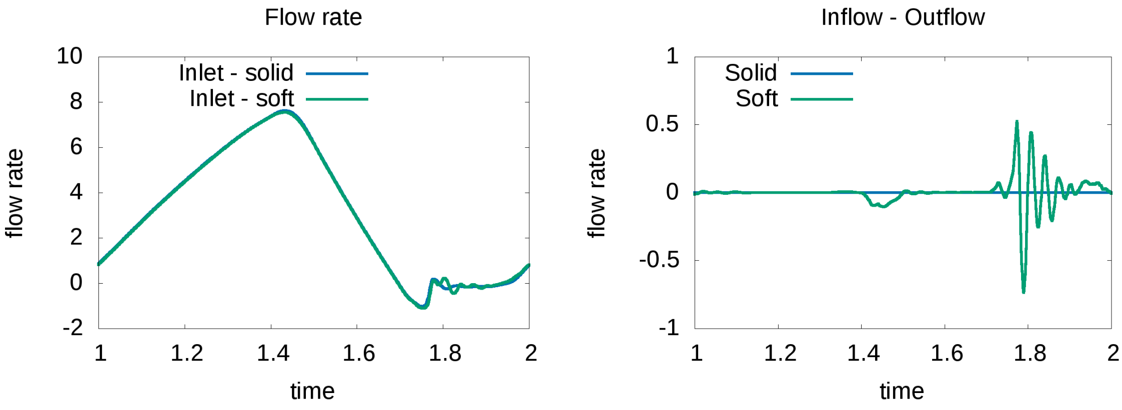

(a) (b)

Figure 6.12: Inlet flow rate and the difference of flow rate between inlet and outlet.

### 6.4.3 Network of valved veins in inferior limbs

To simplify the venous network in inferior limbs for the sake of modelling the simulation, the architecture proposed by Marc [198] in Figure 6.15 is taken into consideration. Superficial and deep veins are connected by perforating veins, and the blood flow in this venous architecture is from superficial to deep vein (from left to right) through the perforating vein and from distal to proximal segments (from bottom to top). In reality, there are many different properties between superficial and deep veins, such as bores, stiffness, and pressure difference. Normally, the deep veins are thicker and harder than the superficial veins, and the wall of the perforating veins is regarded as rigid since the perforating veins are embedded in the muscle.

In this numerical test, the wall's thickness and bore of the deep vein are selected to be identical to those of the superficial vein, but the deep veins' wall is four times harder than the superficial veins' wall. The ratio of bores between superficial and perforating veins is chosen to be $1 : 0.2$, and the wall is assumed to be rigid and undeformable for the perforating vein.

The blood flow in the proposed venous circuit is driven by the pressure difference between four inlets and outlets. To utilize the periodic function of pressure as boundary conditions, equation (6.4) is adopted, and we introduce three different values $P_{in} = 70$, $P_{out} = 70$, and $P_{cen} = 20$ to simplify the expression. The mean pressure is selected to be $p_{mean} = 0$ on every inlet and outlet. For the superficial vein, the amplitudes of pressure functions are chosen as $p_{amp} = P_{out}$ on the inlet and $p_{amp} = 0$ on the outlet. For the deep vein, the amplitudes of pressure functions are defined as $\frac{(P_{out}+P_{in})}{2} - P_{cen}$ on the inlet and $\frac{(P_{out}-P_{in})}{2} - P_{cen}$ on the outlet. With these boundary conditions, the pressure difference between inlet and outlet is $P_{in}$ in the deep vein and $P_{out}$ in the superficial vein. The pressure difference in the perforating vein is roughly $P_{cen}$. The computational domain is discretized into 85000 $(\mathbb{P}1b, \mathbb{P}1)$ elements, and the time increment is chosen as $\delta t = 0.002$.

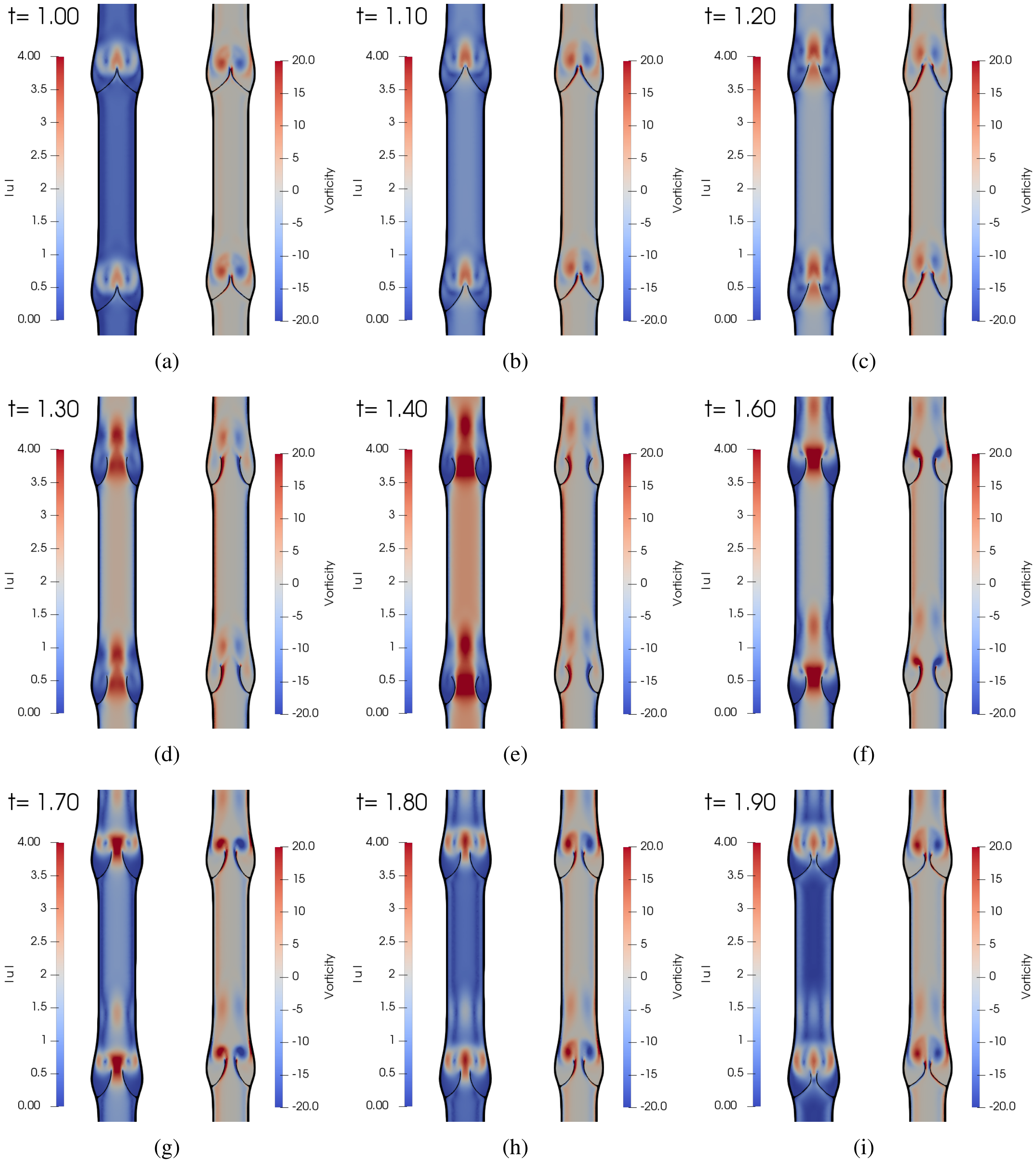

(a) (b) (c) (d) (e) (f) (g) (h) (i)

Figure 6.13: The contours of velocity magnitude (left) and vorticity (right) in two connected venous segments at (a) $t = 1.0$; (b) $t = 1.1$; (c) $t = 1.2$; (d) $t = 1.3$; (e) $t = 1.4$; (f) $t = 1.6$; (d) $t = 1.7$; (e) $t = 1.8$; (f) $t = 1.9$.

The blood flow is driven towards the predicted directions, and the velocity magnitude and vorticity contours of simulation results are shown in Figure 6.16. As mentioned in the

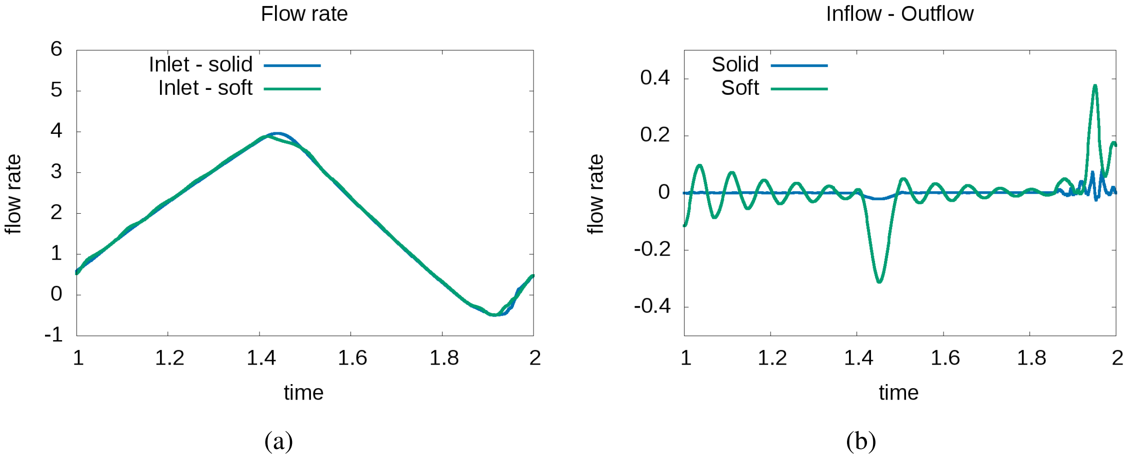

(a) (b)

Figure 6.14: Flow rate of inlet and the difference between inlet/outlet flow rate.

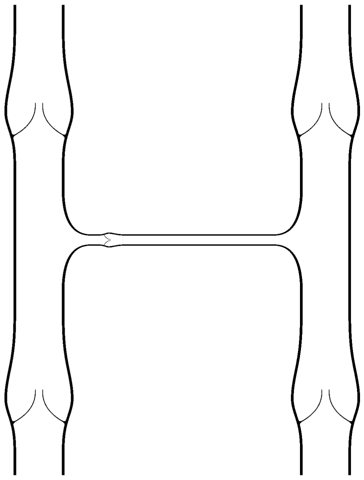

Figure 6.15: Geometry of the connected venous network. The rate of bores between superficial, deep, and perforating veins is 1 : 1 : 0.2

previous section, the first dual vortex was generated by the friction of valves and driven by the blood flow towards downstream in the superficial and deep veins, as shown in Figure 6.16. Then, the vortex gradually dissipated due to the friction. However, vortex pattern is absent in the perforating vein in this numerical test, because the local Reynolds number $Re_L = \frac{uL_p}{\nu} =\approx 0.2Re = 20$ is too low to generate small vortex in the perforating vein.

The flow rates and their difference on inlets are shown in Figure 6.17. One still can observe the vibration of vascular walls in the superficial vein as mentioned in section 6.4.1. The vibration is almost absent in the deep vein. The flow rate difference between inlet and outlet is plotted in Figure 6.17(b). The difference of flow rate in the superficial vein is because the blood flow is driven from the superficial to perforating vein. Therefore, the

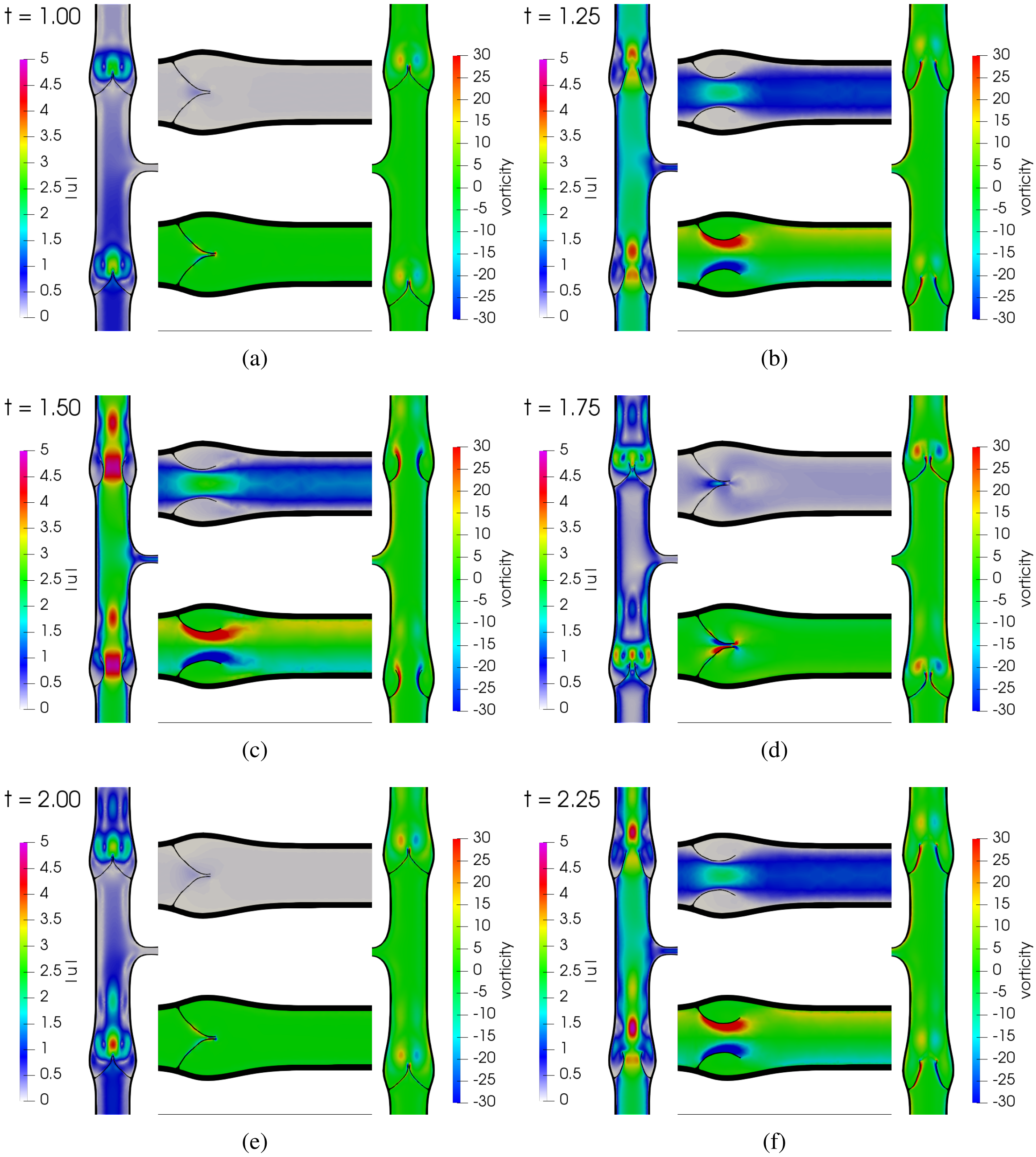

Figure 6.16: The predicted velocity magnitude (left and up) and vorticity contours (low and right) in venous circuit are shown at (a) $t = 1.0$; (b) $t = 1.25$; (c) $t = 1.5$; (d) $t = 1.75$; (e) $t = 2.0$; (f) $t = 2.25$.

tiny oscillation of the flow rate difference in deep veins is owing to the vibrating inflow from the perforating vein.

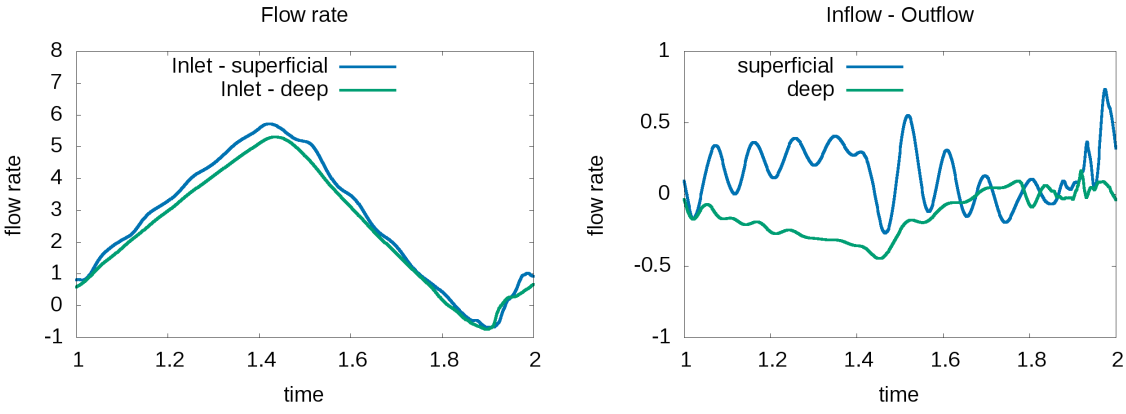

(a) (b)

Figure 6.17: Inlet flow rates and the flow rate difference between inlet and outlet.

# Conclusion, perspectives, and future work

This study aims to develop a numerical solver for general fluid–structure interaction problems, and the realistic implementation focuses on blood flow in valved veins. To simulate opening and closure of valves, it is required two numerical tools: a solver for fluid–structure coupling system and a contact scheme.

The first main contribution is the development of an Eulerian monolithic formulation for fluid–structure interaction problems, coupling of incompressible Newtonian fluid dynamics to incompressible, Mooney–Rivlin model, or compressible, $S^t$ Venant–Kirchhoff (STVK), hyperelastic solid mechanics. An implicit unconditionally stable monolithic finite element scheme based on characteristic Galerkin discretization is studied and proved with energy conservation, and proposed numerical scheme is validated and verified with benchmarks. The numerical results presented show the reliability of proposed Eulerian monolithic formulation for fluid–structure interaction problems.

The second main contribution is the development of a computational contact scheme to deal with problems involved contact. A contact scheme with Lagrange multiplier considering geometrical constrains of colliding bodies is proposed and easily implemented on proposed Eulerian monolithic formulation. Validation and verification of proposed contact scheme is done and compared with referenced results, and it also shows some advantages and drawbacks.

The third main contribution is the successful simulation of blood flow in valved veins with proposed numerical schemes and geometrical models. Blood flow in valved veins is studied under prescribed pressure function at inlet/outlet. Analysis of simulation results relies on contours of velocity magnitude and vorticity. Valves block reflux of blood, and direction of blood flow is from superficial to deep veins and from distal to proximal segments with random selection of pressure boundary condition on inlet/outlet

The main limitation of this study on application of blood flow in valved veins is the lack of experimental data especially on material properties and pressure boundary conditions. The present study shows the proposed solution algorithm is capable of solving the same problem with experimental data or patient–specific fact. Therefore, this study is mainly aimed to develop a stable numerical solver which is capable of solving general fluid–structure problems.

The second limitation is assumption and simplification of our 2D valved veins model.

Ignorance or substitution of force along semi-major axis for 2D modelling valvular dynamics introduces error and possibly leads to totally different results.

To implement the current study to simulate a 3D realistic problem, there are some works left. We can categorize future works into following 5 items:

**Contact scheme**

- contact scheme with friction
- stability analysis of proposed scheme

**Implementation of valved veins**

- coupled with 0D/1D cardiac models as boundary conditions
- patient–specific data
- simulation of 3D valved veins problem

To simulate 3D valved veins problem, the only problem is on computational effort because of considering large amount of elements, more than one million. That's the reason why we have to implement proposed algorithm in parallel with domain decomposition method, with library iHPDDM, but this work is still under progress. Furthermore, simulation results in 3D can help in modifying 2D simplified model.

# Appendices

# Appendix A

# Collapsible vessels

## Contents

Venous mechanical strength comes from three distinguishable layers in media. First layer contains longitudinal muscle fibers, interconnected with elastin fibrils and connective tissue. Middle layer contains wide bundles of smooth muscle cells in circular orientation separated by elastic fibrils. Outer later contains longitudinally- orientated muscle bundles and fibrous tissue.

Veins constitute the compliant compartment of the blood vessel network (vein compliance allows the blood volume to reside mainly – up to 70% – in the venous network). However, veins may experience changes both in cross–sectional area and shape when they are subjected to negative transmural pressures during natural or functional testing maneuvers, although $p$ is uniformly distributed in the entire cross section [62, 199]. The easier the collapse, the thinner the vessel wall or the more superficial from the skin the vessel path (deep thin–walled veins can be modeled by thick–walled vein–like tubes). The dynamics of the fluid are strongly coupled to the mechanics of the flexible vessel wall via the non–linear tube law, which relates $p$ to $A_i$ [200–204]. Tube loading can be such that contact occurs between the opposite walls at one point and, afterward with increasing loading, over a line. At slightly negative transmural pressures, any thin–walled flexible vessel is very compliant, small variations in transmural pressures inducing large changes in cross–sectional area. More details about collapsible tube are in section A.1.

## A.1 Flow in collapsible tubes and veins as example

The collapse is characterized by large variation in cross section $A_i$ under varying transmural pressures $p$, defined as the difference between the internal and the external pressures $p = p_i - p_e$. Studies in collapsible tubes were aimed at understanding the flow behavior in a deformable conduit. Such distinguishing conditions occur rarely in industrial applications but are very common in biological studies such as blood flow in veins and flow in airways

Complexity of flow in collapsible tubes is caused by fluid–structure interaction that gives rise to a state law, the nonlinear *tube law*, which relates $p_t$ to $A_i$.

In order to make the problem simplified and solvable decades ago, consequently, studies before 2D or 3D real model simulation attempted to model features of flow in collapsible tubes with lumped parameter models. Some early theoretical models were based on the assumption of a continuous variation in cross–sectional area without any change in circular shape, the effective cross–sectional area being equal to the collapsed tube at the same pressure, but the mechanical features of collapsible tubes as related to the contact between opposite walls were omitted under the assumption [205, 206]. For the most developed one–dimensional models, they assume the geometry of the flexible pipe is characterized by the cross–sectional area $A_i$ at the throat of the collapsed tube, which depends on the throat transmural pressure [207]. All the theoretical one–dimensional approaches mainly concentrated on limited dynamical aspects because of the complex behavior of the complicated interaction between tube and fluid. Varied types of models may be classified into three kinds:

1. models describing the steady flow;
2. models aimed at stability analysis;
3. models intended for oscillation analysis.

Most of above–mentioned properties of model arise from experimental observation.

## A.2 Starling resistor

Starling resistor is used for classical experiments on flow in collapsible tubes. Experiment equipment shown in Fig. A.1 includes a thin–walled compliant straight pipe (length $L$), fixed on rigid tubings at its ends and enclosed in a rigid transparent chamber with an adjustable chamber pressure $p_e$. The upstream end is connected to a constant–head supply reservoir via an upstream valve, and the downstream end drains the fluid out of the test segment via a possible downstream adjustable constriction. Both the inlet $p_{i1}$ and the outlet $p_{i2}$ internal pressures can be set at fixed values.

By controlling these three different pressure $p_e$, $p_{i1}$ and $p_{i2)}$ relationship between cross–sectional area $A_i$ and transmural pressure $p$ can be observed from the experimental data. Although there exist many validated techniques to measure the outer cross–sectional area at the throat of the thin–walled compliant straight pipe, most of them derive the inner cross–sectional area $A_i$ with the constant wall thickness. In order to avoid the error from

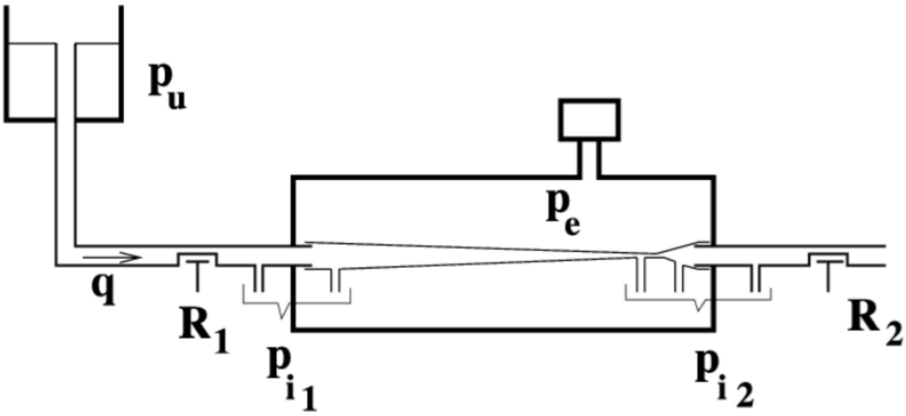

Figure A.1: The Starling resistance. Straight thin–walled flexible pipe mounted on rigid tubes at its ends and enclosed in a rigid transparent chamber The external pressure $p_e$ is adjustable. The flow rate $q$ is caused by the upstream pressure $p_u$. The internal pressures $p_i$ are measured at two stations: (1) either in the downstream segment of the entry rigid tube or in the entrance region of the floppy tube and (2) either more or less upstream from the compliant tube outlet or downstream from it. The results are strongly affected by the location of the pressure measurement sites. Local adjustable constrictions are sometimes added to the flow circuit upstream $R_1$ and downstream $R_2$ from the compliant tube.

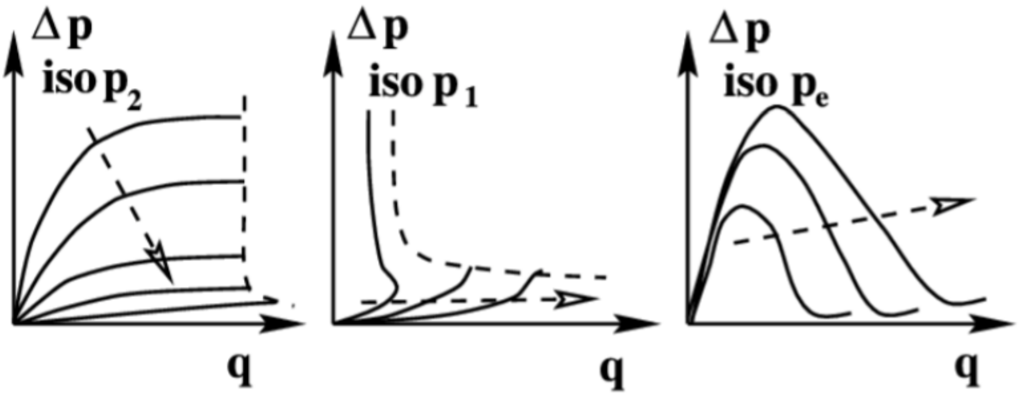

Figure A.2: Relationships between the pressure drop $\Delta p$ and the volume flow rate $q$ for a given constant outlet transmural pressure $p_2$(left) inlet transmural pressure $p_1$(mid), or external pressure $p_e$(right) in the Starling resistor. Dashed line arrows indicate an increase in constant–set algebraic pressure and dashed curves indicate the critical conditions $\Delta p - q$ curves in iso–$p_2$ conditions exhibit pressure drop limitation, flow limitation in iso–$p_1$ conditions, and negative resistance in iso–$p_e$ conditions.

measuring the cross–sectional area $A_i$, the experimental data presented below choose the volume flow rate $q$ as a concerned variable with the cross–sectional area $A_i$.

Experimental data is summarized in Fig. A.2, where $\Delta p = p_{i1} - p_{i2}$, $p_1 = p_{i1} - p_e$ and $p_2 = p_{i2} - p_e$. The detail of experimental setting is well arranged in [202, 208], and the

the Fig. A.2 is pretty clear to portrait the relationship between each variables. The results of this experiment include two critical characteristics. Firstly, it provides the relationship between the cross–sectional area $A_i$ and transmural pressure $p_e$. Secondly, it displays the instabilities (oscillations) that happens in the plateau region of the iso–$p_2$ curves and in the neighborhood of the maximal $q$ of the iso–$p_1$.

## A.3 Collapsible tube law

The unstressed cross–sectional shape of physiological vessels is commonly assumed to be elliptic (ellipticity $k_0$, Fig. A.3). The origin of the two–dimensional Cartesian system $(y,z)$ is located at the ellipse center, and the $x$–axis is along the tube center line with unit vector **i**. The origin of curvilinear abscissa $s$ along the mid–line for every cross–section of the tube wall locates at point $M_0$ of minimal curvature in the unstressed configuration which makes the distance between two opposite walls minimal during the tube deflection. At each point $M$ of the mid line, unit tangent **t**, unit normal **n**, and **i** define the local directed coordinate frame; $\theta$ as the oriented angle between the local horizontal axis and the tangent.

The hypotheses of the tube are listed after: (1) The infinitely long tube is supposed to be straight. (2) The tube wall is thin, homogeneous and purely elastic. (3) Both the geometry and mechanical properties are uniform. (4) $p$ is uniform around the collapsible tube. (5) The bending effects are assumed to be predominant. (6) The wall thickness must be much less than the lowest curvature radius of the wall mid line, namely $h_0(\frac{d\theta}{ds}) << 1$. (7) The wall thickness is assumed to remain constant during the collapse. (8) The mid–surface of wall is deformed without extension.

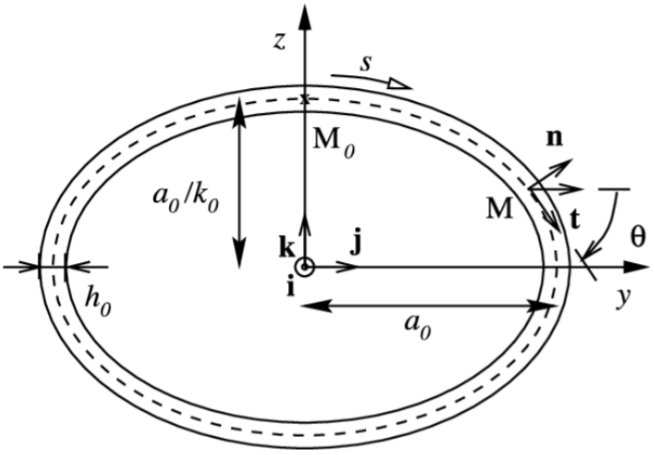

Figure A.3: Ellipticity.

The tube law $A(p)$, i.e. $A$ vs. $p$ relationship, depends mainly on: (1) tube geometry, (2) rheology, (3) prestresses, (4) vicinity loadings, (5) end effects, and (6) stress in the initial configuration (tension, bending). The main geometrical factors are the tube ellipticity $k_0$, and the wall thickness $h_0$. In the collapse, four characteristic transmural pressures are, at least, of interest:

1. Ovalization pressure $p_p$, for which the radius of curvature at mid–surface becomes locally infinite (oval–shaped cross–section with parallel opposite edges).

2. Stream division pressure $p_s$, the greatest pressure associated with two lateral peak velocities within the cross–section.

3. Point–contact pressure $p_c$, at which the opposite faces touch for the first time.

4. Line–contact pressure $p_l$, when the radius of curvature at the contact point becomes infinite.

Because of the different types of pressure load and contact reaction, there are three modes of collapse defined as: (1) **Mode 1**, the one mainly studied in the present work,, corresponds to the collapse before contact $(p_c < p \leq 0)$, characterized by a high tube compliance. The transversal density of the distributed external force $\mathbf{f}$ induced by the pressure load is given by $\mathbf{f} = p\mathbf{n}$. The resultant stress acting from one part of the wall to the other $\mathbf{c}(s)$ is continuous everywhere. (2) **Mode 2** is characterized by a contact at a single point $(p_l < p \leq p_c)$. The curvature at the contact point decreases from a finite value down to zero. A contact reaction appears (see below) and the resultant stress is discontinuous at the contact point $(s = 0)$. The contact generates a local reaction $r_c$ at the contact point $(s = 0)$, which increases when $p$ decreases from $p_c\,(\mathbf{r}_c = \mathbf{r}_{c0}(p_c))$ down to $p_l\,(\mathbf{r}_c = \mathbf{r}_{c0}(p_l))$(Fig. A.4). As soon as $p$ undergoes an infinitesimal decrease, say $p = p_{l-}$, the reaction initiates its splitting into two components $r_l(p_{l-}) = \frac{1}{2}r_{c0}(p_l)$. When $p < p_l$, the reaction is distributed along the contact segment of length $2s_c$, with maxima $r_l$(p) located at both ends of the contact segment $(s = \pm s_c)$. These points associated to concentrated force migrated laterally when $p$ continues to decrease, whereas the reaction amplitude exerted on the line of contact, which spreads out, decreases. (3) **Mode 3** is defined by a contact on a line segment $(p \leq p_l)$. The contact segment appears and lengthens, while the transmural pressure continues to decrease. Besides, the contact phenomenon at $p = p_l$ is displayed by a slight change in direction of the $A(p)$ curve. The contact reaction splits into two concentrated reactions applied at both ends of the contact segment $(s = \pm s_c)$, where $\mathbf{c}$ is discontinuous. The transversal force density $\mathbf{f}$ is thus given by either $\mathbf{f} = p$n along the open part of the cross–section or $\mathbf{f} = (r_d(s) + p)\mathbf{n}$ on the contact line $(r_d(s)$ : normal reaction distribution).

The contact reactions induce discontinuities in first and second derivatives of $A(p)$ at point– and line–contact pressures ( $(\partial A_i/\partial p)|_{p_c}$, $(\partial^2 A_i/\partial p^2)|_{p_l}$ ) [200, 202]. Such discontinuities affect probably the mechanical behavior of the fluid–tube couple, and the discontinuity in the first derivative at $p_c$ is exhibited by a break in the slope of the tube law [201]. The contract is not supposed to occur in the present investigation.

The tube deformation, from rest to the line–contact pressure $p_l$, is illustrated in Fig. A.5, using the dimensionless quantities $\tilde{p} = p/K$ and $\tilde{A}_i = A_i/A_{i_0}$. The bending stiffness $K$, used as the pressure scale, depends on the tube geometry and is proportional to the flexural

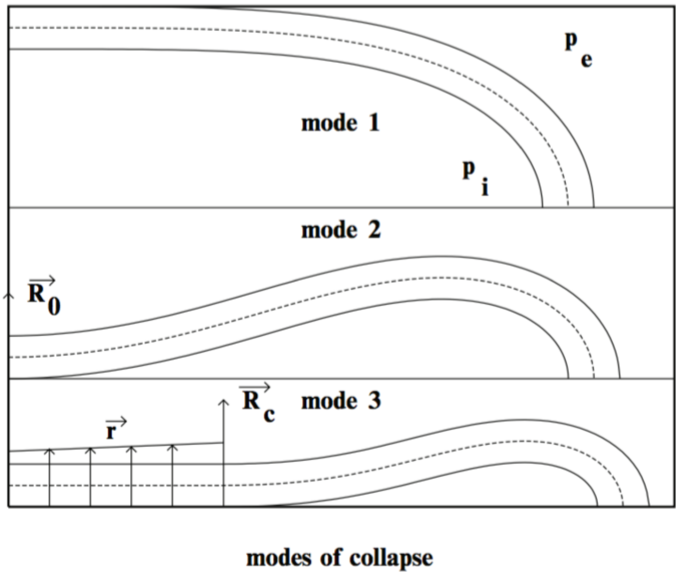

Figure A.4: The three collapse modes in the case $k_0 = 1.6$ and $h_0/a_0 = 0.1$: (**top**) $p_c < p \leq 0$, (**mid**) $p_l \leq p \leq p_c$ and (**bottom**) $p < p_l$. Reaction loading at contact between opposite walls of the flexible pipe ($\mathbf{R} \equiv \mathbf{r}_{c0}, \mathbf{R}_c \equiv \mathbf{r}_l, \mathbf{r} \equiv \mathbf{r}_d$):

$$\mathbf{r}_{c0}(p_c) \longrightarrow \mathbf{r}_{c0}(p_l) \xrightarrow{p<p_l} \begin{cases} \mathbf{r}_l(p) & s = s_c \\ \mathbf{r}_d(s,p) & 0 \leq s < s_c \end{cases}$$

rigidity $D = Eh_0^3/(12(1-\nu))$: $K = 2D/a_0^3$, where $E$ and $\nu$ are the Young modulus and the Poisson coefficient, respectively. Fig. A.5 demonstrates that the tube law is affected by the unstressed ellipticity. The speed scale $(K/\rho)^{1/2}$ is used to normalize the derived quantity $c$.

In the pressure range $p_l \leq p \leq 0$, any analytical expressions are very helpful in collapsible tube flow computations or experimental post–processing. Several expressions have been proposed, but they do not take into account the discontinuity of the tube law and its related physical phenomena. Analytical expressions must insure the continuity of the functions $c(p)$ and the critical flow rate $q*(p)$, except at the contact condition $p = p_c$, the $q*(p)$ curve being piecewise fitted from numerical data. Algebraic expressions based on integration of the critical flow curve use nine coefficients $(\{\kappa_i\}_{i=1}^{9})$ [209]. Relationships $\tilde{p}(\tilde{A})$ have been given for the description of the tube law in the first three pressure intervals:

$$\begin{aligned} \tilde{p} &= \kappa_1^2 \ln \tilde{A}_i - 2\kappa_1\kappa_2/\tilde{A}_i - \kappa_2^2/(2\tilde{A}_i^2 + \kappa_3), && \tilde{p}_l \leq \tilde{p} \leq \tilde{p}_c \\ \tilde{p} &= exp\{2\kappa_4\}\tilde{A}_i^{2(\kappa_5-1)}/2(\kappa_5 - 1) + \kappa_6, && \tilde{p}_c < \tilde{p} \leq \tilde{p}_p \\ \tilde{p} &= exp\{2\kappa_7\}\tilde{A}_i^{2(\kappa_8-1)}/2(\kappa_8 - 1) + \kappa_9, && \tilde{p}_p < \tilde{p} \leq 0 \end{aligned} \tag{A.1}$$

Variations with the tube ellipticity of the coefficients $\kappa_i(i = 1, \ldots, 3$ for the pressure range

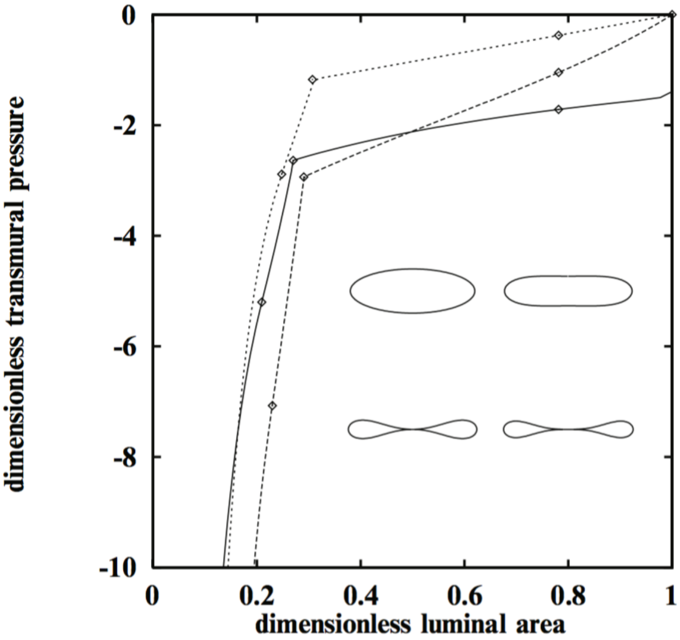

Figure A.5: Numerical $\tilde{p}(\tilde{A}_i)$ laws for three ellipticities $k_0 = 1.005$ (continuous line), 2.8 (dashed line), and 10 (dotted line), with the characteristic values ($\diamond$) corresponding to the displayed characteristic shapes (unstressed elliptical, oval–shaped, point– and line–contact).

$[\tilde{p}_l, \tilde{p}_c]$ ( collapse mode 2 ), $i = 4, ..., 6$ for $[\tilde{p}_c, \tilde{p}_p]$ ( collapse mode 1 ), and $i = 7, ..., 9$ for $[\tilde{p}_p, 0]$ ( collapse mode 1 ) of the analytical generalized tube law (Equation A.1) are given in [198].

## A.4 Main Results

Derivations in [210,211], further studies of section A.2, are about the dynamical system analysis for flow in collapsible tubes and Starling resistor. Results of flow in collapsible with well posed conditions exhibit of low (2–6 Hz), intermediate, and high frequency (over 60 Hz) oscillation, and of small noise–like fluctuations. The data in experiments and simuluations of flow in collapsible tubes include aperiodic oscillatory operating points which may indicate the presence of chaos [210]. Self–excited oscillation applied on the model of collapsible–tube flow is investigated numerically the response of forced oscillation to a limit–cycle oscillation [211].

One of characteristic problems related to collapsible–tube flow is studied in [212,213]. A two–dimension solid tube embedded with a flexible membrane is considered as a model to simulate the transition between laminar and turbulent flow. It's essential to emphasize that the transient phenomena is difficulty of collapsible tube flow mentioned at the beginning.

Other corresponding studies [57, 214] is summarized here. Different collapse mode for cylindrical vessels is studied in [57]. In [214], audible wheezing is usually associated with an airway that is partially collapsed or flattened. Air flow coupled with this flattened flexible conduit produce vibrations, and it's called fluid–dynamic flutter.

# Appendix B

# Summation of proposed monolithic formulation

## Contents

---

To abbreviate and clarify contents of derivation and proof, we only deal with proposed monolithic fomulation with 3D incompressible Mooney–Rivlin model at previous chapter.

Since two types of hyperelastic solid model are considered in this study, proposed monolithic formulation with various solid model are summarized in this chapter with time and spacial discretization in this section.

## B.1 Incompressible solid : Mooney–Rivlin model

### B.1.1 2D formulation

$$
\begin{aligned}
&\int_{\Omega^{n+1}} \left( \rho^{n+1} \frac{\mathbf{u}_h^{n+1} - \mathbf{u}_h^{n} \circ \mathbb{Y}^{n+1}}{\delta t} \cdot \hat{\mathbf{u}}_h - p_h^{n+1} \nabla \cdot \hat{\mathbf{u}}_h - \hat{p}_h \nabla \cdot \mathbf{u}_h^{n+1} \right) + \int_{\Omega_f^{n+1}} \frac{\mu}{2} \mathbf{D}\mathbf{u}_h^{n+1} : \mathbf{D}\hat{\mathbf{u}}_h \\
&\quad + \delta t \int_{\Omega_s^{n+1}} c_1 \left( \mathbf{D}\mathbf{u}_h^{n+1} - \nabla \mathbf{u}_h^{n+1} \nabla^T \tilde{\mathbf{d}}_h^{n} - \nabla \tilde{\mathbf{d}}_h^{n} \nabla^T \mathbf{u}_h^{n+1} \right) : \mathbf{D}\hat{\mathbf{u}}_h \\
&\quad + \int_{\Omega_s^{n+1}} c_1 \left( \mathbf{D}\tilde{\mathbf{d}}_h^{n} - \nabla \tilde{\mathbf{d}}_h^{n} \nabla^T \tilde{\mathbf{d}}_h^{n} \right) : \mathbf{D}\hat{\mathbf{u}}_h = \int_{\Omega_t} \mathbf{f} \cdot \hat{\mathbf{u}}_h \\
&\quad \Omega^{n+1} = \left( \mathbb{Y}^{n+1} \right)^{-1} (\Omega_n) = \left\{ x \colon \mathbb{Y}^{n+1}(x) \in \Omega_n \right\}. \\
&\quad \mathbf{d}_h^{n+1} = \tilde{\mathbf{d}}_h^{n} + \delta t \mathbf{u}_h^{n+1}
\end{aligned}
\tag{B.1}
$$

where $\tilde{\mathbf{d}}^n$ stands for $\mathbf{d}^n(\mathbb{Y}^{n+1})$ and where $\mathbf{d}^n$ is updated by

$$
\mathbf{d}^{n+1} = \mathbf{d}^n \circ \mathbb{Y}^{n+1} + \delta t \mathbf{u}^{n+1} \tag{B.2}
$$

### B.1.2 3D formulation

$$
\begin{aligned}
&\int_{\Omega^{n+1}} \left( \rho^{n+1} \frac{\mathbf{u}_h^{n+1} - \mathbf{u}_h^{n} \circ \mathbb{Y}^{n+1}}{\delta t} \cdot \hat{\mathbf{u}}_h - p_h^{n+1} \nabla \cdot \hat{\mathbf{u}}_h - \hat{p}_h \nabla \cdot \mathbf{u}_h^{n+1} \right) + \int_{\Omega_f^{n+1}} \frac{\mu}{2} \mathbf{D}\mathbf{u}_h^{n+1} : \mathbf{D}\hat{\mathbf{u}}_h \\
&\quad + \delta t \int_{\Omega_s^{n+1}} \left[ 2a_1 \left( \mathbf{D}\mathbf{u}_h^{n+1} - \nabla \mathbf{u}_h^{n+1} \nabla^T \tilde{\mathbf{d}}_h^{n} - \nabla \tilde{\mathbf{d}}_h^{n} \nabla^T \mathbf{u}_h^{n+1} \right) \left( \mathbf{D}\tilde{\mathbf{d}}_h^{n} - \nabla \tilde{\mathbf{d}}_h^{n} \nabla^T \tilde{\mathbf{d}}_h^{n} \right) \right. \\
&\qquad\qquad \left. + a_2^{n+1} \left( \mathbf{D}\mathbf{u}_h^{n+1} - \nabla \mathbf{u}_h^{n+1} \nabla^T \tilde{\mathbf{d}}_h^{n} - \nabla \tilde{\mathbf{d}}_h^{n} \nabla^T \mathbf{u}_h^{n+1} \right) \right] : \mathbf{D}\hat{\mathbf{u}}_h \\
&\quad + \int_{\Omega_s^{n+1}} \left[ a_1 \left( \mathbf{D}\tilde{\mathbf{d}}_h^{n+1} - \nabla \tilde{\mathbf{d}}_h^{n} \nabla^T \tilde{\mathbf{d}}_h^{n} \right)^2 + a_2^{n+1} \left( \mathbf{D}\tilde{\mathbf{d}}_h^{n} - \nabla \tilde{\mathbf{d}}_h^{n} \nabla^T \tilde{\mathbf{d}}_h^{n} \right) \right] : \mathbf{D}\hat{\mathbf{u}}_h = \int_{\Omega_t} \mathbf{f} \cdot \hat{\mathbf{u}}_h \\
&\quad \Omega^{n+1} = \left( \mathbb{Y}^{n+1} \right)^{-1} (\Omega_n) = \left\{ x \colon \mathbb{Y}^{n+1}(x) \in \Omega_n \right\}. \\
&\quad \mathbf{d}_h^{n+1} = \tilde{\mathbf{d}}_h^{n} + \delta t \mathbf{u}_h^{n+1}
\end{aligned}
\tag{B.3}
$$

with

$$
a_1 := c_1, \quad a_2 := \frac{c_1}{2} \left( \mathrm{tr}_{\mathbf{B}}^2 - \mathrm{tr}_{\mathbf{B}^2} - 4 \right) - 2c_2
$$

where $\tilde{\mathbf{d}}^n$ stands for $\mathbf{d}^n(\mathbb{Y}^{n+1})$ and where $\mathbf{d}^n$ is updated by

$$
\mathbf{d}^{n+1} = \mathbf{d}^n \circ \mathbb{Y}^{n+1} + \delta t \mathbf{u}^{n+1} \tag{B.4}
$$

## B.2 Compressible solid : S$^{\mathrm{t}}$–Venant–Kirchhoff model

### B.2.1 2D formulation

$$\begin{aligned}
&\int_{\Omega^{n+1}} \rho^{n+1} \frac{\mathbf{u}_h^{n+1} - \mathbf{u}_h^n \circ \mathbb{Y}^{n+1}}{\delta t} \cdot \hat{\mathbf{u}}_h + \int_{\Omega_f^{n+1}} \left( -p^{n+1} \nabla \cdot \hat{\mathbf{u}} - \hat{p} \nabla \cdot \mathbf{u} + \frac{\mu}{2} \mathbf{D} \mathbf{u}^{n+1} : \mathbf{D} \hat{\mathbf{u}} \right) \\
&\quad + \delta t \int_{\Omega_s^{n+1}} \frac{\beta^{n+1}}{2} \left( \mathbf{D} \mathbf{u}^{n+1} - \nabla \mathbf{u}^{n+1} \nabla^T \tilde{\mathbf{d}}^n - \nabla \tilde{\mathbf{d}}^n \nabla^T \mathbf{u}^{n+1} \right) : \mathbf{D} \hat{\mathbf{u}} \\
&\quad + \int_{\Omega_s^{n+1}} \left[ \frac{\beta^{n+1}}{2} \left( \mathbf{D} \tilde{\mathbf{d}}^n - \nabla \tilde{\mathbf{d}}^n \nabla^T \tilde{\mathbf{d}}^n \right) : \mathbf{D} \hat{\mathbf{u}} + \alpha^{n+1} \nabla \cdot \hat{\mathbf{u}} \right] = \int_{\Omega^{n+1}} \mathbf{f} \cdot \hat{\mathbf{u}}
\end{aligned}$$

with

$$\begin{cases} \alpha = \frac{\lambda_s}{2} \left( \mathrm{tr}_{\mathbf{B}} - 2 \right) \left( \mathrm{tr}_{\mathbf{B}} - J^2 \right) + \mu_s \mathrm{tr}_{\mathbf{B}} \left( \mathrm{tr}_{\mathbf{B}} - J^2 - 1 \right) \\ \beta = \frac{\lambda_2}{2} \left( \mathrm{tr}_{\mathbf{B}} - 2 \right) + \mu_s \left( \mathrm{tr}_{\mathbf{B}} - 1 \right) J^2 \end{cases} \tag{B.5}$$

### B.2.2 3D formulation

$$\begin{aligned}
&\int_{\Omega^{n+1}} \rho^{n+1} \frac{\mathbf{u}_h^{n+1} - \mathbf{u}_h^n \circ \mathbb{Y}^{n+1}}{\delta t} \cdot \hat{\mathbf{u}}_h + \int_{\Omega_f^{n+1}} \left( -p^{n+1} \nabla \cdot \hat{\mathbf{u}} - \hat{p} \nabla \cdot \mathbf{u} + \frac{\mu}{2} \mathbf{D} \mathbf{u}^{n+1} : \mathbf{D} \hat{\mathbf{u}} \right) \\
&\quad + \delta t \int_{\Omega_s^{n+1}} \Big[ \gamma^{n+1} \left( \mathbf{D} \mathbf{u}^{n+1} - \nabla \mathbf{u}^{n+1} \nabla^T \tilde{\mathbf{d}}^n - \nabla \tilde{\mathbf{d}}^n \nabla^T \mathbf{u}^{n+1} \right) \left( \mathbf{D} \tilde{\mathbf{d}}^n - \nabla \tilde{\mathbf{d}}^n \nabla^T \tilde{\mathbf{d}}^n \right) \\
&\qquad + \frac{\beta^{n+1}}{2} \left( \mathbf{D} \mathbf{u}^{n+1} - \nabla \mathbf{u}^{n+1} \nabla^T \tilde{\mathbf{d}}^n - \nabla \tilde{\mathbf{d}}^n \nabla^T \mathbf{u}^{n+1} \right) \Big] : \mathbf{D} \hat{\mathbf{u}} \\
&\quad + \int_{\Omega_s^{n+1}} \left[ \frac{\gamma^{n+1}}{2} \left( \mathbf{D} \tilde{\mathbf{d}}^n - \nabla \tilde{\mathbf{d}}^n \nabla^T \tilde{\mathbf{d}}^n \right)^2 : \mathbf{D} \hat{\mathbf{u}} + \frac{\beta^{n+1}}{2} \left( \mathbf{D} \tilde{\mathbf{d}}^n - \nabla \tilde{\mathbf{d}}^n \nabla^T \tilde{\mathbf{d}}^n \right) : \mathbf{D} \hat{\mathbf{u}} + \alpha^{n+1} \nabla \cdot \hat{\mathbf{u}} \right] \\
&\quad = \int_{\Omega^{n+1}} \mathbf{f} \cdot \hat{\mathbf{u}}
\end{aligned}$$

with

$$\begin{cases} \alpha = \frac{\lambda_s}{4} \left( \mathrm{tr}_{\mathbf{B}} - 3 \right) \left( 2\mathrm{tr}_{\mathbf{B}} - \mathrm{tr}_{\mathbf{B}}^2 + \mathrm{tr}_{\mathbf{B}^2} + 2J^2 \right) + \frac{\mu_s}{2} \mathrm{tr}_{\mathbf{B}} \left( 2\mathrm{tr}_{\mathbf{B}} + \mathrm{tr}_{\mathbf{B}^2} - \mathrm{tr}_{\mathbf{B}}^2 - 2 + 2J^2 \right) \\ \beta = \frac{\lambda_s}{4} \left( \mathrm{tr}_{\mathbf{B}} - 3 \right) \left( \mathrm{tr}_{\mathbf{B}}^2 - \mathrm{tr}_{\mathbf{B}^2} - 4J^2 \right) + \frac{\mu_s}{2} \left( \mathrm{tr}_{\mathbf{B}}^3 - \mathrm{tr}_{\mathbf{B}} \mathrm{tr}_{\mathbf{B}^2} - \mathrm{tr}_{\mathbf{B}}^2 + \mathrm{tr}_{\mathbf{B}^2} + 2J^2 - 4\mathrm{tr}_{\mathbf{B}} J^2 \right) \\ \gamma = \frac{\lambda_s}{2} \left( \mathrm{tr}_{\mathbf{B}} - 3 \right) J^2 + \mu_s \left( \mathrm{tr}_{\mathbf{B}} - 1 \right) J^2 \end{cases}$$

# Appendix C

# Domain decomposition methods

## Contents

Parallel computing is getting more and more important in this decade. For scientific computing, it becomes more and more important to develop parallel algorithms to shorten computational time so as to study more complicated problems. Domain decomposition methods is one way to parallelize linear algebra solvers. This chapter introduces the concept of domain decomposition method, and more details of its analysis can be found in [120, 215]. Additionally, all contents in this chapter are implemented in library *HPDDM* (High-performance domain decomposition methods), an available plug-in *FreeFem++* library.

To make contents more clear and understandable, Poisson equation is considered as an example in this whole chapter. In first section, four different Schwarz methods are present and compared with their solution algorithms and algebraic forms. Second, Krylov method is introduced to solve linear systems, and the discussion of scalability and preconditioners is presented.

## C.1 Schwarz method

### C.1.1 Preliminary: original Schwarz method

Consider the Poisson problem witch consists of finding $u : \Omega \to \mathbb{R}$ such that

$$\begin{cases} -\Delta(u) = f & \text{in } \Omega \\ u = 0 & \text{on } \partial\Omega \end{cases} \tag{C.1}$$

Computational domain $\Omega$ can be divided into $\Omega_1$ and $\Omega_2$ with/without overlapping.

**Definition C.1** (Original Schwarz algorithm)**.** The Schwarz algorithm is an iterative method based on solving subproblems alternatively in domains $\Omega_1$ and $\Omega_2$. It updates $\left(u_1^n, u_2^n\right) \to \left(u_1^{n+1}, u_2^{n+1}\right)$ by

$$\begin{cases} -\Delta\left(u_1^{n+1}\right) = f & \text{in } \Omega_1 \\ u_1^{n+1} = 0 & \text{on } \partial\Omega_1 \cap \partial\Omega \\ u_1^{n+1} = u_2^n & \text{on } \partial\Omega_1 \cap \overline{\Omega_2} \end{cases} \quad \textit{then}, \quad \begin{cases} -\Delta\left(u_2^{n+1}\right) = f & \text{in } \Omega_2 \\ u_2^{n+1} = 0 & \text{on } \partial\Omega_2 \cap \partial\Omega \\ u_2^{n+1} = u_1^{n+1} & \text{on } \partial\Omega_2 \cap \overline{\Omega_1} \end{cases} \tag{C.2}$$

Convergence of the algorithm is proved by Schward, but the algorithm still sequentially solves one subproblem by one subproblem. With a minor change of the algorithm, each subproblem becomes independent from each other at any iteration step, and convergence can be proved with the maximum principle.

It is required to define extension operators and a partition of unity to reconstruct algorithms with a global function instead of functions defined at each subdomain.

**Definition C.2** (Extension operators and a partition of unity)**.** Let $E_i$ be the extension operator such that $E_i(\omega_i) : \Omega \to \mathbb{R}$ is the extension of a function $\omega_i : \Omega_i \to \mathbb{R}$ and zero outside $\Omega_i$. One can also define the partition of unity function $\chi_i : \Omega_i \to \mathbb{R}$, $\chi_i \geq 0$, and $\chi_i(x) = 0$ for $x \in \partial\Omega_i \setminus \partial\Omega$ and such that

$$\omega = \sum_{i=1}^{2} E_i(\chi_i \omega_i) \tag{C.3}$$

for any function $\omega : \Omega \to \mathbb{R}$

#### Block Jacobi algorithm

From a linear algebra point of view, Schwarz algorithm is a variant of block Jacobi algorithm. A linear system $A\mathbf{U} = \mathbf{F}$ with a matrix $A$ of size $m \times m$, a right-hand side $\mathbf{F} \in \mathbb{R}^m$, and a solution $\mathbf{U} \in \mathbb{R}^m$, where $m$ is a non-zero integer. The set of indices $\{1, ..., m\}$ is partitioned into two sets

$$\mathcal{N}_1 := \{1, ..., m_s\} \text{ and } \mathcal{N}_2 := \{m_s + 1, ..., m\}$$

Let $\mathbf{U}_1 := (U_k)_{k\in\mathcal{N}_1} := \mathbf{U}_{|\mathcal{N}_1}$, $\mathbf{U}_2 := (U_k)_{k\in\mathcal{N}_2} := \mathbf{U}_{|\mathcal{N}_2}$ and similarly $\mathbf{F}_1 := \mathbf{F}_{|\mathcal{N}_1}$, $\mathbf{F}_2 := \mathbf{F}_{|\mathcal{N}_2}$. The linear system has the following block form:

$$\begin{pmatrix} A_{11} & A_{12} \\ A_{21} & A_{22} \end{pmatrix} \begin{pmatrix} \mathbf{U}_1 \\ \mathbf{U}_2 \end{pmatrix} = \begin{pmatrix} \mathbf{F}_1 \\ \mathbf{F}_2 \end{pmatrix}, \tag{C.4}$$

where $A_{ij} := A_{|\mathcal{N}_i\times\mathcal{N}_j}$, $1 \le i,j \le 2$

**Definition C.3** (Block Jacobi algorithm)**.** The block Jacobi algorithm reads as

$$\begin{pmatrix} A_{11} & 0 \\ 0 & A_{22} \end{pmatrix} \begin{pmatrix} \mathbf{U}_1^{n+1} \\ \mathbf{U}_2^{n+1} \end{pmatrix} = \begin{pmatrix} A_{11} & 0 \\ 0 & A_{22} \end{pmatrix} \begin{pmatrix} \mathbf{U}_1^{n} \\ \mathbf{U}_2^{n} \end{pmatrix} + \begin{pmatrix} \mathbf{F}_1 \\ \mathbf{F}_2 \end{pmatrix} - A \begin{pmatrix} \mathbf{U}_1^{n} \\ \mathbf{U}_2^{n} \end{pmatrix} \tag{C.5}$$

or equivalently as

$$\begin{pmatrix} A_{11} & 0 \\ 0 & A_{22} \end{pmatrix} \begin{pmatrix} \mathbf{U}_1^{n+1} \\ \mathbf{U}_2^{n+1} \end{pmatrix} = \begin{pmatrix} \mathbf{F}_1 - A_{12}\mathbf{U}_2^{n} \\ \mathbf{F}_2 - A_{21}\mathbf{U}_1^{n} \end{pmatrix} \tag{C.6}$$

**Definition C.4** (Restriction operator)**.** We introduce $R_i$ as the restriction operator from $\mathcal{N}_i$ into $\mathcal{N}$ and $A_{ii} = R_i A R_i^T$

**Definition C.5** (Compact form of the block Jacobi algorithm)**.** The algorithm C.5 can be rewritten as

$$\mathbf{U}^{n+1} = \mathbf{U}^{n} + \sum_{i=1}^{\mathcal{N}} \left( R_i^T \left( R_i A R_i^T \right)^{-1} R_i \right) \mathbf{r}^n \tag{C.7}$$

where $\mathbf{r}^n = \mathbf{F} - A\mathbf{U}^n$ is the residual for the equation.

we can recast the definition C.5 into

$$\mathbf{U}^{n+1} = \mathbf{U}^{n} + M_{BJ}\mathbf{r}^n$$

where $M_{BJ} = \sum_{i=1}^{\mathcal{N}} \left( R_i^T \left( R_i A R_i^T \right)^{-1} R_i \right)$. For each Schwarz algorithm, the corresponding matrix is derived.

**Definition C.6** (Algebraic partition of unity)**.** At the discrete level, the main ingredients of the partition of unity are

1. a set of indices of degree of freedom $\mathcal{N}$ and a decomposition into $N$ subsets $\mathcal{N} = \bigsqcup_{i=1}^{N} \mathcal{N}_i$ is needed;

2. a vector $\mathbf{U} \in \mathbb{R}^{\#\mathcal{N}}$;

3. the restriction of a vector $\mathbf{U} \in \mathbb{R}^{\#\mathcal{N}}$ to a subdomain $\Omega_i$, $1 \le i \le N$, which can be expressed as $R_i\mathbf{U}$ where $R_i$ is a rectangular $\#\mathcal{N} \times \#\mathcal{N}$ Boolean matrix (the extension operator will be the transpose matrix $R_i^T$);

4. the partition of unity "function" at the discrete level which corresponds to diagonal matrics of size $\#\mathcal{N} \times \#\mathcal{N}$ with non-negative entries such that for all vectors $\mathbf{U} \in \mathbb{R}^{\#\mathcal{N}}$

$$\mathbf{U} = \sum_{i=1}^{N} R_i^T D_i R_i \mathbf{U}$$

or in other words

$$\mathbf{I}_d = \sum_{i=1}^{N} R_i^T D_i R_i \tag{C.8}$$

where $\mathbf{I}_d \in \mathbb{R}^{\#\mathcal{N} \times \#\mathcal{N}}$ is the identity matrix.

Three different Schwarz algorithms are introduced in the following sections with their solution algorithms and their matrix forms.

### C.1.2 Additive Schwarz method

Local correcting function at each subdomain is summed up directly to calculate the global correcting function with extension operators. The corresponding correcting matrix is equal to

$$M_{ASM} = \sum_{i=1}^{\mathcal{N}} \left( R_i^T \left( R_i A R_i^T \right)^{-1} R_i \right). \tag{C.9}$$

---

**Algorithm C.1** ASM algorithm at the continuous level

1. Compute the residual $r^n : \Omega \to \mathbb{R}$:

$$r^n := f + \Delta \left( u^n \right).$$

2. For $i = 1, ..., \mathcal{N}$, solve for a local correction $v_i^n$:

$$-\Delta \left( v_i^n \right) = r^n \text{ in } \Omega_i \text{ , } v_i^n = 0 \text{ on } \partial \Omega_i.$$

3. Update $u^{n+1}$:

$$u^{n+1} = u^n + \sum_{i=1}^{\mathcal{N}} E_i \left( v_i^n \right)$$

---

### C.1.3 Restricted additive Schwarz method

This method is equivalent to the Schwarz method. With a partition of unity, variable can be updated more correctly on overlapping region. The corresponding correcting matrix equals

$$M_{RAS} = \sum_{i=1}^{\mathcal{N}} \left( R_i^T D_i \left( R_i A R_i^T \right)^{-1} R_i \right). \tag{C.10}$$

---

**Algorithm C.2** RAS algorithm at the continuous level

---

1. Compute the residual $r^n : \Omega \to \mathbb{R}$:

$$r^n := f + \Delta(u^n).$$

2. For $i = 1, ..., \mathcal{N}$, solve for a local correction $v_i^n$:

$$-\Delta(v_i^n) = r^n \text{ in } \Omega_i, \; v_i^n = 0 \text{ on } \partial\Omega_i.$$

3. Update $u^{n+1}$:

$$u^{n+1} = u^n + \sum_{i=1}^{\mathcal{N}} E_i(\chi_i v_i^n)$$

---

### C.1.4 Optimized restricted additive Schwarz method

Instead of Dirichlet bondary conditions, Robin boundary conditions are implemented as the transmission conditions at interfaces between subdomains in optimized restricted additive Schwarz method proposed by P. Lions at 1990. It is practically applied to both overlapping and nonoverlapping subdomains. With $\alpha$ and $\eta$ being positive constants, it is crucial to point out that stiffness is modified at interface because of Robin conditions. The corresponding correcting matrix equals

$$M_{ORAS} = \sum_{i=1}^{\mathcal{N}} \left( R_i^T D_i V_i^n \right) \quad \text{, where } A_{i,Robin} V_i^n = R_i r^n \tag{C.11}$$

where $A_{i,Robin} = K_i + B_j^T \alpha M_{\Gamma_{ij}} B_i$ are local $\eta - \Delta$ operators along with the interface conditions $\partial_n + \alpha$ at discretizing level. $K_i$ is a local matrix as a combination of the stiffness and mass matrices, and $M_{\Gamma_{ij}}$ is the interface mass matrix $M_{\Gamma_{ij}} v_i^n = \int_{\Gamma_{ij}} v_i^n \hat{v} d\Gamma$ with the test function $\hat{v}$. $B_i$ is the discrete trace operator which is just the Boolean matrix corresponding to the decomposition and they can extract every boundary degree of freedom.

Robin boundary condition is not the most general interface condition. Rather than giving the general conditions in a priori form, it is possible to derive them so as to have the fastest convergence. It's established the existence of interface conditions which are optimal in terms of iteration counts.

To sum up, ORAS methods apply Robin boundary conditions at interfaces. It is possible to to achieve the fastest convergence with the optimal selection of positive coefficient

**Algorithm C.3** ORAS algorithm at the continuous level

```
1. Compute the residual $r^n : \Omega \to \mathbb{R}$:
       $r^n := f - (\eta - \Delta)(u^n)$.
2. For $i = 1, ..., \mathcal{N}$, solve for a local correction $v_i^n$:
       $(\eta - \Delta)(v_i^n) = r^n$   in   $\Omega_i$,
       $v_i^n = 0$   on   $\partial\Omega_i \cup \partial\Omega$,
       $\left(\frac{\partial}{\partial \mathbf{n}_i} + \alpha\right)(v_i^n) = 0$   on   $\partial\Omega_i / \partial\Omega$
3. Update $u^{n+1}$:
       $u^{n+1} = u^n + \sum_{i=1}^{\mathcal{N}} E_i(\chi_i v_i^n)$
```

$\alpha$. Besides Poisson equation, it is feasible to derive a different and optimized coefficient for each distinct equation. Additionally, coefficient $\alpha$ is not unique for each equation. So, users can derive a value to adapt user–proposed scheme. For a further study, one can refer to book [120].

## C.2 Krylov method – GMRES method

After decomposing the computational domain, we consider subproblems at each subdomain instead of the global problem. A linear algebra solver is required to solve linear system constructed by discretizing a weak formulation for each subproblem.

In this section, one Krylov method, Generalized Minimal RESidual (GMRES) method, is introduced to solve an asymmetric linear system with domain decomposition methods as preconditioners.

In *minimal residual method*, an iterative algorithm is proposed to minimize the Euclidean norm of the residual, but the linear system gradually becomes ill-conditioned due to the selected basis without a particular structure.

To make the system easy to solve, the GMRES method adapts the Gram–Schmidt orthogonalization of the basis in the Krylov space carried out with *Arnoldi method*. An equivalent problem is formed with an upper Hessenberg matrix $H_n$ generated by *Arnoldi method*. The problem is easy to solve after QR decomposition of $H_n$. The resulting iterative procedure is given in Algorithm C.4.

For a linear system with the dimension of $N$, the GMRES method converges in $N$ iterations. Considering the matrix $V_n$ and the $QR$ factorization of $H_n$, the requirement of

**Algorithm C.4** GMRES algorithm

```
Compute $\mathbf{r}_0 = b - A\mathbf{x}_0$, $\beta = ||\mathbf{r}_0||_2$, $\mathbf{v}_1 = \mathbf{r}/\beta$, and $\xi_1 = \beta$
for n=1,2,... do                                                ▷ Iteration loop
    $\mathbf{w}_{n+1} = A\mathbf{v}_n$                                        ▷ Start of the Arnoldi method
    for i=1,2,...,n do
        $(H_n)_{i,n} = (\mathbf{w}_{n+1}, \mathbf{v}_i)$.
        $\mathbf{w}_{n+1} = \mathbf{w}_{n+1} - (H_n)_{i,n}\mathbf{v}_i$
    end for
    $(H_n)_{n+1,n} = ||\mathbf{w}_{n+1}||_2$
    if $(H_n)_{n+1,n} \neq 0$ then
        $\mathbf{v}_{n+1} = \mathbf{w}_{n+1}/(H_n)_{n+1,n}$
    end if                                                      ▷ End of the Arnoldi method
    for i=1,2,...,n-1 do                                        ▷ Applying Givens rotation
        $$\begin{pmatrix} (H_n)_{i,n} \\ (H_n)_{i+1,n} \end{pmatrix} = \begin{pmatrix} \bar{c}_i & s_i \\ -s_i & \bar{c}_i \end{pmatrix} \begin{pmatrix} (H_n)_{i,n} \\ (H_n)_{i+1,n} \end{pmatrix}$$
    end for
    Compute givens rotation $\bar{c}_n = |c_n|$
        $$c_n = (H_n)_{n,n} / \sqrt{(H_n)_{n,n}^2 + (H_n)_{n+1,n}^2}\,,\ s_n = (H_n)_{n+1,n} / \sqrt{(H_n)_{n,n}^2 + (H_n)_{n+1,n}^2}$$
    Update $(H_n)_{n,n} = \bar{c}_n (H_n)_{n,n} + s_n (H_n)_{n+1,n}$, and $(H_n)_{n+1,n} = 0$
    Update $(\xi_n, \xi_{n+1}) = (\bar{c}_n\xi_n, -s_n\xi_{n+1})$        ▷ Update the residual vector
    Solve the triangular system $\tilde{H}\mathbf{y} = (\xi_1, \xi_2, ..., \xi_n)^T$
    Update $\mathbf{x}_n = \mathbf{x}_0 + [\mathbf{v}_1\mathbf{v}_2 \cdots \mathbf{v}_n]\,\mathbf{y}$                     ▷ Calculate the results
    Check convergence on residual norm $\xi_{n+1}$; continue if necessary
end for
```

storage in memory has the order of $nN$ at the iteration $n$. When $n$ is relatively small to $N$, the cost of memory is negligible. However, the cost increases and becomes problematic when $n$ gets larger. A restarted version of the algorithm is introduced to avoid the problem by using the current approximation as a starting point after each $j$ iteration. The restarted version does not, however, guarantee the convergence property in a finite number of iterations.

## C.3 Scalability

With spatial decomposition of the computational domain, Schwarz methods prove and show the convergence by solving the subproblems instead of the global problem. However, global convergence is getting worse when the number of subdomains increases. It's also called not scalable for domain decomposition methods based solely on the local subdomain solutions. It is mainly because of the weak connection/communication on "far" subproblems, and it takes "time" (iteration times) to convey their information between each subdomain. Therefore, it is essential to figure out how to make domain decomposition methods more scalable.

Two-level methods are valid to enhance the convergence rate and make scalability possible with the preconditioner enriched by the solution of a coarse problem whose size is the order of the subdomains number. Thanks to Nicolaides coarse spaces [120], analysis and derivation are introduced. Furthermore, GenEO (Generalized Eigenvalue in the Overlap) method is considered to achieve targeted convergence rate.

## C.4 Numerical test

In *FreeFem++*, it is easy to implement the domain decomposition methods with one plug-in library *HPDDM*. Also, there are many keywords, which correspond to variant Krylov methods, Schwarz methods, restarted point $j$, et al. As mentioned in the previous section, it is possible to achieve the targeted convergence rate by optimizing the selection of parameters for different problems. One can find some examples of Helmholtz equation in [120].

This study is focused on fluid–structure interaction problems, which concern the effect of the interface between fluid and structure. For every body–fitted method, including this study, the meshes follow the deformation of the interface or the computational domain, and the mesh regeneration is applied to avoid skewness of elements. However, for domain decomposition methods, the mesh regeneration requires an incredibly large storage memory to interpolate variables from local mesh to new global mesh. Except some special treatments of interface between fluid and solid, such as immersed boundary methods and level set methods, solving problems involved fluid–structure interaction is naturally hard to utilize domain decomposition methods.

A parallel efficiency test is discussed with a three dimensional problem in section 4.4.1, and the computational domain is discretized into 240000 elements, with mesh being refined near the surface of the elastic plate, and roughly 200000 variables. The following results show the time for solving the matrix in each iteration. The overall efficiency is good enough for solving the fluid–structure interaction problems. The main problem in present study is about the requirement of storage memory and communication of variables.

Table C.1: Computational time and efficiency

| CPU cores | solving time (s) | efficiency |
|---|---|---|
| 2 | 403.738 | nan |
| 4 | 307.304 | 2.63 |
| 8 | 116.092 | 6.96 |
| 16 | 56.1008 | 14.39 |
| 32 | 38.8878 | 20.76 |

## C.5 Concluding remarks

In this chapter, four Schwarz methods are presented and compared with their solution algorithms and algebraic forms. In Krylov method, GMRES, is introduced to solve the subproblems on each subdomain. To achieve the scalability of parallel solver, two-level method is taken into consideration with the preconditioner enriched by the solution of a coarse problem. By solving a three dimensional test with the proposed Eulerian monolithic formulation, the efficiency of the parallel solver from the library *HPDDM* is shown.

The work is still undergoing to parallelize the proposed Eulerian monolithic formulation with the domain decomposition method.

# Appendix D

# Computational domain – 3D geometry

Unlike the 2D geometry, it is too complicated to build a 3D domain with the combination of surfaces bounded by borders transformed from 2D, referring to section 6.2.1. With the help of software *gmsh* and the extended library *OpenCASCADE*, it is feasible to construct a 3D geometrical model for vein. Detailed information of *gmsh* can refer its documentation [189].

The geometry is composed with three partitions: vascular wall, valves, and fluid. Vascular wall is defined as the volume generated from a rotating surface which is similar to 2D geometry. Two dimensional cross section of valves is bounded by two elliptic arcs with the specified thickness of valves at two ends that are smoothly closed with curves. The volume of valve can be obtained by prolonging the cross section along major axis, and the duplication is generated by mirror symmetry along plane of major axis.

The final 3D geometry plotted in D.1 can be obtained by boolean operators in *OpenCASCADE* to trim and adhere the volume of the vascular wall and valves.

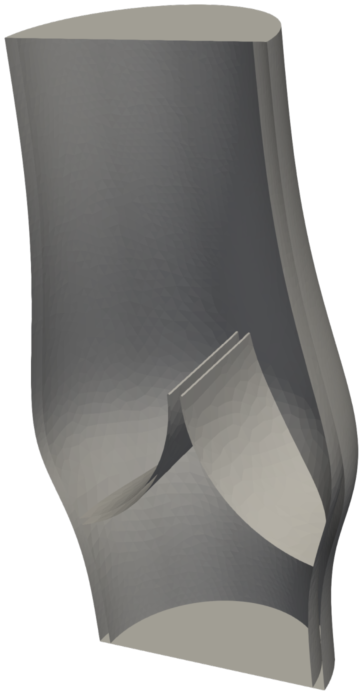

Figure D.1: 3D geometry of valved vein.

# Bibliography

[1] A. Fronek, M. H. Criqui, J. Denenberg, and R. D. Langer, "Common femoral vein dimensions and hemodynamics including Valsalva response as a function of sex, age, and ethnicity in a population study," *Journal of Vascular Surgery*, vol. 33, pp. 1050–1056, May 2001.

[2] P. Human, T. Franz, J. Scherman, L. Moodley, and P. Zilla, "Dimensional analysis of human saphenous vein grafts: Implications for external mesh support," *The Journal of Thoracic and Cardiovascular Surgery*, vol. 137, pp. 1101–1108, May 2009.

[3] M. Kalteis, I. Berger, S. Messie-Werndl, R. Pistrich, W. Schimetta, W. Pölz, and F. Hieller, "High ligation combined with stripping and endovenous laser ablation of the great saphenous vein: Early results of a randomized controlled study," *Journal of Vascular Surgery*, vol. 47, pp. 822–829, Apr. 2008.

[4] L. H. Rasmussen, L. Bjoern, M. Lawaetz, B. Lawaetz, A. Blemings, and B. Eklöf, "Randomised clinical trial comparing endovenous laser ablation with stripping of the great saphenous vein: Clinical outcome and recurrence after 2 years," *European Journal of Vascular and Endovascular Surgery*, vol. 39, pp. 630–635, May 2010.

[5] A. C. Seidel, F. Miranda Jr., Y. Juliano, and N. F. Novo, "Relationship between the diameter of great saphenous vein and body mass index," *Jornal Vascular Brasileiro*, vol. 4, pp. 265–269, Sept. 2005.

[6] F. H. Warkentine, M. C. Pierce, D. Lorenz, and I. K. Kim, "The anatomic relationship of femoral vein to femoral artery in euvolemic pediatric patients by ultrasonography: Implications for pediatric femoral central venous access," *Academic Emergency Medicine*, vol. 15, pp. 426–430, May 2008.

[7] P. Beddy, T. Geoghegan, N. Ramesh, O. Buckley, J. O'Brien, J. Colville, and W. C. Torreggiani, "Valsalva and gravitational variability of the internal jugular vein and common femoral vein: Ultrasound assessment," *European Journal of Radiology*, vol. 58, pp. 307–309, May 2006.

[8] C. Sheng, S. N. Sarwal, K. C. Watts, and A. E. Marble, "Computational simulation of blood flow in human systemic circulation incorporating an external force field," *Medical and Biological Engineering and Computing*, vol. 33, pp. 8–17, Jan. 1995.

[9] J. L. Sandri, F. S. Barros, S. Pontes, C. Jacques, and S. X. Salles-Cunha, "Diameter-reflux relationship in perforating veins of patients with varicose veins," *Journal of Vascular Surgery*, vol. 30, pp. 867–875, Nov. 1999.

[10] C.-S. Poon and C. K. Merrill, "Decrease of cardiac chaos in congestive heart failure," *Nature*, vol. 389, pp. 492–495, Oct. 1997.

[11] O. Frank, "The basic shape of the arterial pulse. First treatise: Mathematical analysis," *Journal of Molecular and Cellular Cardiology*, vol. 22, pp. 255–277, Mar. 1990.

[12] S. Ii, K. Sugiyama, S. Takeuchi, S. Takagi, and Y. Matsumoto, "An implicit full Eulerian method for the fluid-structure interaction problem," in *International journal for numerical methods in fluids*, vol. 65, pp. 150–165, Wiley, 2011.

[13] I. E. Idel'cik, *Mémento des pertes de charge et de pertes de charge par frottement [Handbook of singular and friction head losses].* Eyrolles, 1969.

[14] J. H. Gerrard and M. D. Hughes, "The flow due to an oscillating piston in a cylindrical tube: a comparison between experiment and a simple entrance flow theory," *Journal of Fluid Mechanics*, vol. 50, pp. 97–106, Nov. 1971.

[15] H. B. Atabek and C. C. Chang, "Oscillatory flow near the entry of a circular tube," *Zeitschrift für angewandte Mathematik und Physik ZAMP*, vol. 12, pp. 185–201, May 1961.

[16] C. C. Chang and H. B. Atabek, "The inlet length for oscillatory flow and its effects on the determination of the rate of flow in arteries," *Physics in Medicine and Biology*, vol. 6, no. 2, p. 303, 1961.

[17] H. J. Obremski, M. V. Morkovin, M. Landahl, A. R. Wazzan, and T. T. Okamura, "A portfolio of stability characteristics of incompressible boundary layers," tech. rep., Mar. 1969.

[18] C. V. Kerczek and S. H. Davis, "Linear stability theory of oscillatory Stokes layers," *Journal of Fluid Mechanics*, vol. 62, pp. 753–773, Feb. 1974.

[19] P. Hall and K. H. Parker, "The stability of the decaying flow in a suddenly blocked channel," *Journal of Fluid Mechanics*, vol. 75, pp. 305–314, May 1976.

[20] O. Reynolds, "On the experimental investigation of the circumstances which determine whether the motion of water in parallel channels shall be direct of sinuous and of the law of resistance in parallel channels," *Philosophical Transactions of the Royal society of London*, p. 174, 1883.

[21] O. Reynolds, "On the dynamical theory of incompressible viscous fluids and the determination of the criterion," *Philosophical Transactions of the Royal Society of London. A*, vol. 186, pp. 123–164, 1895.

[22] J. C. Stettler and A. K. M. F. Hussain, “On transition of the pulsatile pipe flow,” *Journal of Fluid Mechanics*, vol. 170, pp. 169–197, Sept. 1986.

[23] T. Sarpkaya, “Experimental determination of the critical Reynolds number for pulsating Poiseuille flow,” *Journal of Basic Engineering*, vol. 88, pp. 589–598, Sept. 1966.

[24] R. Akhavan, R. D. Kamm, and A. H. Shapiro, “An investigation of transition to turbulence in bounded oscillatory Stokes flows part 1: experiments,” *Journal of Fluid Mechanics*, vol. 225, pp. 395–422, Apr. 1991.

[25] M. Hino, M. Sawamoto, and S. Takasu, “Experiments on transition to turbulence in an oscillatory pipe flow,” *Journal of Fluid Mechanics*, vol. 75, pp. 193–207, May 1976.

[26] M. Ohmi, M. Iguchi, K. Kakehashi, and T. Masuda, “Transition to turbulence and velocity distribution in an oscillating pipe flow,” *Bulletin of JSME*, vol. 25, no. 201, pp. 365–371, 1982.

[27] E. L. Yellin, “Laminar-turbulent transition process in pulsatile flow,” *Circulation Research*, vol. 19, pp. 791–804, Oct. 1966.

[28] R. M. Nerem and W. A. Seed, “An in vivo study of aortic flow disturbances,” *Cardiovascular Research*, vol. 6, pp. 1–14, Jan. 1972.

[29] C. Clarion and R. Pelissier, “A theoretical and experimental study of the velocity distribution and transition to turbulence in free oscillatory flow,” *Journal of Fluid Mechanics*, vol. 70, pp. 59–79, July 1975.

[30] R. M. Nerem, W. A. Seed, and N. B. Wood, “An experimental study of the velocity distribution and transition to turbulence in the aorta,” *Journal of Fluid Mechanics*, vol. 52, pp. 137–160, Mar. 1972.

[31] M. J. Lighthill, “Physiological fluid dynamics: a survey?,” *Journal of Fluid Mechanics*, vol. 52, pp. 475–497, Apr. 1972.

[32] D. Bluestein and S. Einav, “Transition to turbulence in pulsatile flow through heart valves—a nodified stability approach,” *Journal of Biomechanical Engineering*, vol. 116, pp. 477–487, Nov. 1994.

[33] P. Snabre, M. Bitbol, and P. Mills, “Cell disaggregation behavior in shear flow,” *Biophysical Journal*, vol. 51, pp. 795–807, May 1987.

[34] S. Chien, “Shear dependence of effective cell volume as a determinant of blood viscosity,” *Science*, vol. 168, pp. 977–979, May 1970.

[35] M. Thiriet, G. MartinBorret, and F. Hecht, “Shear-thinning flow in a bend and in a planar symmetrical bifurcation. Application to the blood flow in large vessels.,” *Journal de Physique III*, vol. 6, no. 4, pp. 529–542, 1996.

[36] E. Pl and B. De, “A comparison of rheological constitutive functions for whole human blood.,” *Biorheology*, vol. 17, pp. 235–247, Dec. 1979.

[37] K. R. Rajagopal and A. R. Srinivasa, “A thermodynamic frame work for rate type fluid models,” *Journal of Non-Newtonian Fluid Mechanics*, vol. 88, pp. 207–227, Jan. 2000.

[38] M. Anand and K. R. Rajagopal, “A mathematical model to describe the change in the constitutive character of blood due to platelet activation,” *Comptes Rendus Mécanique*, vol. 330, no. 8, pp. 557–562, 2002.

[39] A. L. Fogelson, “A mathematical model and numerical method for studying platelet adhesion and aggregation during blood clotting,” *Journal of Computational Physics*, vol. 56, pp. 111–134, Oct. 1984.

[40] C. Cobelli, G. Federspil, G. Pacini, A. Salvan, and C. Scandellari, “An integrated mathematical model of the dynamics of blood glucose and its hormonal control,” *Mathematical Biosciences*, vol. 58, pp. 27–60, Feb. 1982.

[41] M. A. Khanin and V. V. Semenov, “A mathematical model of the kinetics of blood coagulation,” *Journal of Theoretical Biology*, vol. 136, pp. 127–134, Jan. 1989.

[42] E. E. Tzirtzilakis, “A mathematical model for blood flow in magnetic field,” *Physics of Fluids*, vol. 17, p. 077103, July 2005.

[43] M. E. Orme and M. A. J. Chaplain, “A mathematical model of vascular tumour growth and invasion,” *Mathematical and Computer Modelling*, vol. 23, pp. 43–60, May 1996.

[44] M.-C. Hsu, D. Kamensky, Y. Bazilevs, M. S. Sacks, and T. J. R. Hughes, “Fluid–structure interaction analysis of bioprosthetic heart valves: significance of arterial wall deformation,” *Computational Mechanics*, vol. 54, pp. 1055–1071, Aug. 2014.

[45] T. E. Tezduyar and S. Sathe, “Modelling of fluid–structure interactions with the space–time finite elements: Solution techniques,” *International Journal for Numerical Methods in Fluids*, vol. 54, pp. 855–900, June 2007.

[46] K. Stein, R. Benney, V. Kalro, T. E. Tezduyar, J. Leonard, and M. Accorsi, “Parachute fluid–structure interactions: 3-D computation,” *Computer Methods in Applied Mechanics and Engineering*, vol. 190, pp. 373–386, Oct. 2000.

[47] K. Takizawa, T. E. Tezduyar, and A. Buscher, "Space–time computational analysis of MAV flapping-wing aerodynamics with wing clapping," *Computational Mechanics*, vol. 55, pp. 1131–1141, Jan. 2015.

[48] R. van Loon, P. D. Anderson, F. N. van de Vosse, and S. J. Sherwin, "Comparison of various fluid–structure interaction methods for deformable bodies," *Computers & Structures*, vol. 85, pp. 833–843, June 2007.

[49] M. J. McHenry, J. A. Strother, and S. M. v. Netten, "Mechanical filtering by the boundary layer and fluid–structure interaction in the superficial neuromast of the fish lateral line system," *Journal of Comparative Physiology A*, vol. 194, pp. 795–810, Aug. 2008.

[50] I. Lee and H. Choi, "A discrete-forcing immersed boundary method for the fluid–structure interaction of an elastic slender body," *Journal of Computational Physics*, vol. 280, pp. 529–546, Jan. 2015.

[51] L. Goubergrits and K. Affeld, "Numerical estimation of blood damage in artificial organs," *Artificial Organs*, vol. 28, pp. 499–507, May 2004.

[52] P. Verdonck, "The role of computational fluid dynamics for artificial organ design," *Artificial Organs*, vol. 26, pp. 569–570, July 2002.

[53] G. W. Burgreen, J. F. Antaki, Z. Wu, and A. J. Holmes, "Computational fluid dynamics as a development tool for rotary blood pumps," *Artificial Organs*, vol. 25, pp. 336–340, May 2001.

[54] J. Hron and S. Turek, "A monolithic FEM solver for an ALE formulation of fluid-structure interaction with configuration for numerical benchmarking," 2006.

[55] H. J. Obremski and A. A. Fejer, "Transition in oscillating boundary layer flows," *Journal of Fluid Mechanics*, vol. 29, pp. 93–111, July 1967.

[56] C. Kleinstreuer, M. Lei, and J. Archie, *Hemodynamics simulations and optimal computer-aided designs of branching blood vessels*. CRC Press, Boca Raton, Florida, 2001.

[57] B. Dion, S. Naili, J. Renaudeaux, and C. Ribreau, "Buckling of elastic tubes: study of highly compliant device," *Medical and Biological Engineering and Computing*, vol. 33, no. 2, pp. 196–201, 1995.

[58] A. I. Katz, Y. Chen, and A. H. Moreno, "Flow through a collapsible tube," *Biophysical Journal*, vol. 9, pp. 1261–1279, Oct. 1969.

[59] T. J. Pedley, B. S. Brook, and R. S. Seymour, "Blood pressure and flow rate in the giraffe jugular vein," *Philosophical Transactions of the Royal Society of London B: Biological Sciences*, vol. 351, pp. 855–866, July 1996.

[60] C. Ribreau and M. Thiriet, “Ecoulements veineux,” *Biomécanique des fluides et des tissus*, no. 7, pp. 131–178, 1998.

[61] M. Thiriet and C. Ribreau, “Computational flow in a collapsed tube with wall contact,” *Mécanique & Industries*, vol. 1, pp. 349–364, July 2000.

[62] M. Thiriet, S. Naili, A. Langlet, and C. Ribreau, “Flow in thin-walled collapsible tubes,” in *Biofluid Methods in Vascular and Pulmonary Systems*, vol. IV of *Biomechanical Systems. Techniques and Applications*, pp. 10–1–10–43, Boca Raton, Florida: CRC Press, 2001.

[63] M. Thiriet, M. Bonis, A. S. Adedjouma, C. Hatzfeld, and J. P. Yvon, “Experimental and theoretical models of flow during forced expiration: pressure and pressure history dependence of flow rate,” *Medical & Biological Engineering & Computing*, vol. 25, pp. 551–559, Sept. 1987.

[64] D. Begis, C. Delpuech, P. Le Tallec, L. Loth, M. Thiriet, and M. Vidrascu, “A finite-element model of tracheal collapse,” *Journal of Applied Physiology*, vol. 64, pp. 1359–1368, Apr. 1988.

[65] M. Thiriet, M. Bonis, A. S. Adedjouma, and J. P. Yvon, “A numerical model of expired flow in a monoalveolar lung model subjected to pressure ramps.,” *Journal of Biomechanical Engineering*, vol. 111, pp. 9–16, Feb. 1989.

[66] M. Thiriet, J. M. Maarek, D. A. Chartrand, C. Delpuech, L. Davis, C. Hatzfeld, and H. K. Chang, “Transverse images of the human thoracic trachea during forced expiration,” *Journal of Applied Physiology*, vol. 67, pp. 1032–1040, Sept. 1989.

[67] E. Hachem, S. Feghali, T. Coupez, and R. Codina, “A three-field stabilized finite element method for fluid-structure interaction: elastic solid and rigid body limit,” *International Journal for Numerical Methods in Engineering*, vol. 104, pp. 566–584, Nov. 2015.

[68] B. Hübner, E. Walhorn, and D. Dinkler, “A monolithic approach to fluid–structure interaction using space–time finite elements,” *Computer Methods in Applied Mechanics and Engineering*, vol. 193, pp. 2087–2104, June 2004.

[69] J. Degroote, K.-J. Bathe, and J. Vierendeels, “Performance of a new partitioned procedure versus a monolithic procedure in fluid–structure interaction,” *Computers & Structures*, vol. 87, pp. 793–801, June 2009.

[70] M. Heil, A. L. Hazel, and J. Boyle, “Solvers for large-displacement fluid–structure interaction problems: segregated versus monolithic approaches,” *Computational Mechanics*, vol. 43, pp. 91–101, Mar. 2008.

[71] C. Michler, S. J. Hulshoff, E. H. van Brummelen, and R. de Borst, "A monolithic approach to fluid–structure interaction," *Computers & Fluids*, vol. 33, pp. 839–848, June 2004.

[72] Y. Bazilevs, V. M. Calo, T. J. R. Hughes, and Y. Zhang, "Isogeometric fluid-structure interaction: theory, algorithms, and computations," *Computational Mechanics*, vol. 43, pp. 3–37, Aug. 2008.

[73] M. A. Fernández, J.-F. Gerbeau, and C. Grandmont, "A projection semi-implicit scheme for the coupling of an elastic structure with an incompressible fluid," *International Journal for Numerical Methods in Engineering*, vol. 69, pp. 794–821, Jan. 2007.

[74] C. Bertoglio, D. Barber, N. Gaddum, I. Valverde, M. Rutten, P. Beerbaum, P. Moireau, R. Hose, and J.-F. Gerbeau, "Identification of artery wall stiffness: In vitro validation and in vivo results of a data assimilation procedure applied to a 3d fluid–structure interaction model," *Journal of Biomechanics*, vol. 47, pp. 1027–1034, Mar. 2014.

[75] J. Donea, S. Giuliani, and J. P. Halleux, "An arbitrary Lagrangian-Eulerian finite element method for transient dynamic fluid-structure interactions," *Computer Methods in Applied Mechanics and Engineering*, vol. 33, no. 1–3, pp. 689–723, 1982.

[76] C. S. Peskin, "Flow patterns around heart valves: A numerical method," *Journal of Computational Physics*, vol. 10, no. 2, pp. 252–271, 1972.

[77] R. Ghias, R. Mittal, and H. Dong, "A sharp interface immersed boundary method for compressible viscous flows," *Journal of Computational Physics*, vol. 225, pp. 528–553, July 2007.

[78] W. K. Liu, Y. Liu, D. Farrell, L. Zhang, X. S. Wang, Y. Fukui, N. Patankar, Y. Zhang, C. Bajaj, J. Lee, J. Hong, X. Chen, and H. Hsu, "Immersed finite element method and its applications to biological systems," *Computer Methods in Applied Mechanics and Engineering*, vol. 195, pp. 1722–1749, Feb. 2006.

[79] S. Xu and Z. J. Wang, "An immersed interface method for simulating the interaction of a fluid with moving boundaries," *Journal of Computational Physics*, vol. 216, no. 2, pp. 454–493, 2006.

[80] T.-R. Lee, Y.-S. Chang, J.-B. Choi, D. W. Kim, W. K. Liu, and Y.-J. Kim, "Immersed finite element method for rigid body motions in the incompressible Navier–Stokes flow," *Computer Methods in Applied Mechanics and Engineering*, vol. 197, pp. 2305–2316, Apr. 2008.

[81] R. Mittal and G. Iaccarino, "Immersed boundary methods," *Annual Review of Fluid Mechanics*, vol. 37, no. 1, pp. 239–261, 2005.

[82] L. Lee and R. LeVeque, “An immersed interface method for incompressible Navier–Stokes equations,” *SIAM Journal on Scientific Computing*, vol. 25, pp. 832–856, Jan. 2003.

[83] J. M. Stockie and B. R. Wetton, “Analysis of stiffness in the immersed boundary method and implications for time-stepping schemes,” *Journal of Computational Physics*, vol. 154, pp. 41–64, Sept. 1999.

[84] M. N. Linnick and H. F. Fasel, “A high-order immersed interface method for simulating unsteady incompressible flows on irregular domains,” *Journal of Computational Physics*, vol. 204, pp. 157–192, Mar. 2005.

[85] J. Yang and E. Balaras, “An embedded-boundary formulation for large-eddy simulation of turbulent flows interacting with moving boundaries,” *Journal of Computational Physics*, vol. 215, no. 1, pp. 12–40, 2006.

[86] S. Osher and J. A. Sethian, “Fronts propagating with curvature-dependent speed: Algorithms based on Hamilton-Jacobi formulations,” *Journal of Computational Physics*, vol. 79, no. 1, pp. 12–49, 1988.

[87] J. A. Sethian and P. Smereka, “Level set methods for fluid interfaces,” *Annual Review of Fluid Mechanics*, vol. 35, no. 1, pp. 341–372, 2003.

[88] N. Jenkins and K. Maute, “Level set topology optimization of stationary fluid-structure interaction problems,” *Structural and Multidisciplinary Optimization*, vol. 52, pp. 179–195, Mar. 2015.

[89] M. Sussman, P. Smereka, and S. Osher, “A level set approach for computing solutions to incompressible two-phase flow,” *Journal of Computational Physics*, vol. 114, pp. 146–159, Sept. 1994.

[90] E. Hachem, S. Feghali, T. Coupez, and R. Codina, “A three-field stabilized finite element method for fluid-structure interaction: elastic solid and rigid body limit,” *International Journal for Numerical Methods in Engineering*, vol. 104, pp. 566–584, Nov. 2015.

[91] W. F. Noh and P. Woodward, “SLIC (simple line interface calculation),” in *Proceedings of the Fifth International Conference on Numerical Methods in Fluid Dynamics June 28 – July 2, 1976 Twente University, Enschede*, vol. 59 of *Lecture Notes in Physics*, pp. 330–340, Springer Berlin Heidelberg, 1976.

[92] I. Chakraborty, G. Biswas, and P. S. Ghoshdastidar, “A coupled level-set and volume-of-fluid method for the buoyant rise of gas bubbles in liquids,” *International Journal of Heat and Mass Transfer*, vol. 58, pp. 240–259, Mar. 2013.

[93] C. W. Hirt and B. D. Nichols, "Volume of fluid (VOF) method for the dynamics of free boundaries," *Journal of Computational Physics*, vol. 39, pp. 201–225, Jan. 1981.

[94] D. Gueyffier, J. Li, A. Nadim, R. Scardovelli, and S. Zaleski, "Volume-of-fluid interface tracking with smoothed surface stress methods for three-dimensional flows," *Journal of Computational Physics*, vol. 152, pp. 423–456, July 1999.

[95] D. A. Hoang, V. Van Steijn, L. M. Portela, M. T. Kreutzer, and C. R. Kleijn, "Benchmark numerical simulations of segmented two-phase flows in microchannels using the Volume of Fluid method," *Computers & Fluids*, vol. 86, pp. 28–36, Nov. 2013.

[96] R. A. Gingold and J. J. Monaghan, "Smoothed particle hydrodynamics: theory and application to non-spherical stars," *Monthly Notices of the Royal Astronomical Society*, vol. 181, pp. 375–389, Dec. 1977.

[97] M. R. Bate and A. Burkert, "Resolution requirements for smoothed particle hydrodynamics calculations with self-gravity," *Monthly Notices of the Royal Astronomical Society*, vol. 288, pp. 1060–1072, July 1997.

[98] J. J. Monaghan, "Smoothed particle hydrodynamics," *Reports on Progress in Physics*, vol. 68, no. 8, p. 1703, 2005.

[99] Y.-H. Hwang, "Smoothing difference scheme in a moving particle method," *Numerical Heat Transfer, Part B: Fundamentals*, vol. 60, pp. 203–234, Sept. 2011.

[100] G. A. Buxton and N. Clarke, "Computational phlebology: the simulation of a vein valve," *Journal of Biological Physics*, vol. 32, pp. 507–521, Feb. 2007.

[101] C. Tang, L. Zhu, G. Akingba, and X.-Y. Lu, "Viscous flow past a collapsible channel as a model for self-excited oscillation of blood vessels," *Journal of Biomechanics*, vol. 48, pp. 1922–1929, July 2015.

[102] X. Liu, F. Pu, Y. Fan, X. Deng, D. Li, and S. Li, "A numerical study on the flow of blood and the transport of LDL in the human aorta: the physiological significance of the helical flow in the aortic arch," *American Journal of Physiology - Heart and Circulatory Physiology*, vol. 297, pp. H163–H170, July 2009.

[103] S. Salmon, M. Thiriet, and J.-F. Gerbeau, "Medical image – based computational model of pulsatile flow in saccular aneurisms," *ESAIM: Mathematical Modelling and Numerical Analysis*, vol. 37, pp. 663–679, July 2003.

[104] J.-D. Boissonnat, R. Chaine, P. Frey, G. Malandain, S. Salmon, E. Saltel, and M. Thiriet, "From arteriographies to computational flow in saccular aneurisms: the INRIA experience," *Medical Image Analysis*, vol. 9, pp. 133–143, Apr. 2005.

[105] Y. Qui, R. C. Quijano, S. K. Wang, and P. N. H. C. Hwang, "Fluid dynamics of venous valve closure," *Annals of Biomedical Engineering*, vol. 23, pp. 750–759, Nov. 1995.

[106] S. E. Rittgers, M. T. Oberdier, and S. Pottala, "Physiologically-based testing system for the mechanical characterization of prosthetic vein valves," *BioMedical Engineering OnLine*, vol. 6, no. 1, pp. 1–12, 2007.

[107] C. D. Buescher, B. Nachiappan, J. M. Brumbaugh, K. A. Hoo, and H. F. Janssen, "Experimental studies of the effects of abnormal venous valves on fluid flow," *Biotechnology progress*, vol. 21, no. 3, pp. 938–945, 2005.

[108] K.-H. Nam, E. Yeom, H. Ha, and S.-J. Lee, "Velocity field measurements of valvular blood flow in a human superficial vein using high-frequency ultrasound speckle image velocimetry," *The International Journal of Cardiovascular Imaging*, vol. 28, pp. 69–77, Dec. 2010.

[109] A. J. Narracott, C. Zervides, V. Diaz, D. Rafiroiu, P. V. Lawford, and D. R. Hose, "Analysis of a mechanical heart valve prosthesis and a native venous valve: Two distinct applications of FSI to biomedical applications," *International Journal for Numerical Methods in Biomedical Engineering*, vol. 26, pp. 421–434, Mar. 2010.

[110] C. Zervides and A. D. Giannoukas, "Computational phlebology: reviewing computer models of the venous system," *Phlebology*, vol. 28, pp. 209–218, June 2013.

[111] M. Astorino, J.-F. Gerbeau, O. Pantz, and K.-F. Traoré, "Fluid–structure interaction and multi-body contact: Application to aortic valves," *Computer Methods in Applied Mechanics and Engineering*, vol. 198, pp. 3603–3612, Sept. 2009.

[112] J. De Hart, F. P. T. Baaijens, G. W. M. Peters, and P. J. G. Schreurs, "A computational fluid-structure interaction analysis of a fiber-reinforced stentless aortic valve," *Journal of Biomechanics*, vol. 36, pp. 699–712, May 2003.

[113] T. Dunne and R. Rannacher, "Adaptive finite element approximation of fluid-structure interaction based on an Eulerian variational formulation," in *Fluid-Structure Interaction*, pp. 110–145, Springer, Berlin, Heidelberg, 2006.

[114] R. Rannacher and T. Richter, "An adaptive finite element method for fluid-structure interaction problems based on a fully Eulerian formulation," in *Fluid Structure Interaction II*, pp. 159–191, Springer, Berlin, Heidelberg, 2011.

[115] O. Pironneau, "On the transport-diffusion algorithm and its applications to the Navier-Stokes equations," *Numerische Mathematik*, vol. 38, pp. 309–332, Oct. 1982.

[116] C.-Y. Chiang, O. Pironneau, T. W. H. Sheu, and M. Thiriet, "Numerical study of a 3d Eulerian monolithic formulation for incompressible fluid-structures systems," *Fluids*, vol. 2, p. 34, June 2017.

[117] O. Pironneau, "An energy preserving monolithic Eulerian fluid-structure numerical Scheme," *arXiv:1607.08083 [physics]*, July 2016.

[118] O. Pironneau, "Numerical study of a monolithic fluid–structure formulation," in *Variational Analysis and Aerospace Engineering*, no. 116 in Springer Optimization and Its Applications, pp. 401–420, Springer International Publishing, 2016.

[119] F. Hecht and O. Pironneau, "An energy stable monolithic Eulerian fluid-structure finite element method," *International Journal of Numerical Methods in Fluid*, 2017.

[120] V. Dolean, P. Jolivet, and F. Nataf, *An introduction to domain decomposition methods*. Other Titles in Applied Mathematics, Society for Industrial and Applied Mathematics, Nov. 2015.

[121] Y. Deleuze, *Modeling and simulation of transport during acupuncture*. Ph.D. Thesis, Université Pierre et Marie Curie ; National Taiwan University, Sept. 2015.

[122] M. Boulakia, "Existence of weak solutions for the motion of an elastic structure in an incompressible viscous fluid," *Comptes Rendus Mathematique*, vol. 336, pp. 985–990, June 2003.

[123] D. Coutand and S. Shkoller, "Motion of an elastic solid inside an incompressible viscous fluid," *Archive for Rational Mechanics and Analysis*, vol. 176, pp. 25–102, Mar. 2005.

[124] J.-P. Raymond and M. Vanninathan, "A fluid–structure model coupling the Navier–Stokes equations and the Lamé system," *Journal de Mathematiques Pures et Appliquees*, vol. 3, no. 102, pp. 546–596, 2014.

[125] F. Hecht, "New development in freefem++," *Journal of Numerical Mathematics*, vol. 20, no. 3-4, pp. 251–266, 2013.

[126] A. J. Chorin, "A numerical method for solving incompressible viscous flow problems," *Journal of Computational Physics*, vol. 135, pp. 118–125, Aug. 1997.

[127] R. Temam, "Une méthode d'approximation de la solution des équations de Navier-Stokes," *Bulletin de la Société Mathématique de France*, vol. 96, pp. 115–152, 1968.

[128] M. Bercovier, "Perturbation of mixed variational problems. Application to mixed finite element methods," *RAIRO. Analyse numérique*, vol. 12, no. 3, pp. 211–236, 1978.

[129] M. Shinbrot, "The mathematical theory of viscous incompressible flow," *SIAM Review*, vol. 13, pp. 103–106, Jan. 1971.

[130] I. Babuška, "Error-bounds for finite element method," *Numerische Mathematik*, vol. 16, pp. 322–333, Jan. 1971.

[131] F. Brezzi, "On the existence, uniqueness and approximation of saddle-point problems arising from Lagrangian multipliers," *Publications mathématiques et informatique de Rennes*, no. S4, pp. 1–26, 1974.

[132] P.-A. Raviart and J. M. Thomas, *Introduction à l'analyse numérique des équations aux dérivées partielles*. Masson, 1983. Google-Books-ID: _zDvAAAAMAAJ.

[133] R. Schreiber and H. B. Keller, "Driven cavity flows by efficient numerical techniques," *Journal of Computational Physics*, vol. 49, pp. 310–333, Feb. 1983.

[134] H. Nishida and N. Satofuka, "Higher-order solutions of square driven cavity flow using a variable-order multi-grid method," *International Journal for Numerical Methods in Engineering*, vol. 34, pp. 637–653, Mar. 1992.

[135] U. Ghia, K. N. Ghia, and C. T. Shin, "High-Re solutions for incompressible flow using the Navier-Stokes equations and a multigrid method," *Journal of Computational Physics*, vol. 48, pp. 387–411, Dec. 1982.

[136] E. Erturk, T. C. Corke, and C. Gökçöl, "Numerical solutions of 2-D steady incompressible driven cavity flow at high Reynolds numbers," *International Journal for Numerical Methods in Fluids*, vol. 48, pp. 747–774, July 2005.

[137] K. W. P. Eric, I. Gianluca, S. H. O. Andrew, and G. Matteo, "Numerical studies of high Reynolds numbers flow past a stationary and rotating sphere," Dec. 2009.

[138] P.-H. Chiu, R.-K. Lin, and T. W. H. Sheu, "A differentially interpolated direct forcing immersed boundary method for predicting incompressible Navier–Stokes equations in time-varying complex geometries," *Journal of Computational Physics*, vol. 229, pp. 4476–4500, June 2010.

[139] P. M. Gresho, S. T. Chan, R. L. Lee, and C. D. Upson, "A modified finite element method for solving the time-dependent, incompressible Navier-Stokes equations. Part 2: Applications," *International Journal for Numerical Methods in Fluids*, vol. 4, pp. 619–640, July 1984.

[140] S. Marrone, A. Colagrossi, M. Antuono, G. Colicchio, and G. Graziani, "An accurate SPH modeling of viscous flows around bodies at low and moderate Reynolds numbers," *Journal of Computational Physics*, vol. 245, pp. 456–475, July 2013.

[141] C. Shu, N. Liu, and Y. T. Chew, "A novel immersed boundary velocity correction–lattice Boltzmann method and its application to simulate flow past a circular cylinder," *Journal of Computational Physics*, vol. 226, pp. 1607–1622, Oct. 2007.

[142] W. C. L. Shih, C. Wang, D. Coles, and A. Roshko, “Experiments on flow past rough circular cylinders at large Reynolds numbers,” *Journal of Wind Engineering and Industrial Aerodynamics*, vol. 49, pp. 351–368, Dec. 1993.

[143] D. J. Tritton, “Experiments on the flow past a circular cylinder at low Reynolds numbers,” *Journal of Fluid Mechanics*, vol. 6, pp. 547–567, Nov. 1959.

[144] M. Tabata and S. Fujima, “Finite-element analysis of high Reynolds number flow past a circular cylinder,” *Journal of Computational and Applied Mathematics*, vol. 38, pp. 411–424, Dec. 1991.

[145] R. D. Henderson, “Nonlinear dynamics and pattern formation in turbulent wake transition,” *Journal of Fluid Mechanics*, vol. 352, pp. 65–112, Dec. 1997.

[146] E. M. Saiki and S. Biringen, “Numerical simulation of a cylinder in uniform flow: Application of a virtual boundary method,” *Journal of Computational Physics*, vol. 123, pp. 450–465, Feb. 1996.

[147] A. Roshko, “On the drag and shedding frequency of two-dimensional bluff bodies,” July 1954.

[148] B. E and R. Wille, “Periodic flow phenomena,” *Annual Review of Fluid Mechanics*, vol. 4, no. 1, pp. 313–340, 1972.

[149] B. Fornberg, “Steady viscous flow past a circular cylinder up to Reynolds number 600,” *Journal of Computational Physics*, vol. 61, pp. 297–320, Nov. 1985.

[150] K. J. Bathe and E. L. Wilson, “NONSAP — A nonlinear structural analysis program,” *Nuclear Engineering and Design*, vol. 29, pp. 266–293, Dec. 1974.

[151] S. Turek and J. Hron, “Proposal for numerical benchmarking of fluid-structure interaction between an elastic object and laminar incompressible flow,” in *Fluid-Structure Interaction*, pp. 371–385, Springer, Berlin, Heidelberg, 2006.

[152] T. Richter, “A fully Eulerian formulation for fluid–structure-interaction problems,” *Journal of Computational Physics*, vol. 233, pp. 227–240, Jan. 2013.

[153] W. A. Wall, “Fluid-struktur-interaktion mit stabilisierten finiten elementen,” 1999.

[154] T. Wick, “Fluid-structure interactions using different mesh motion techniques,” *Computers & Structures*, vol. 89, pp. 1456–1467, July 2011.

[155] J. P. Gomes and H. Lienhart, “Experimental benchmark: Self-excited fluid-structure interaction test cases,” in *Fluid Structure Interaction II*, pp. 383–411, Springer, Berlin, Heidelberg, 2011.

[156] A. Kalmbach, *Experimental investigations on vortex-induced fluid-structure interaction benchmarks and corresponding numerical RANS predictions*. PhD thesis, 2015.

[157] A. Kalmbach and M. Breuer, "Experimental PIV/V3v measurements of vortex-induced fluid–structure interaction in turbulent flow—A new benchmark FSI-PfS-2a," *Journal of Fluids and Structures*, vol. 42, pp. 369–387, Oct. 2013.

[158] G. De Nayer, A. Kalmbach, M. Breuer, S. Sicklinger, and R. Wüchner, "Flow past a cylinder with a flexible splitter plate: A complementary experimental–numerical investigation and a new FSI test case (FSI-PfS-1a)," *Computers & Fluids*, vol. 99, pp. 18–43, July 2014.

[159] J. P. Gomes and H. Lienhart, "Fluid–structure interaction-induced oscillation of flexible structures in laminar and turbulent flows," *Journal of Fluid Mechanics*, vol. 715, pp. 537–572, Jan. 2013.

[160] M. Luhar and H. M. Nepf, "Flow-induced reconfiguration of buoyant and flexible aquatic vegetation," *Limnology and Oceanography*, vol. 56, pp. 2003–2017, Nov. 2011.

[161] F.-B. Tian, H. Dai, H. Luo, J. F. Doyle, and B. Rousseau, "Fluid–structure interaction involving large deformations: 3d simulations and applications to biological systems," *Journal of Computational Physics*, vol. 258, pp. 451–469, Feb. 2014.

[162] A. Hessenthaler, N. R. Gaddum, O. Holub, R. Sinkus, O. Röhrle, and D. Nordsletten, "Experiment for validation of fluid-structure interaction models and algorithms," *International Journal for Numerical Methods in Biomedical Engineering*, Jan. 2017.

[163] K. Taira and T. Colonius, "The immersed boundary method: A projection approach," *Journal of Computational Physics*, vol. 225, pp. 2118–2137, Aug. 2007.

[164] J.-I. Choi, R. C. Oberoi, J. R. Edwards, and J. A. Rosati, "An immersed boundary method for complex incompressible flows," *Journal of Computational Physics*, vol. 224, pp. 757–784, June 2007.

[165] M. Coutanceau and R. Bouard, "Experimental determination of the main features of the viscous flow in the wake of a circular cylinder in uniform translation. Part 1. Steady flow," *Journal of Fluid Mechanics*, vol. 79, pp. 231–256, Feb. 1977.

[166] D. Russell and Z. Jane Wang, "A cartesian grid method for modeling multiple moving objects in 2d incompressible viscous flow," *Journal of Computational Physics*, vol. 191, pp. 177–205, Oct. 2003.

[167] E. Stålberg, A. Brüger, P. Lötstedt, A. V. Johansson, and D. S. Henningson, "High order accurate solution of flow past a circular cylinder," *Journal of Scientific Computing*, vol. 27, pp. 431–441, June 2006.

[168] D. Calhoun, “A Cartesian grid method for solving the two-dimensional stream function-vorticity equations in irregular regions,” *Journal of Computational Physics*, vol. 176, pp. 231–275, Mar. 2002.

[169] J. A. Wright and R. W. Smith, “An edge-based method for the incompressible Navier–Stokes equations on polygonal meshes,” *Journal of Computational Physics*, vol. 169, pp. 24–43, May 2001.

[170] C. H. K. Williamson and G. L. Brown, “A series in $1/\sqrt{Re}$ to represent the strouhal–reynolds number relationship of the cylinder wake,” *Journal of Fluids and Structures*, vol. 12, pp. 1073–1085, Nov. 1998.

[171] J. T. Holden, “On the finite deflections of thin beams,” *International Journal of Solids and Structures*, vol. 8, pp. 1051–1055, Aug. 1972.

[172] J. P. Gomes, S. Yigit, H. Lienhart, and M. Schäfer, “Experimental and numerical study on a laminar fluid–structure interaction reference test case,” *Journal of Fluids and Structures*, vol. 27, pp. 43–61, Jan. 2011.

[173] M. L. Larma, *Coupling schemes and unfitted mesh methods for fluid-structure interaction*. Ph.D. Thesis, Université Pierre et Marie Curie - Paris VI, 2016.

[174] P. Wriggers, *Computational contact mechanics*. Berlin, Heidelberg: Springer Berlin Heidelberg, 2006.

[175] Y.-C. Lin, R. T. Haftka, N. V. Queipo, and B. J. Fregly, “Surrogate articular contact models for computationally efficient multibody dynamic simulations,” *Medical Engineering & Physics*, vol. 32, pp. 584–594, July 2010.

[176] F. Pfeiffer and C. Glocker, *Multibody dynamics with unilateral contacts*. John Wiley & Sons, July 1996. Google-Books-ID: XrZN_TBfiGcC.

[177] S. Frei, *Eulerian finite element methods for interface problems and fluid-structure interactions*. Dissertation, 2016.

[178] L. D. Lorenzis, P. Wriggers, and G. Zavarise, “A mortar formulation for 3d large deformation contact using NURBS-based isogeometric analysis and the augmented Lagrangian method,” *Computational Mechanics*, vol. 49, pp. 1–20, July 2011.

[179] D. Kamensky, M. Hsu, D. Schillinger, J. Evans, A. Aggarwal, Y. Bazilevs, M. Sacks, and T. Hughes, “A variational immersed boundary framework for fluid-structure interaction: Isogeometric implementation and application to bioprosthetic heart valves,” *Computer Methods in Applied Mechanics and Engineering*, pp. 14–12, 2014.

[180] I. Temizer, “A mixed formulation of mortar-based contact with friction,” *Computer Methods in Applied Mechanics and Engineering*, vol. 255, pp. 183–195, Mar. 2013.

[181] K. A. Fischer and P. Wriggers, “Frictionless 2d contact formulations for finite deformations based on the mortar method,” *Computational Mechanics*, vol. 36, pp. 226–244, Apr. 2005.

[182] K. A. Fischer and P. Wriggers, “Mortar based frictional contact formulation for higher order interpolations using the moving friction cone,” *Computer Methods in Applied Mechanics and Engineering*, vol. 195, pp. 5020–5036, July 2006.

[183] R. Weyler, J. Oliver, T. Sain, and J. C. Cante, “On the contact domain method: A comparison of penalty and Lagrange multiplier implementations,” *Computer Methods in Applied Mechanics and Engineering*, vol. 205–208, pp. 68–82, 2012.

[184] K. Ito and K. Kunisch, “Semi–smooth Newton methods for variational inequalities of the first kind,” *ESAIM: Mathematical Modelling and Numerical Analysis - Modélisation Mathématique et Analyse Numérique*, vol. 37, no. 1, pp. 41–62, 2003.

[185] F. Lurie, R. L. Kistner, B. Eklof, and D. Kessler, “Mechanism of venous valve closure and role of the valve in circulation: a new concept,” *Journal of Vascular Surgery*, vol. 38, pp. 955–961, Nov. 2003.

[186] F. Lurie, R. L. Kistner, and B. Eklof, “The mechanism of venous valve closure in normal physiologic conditions,” *Journal of Vascular Surgery*, vol. 35, pp. 713–717, Apr. 2002.

[187] R. Gottlob and R. May, *Venous valves. Wien.* New York: Springer-Verlag, 1986.

[188] J. V. Basmajian, “The distribution of valves in the femoral, external iliac, and common iliac veins and their relationship to varicose veins,” *Surgery, Gynecology & Obstetrics*, vol. 95, pp. 537–542, Nov. 1952.

[189] C. Geuzaine and J.-F. Remacle, “Gmsh: A 3-D finite element mesh generator with built-in pre- and post-processing facilities,” *International Journal for Numerical Methods in Engineering*, vol. 79, pp. 1309–1331, Sept. 2009.

[190] M. Grigioni, C. Daniele, U. Morbiducci, C. Del Gaudio, G. D’Avenio, A. Balducci, and V. Barbaro, “A mathematical description of blood spiral flow in vessels: application to a numerical study of flow in arterial bending,” *Journal of Biomechanics*, vol. 38, pp. 1375–1386, July 2005.

[191] F. P. T. Baaijens, “A fictitious domain/mortar element method for fluid–structure interaction,” *International Journal for Numerical Methods in Fluids*, vol. 35, pp. 743–761, Apr. 2001.

[192] A. Quarteroni, M. Tuveri, and A. Veneziani, “Computational vascular fluid dynamics: problems, models and methods,” *Computing and Visualization in Science*, vol. 2, pp. 163–197, Mar. 2000.

[193] M. Hirschvogel, M. Bassilious, L. Jagschies, S. M. Wildhirt, and M. W. Gee, "A monolithic 3d-0d coupled closed-loop model of the heart and the vascular system: Experiment-based parameter estimation for patient-specific cardiac mechanics: 3d-0d coupled closed-loop model of the heart," *International Journal for Numerical Methods in Biomedical Engineering*, 2016.

[194] L. Formaggia, J. F. Gerbeau, F. Nobile, and A. Quarteroni, "On the coupling of 3d and 1d Navier–Stokes equations for flow problems in compliant vessels," *Computer Methods in Applied Mechanics and Engineering*, vol. 191, pp. 561–582, Dec. 2001.

[195] L. Formaggia, J. Gerbeau, F. Nobile, and A. Quarteroni, "Numerical treatment of defective boundary conditions for the Navier–Stokes equations," *SIAM Journal on Numerical Analysis*, vol. 40, pp. 376–401, Jan. 2002.

[196] Y. Bazilevs, M.-C. Hsu, D. J. Benson, S. Sankaran, and A. L. Marsden, "Computational fluid–structure interaction: methods and application to a total cavopulmonary connection," *Computational Mechanics*, vol. 45, pp. 77–89, Sept. 2009.

[197] M. Thiriet, *Biology and mechanics of blood flows. Part I: Biology.* CRM Series in Mathematical Physics, Springer, NY, 2008.

[198] M. Thiriet, *Biology and mechanics of blood flows. Part II: Mechanics and medical aspects.* Springer Science & Business Media, Dec. 2007.

[199] A. H. Shapiro, "Steady flow in collapsible tubes," *Journal of Biomechanical Engineering*, vol. 99, pp. 126–147, Aug. 1977.

[200] E. Kresch and A. Noordergraaf, "Cross-sectional shape of collapsible tubes," *Biophysical Journal*, vol. 12, pp. 274–294, Mar. 1972.

[201] M. Bonis, C. Ribreau, and G. Verchery, "Etude expérimentale et théorique de l'aplatissement d'un tube élastique en dépression," *Journal de Mecanique Appliquee*, vol. 5, no. 2, pp. 123–144, 1981.

[202] M. Bonis and C. Ribreau, "Wave speed in noncircular collapsible ducts," *Journal of Biomechanical Engineering*, vol. 103, pp. 27–31, Feb. 1981.

[203] J. Flaherty, J. Keller, and S. Rubinow, "Post buckling behavior of elastic tubes and rings with opposite sides in contact," *SIAM Journal on Applied Mathematics*, vol. 23, pp. 446–455, Dec. 1972.

[204] C. Ribreau, S. Naili, M. Bonis, and A. Langlet, "Collapse of thin-walled elliptical tubes for high values of major-to-minor axis ratio," *Journal of Biomechanical Engineering*, vol. 115, pp. 432–440, Nov. 1993.

[205] S. I. Rubinow and J. B. Keller, "Flow of a viscous fluid through an elastic tube with applications to blood flow," *Journal of Theoretical Biology*, vol. 35, pp. 299–313, May 1972.

[206] R. Wild, T. J. Pedley, and D. S. Riley, "Viscous flow in collapsible tubes of slowly varying elliptical cross-section," *Journal of Fluid Mechanics*, vol. 81, pp. 273–294, June 1977.

[207] C. D. Bertram, "Two modes of instability in a thick-walled collapsible tube conveying a flow," *Journal of Biomechanics*, vol. 15, pp. 223–224, Jan. 1982.

[208] W. A. Conrad, "Pressure–flow relationships in collapsible tubes," *IEEE Transactions on Bio-Medical Engineering*, vol. 16, pp. 284–295, Oct. 1969.

[209] C. Ribreau, *Sur la loi d'état, la loi de perte de charge, et la nature de l'écoulement permanent en conduite collabable inclinée*. Paris 12, Jan. 1991.

[210] C. D. Bertram, C. J. Raymond, and T. J. Pedley, "Application of nonlinear dynamics concepts to the analysis of self-excited oscillations of a collapsible tube conveying a fluid," *Journal of Fluids and Structures*, vol. 5, pp. 391–426, July 1991.

[211] J. She and C. D. Bertram, "Numerical simulation of collapsible-tube flows with sinusoidal forced oscillations," *Bulletin of Mathematical Biology*, vol. 58, pp. 1023–1046, Nov. 1996.

[212] X. Y. Luo and T. J. Pedley, "A numerical simulation of unsteady flow in a two-dimensional collapsible channel," *Journal of Fluid Mechanics*, vol. 314, pp. 191–225, May 1996.

[213] T. J. Pedley and X. Y. Luo, "Modelling flow and oscillations in collapsible tubes," *Theoretical and Computational Fluid Dynamics*, vol. 10, pp. 277–294, Jan. 1998.

[214] J. B. Grotberg and S. H. Davis, "Fluid-dynamic flapping of a collapsible channel: Sound generation and flow limitation," *Journal of Biomechanics*, vol. 13, pp. 219–230, Jan. 1980.

[215] P. Jolivet, F. Hecht, F. Nataf, and C. Prud'homme, "Scalable domain decomposition preconditioners for heterogeneous elliptic problems," in *Proceedings of the International Conference on High Performance Computing, Networking, Storage and Analysis*, SC '13, (New York, NY, USA), pp. 80:1–80:11, ACM, 2013.

# List of Figures

# List of Tables

# Scripts

# Abstract

The present work aims at developing a numerical solver for fluid–structure interaction (FSI) problems, especially those encountered in biology such as blood circulation in valved veins. Blood flow is investigated using anatomically and physically relevant models.

Computational procedures are conceived, designed, and implemented in a platform that couples the cheapest cost and the fastest processing using high-performance computing.

The first aspect of FSI problems is related to management of algorithm stability. An Eulerian monolithic formulation based on the characteristic method unconditionally achieves stability and introduce a first order in time approximation with two distinct hyperelastic material models.

The second aspect deals with between-solid domain contact such as that between valve leaflets during closure and in the closed state over a finite surface, which avoid vcusp tilting and back flow. A contact algorithm is proposed and validated using benchmarks.

Computational study of blood flow in valved veins is investigated, once the solver was verified and validated. The 2D computational domain comprises a single basic unit or the ladder-like model of a deep and superficial veins communicating by a set of perforating veins. A 3D mesh of the basic unit was also built. Three-dimensional computation relies on high performance computing.

Blood that contains cells and plasma is a priori a heterogeneous medium. However, it can be assumed homogeneous in large blood vessels, targets of the present study. Red blood capsules that represent the vast majority of blood cells (97%) can deform and aggregate, influencing blood rheology. However, in large veins, in the absence of stagnant flow regions, blood behaves as a Newtonian fluid.

Blood flow dynamics is strongly coupled to vessel wall mechanics. Deformable vascular walls of large veins and arteries are composed of three main layers (intima, media, and adventitia) that consist of composite material with a composition specific to each layer. In the present work, the wall rheology is assumed to be a Mooney–Rivlin material.

**Keywords** : blood flow; eulerian monolithic formulation; fluid–structure interaction; hyperelastic model; Mooney–Rivlin model; $\mathrm{S^t}$–Venant–Kirchhoff model; finite element method; FreeFem++ solver; valved veins

# Résumé

Le travail de cette thèse a pour objectif de développè un solveur dèdié aux problèmes d'interaction fluide–structure (IFS), en particulier ceux rencontré en biologie, tels que la dynamique d'un écoulement sanguin à travers des tronçons veineux munis de valves. La circulation du sang est étudée à l'aide de modèles pertinents sur les plans anatomique et physique

Des procédures computationelles sont conçues et implémentées à l'aide d'une plateforme de calcul avec un protocole couplant le moindre coût et la rapidité de calcul par des techniques de calcul haute performance.

Le premier aspect des problèmes d'IFS concerne la gestion de la stabilité. Une formulation monolithique eulerienne basée sur la méthode des caractéristiques assure la stabilité unconditionelle et introduit une approximation du premier ordre en temps avec deux modèles distincts de matériaux hyperelastiques.

Le second aspect est relatif au contact entre deux parties du domain solide, tel celui apparaissant entre deux valvules au cours de la fermeture de la valve et à l'état fermé sur un surface valvulaire relativement importante. Un algorithme de contact est proposé and validé à l'aide de tests de référence.

L'étude computationelle de l'écoulement sanguin à travers des tronçons veineux munis de valves est mené, une fois le solveur IFS vérifié and validé. Le domaine computationel bidimensionnel est soit constitué d'une simple unité de base, soit du modèle de circuit veineux en forme d'échelle avec une veine superficielle et une profonde, communicant par une série de veines perforantes. Un maillage tridimensionnel de l'unité de base a été construit. Les simulations dans ce domaine tridimensionel nécessite le recours au calcul haute performance.

Le sang contient des cellules and du plasma; il est a priori hétérogène. Toutefois, il peut être considéré homogène dans les vaisseaux sanguins de gros calibre, les cibles de cette étude. Les erythrocytes (en fait des capsules contenant essentiellement une solution d'hémoglobine pour le transport de l'oxygène), qui représentent la majorité des cellules sanguines (97%), peuvent se déformer et s'aggréger selon une certain dynamique, influencant la rhéologie du sang. Cependant, dans les grosses veines, en l'absence of régions où le sang stagne, le sang se comporte comme un fluide newtonien.

La dynamique de l'écoulement sanguin est fortement couplée à la méchanique de la paroi vasculaire. La paroi déformable des veines et artères de gros calibre est composée de trois couches principales (l'intima, la media, et l'adventitia) constituées de matériaux composites ayant une composition spécifique dans chaque couche. Dans ce travail, la rhéologie de la paroi est supposée être représentée par un matériau du type Mooney–Rivlin.

**Keywords** : écoulement sanguin; formulation monolithique eulerienne; interaction fluide–structure; matériau hyperélastique; méthode des éléments finis; modèle de Mooney–Rivlin; modèle de $\mathrm{S}^{\mathrm{t}}$–Venant–Kirchhoff; solveur FreeFem++; veine valvulée